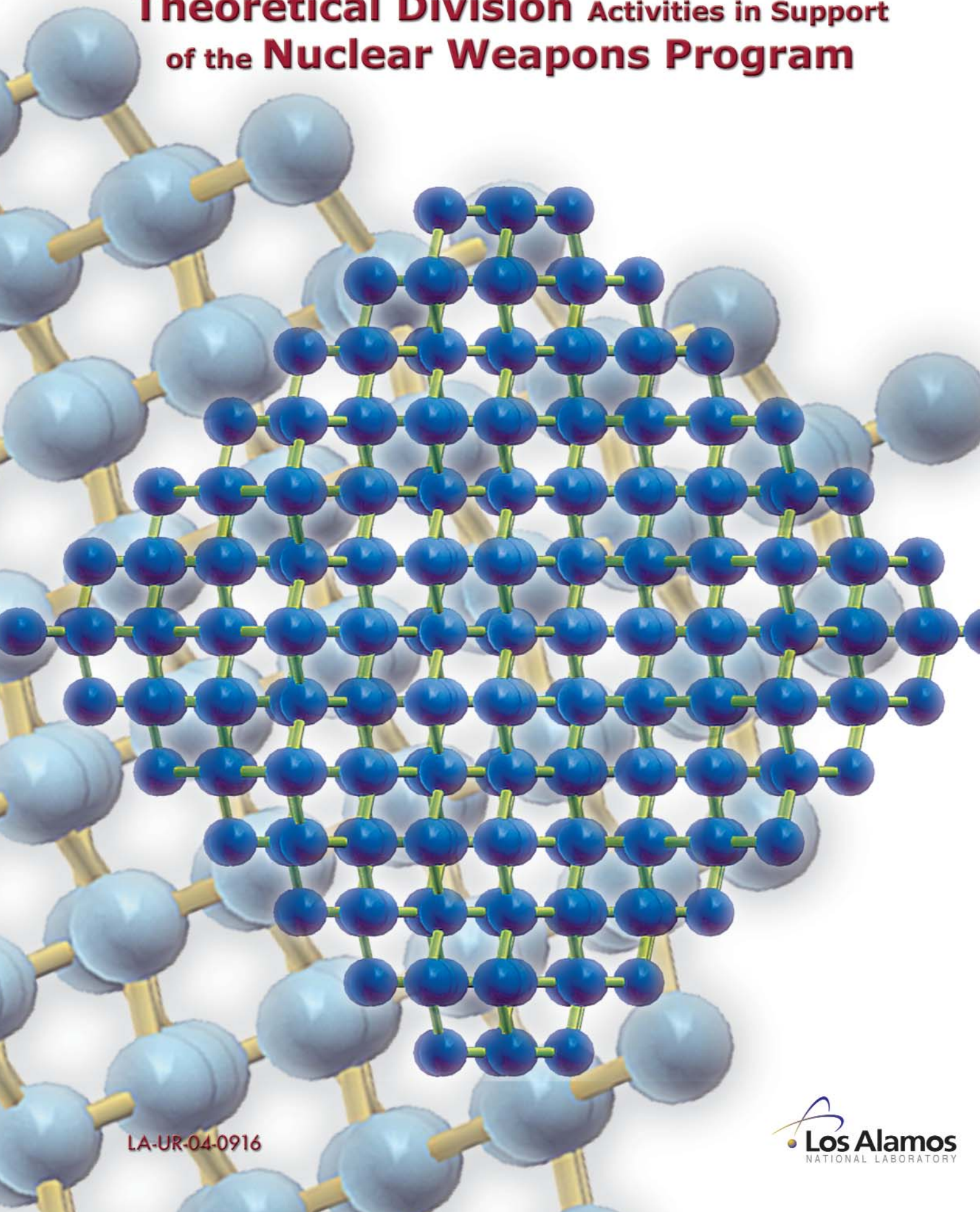


Theoretical Division Activities in Support of the Nuclear Weapons Program



LA-UR-04-0916



Published by Los Alamos National Laboratory, Theoretical Division

Publication Design: Shirley Veenis

Proof Editor: Jody Shepard

LA-UR-04-0916

Los Alamos National Laboratory, an affirmative action/equal opportunity employer, is operated by the University of California for the U.S. Department of Energy under contract W-7405-ENG-36. By acceptance of this article, the publisher recognizes that the U.S. Government retains a nonexclusive, royalty-free license to publish or reproduce the published form of this contribution, or to allow others to do so, for U.S. Government purposes. Los Alamos National Laboratory requests that the publisher identify this article as work performed under the auspices of the U.S. Department of Energy. Los Alamos National Laboratory strongly supports academic freedom and a researcher's right to publish; as an institution, however, the Laboratory does not endorse the viewpoint of a publication or guarantee its technical correctness.

A U.S. Department of Energy Laboratory



Theoretical Division Activities in Support of the Nuclear Weapons Program

Theoretical Division Leader

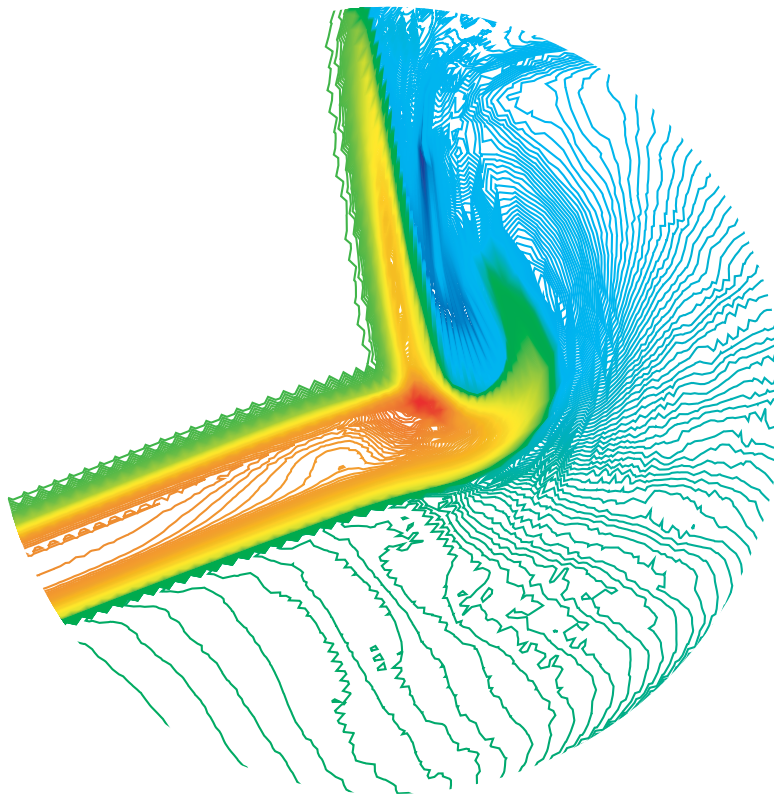
Alan R. Bishop

Theoretical Division Deputy Division Leader

Paul J. Dotson

Nuclear Weapons Advisor

Francis H. Harlow



Contents

Equation of State

Liquid Dynamics Estimates of the Viscosity Coefficient of Liquid Metals, 2

Eric D. Chisolm and Duane C. Wallace, T-1

Estimating the Accuracy of the TFD Cold Curve, 4

Eric D. Chisolm, Scott D. Crockett, Duane C. Wallace,
and John M. Wills, T-1

Extending the CCW EOS: Extending the Cold and Nuclear Contributions, to High Compression, 6

Eric D. Chisolm, Scott D. Crockett, and Duane C. Wallace, T-1

Unified Model of the Gruneisen Parameter, Melting Temperature, and Shear Modulus, 8

Leonid Burakovsky, T-1 and Dean L. Preston, X-7

Variation of Thermal and Cold Curve Contributions to Thermodynamic Functions along the Hugoniot, 10

Eric D. Chisolm, Scott D. Crockett, and Duane C. Wallace, T-1

A Comparison of Theory and Experiment of the Bulk Sound Velocity in Aluminum Using a Two-Phase EOS, 12

Scott D. Crockett, Eric D. Chisolm, and Duane C. Wallace, T-1

Equation of State Developments in T-1, 14

Eric D. Chisolm, Scott D. Crockett, Giulia De Lorenzi-Venneri, Denise C.
George, J. D. Johnson, Duane C. Wallace, and John M. Wills, T-1

Fluid Dynamics

Atomistic Description of Rayleigh-Taylor Instabilities, 18

Kai Kadau and Peter S. Lomdahl, T-11; Timothy C. Germann, X-7; Brad Lee
Holian, T-12; Guy Dimonte, X-4; Nicolas G. Hadjiconstantinou, Massachusetts
Institute of Technology; Berni Alder, Lawrence Livermore National Laboratory

Simulation of Multiphase Flow in Centrifugal Contactors for Process Intensification at TA-55, 20

Nely Padial-Collins and W. Brian VanderHeyden, T-3

Two-Mesh Computation for the Telluride Casting Project, 22

Andrew P. Kuprat, T-1

- Extension of the KIVA Particle/Spray Model to Flows with Compressible Particles, 24**
Peter J. O'Rourke and David J. Torres Group, T-3
- ALE INC. New 2D ALE Code on General Polygonal Meshes, 26**
Raphaël Loubère and Mikhail J. Shashkov, T-7
- Curvature Estimation for Unstructured Triangulations of Surfaces, 28**
Rao V. Garimella and Blair K. Swartz, T-7
- Mimetic Finite Difference Methods for Diffusion Equations on Non-Orthogonal AMR Meshes, 30**
Konstantin Lipnikov and Mikhail Shashkov, T-7; Jim Morel, CCS-2
- Multilevel Accelerated Optimization for Problems in Grid Generation, 32**
Markus Berndt and Mikhail J. Shashkov, T-7
- Numerical Methods for Simulation of the Heating through Electromagnetic Induction, 34**
Mikhail J. Shashkov, T-7; Neil Carlson, Independent Consultant
- Parallel, Scalable, and Robust Multigrid for Diffusion Problems on Structured Grids, 36**
John D. Moulton, Travis M. Austin, Markus Berndt, Benjamin K. Bergen, and Joel E. Dendy, T-7
- A Software Component for a Sign-Preserving and Linearity-Preserving ALE Remapping Method, 38**
Martin F. Staley and Mikhail J. Shashkov, T-7

Atomic Physics

- ATOMIC Benchmark Opacity Calculation, 42**
Joseph Abdallah, Jr., Peter Hakel, David P. Kilcrease, Norman H. Magee, Stephane F. Mazevet, and Manolo E. Sherrill, T-4; Christopher J. Fontes and Honglin Zhang, X-5
- Benchmarking Aluminum Opacity Libraries using Quantum Molecular Dynamics, 44**
Stephane F. Mazevet, Lee A. Collins, and Norman H. Magee, T-4; Joel D. Kress, T-12; Eric D. Chisolm and Scott Crockett, T-1; and M. Desjournais, Sandia National Laboratory
- Generating a Portable Version of CATS, 48**
Manolo E. Sherrill, T-4
- Quantum Molecular Dynamics Simulations of Shocked Nitrogen Oxide, 50**
Stephane F. Mazevet and Lee A. Collins, T-4; Joel D. Kress, T-12; and P. Blottiau, DPTA

Time Dependent Boltzmann-Kinetic Model of the X-rays Produced by the Ultrashort Pulse Laser Irradiation of Argon Clusters, 54

Joseph Abdallah, Jr. and George Csanak, T-4

Nuclear Physics

Data for Charged-Particle Capture Reactions, 58

Gerald M. Hale, T-16

Iridium Nuclear Cross Sections for Radchem, 60

Patrick Talou, Mark B. Chadwick, and Robert MacFarlane, T-16;
Ronald O. Nelson, LANSCE-3; Holly R. Trellue, D-5; Morgan C. White
and Stephanie C. Frankle, X-5; and Nikolaos Fotiadis, LANSCE

New Suite of Evaluated Nuclear Reaction Cross Sections on Uranium Isotopes, 62

Phillip G. Young, Patrick Talou, Robert MacFarlane, Mark B. Chadwick,
Toshihiko Kawano, David G. Madland, Peter Möller,
and William B. Wilson, T-16

Studies of Fission-Product Yields with Improved Data Bases for β -Decay Half-Lives and Delayed Neutron-Emission Probabilities, 64

Peter Möller, T-16 and William B. Wilson, T-4

The ^8Be Nuclear Data Evaluation, 70

Philip R. Page and Gerald M. Hale, T-16

The Physics of Yttrium Equivalence for Radiochemical Detectors, 72

Anna C. Hayes and Gerard Jungman, T-6

Plasma Physics

Plasmon Pole Approximation for Warm Dense Matter Calculations: Application to Temperature Relaxation in Nonequilibrium Systems, 76

Michael S. Murillo, T-15 and George Csanak, T-4

Exact Treatment of Ion Collective Modes in the Fermi Golden Rule Description of Temperature Relaxation, 78

George Csanak, T-4; Michael S. Murillo, T-15; William S. Daughton, X-1

Chemical and Molecular Physics

Theoretical Studies of Surface Chemistry and Bulk Electronic Structure of Actinide Materials, 84

P. Jeffrey Hay, Joel D. Kress, and Hank Ashbaugh, T-12

Mesoscale Modeling of Nanocrystalline Metals, 86

Cynthia Reichhardt, Brad Lee Holian, Joel D.Kress, and Antonio Redondo, T-12

All-electron Density Functional Studies of Hydrostatic Compression of Pentaerythritol Tetranitrate (PETN), 88

Chee Kwan Gan, T-12; Thomas D. Sewell, T-14; and Matt Challacombe, T-12

Quantum Chemical and Classical Studies of The High Pressure Phase of Teflon, 90

Holmann V. Brand, X-7; Dana M. Dattelbaum, MST-7; Jessica M. Ryan and Kerri Jean Kress, X-7; and Neil J. Henson, T-12

Models for the Aging of Fogbank, 92

Edward M. Kober, T-14

Theory and Simulation of Polymer Aging: Degradation via Free-Radical Oxidation, 94

Joel D. Kress, T-12; Mike Salazar, Union Univ.; and Russell T Pack, T-12

Condensed Matter and Material Science

Atomistic Understanding of Ti Phase Transformations, 98

Robert C. Albers, T-11; Sven P. Rudin, T-1; S. G. Srivilliputhur, MST-8; in collaboration with M. D. Jones, SUNY-Buffalo; R. G. Hennig, D. R. Trinkle, and J. W. Wilkins, Ohio State; D. M. Hatch and H. T. Stokes, BY Univ.

Modeling Phase Transformations in Solids, 100

Francis L. Addessio, T-3 and Dennis B. Hayes, DX-2

Structural Phase Transitions in Ga: Massive Parallel Implementation and Application of the Modified Embedded-Atom Method, 102

Kai Kadau, T-11; Timothy C. Germann, X-7; Peter S. Lomdahl, T-11; and Brad Lee Holian, T-12

Molecular-Dynamics Study of Mechanical Deformation in Nano-Crystalline Metals, 104

Kai Kadau, T-11; Timothy C. Germann, X-7; Peter S. Lomdahl, T-11; and Brad Lee Holian, T-12

Elastic Moduli of Multiblock Copolymers, 106

Russell B. Thompson, Kim Ø. Rasmussen, and Turab Lookman, T-11; and Edward M. Kober, T-14

Improved Continuum Models for Polymers and Associated Experiments, 108

Brad E. Clements and Eric M. Mas, T-1; Dana M. Dattelbaum, Edward B. Orler, and Eric Brown, MST-7; Philip Rae and George T. Gray III, MST-8; Stephen Sheffield and David L. Robbins, DX-2; Neil J. Henson, T-12; Eric N. Harstad, T-3; Luca A. Maciucescu and Matthew W. Lewis, ESA-WR; Holmann V. Brand, Kerri Jean Kress, and Jessica M. Ryan, X-7

Direct Numerical Simulations of PBX 9501, 110

Eric M. Mas, Brad E. Clements, and Denise C. George, T-1

HMX Crystal Diameter Distributions From Image Analysis, 114

Bernd R. Schlei, T-1

Developments Toward a Continuum-Level Non-Spherical Void Growth Model Using a Micro-Mechanics Basis, 116

Brad E. Clements and Eric M. Mas, T-1; and Paul J. Maudlin, T-3

Predicting Strain Localization in Anisotropic Materials, 118

Q. Ken Zuo, Justin R. Smith, Paul J. Maudlin, and Francis L. Addessio, T-3

Lattice Effects in Gallium-Doped Plutonium, 120

Sven P. Rudin and John M. Wills, T-1

New Pseudostructure for α -Pu, 122

M. Johan Bouchet and Robert C. Albers, T-11

Stable and Unstable Phonon Modes in and around bcc Plutonium, 124

Sven P. Rudin, T-1

Accelerated Dynamics Study of Vacancies in Pu, 126

Blas P. Uberuaga and Arthur F. Voter, T-12; and Steven M. Valone and Michael Baskes, MST-8

The Promise of Liquid Dynamics Theory, 130

Giulia De Lorenzi-Venneri and Duane C. Wallace, T-1

Detonation and Shock

β -HMX Isotherms at Multiple Temperatures and Liquid HMX Equation of State, 134

Eugenio Jaramillo and Thomas D. Sewell, T-14

Molecular Dynamics Studies of Reactive Processes in RDX II: Shock Loading, 136

Alejandro H. Strachan, T-14

Molecular Dynamics Studies of Reactive Processes in RDX I: Thermal Loading, 140

Alejandro H. Strachan, T-14

Fundamental Detonation Behavior from Molecular Dynamics Simulations, 144
Andrew J. Heim, T-14/UC-Davis; Timothy C. Germann, X-7; Brad Lee Holian
and Edward M. Kober, T-14; and Niels G. Jensen, UC-Davis

How Do Hotspots Happen?, 146
Brad Lee Holian, T-12 and Timothy C. Germann, X-7

Pore Collapse and Hot Spots, 148
Ralph Menikoff, T-14

Detonation Products Equation of State, 150
M. Sam Shaw, T-14

High-Explosives Safety Study, Update, 152
Qisu Zou, Duan Z. Zhang, W. Brian VanderHeyden, Francis H. Harlow,
and Nely Padial-Collins, T-3

Numerical Simulation of Stress Wave Propagation in PBXs, 154
Scott G. Bardenhagen, T-14

On Validating SCRAM, 156
John K. Dienes, John Middleditch, and Q. Ken Zuo, T-3

Constitutive Model Development for Filled Polymer Systems, 158
Edward M. Kober, T-14; and James S. Smith and Grant D. Smith, Univ. Utah

Numerical Simulation of Full Densification of Foams, 160
Scott G. Bardenhagen, T-14

Modeling the Dynamic Response of Disordered Cellular Materials, 162
Mark W. Schraad and Francis H. Harlow, T-3

Polymer and Foam Products Equation of State, 164
M. Sam Shaw, T-14

Astrophysics

Code Verification for Thermonuclear Supernovae, 168
Peter A. Milne, T-6; Aimee L. Hungerford, CCS-4; and Christopher L. Fryer, T-6

Theoretical Division Activities in Support of the Nuclear Weapons Program

Introduction

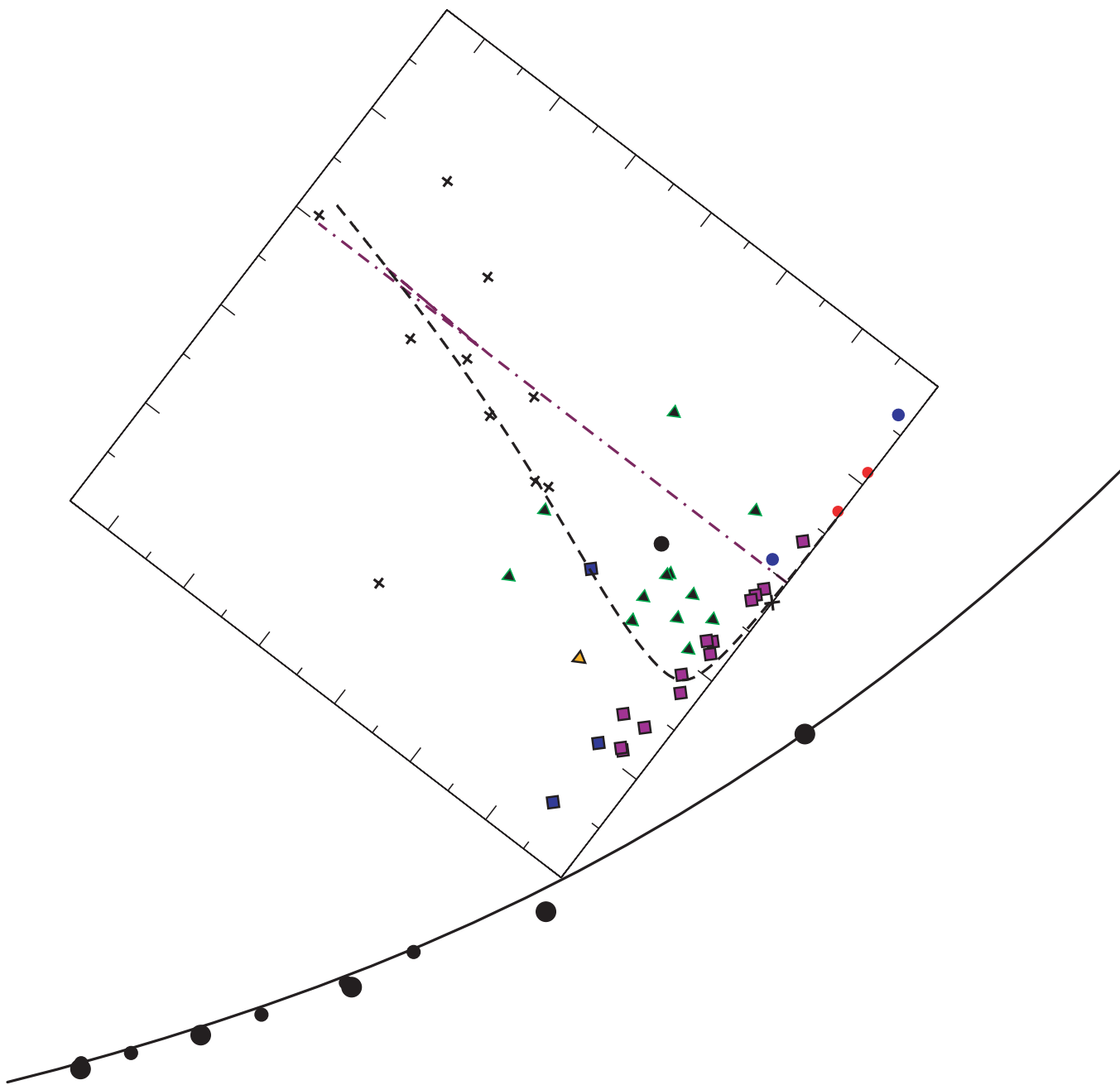
Theoretical Division plays an important role in the Nuclear Weapons program at Los Alamos, providing a significant amount of the underlying theoretical and modeling capability in the areas of dynamic materials response and equation of state, nuclear and atomic physics, plasma physics, fluid mechanics, and computational methods for the Laboratory. These capabilities are brought to bear, in collaboration with our colleagues elsewhere in the Laboratory, on the increasingly challenging problems arising from the Stockpile Stewardship Program. In order to validate a truly predictive simulation capability, the fidelity of the underlying physics descriptions must continue to improve, and this requires the development and implementation of more sophisticated physics models into the simulation codes, in a close partnership with our experimental, modeling, and simulation capabilities.

In addition to providing much of the theoretical physics capability to the NW program, Theoretical Division also has the responsibility for the management of the ASC Materials and Physics Program, which plans and supports this work throughout the Laboratory, building inter-divisional teams of researchers from the various technical organizations. The Division then has the responsibility to work with other sub-programs with ASC, and with the experimental programs, to implement and validate these models and to strive for the predictive simulation tools that are needed to address the Laboratory's responsibilities for Stockpile Stewardship.

Paul J. Dotson
Deputy Division Leader, Theoretical Division
Program Manager, ASC Materials and Physics Program



Equation of State



Liquid Dynamics Estimates of the Viscosity Coefficient of Liquid Metals

Eric D. Chisolm and Duane C. Wallace,
T-1; echisolm@lanl.gov

Values of the viscosity coefficient η for liquid metals, over a wide range of densities and for all temperatures above melting, are needed for computer simulations related to the function of primary nuclear explosive systems. Viscosity measurements have been conducted only at a pressure of 1 bar, so this need can be met only by developing means for predicting η when data are unavailable. With this in mind, we have created a simple semiempirical method for calculating η which uses a liquid dynamics model developed by Wallace [1] to compute the self-diffusion coefficient D , and then determines η from the Stokes-Einstein relation. We tested the accuracy of this technique by computing D and η for 21 liquid metals at melt at a pressure of 1 bar; we then compared the D results to experiment for 14 of these metals (no data are available for the others),

and we compared with η results for all 21 metals; we found

$$\begin{aligned} D_{theory} / D_{expt} &= 1.03 \pm 0.18 \\ \eta_{theory} / \eta_{expt} &= 1.00 \pm 0.18, \end{aligned}$$

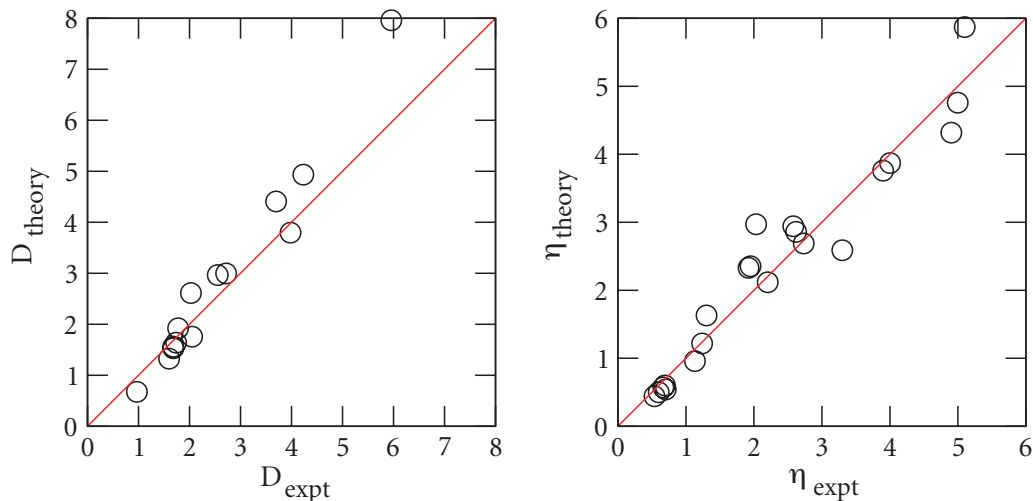
as also shown in Figure 1. This is a noticeable improvement over other empirical models; for example, one of the best such models, the Da Andrade formula, was used to compute η for 20 liquid metals at melt at 1 bar (Table III of [2]), with the result

$$\eta_{theory} / \eta_{expt} = 1.15 \pm 0.34.$$

In fact, this technique is not much less accurate than first principles molecular dynamics calculations [3], while being considerably less computationally intensive.

This method provides an easy means of computing η , and it can easily be extended to arbitrary densities purely theoretically by means of electronic structure calculations of θ_0 as a function of density. Since θ_0 is also used in the newer means of generating equations of state currently under development [4], this method also provides a connection

Figure 1—
 D_{theory} vs. D_{expt}
for 14 metals and
 η_{theory} vs. η_{expt}
for 21 metals, all
at melt at 1 bar.



between equilibrium and transport properties. In order to use these results at higher temperatures, though, the model in [1] must be extended to include temperature dependence. This work could be completed in the foreseeable future, providing a means for computing η for primary calculations over the full range of ρ and T they require.

This work is described in further detail in LA-UR-03-6847.

[1] D. C. Wallace, *Phys. Rev. E* **58**, 538 (1998).

[2] J. A. Alonso and N. H. March, *Phys. Rev. E* **60**, 4125 (1999).

[3] D. Alfe and M. J. Gillan, *Phys. Rev. Lett.* **81**, 5161 (1998).

[4] E. D. Chisolm, S. D. Crockett, and D. C. Wallace, *Phys. Rev. B* **68**, 104103 (2003).



Estimating the Accuracy of the TFD Cold Curve

Eric D. Chisolm, Scott D. Crockett, Duane C. Wallace, and John M. Wills, T-1; echisolm@lanl.gov

A component in the standard decomposition of equations of state (EOS) at Los Alamos is the cold curve, the electronic contribution to the $T=0$ isotherm. It is known that the cold curve predicted by the Thomas-Fermi-Dirac (TFD) model converges to the true quantum mechanical cold curve as compression increases without bound; however, it is not known how rapidly this convergence occurs. Early efforts to determine this [1] suggested the two had converged by a pressure of 10 Mbar; however, later calculations showed that convergence had not occurred by 100 Mbar for some materials [2]. Since the SESAME tables require the cold curve for a material up to compressions around 10^4 , well beyond any practical electronic structure calculation at the moment, and since TFD yields results much more easily than density functional theory, it is of great interest to establish the compression, if any, at which TFD correctly predicts the cold curve pressure to a given accuracy, say 10%.

To try to determine this, we reviewed some basic theoretical properties of TFD, which allowed us to conclude only that convergence will require compressions above 10^4 for all but the smallest values of Z ; beyond this, however, we could conclude nothing about the magnitude, sign, or density dependence of the discrepancy. We then turned to numerical comparisons of TFD with electronic structure

calculations of the cold curve for two elements, Al and Li.

The Al results are a compilation of three separate electronic structure calculations; only one calculation was available for Li. In both cases we see the general feature that the TFD pressure is too high near normal density; this is because TFD has much weaker binding, hence much larger zero-pressure volume, than electronic structure theory. In Al, the error oscillates from positive to negative twice, then remains positive and decreases monotonically, down to 5% at $\eta = 60$ ($P = 9000$ Mbar) and 1% at $\eta = 300$ ($P = 10^5$ Mbar). It is reasonable that the error continues to approach zero as compression increases. The less extensive Li results show no such trend; the error fluctuates around 5% at compressions up to 60, showing no evidence of a steady decrease. Thus these two test cases give us little guidance for understanding how rapidly TFD approaches the true quantum mechanical cold curve as a function of compression.

Given these uncertain results, we make two recommendations regarding the construction of cold curves for EOS: (1) experimental data and density functional theory results should be used in combination to construct the cold curve whenever possible, and (2) when this is not possible, the TFD cold curve should be tacked on where the density functional theory result terminates. In the first case, we can have great confidence in the accuracy of the cold curve; we have less confidence in the second case, particularly at the lowest compressions where TFD is used.

This work is described in more detail in LA-UR-03-7346.

[1] H. Jensen, *Z. Physik* **111**, 373 (1938).

[2] W. G. Zittel, J. Meyer-ter-Vehn, J. C. Boettger, and S. B. Trickey, *J. Phys. F: Met. Phys.* **15**, L247 (1985).

19

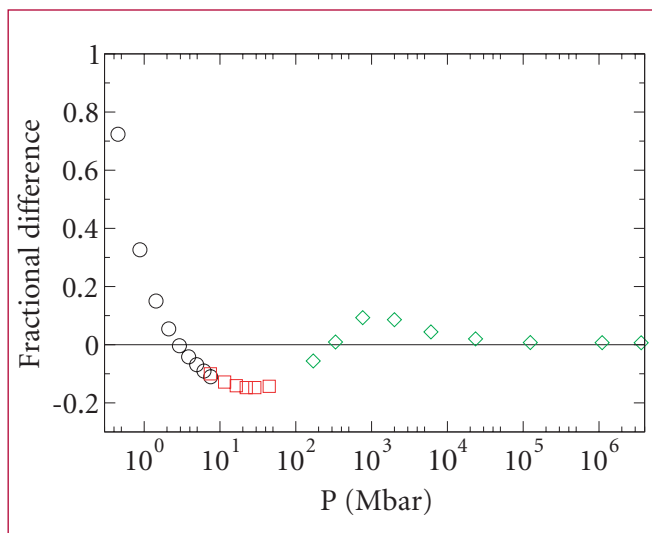


Figure 1—
The fractional deviation of the $T=0$, $Z=13$ TFD pressure from the electronic pressure predicted at $T=0$ for Al by electronic structure calculations, as a function of pressure.

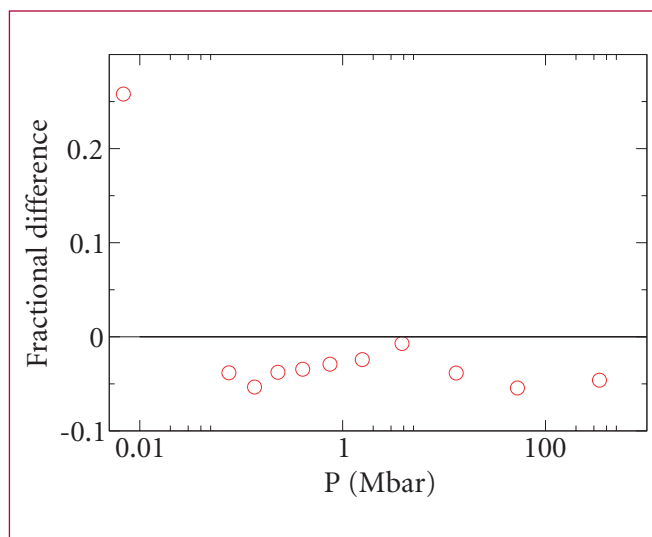


Figure 2—
The deviation of the $T=0$, $Z=3$ TFD pressure from the electronic pressure predicted at $T=0$ for Li.

Extending the CCW EOS: Extending the Cold and Nuclear Contributions to High Compression

Eric D. Chisolm, Scott D. Crockett, and Duane C. Wallace, T-1; echisolm@lanl.gov

Recent work in T-1 has been undertaken to apply the results summarized in [1] to make new equations of state (EOS) for real materials in the "condensed matter regime" ($\rho \geq \rho_{\text{ref}}$), and to extend the procedures as necessary to generate new SESAME tables, intended to be the most accurate such tables it is possible to produce. We refer to EOS developed in this program by the initials CCW, standing for the authors of the first paper to make such an EOS [2].

The range of this first EOS is limited to compressions between 1.0 and 2.2 and temperatures below 3 eV by (a) the availability of density functional theory (DFT) and experimental results required as inputs and (b) the requirement that the temperature is not so high that the nuclear motion becomes gaslike, rendering the liquid theory inapplicable (for a review of the liquid theory, see [3]). This range is still considerable, but a typical SESAME EOS [4] covers compressions from 10^4 to 10^4 and temperatures up to 10^5 eV; thus to construct SESAME EOS using this theory we must consider how to extend its range of validity substantially. This requires meeting two challenges:

1. We must develop a means to extend the EOS to higher densities, where DFT and experimental results are not available but the theory is still sound.
2. We must extend the theory itself to high temperatures, where the nuclear

motion becomes gaslike, and to densities below ρ_{ref} .

Here we report our progress on the first challenge; later work will address the issues that remain.

Our strategy is to rely on basic conclusions from condensed matter theory and observed trends in low-compression material behavior to form a picture of a generic material at extreme compressions; we then develop both the thermal properties of this high-compression state and interpolations between this state and our original EOS. Specifically, since nonmetals become metals under high compression while metals remain metallic, we assume all elements at high compressions to be a generic metal in both phases, with thermodynamic properties that depend only on density and temperature (no crystal structure dependence, no distinct solid phases). Since both crystal and liquid are metallic, melting is "normal" (no significant change in electronic structure at melt; see [3]), at high compressions. This picture of a structureless metal crystal that melts normally to a metal liquid is what we will investigate at high compressions, together with the required interpolations.

A CCW EOS requires several inputs for each phase: the cold curve Φ_0 ; the quantities θ_0 and θ_2 , calculated from moments of the phonon spectrum and used in the nuclear contribution to the EOS; and the electronic density of states $n(\epsilon)$. The melt curve $T_m(P)$, which follows from the crystal and liquid EOS jointly, is also useful. Here we will describe extensions of the cold curve, nuclear parts, and T_m , leaving the electronic part to a later report. For the crystal cold curve, we draw on the Thomas-Fermi-Dirac (TFD) one-atom

statistical model, which carries no dependence on the particular crystal structure. It is known that $T = 0$ TFD converges to the true cold curve in the limit of infinite compression, but it is not known how the error term behaves [5]. In the absence of such knowledge, we simply interpolate between the CCW EOS cold curve and the TFD cold curve such that the interpolation is twice differentiable at the point where our knowledge of the CCW cold curve ends.

The quantity needed to extend θ_0 and θ_2 to high densities is the Gruneisen parameter γ_0 , which can be integrated to yield θ_0 , from which θ_2 can be approximated to a high degree of precision. The rule $\rho\gamma = \text{constant}$, often used in shock studies, not helpful here because γ is the total Gruneisen parameter, which is close to γ_0 at compressions of two to three at most along the Hugoniot (beyond this point the electrons, not the nuclei, dominate). However, results from the one-component plasma at high densities [6] suggest $\gamma_0 \rightarrow 1/2$ as a possible limit. Once the limit is determined, γ_0 from the CCW EOS can be interpolated to it, allowing computation of θ_0 , θ_2 , and the nuclear contributions in both phases.

We find the melt curve and liquid cold curve by using the melt rule on page 236 of [1] to calculate $T_m(\rho_{lm})$, where ρ_{lm} is the density of the liquid at melt, at high compressions. We then smoothly join this curve to the low-compression melt curve from the CCW EOS, and finally we determine $T_m(P)$ and ϕ_0^1 iteratively; we guess Φ_0^1 , calculate the difference in Gibbs free energies between liquid and crystal along the melt curve, and use the result to correct Φ_0^1 , continuing until the difference becomes negligible.

At this point, the remaining tasks are:

1. to extend the electronic excitation contribution to higher compressions and
2. extend the theory itself down in density and up in temperature. Work in these areas is underway and will be described in later reports.

Details of this work can be found in LA-UR-03-7344.

[1] D. C. Wallace, *Statistical Physics of Crystals and Liquids* (World Scientific, Singapore, 2002).

[2] E. D. Chisolm, S. D. Crockett, and D. C. Wallace, *Phys. Rev. B* **68**, 104103 (2003).

[3] E. D. Chisolm and D. C. Wallace, *J. Phys.: Condens. Matter* **13**, R739 (2001).

[4] S. P. Lyon and J. D. Johnson, "T-1 Handbook of the Sesame Equation of State Library," Los Alamos Report LA-CP-98-100.

[5] E. D. Chisolm, S. D. Crockett, D. C. Wallace, and J. M. Wills, "Estimating the Accuracy of the TFD Cold Curve," Los Alamos Report (see p. 4 of this volume).

[6] D. A. Young, *Phase Diagrams of the Elements* (Univ. of California Press, Berkeley, 1991).



Unified Model of the Gruneisen Parameter, Melting Temperature, and Shear Modulus

L. Burakovsky, T-1 and D. L. Preston, X-7, burakov@lanl.gov

A reliable model of the adiabatic (isentropic) shear modulus of a polycrystalline solid at temperatures up to the melting temperature, and up to megabar pressures is needed for many applications. It is generally assumed that the ratio of the plastic flow stress (shear stress necessary to induce plastic deformation at a given strain rate) to the shear modulus is approximately independent of pressure. In other words, the predominant pressure dependence of the plastic flow stress is contained in the shear modulus. An accurate, simple analytic (for fast evaluation) model of the shear modulus is therefore essential for numerical simulations of material deformation over extremes of pressure and temperature.

We have developed a new unified analytic model of the Gruneisen parameter, melting temperature and shear modulus. It is based on three essential components. First is a relation between the melting temperature and the shear modulus at melt obtained from our dislocation-mediated melting model. The second ingredient is a relation between the Gruneisen parameter and the density derivative of the zero-temperature shear modulus, and the third is a linear approximation for the temperature dependence of the shear modulus at a given density. The model allows one to construct all three, the Gruneisen parameter, melting

curve, and shear modulus, in terms of a common set of input parameters, thus providing independent tests for its validity, by comparing each of the three to the corresponding data.

The reliability of the model has been proven by means of good to excellent agreement of the predicted melting curves and shear moduli to available experimental data and theoretical calculations on over a quarter of the elements in the periodic table.

The model has been used for the construction of the new SESAME melting curve and shear modulus tables. In Figures 1 and 2, new SESAME shear modulus tables (solid curves) are compared to experimental data and theoretical calculations (points of different sizes) for iron and gold, respectively, to compressions of two.



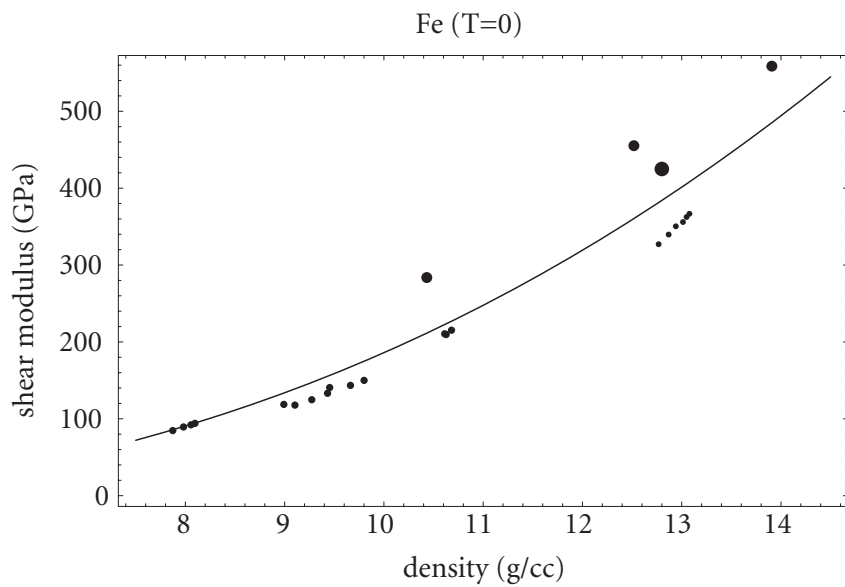


Figure 1—
Shear Modulus (GPa).

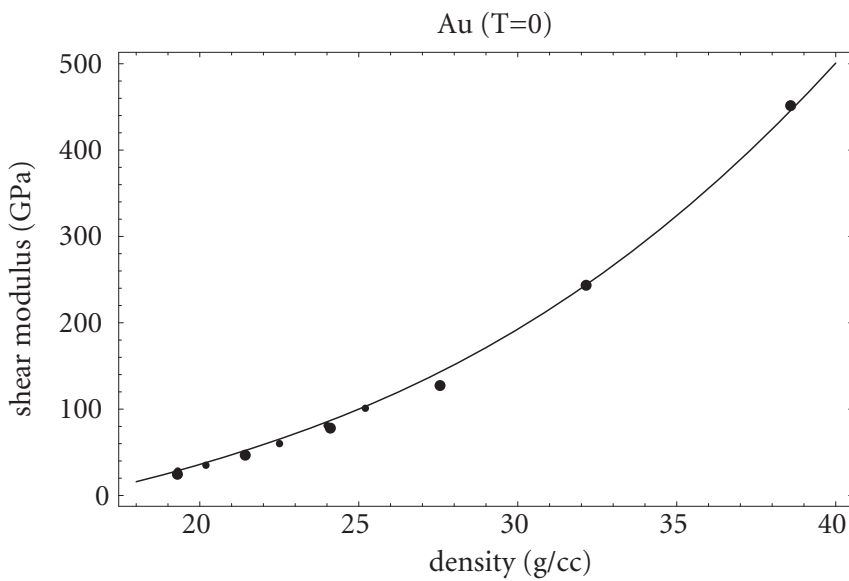


Figure 2—
Shear Modulus (GPa).

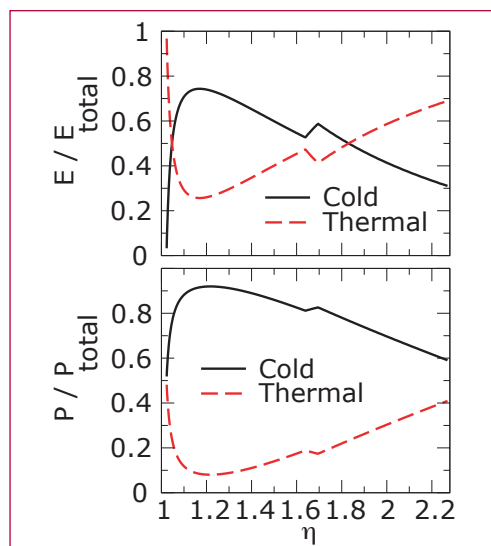
Variation of Thermal and Cold Curve Contributions to Thermodynamic Functions along the Hugoniot

Eric D. Chisolm, Scott D. Crockett, and Duane C. Wallace, T-1; echisolm@lanl.gov

Figure 1— Cold curve and thermal energy and pressure as fractions of total energy and pressure along the Hugoniot.

Equations of state (EOS) constructed in the program in T-1 consist of three parts: the cold curve ($T=0$ isotherm), the thermal contribution from the nuclei, and the thermal contribution from the electrons. A material's EOS, together with the Rankine-Hugoniot relations, determine the material's principal Hugoniot, the set of all equilibrium states accessible by a single shock from room temperature and pressure. The importance of each part of the EOS in determining the Hugoniot varies with pressure; standard shock physics lore asserts that (1) the cold curve dominates the Hugoniot at low pressures and (2) at high pressures, the thermal components dominate over the cold curve, with the electronic thermal part dominating over the rest at very high P . It is not clear, however, where the low pressure regime ends, where the high pressure regime begins, and exactly what happens in between. To try to make these assertions more quantitative we have used the EOS for Al we developed in [1] to compute each contribution to the energy, entropy, and pressure along the Hugoniot, allowing us to study how they vary relative to one another as pressure increases.

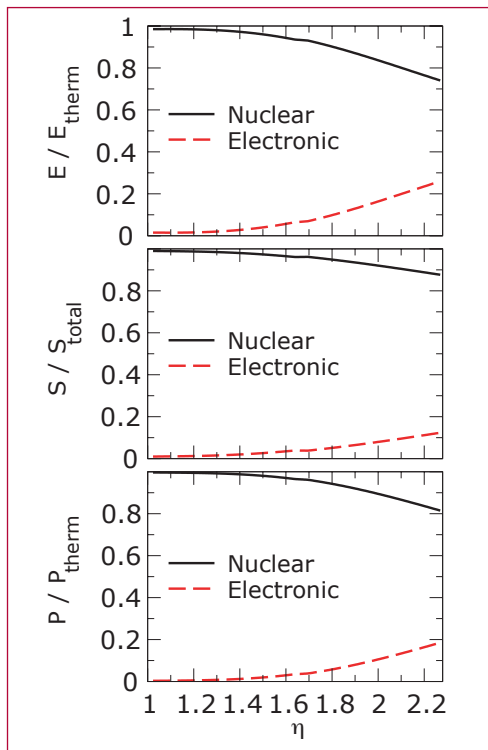
The range of validity of our EOS allowed us to calculate the Hugoniot to a compression $\eta = \rho/\rho_{\text{ref}} = 2.28$. Over this range, Figure 1 shows the cold curve and



total thermal (nuclear plus electronic) contributions to the energy and pressure, respectively, as fractions of the total energy and pressure. By $\eta=1.83$ ($P = 225$ GPa) the energy is dominated by the thermal contribution, and the pressure is on track to suffer a similar fate by $\eta = 2.5$ or so. Thus we see that by moderate compressions the thermal contribution to the EOS is non-negligible along the Hugoniot.

To see how the two thermal contributions compare, Figure 2 shows the nuclear and electronic contributions separately as fractions of the thermal energy, entropy, and pressure. (We did not discuss entropy in the previous paragraph because it is purely thermal.) The nuclear part clearly dominates through the entire range, dominating most in entropy and least in energy. Thus in this compression range, unsurprisingly, it is the nuclear thermal contribution, not the electronic contribution, which is most important.

Finally, in [1] we saw that the P - ρ Hugoniot predicted by this EOS agrees with available data to an accuracy of 1% or so, which suggests the following



question: How much could one change any one contribution to the pressure along the Hugoniot without spoiling the agreement with experiment? The answer is found in Figure 3, which shows as a function of compression the fractional change in each part of the pressure along the Hugoniot required to shift the total pressure by 1%. Clearly the Hugoniot is sensitive to very small changes in the cold curve pressure, on the order of 1 to 2% at all compressions, but for $\eta \geq 1.8$ it is sensitive also to the nuclear contribution at the 5% level. Even the electronic contribution is significant at the higher pressures; at compressions above 2.1, a 20% change in the electronic part is sufficient to shift the total pressure out of agreement with experiment. Thus it is clear that while the cold curve contribution dominates, the nuclear thermal contribution still contributes significantly throughout the domain of validity of this EOS, and at the high end

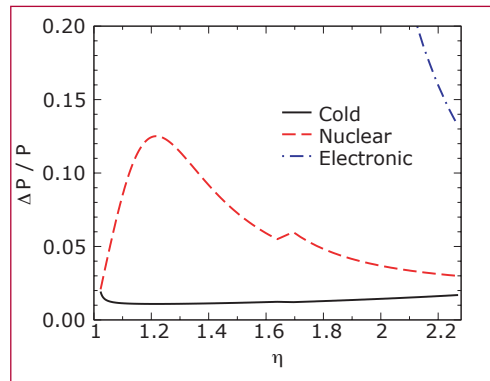


Figure 2— Nuclear and electronic energy, entropy, and pressure as fractions of thermal contribution along the Hugoniot.

Figure 3— Fractional change in cold curve, nuclear thermal, or electronic thermal pressure required to shift total pressure along the Hugoniot by 1%.

even the electronic part should be determined accurately to achieve acceptable agreement with available data.

Although these results were found specifically for Aluminum, we expect all metals across the periodic table to follow similar trends as functions of compression, differing primarily by a scale factor of around two for the heavier metals. Hence we argue that both the thermal nuclear and thermal electronic contributions to the EOS need to be understood to some accuracy to properly account for Hugoniot data at compressions of two and higher.

[1] E. D. Chisolm, S. D. Crockett, and D. C. Wallace, *Phys. Rev. B* **68**, 104103 (2003).



A Comparison of Theory and Experiment of the Bulk Sound Velocity in Aluminum Using a Two-Phase EOS

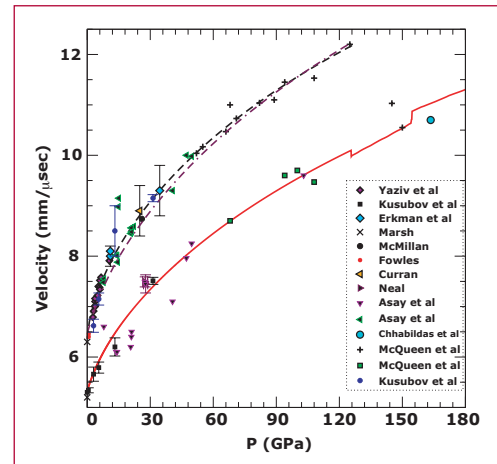
Scott D. Crockett, Eric D. Chisolm,
and Duane C. Wallace, T-1,
echisolm@lanl.gov

Figure 1— c_l and c_b vs P on the Hugoniot. The solid line is the calculated c_b from our EOS. The dashed line is a numerical fit to c_l , Eq. (1), and the dot-dashed line results from setting G_S / B_S equal to a constant. The data at $P = 0$ from Marsh are from ultrasonic measurements.

The following is a summary of work that has been published and presented at the 13th SCCM symposium [4] (LAUR-03-5088).

An aluminum equation of state was created recently using results from lattice dynamics, liquid dynamics, and electronic structure theory [1]. With this EOS, we calculated the adiabatic bulk modulus and bulk sound velocity. We then compared the results of these calculations to experimental bulk sound speed measurements along the Hugoniot. The comparison of theory and experiment is an additional guide to testing the validity of an EOS. The data covers the part of the Hugoniot that crosses the solid-liquid coexistence region, allowing us to test the EOS in the two phase region. Using longitudinal sound speed data and the bulk modulus from the EOS, a reasonable estimate of the shear modulus is computed, and this estimate can be used to test approximations for the shear modulus.

The longitudinal sound velocity c_l and the bulk sound velocity c_b are commonly measured in shock experiments. For the solid phase, the leading edge of the rarefaction wave is presumed to travel at the velocity c_l . This leading edge is observed as an initial drop in the wave profile. The velocity c_b is identified by a second drop in the wave profile where the material response changes from elastic to plastic. It is important to note that for the liquid phase, longitudinal waves



do not propagate and the leading edge of the rarefaction wave travels at the bulk sound velocity. The theoretical c_b for pure aluminum along the Hugoniot is compared with experiment in Figure 1. Notice that the theory shows a slight decrease in c_b through the solid-liquid two phase region. This reflects the fact that the P - ρ adiabats cross the solid-liquid two-phase region at a slightly smaller slope than in the separate solid and liquid phases. The figure illustrates that our theory is in excellent agreement with experiment for c_b , or equivalently for B_S .

Using the longitudinal sound velocity data we can learn something about the shear modulus. The shear modulus is an important material property and is needed to calculate plastic flow processes in hydrodynamic codes. In explosively driven processes, the shear modulus is needed over a wide range of the equation of state surface, and not just in the vicinity of the Hugoniot. An estimate of G_S for the solid phase at all temperatures up to melt and to pressures of a megabar or so, reliable to an accuracy of 25%, would be most useful for practical hydrodynamical calculations. Using a previously developed an approximation for G_S based on setting $G_S / B_S = \text{constant}$, where the constant is to be determined separately for each metal [2], allows us to calculate G_S from an equation of state at any pressure and

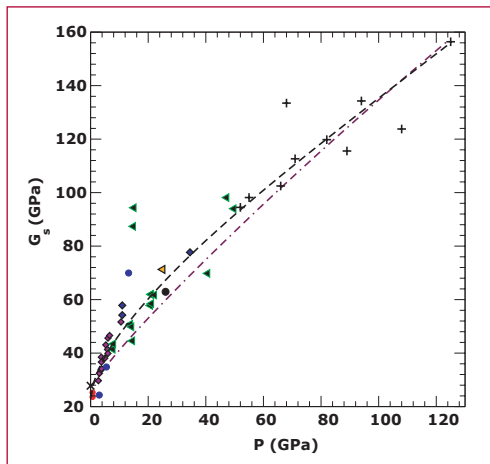


Figure 2—
 G_S vs P on the
Hugoniot.

density, since B_S can be calculated from the equation of state. The approximation was developed from a study of ultrasonic data, and it was used in making qualitative estimates of strength and dissipative effects in overdriven shocks in metals. With the data we have collected for aluminum we can now test this approximation up to 125 GPa along the Hugoniot, the point where aluminum starts to melt.

From the theory for an isotropic material, we have

$$\rho c_l^2 = B_S + 4/3 G_S.$$

We used this equation, together with the experimental data for c_l from Figure 1 and with ρ and B_S determined from our EOS, to accurately calculate G_S along the Hugoniot. The results are shown by the points in Figure 2. The ratio G_S / B_S from the G_S points of Figure 2, and again with B_S from our EOS, is shown by the points in Figure 3.

To approximate G_S / B_S by a constant, we might choose any one of three values: 0.37, the mean value of the points in Figure 3, 0.36, the ultrasonic value for 2024 aluminum at $P = 0$ and 295 K, or 0.35, the ultrasonic value for pure aluminum at $P = 0$ and 295 K. At the level of accuracy we are concerned with, all

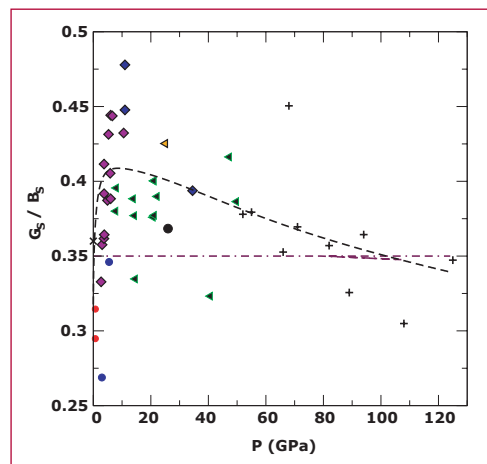


Figure 3—
 G_S / B_S vs P on the
Hugoniot. The dashed
line is a result of using
the numerical fit for
 c_l and the equation of
state for B_S and Eq.
(1) to calculate G_S .

these constants are equally acceptable. Further, to an accuracy of 10% in G_S , any of these constants for G_S / B_S is as good as the fitted curve in Figure 3. The result for $G_S / B_S = 0.35$ is shown by Figure 3.

We compare theory and experiment for sound velocities in aluminum, and reach the following conclusions. The bulk sound velocity c_b , or equivalently the bulk modulus B_S from our aluminum EOS is in excellent agreement with experiment on the Hugoniot, throughout the solid and two-phase regions. The approximation $G_S / B_S = \text{constant}$ agrees with experiment within error bars, on the Hugoniot through the solid phase. We expect this approximation to hold equally well away from the Hugoniot, throughout the entire solid phase region.

- [1] E. D. Chisolm, S. D. Crockett, and D. C. Wallace, *Phys. Rev B* **68**, 104103 (2003).
- [2] Wallace, D. C., *Phys. Rev. B* **24**, 5607 (1981).
- [3] Wallace, D. C., *Statistical Physics of Crystals and Liquids*, (World Scientific, 2002).
- [4] "A comparison of theory and experiment of the bulk sound velocity in aluminum using a two-phase EOS," S. Crockett, E. Chisolm, D. Wallace, appearing in SCCM 2003 proceedings.

Equation of State Developments in T-1

Eric D. Chisolm, Scott D. Crockett, Giulia De Lorenzi-Venneri, Denise C. George, J. D. Johnson, Duane C. Wallace, and John M. Wills, T-1. echisolm@lanl.gov

We released an updated version of the unclassified and classified SESAME databases on January 31, 2003. We released the unclassified database with eleven modified and three new materials (see memo t1-2003-02-07-sdc).

A new SESAME Aluminum equation of state (EOS) has been produced. A manuscript with the details is currently being written. Also, several classified EOS have been modified. Three new classified materials have also been created.

A new cold curve for elemental Pu has been calculated, using a first-principles electronic structure method, in the range of compression $V_0/V = 0.5$ to 100. Several candidate structures were evaluated, including two experimentally suggested high-pressure structures and a theoretical simple monoclinic phase found to have a low energy over a certain pressure range. The result is being evaluated in the context of the SESAME Pu EOS to assess the impact of the difference. A document, "A calculated cold curve for elemental Pu," is in preparation.

We have served the user community by delivering a modified test plutonium EOS with some physics improvements. Also, six versions of modified plutonium EOSs were provided for sensitivity studies. J. D. Johnson's paper with Carl Greeff (X-7) on plutonium was

published in *Defense Research Review*. A long memo on other issues about plutonium (coauthor Carl Greeff) was distributed.

We have merged the opacity comment tables into the opacity library as a service to T-4.

We have performed work on a new technique for constructing elemental solid and liquid EOS, using results from lattice dynamics, liquid dynamics, and density functional theory.

(a) We have published a full description of the technique (E. D. Chisolm, S. D. Crockett, and D. C. Wallace, *Phys. Rev. B* **68**, 104103 (2003)), and we are continuing our efforts to extend this technique over the entire range required for a SESAME EOS. Our results on the extension problem thus far are described in LA-UR-03-7344 and the report on page 6 of this volume.

(b) We have constructed an EOS for Al using these techniques, and we have used it to study the relative contributions of each part of the EOS (cold, nuclear, electronic) to the thermodynamic functions along the Hugoniot, attempting to understand when each part dominates. Our results are described in LA-UR-03-4928 and the report on page 10 of this volume.

(c) We have also compared the bulk sound speeds predicted by this EOS with experimental data, finding good agreement, and we tested a conjecture concerning the shear modulus by comparing with longitudinal sound speed data, again finding good agreement. Our results are described in LA-UR-03-5088 and the report on page 12 of this volume.

We have continued development of liquid dynamics theory, which has now

reached the stage where it can provide accurate equations of state for liquid metals at all compressions (as shown in the previous point). We have also recently developed two applications: (a) We have created a semi-empirical method for computing the viscosity coefficient of a liquid metal at melt over a range of densities, using either liquid entropy data or density functional theory. The method is described in more detail in LA-UR-03-6847 and the report on page 2 of this volume.

(b) We have also applied the theory to inelastic neutron scattering, as described in the report on page 130 of this volume.

We have surveyed theoretical and computational results to better understand at what compression the cold curve of a material is correctly described by the Thomas-Fermi-Dirac (TFD) model. Our results are described in LA-UR-03-7346 and the report on page 4 of this volume.

We have kept abreast of the controversy over the laser shock data on deuterium. This included service on a panel discussion at the International Conference on Strongly Coupled Coulomb Systems in 2002 and attending a workshop in January of 2003. After the workshop J. D. Johnson felt that it was time to declare victory on the side of the Sandia data. He then wrote a summary memo and distributed such to some managers. We have also completed modifying the total table of our existing deuterium EOS, taking into account the Sandia data, diamond anvil data, gas gun data, and molecular dynamics/Monte Carlo modeling. We have corrected two mistakes. Work is now underway to modify the subtables, including correcting a mistake in the electronic table.

We were represented in varying capacities for four committees/meeting series on planning the future of materials work. These are the X-Division Science Council, the Shivano MATWOG, Paul Dotson's study group, and the headquarters workshop at Livermore.

We have rewritten Opensesame in FORTRAN 90.

(a) It takes advantage of modern programming features of the language: pointers, dynamic memory, derived types, and modular structure.

(b) Input to Opensesame is now specified in namelist format.

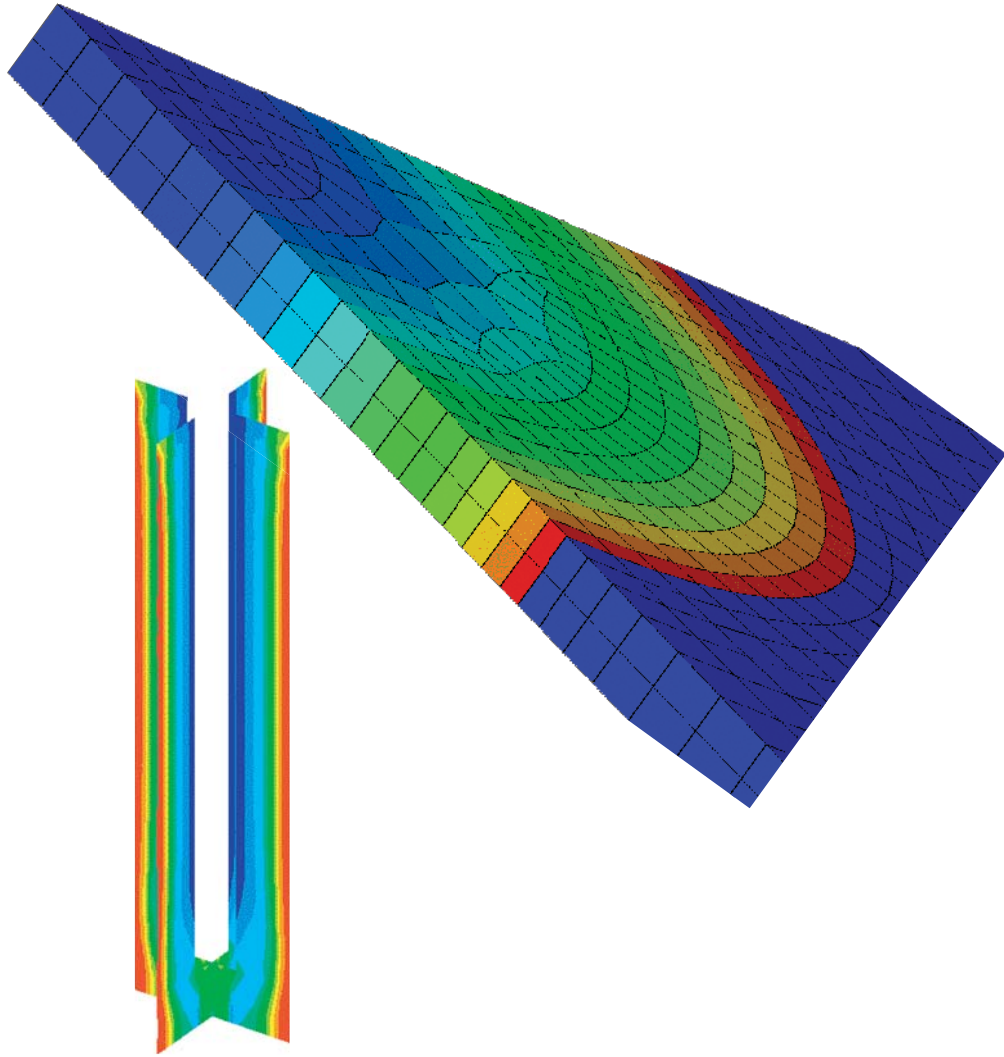
(c) The Opensesame GUI has been modified to provide namelist input to correspond to item (b).

(d) Documentation may be found at <http://t12www.lanl.gov/home/opensesame>.

We have begun an analysis of the numerical vulnerabilities in Grizzly and Opensesame that lead to different results on different platforms.



Fluid Dynamics



Atomistic Description of Rayleigh-Taylor Instabilities

Kai Kadau, T-11; Timothy C. Germann, X-7; Peter S. Lomdahl, T-11; Brad Lee Holian, T-12; Guy Dimonte, X-4; Nicolas G. Hadjiconstantinou, Massachusetts Institute of Technology; and Berni Alder, Lawrence Livermore National Laboratory; kkadau@lanl.gov

We investigate the evolution of 3-dimensional (3D) Rayleigh-Taylor (RT) instabilities, which occur when a heavy fluid is laid on top of a light fluid under the influence of a gravitational field [1]. A series of quasi two-dimensional (2-D) atomistic computer simulations involving up to a million atoms, reveal that thermal atomistic disturbances build up long-wavelength instabilities, which eventually lead to a turbulent growth of bubbles

into the heavier and spikes into the light fluid, see Figure 1. After the development of an unstable spectrum of waves at the interface, the most dominant wave leads to a growth of the mixing that is approximately quadratic in time, Figure 2, in accordance with experimental observations and theoretical approaches [2]. For small Mach numbers M ($M^2 = \lambda g / c_h^2$ is the dimensionless compressibility, with λ = wavelength of perturbation, g = gravitational constant, c_h = sound velocity of the heavier fluid) the growth coefficients observed only depend on the magnitude of the gravitational constant and the Adwood number (density difference divided by the sum of densities). Larger Mach numbers lead to increased mixing due to compressibility effects.

So far, only 2-D atomistic simulations of the discussed fluid instability have been published, but these neglect compressibility effects and 3-D features

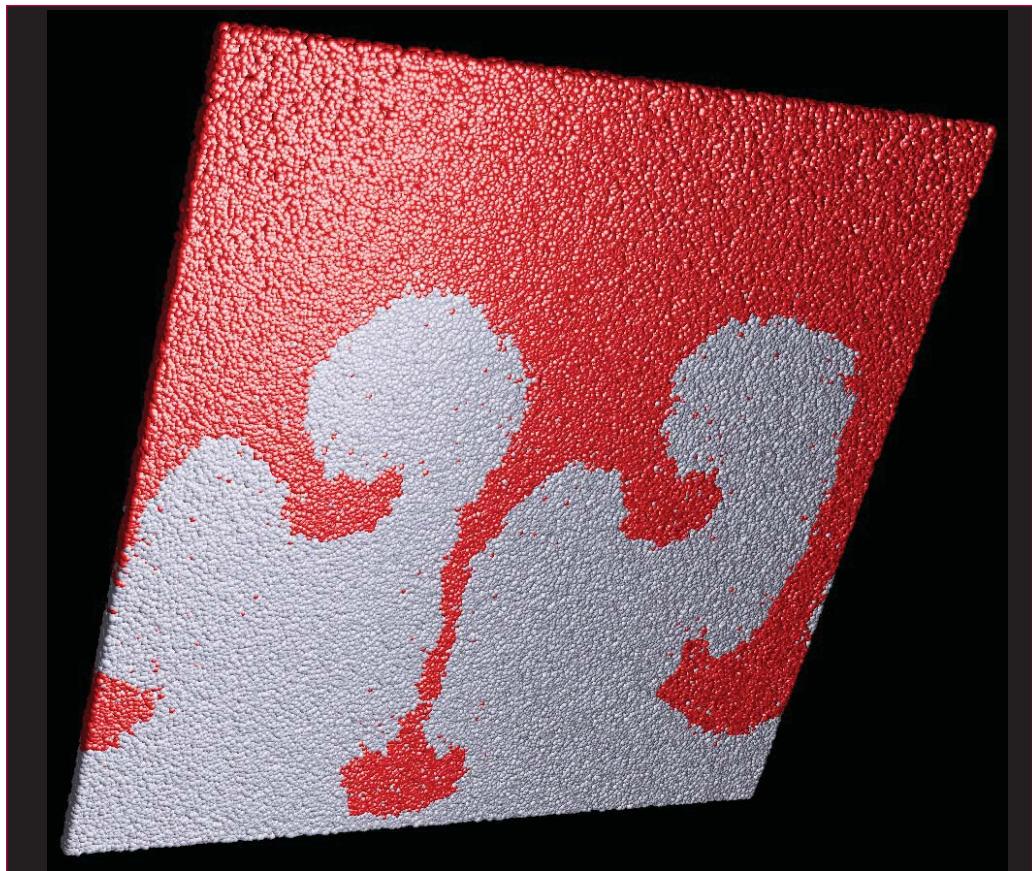


Figure — Turbulent Rayleigh-Taylor mixing on the atomic scale in a pseudo 3-dimensional system: A heavy fluid (red spheres) and a light fluid (gray spheres) penetrate each other under the influence of a downward gravitational field.

[3]. Experimental studies, as well as numerical hydrodynamic calculations, show contradictory results [4]. Therefore, the atomistic simulations performed here will help to illuminate these issues.

Acknowledgements:

This work has been supported by the U.S. Department of Energy.

[1] The SPASM (“Scalable Parallel Short-range Molecular dynamics”) code is described in: Peter S. Lomdahl, P. Tamayo, N. Grønbech-Jensen, and D. M. Beazley, in *Proceedings of Supercomputing 93*, G. S. Ansell, Ed. (IEEE Computer

Society Press, Los Alamitos, CA, 1993), 520; D. M. Beazley and Peter S. Lomdahl, *Computers in Physics* **11**, 230 (1997); see also <http://bifrost.lanl.gov/MD/MD.html>.

[2] P. F. Linden, J. M. Redondo, and D. L. Youngs, *Journal of Fluid Mechanics* **265**, 97 (1994).

[3] W. Dzwiniel, W. Alda, M. Pogoda, and D. A. Yuen, *Physica D* **137**, 157 (2000).

[4] J. Glimm, J. W. Grove, X. L. Li, W. Oh, and D. H. Sharp, *Journal of Computational Physics* **169**, 652 (2001).

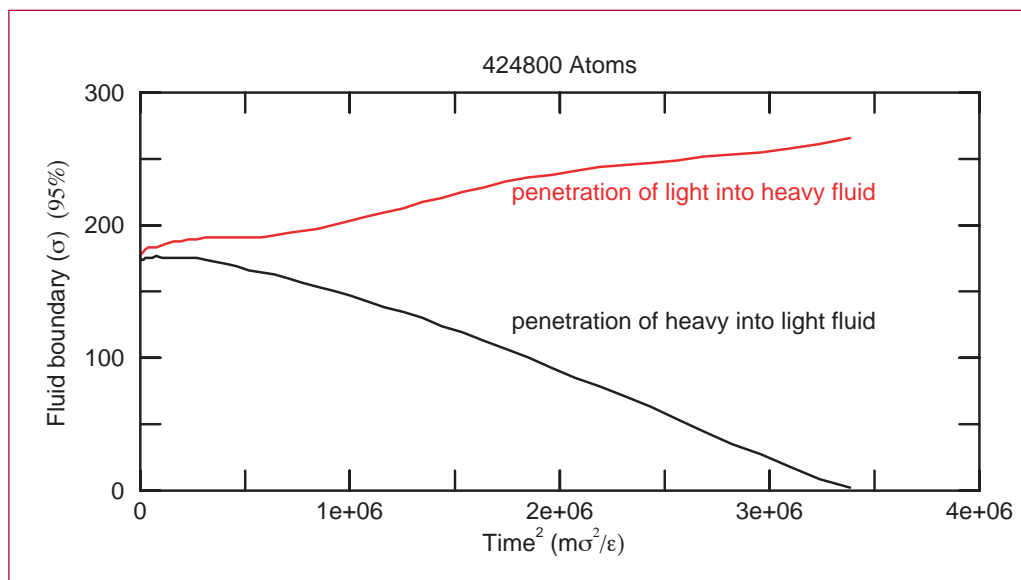


Figure 2— Penetration depth of bubbles/spikes into the heavy/light fluid for a quasi 2-dimensional Rayleigh-Taylor instability. After the initial development of a spectrum of unstable waves at the interface, the growth is approximately quadratic in time.

Simulation of Multiphase Flow in Centrifugal Contactors for Process Intensification at TA-55

*Nely Padial-Collins
and W. Brian VanderHeyden, T-3;
nelylanl@lanl.gov*

The T-3 Group began work on the simulation of mixing and separation of two-phase flow in the TA-55 centrifugal contactor in the last half of FY03. The contactors are used to recover actinides from acid solutions through contact with paraffinic hydrocarbons, [1]. Centrifugal contactors are attractive for this service for many reasons including criticality issues. The ultimate goal of the project is to use simulation to help increase the capacity of the contactors, [1]. With increased capacity, valuable floor space at TA-55 would be made available for other purposes. In the following, the basics of the contactor are

discussed along with a summary of results from FY03 and plans for FY04.

Background

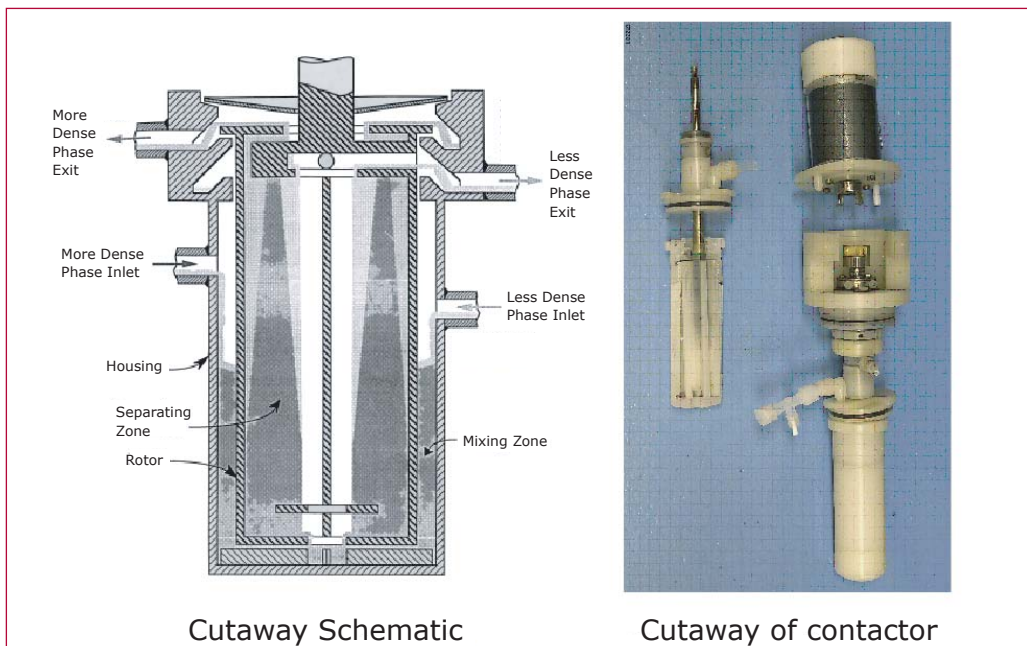
A cutaway schematic diagram and photograph of the contactor is shown in Figure 1.

The inner cylindrical element of the contactor is rotated at around 3600 rpm with a motor. The aqueous (acid) and organic (paraffin) are pumped into the annular chamber where there is mixing from Taylor-Couette flow and multiphase turbulence. The mixed two-phase flow proceeds through stationary vanes at the bottom of the annular chamber and then enters the inner rotating chamber. In the inner chamber, separation occurs due to centrifugation. The aqueous and organic phases exit the chamber at the top through a set of weirs placed at different radii.

FY03 Work Package Objectives

- Demonstrate multiphase flow simulation in contactor geometry –June 2003.

Figure 1—
Cutaway
Schematic
and Photo.



- Demonstrate multiphase flow with mass transfer on a base case. Both objectives were met.

FY03 Accomplishments

The FY03 work included the implementation and testing of a rotating frame effect (centrifugal and Coriolis forces), development and installation of an impeller force model, a species and phase mass transfer model, the generation of several detailed 3-D meshes based on the contactor, and the calibration of a droplet drag model as well as several 3-D simulations. In addition, a data link to the RAVE facility was established and prototype 3-D visualization movies of the data from the base case simulation were developed and demonstrated. Finally, an extensive literature survey was performed that yielded an interesting data set for code validation [2]. The data set provides experimental information on the maximum throughput of the contactor as a function of the ratio of the flow rates of the organic and aqueous phases. It is anticipated that this information will be used in FY04 for model validation and as a basis for potential process intensification studies of the contactor.

Below are illustrations showing the contactor meshes and flow field results from

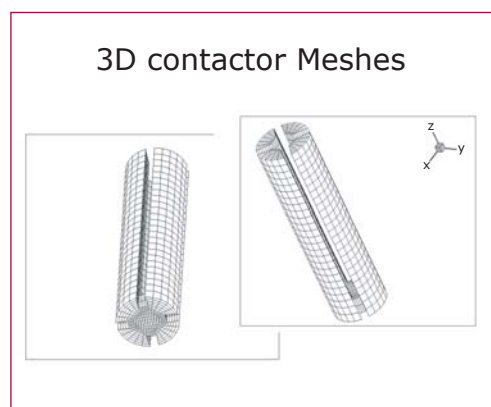


Figure 2—
3-D meshes for
contactors.

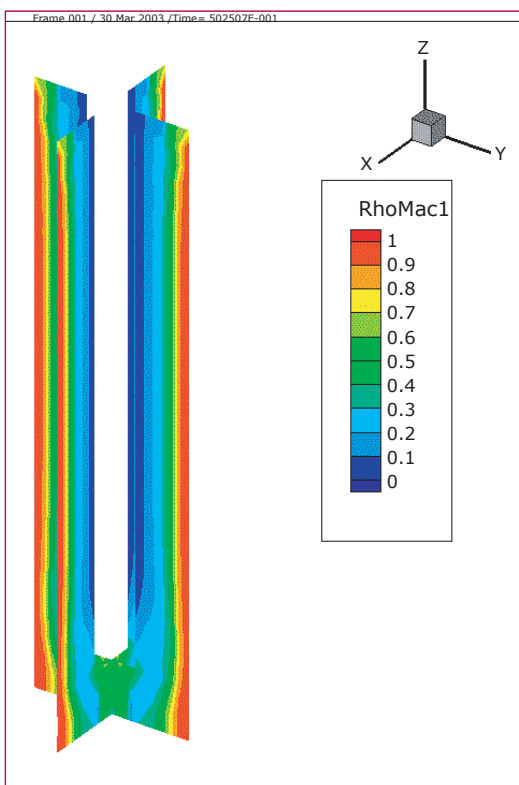


Figure 3—
Phase distribution
in z-y and z-x
plane.

the 3-D demonstration calculation.

[1] Stephen L. Yarbrow and Stephen B. Schreiber, "Using Process Intensification in the Actinide Processing Industry," *Journal of Chemical Technology and Biotechnology* **78** (2–3), 254–259 (2003).

[2] R. A. Leonard, G. J. Bernstein, A. A. Ziegler, and R. H. Pelto, "Annular Centrifugal Contactors for Solvent Extraction," *Separation Science and Technology* **15**, 925–943 (1980).

Two-Mesh Computation for the Telluride Casting Project

Andrew P. Kuprat, T-1; kuprat@lanl.gov

This past year, T-1 devised and implemented a two-mesh capability for the ASCI funded Telluride project (a collaboration involving MST, CCS, T, and other divisions), which is now available in the 3-D Truchas casting simulation code. Truchas simulates the entire casting process: flow of molten alloy, heat transfer, solidification of alloy, induced stresses, etc.

The two-mesh capability that we implemented allows Truchas to compute electromagnetic fields and the resulting inductive heating source terms on a tetrahedral mesh (using a finite element method that requires tetrahedra for computation) and transfer the heat source terms onto the regular hexahedral mesh used for heat flow and phase change computation.

More generally, the two-mesh capability allows the transfer of any cell-based field computed on a tetrahedral mesh to a cell-based field on an unstructured hexahedral mesh. Conservation is obeyed; i.e., the integral of the field over the tetrahedral mesh is equal to the integral of the mapped field over the hexahedral mesh, to within round-off error.

With the new two-mesh capability, different kinds of physics requiring

different kinds of meshes can now be coupled. Truchas requires this capability for coupling electromagnetism and heat-flow, but other physical combinations are of course possible.

Figures 1 and 2 represent a demonstration of this capability. In Figure 1, we have the heat source field as computed on the tetrahedral mesh. In Figure 2, we see the heat source field as mapped conservatively onto the hexahedral mesh.

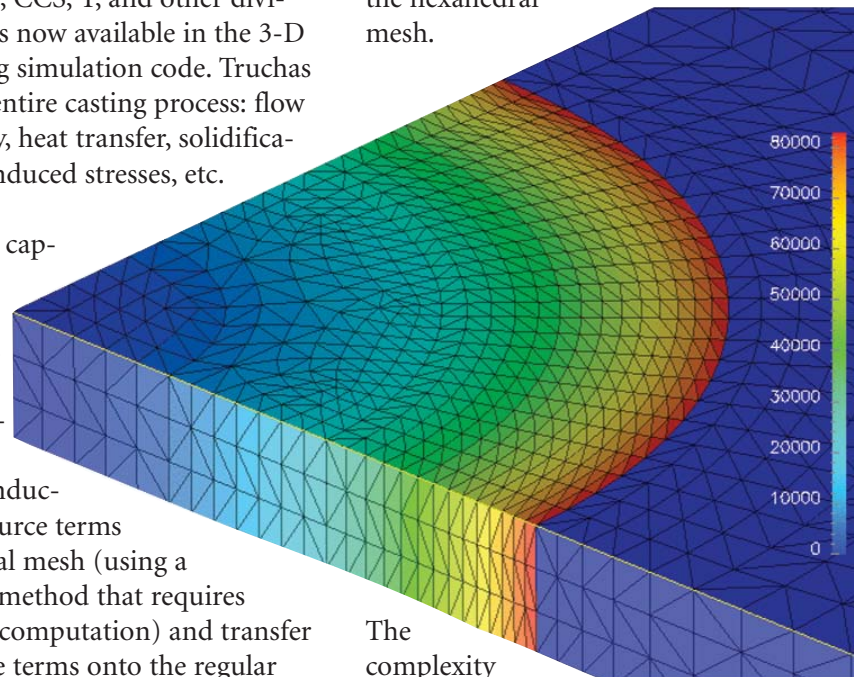


Figure 1—Truchas tetrahedral mesh for electromagnetic inductive heating computation. The dark blue outer region represents vacuum where inductive heating does not take place. The inner “quarter cylinder region represents graphite, which experiences inductive heating. The heat source is strongest near the curved surface of the graphite (red color) where the electromagnetic fields do not have to penetrate very far. Units are in Joules per cubic meter.

The complexity of the mesh mapping is of order $N \log N$, where N is a bound on the number of elements in the two meshes. This low complexity implies that mesh mapping is feasible between very large meshes. In fact, computation of the mesh mapping for a typical electromagnetics/heat transfer simulation takes up a small fraction of the overall run time.



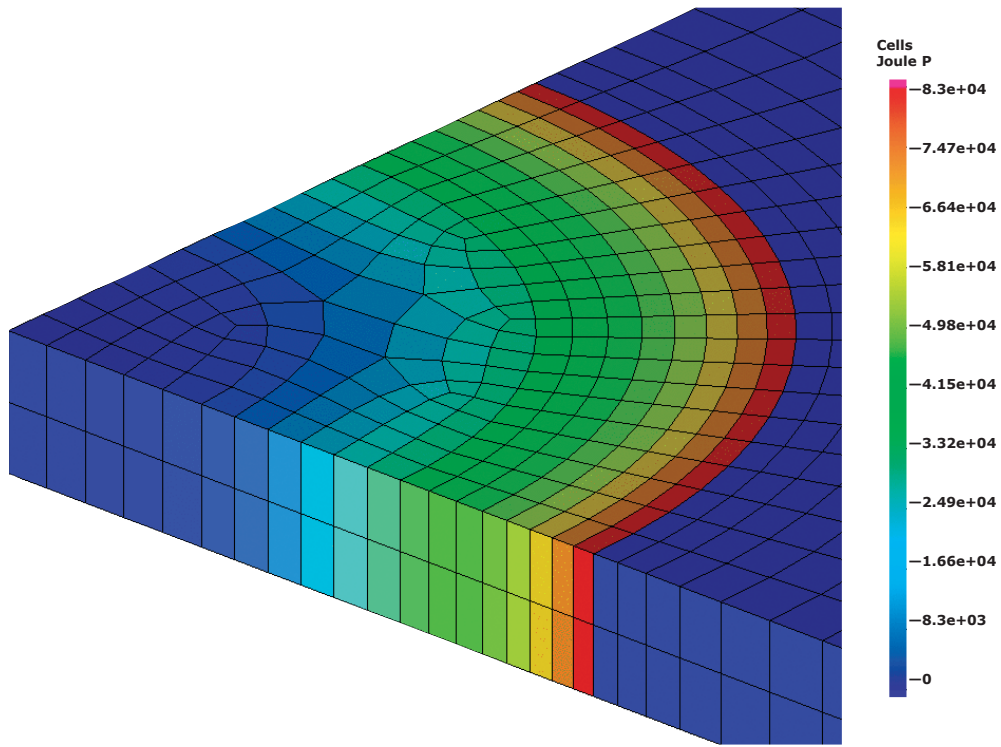


Figure 2—
 Truchas hexahedral
 mesh for heat flow
 computation. The
 heat source field of
 Figure 1 has been
 conservatively
 mapped onto this
 hexahedral mesh.
 The mapping is
 conservative over
 both the vacuum
 and graphite regions.
 Thus, there is no
 spurious mapping
 of heat onto the
 vacuum region of the
 hexahedral mesh.

Extension of the KIVA Particle/Spray Model to Flows with Compressible Particles

*Peter J. O'Rourke and David J. Torres,
T-3; pjor@lanl.gov*

In work supported by ASCI's Turbulence Mix Project, we are extending the highly successful KIVA [1] particle/spray model to flows with compressible particles. The KIVA model uses a Monte Carlo particle method to solve the equations for a two-phase, gas-particle flow in which the particles have a distribution of sizes. In the KIVA code, it is assumed that the particle material is incompressible. This assumption is not valid in flows in which the particles experience large changes in pressure and temperature, such as occur when shocks pass over the particles. This work is motivated by the need to relax the assumption of incompressibility.

Our extended equations incorporate the following additional physical effects into the KIVA model [2]. First, the density of the particle material, and hence particle sizes, can vary according to an arbitrary equation of state. Second, there can be both reversible compressive and viscous heating of particle material. Third, the particles can experience accelerations due to large gradients in the pressure field of the two-phase mixture. All physical effects included in the KIVA model have been retained—including particle aerodynamic drag, gas/particle heat transfer and particle vaporization, and particle dispersion due to interaction with gas-phase turbulence.

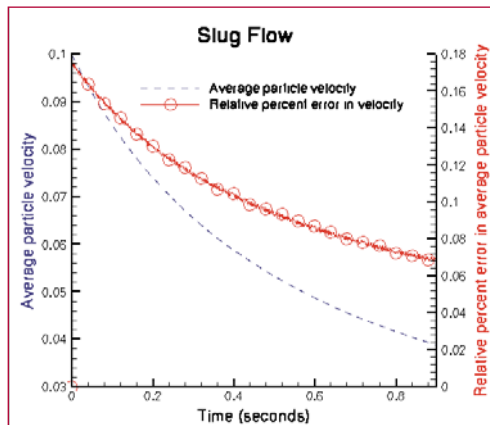
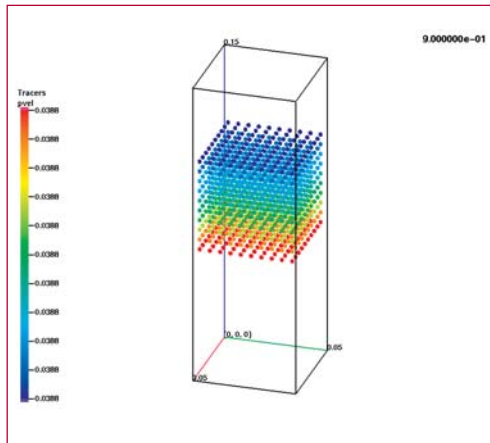
The finite difference approximations [3] of this extended model are formulated

for both co-located variables hydrodynamics codes, such as the CHAD code [4] being developed by Group T-3, and for staggered-mesh codes, such as KIVA. For either type of code, two particle-model subroutines, which are called from the main hydrodynamics solver, provide the computational interface to the coupled gas/particle equations. The new finite-difference approximations improve upon those of KIVA in many ways, two of which we mention here. First, the energy of the combined gas-particle system is numerically conserved. (The KIVA finite-difference approximations conserve mass and momentum, but not energy.) Second, in the staggered-mesh case, we propose an improved method for calculating momentum exchange that reduces spurious numerical velocity fluctuations in calculations with vaporizing particles.

Implementation of the approximations in CHAD is well underway because portions of the KIVA particle/spray model had already been incorporated in a CHAD module a number of years ago for another project [5]. This old implementation, which assumes incompressible particles moving in an ideal gas, was largely undocumented and untested. In recent progress, we have updated the computational interface for this old particle module so that it is compatible with the latest version of CHAD.

We have also begun testing of the particle module in comparisons with known analytic solutions. One of these tests is of the deceleration of a uniform slug of particles moving relative to a gas, and the resulting acceleration of a gas in which this slug is embedded. This problem tests the implementation of the particle drag terms, as well as conservation of momentum and energy in the

combined gas-particle mixture. The slug of particles is uniformly distributed across the cross-section of a rectangular channel, as shown in Figure 1, and moves in the direction of the long dimension of the channel. Periodic boundary conditions are imposed on the top and bottom boundaries of the channel. The plot in Figure 2 shows the relative error between the computed and analytic solutions for the particle velocities. This error is always less than 0.18%.



[1] A. A. Amsden, P. J. O'Rourke, and T. D. Butler, "KIVA-II: A Computer Program for Chemically Reactive Flows with Sprays," Los Alamos National Laboratory Report LA-11560-MS (May 1989).

[2] P. J. O'Rourke and D. J. Torres, "Extension of the KIVA Particle/Spray Model to Flows with Compressible Particles and Large Pressure Gradients," Los Alamos Report LA-UR-03-2918 (April 2003).

[3] P. J. O'Rourke and D. J. Torres, "Finite Difference Approximation of the Equations of the Extended KIVA Particle/Spray Model," Los Alamos Report LA-UR-03-2917 (April 2003).

[4] P. J. O'Rourke and M. S. Sahota, "NO-UTOPIA: The Flow Solver for the CHAD Computer Program," Los Alamos National Laboratory Report (in preparation).

[5] M. S. Hubbard and P. J. O'Rourke, unpublished work.

Figure 1— Particle positions at end of particle-slug calculation. The particles are colored according to their velocity, which are all equal to 0.0388 to three significant figures. The particle velocities are spatially constant in the analytic solution.

Figure 2— Particle velocities and relative error between analytic and computed particle velocities, versus time.

ALE INC. New 2-D ALE Code on General Polygonal Meshes

Raphaël Loubère and Mikhail J. Shashkov,
T-7; loubere@lanl.gov

In this work we have developed a 2-D unstructured Arbitrary-Lagrangian-Eulerian code. This code is devoted to solve CFD problems for general polygonal meshes with fixed connectivity. Main components of the method are

I— a Lagrangian scheme. Each polygon is split into subcells. The compatible Lagrangian hydrodynamics equations are solved during one time step and the mesh is moved according to the fluid velocity [7], [8], [5], [6].

II— an untangling process that ensures the validity of the mesh, if the mesh was tangled as a result of the Lagrangian step. The method finds an untangled mesh which is as close as possible to the previous Lagrangian grid [4], [3], [9].

III— a reference rezone Jacobian strategy, which improves the quality of the untangled mesh and, at the same time, requires the new mesh to be close to the original untangled grid (from step II) and preserve interfaces between materials [2].

IV— a remapping method, which gives the linear and bound preserving remapped hydrodynamics variables on the new mesh [1],[11].

These four steps have been adapted to the subcell description of the scheme and the polygonal meshes. The untangling and the reference rezone Jacobian processes deal now with general polygonal meshes and preserve the interfaces between materials. The remapping step is performed from a subcell point of view.

Code can be used as a purely Lagrangian one (only step I is used), an ALE one (x Lagrangian steps are performed then steps II, III, IV are activated) or as an Eulerian one (steps I and IV are used and the remapping is done on the same initial grid).

Some examples of simulations using ALE INC. code are presented on methods on the unstructured 3-D grids.

Figure 1 shows the triple point problem, this simulates the interaction between a planar shock wave and a heavy corner shape obstacle, the mesh is presented. The Dukowicz problem is solved with an unstructured mesh, the results are shown in Figure 2.

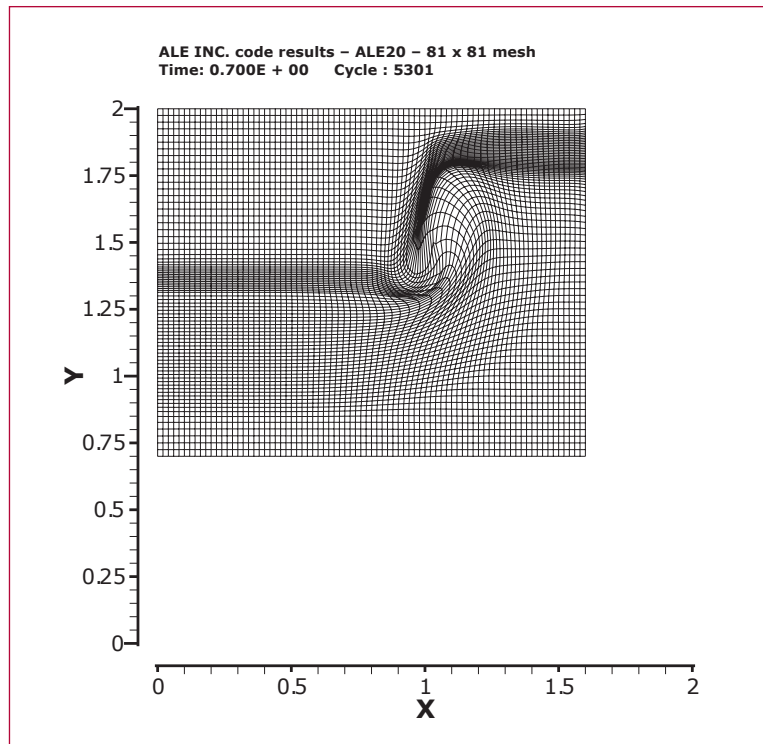


Figure 1—
Triple point
problem—Uniform
logical rectangular
grids, 81 x 81.

[1] L. G. Margolin and M. J. Shashkov, "Second-order Sign-preserving Conservative Interpolation (remapping) on General Grid," *Journal of Computational Physics* **184**, 266–298 (2003).

[2] P. Knupp, L. G. Margolin, and M. J. Shashkov, "Reference Jacobian Optimization-based Rezone Strategies for Arbitrary Lagrangian Eulerian Methods," *Journal of Computational Physics* **176** 93–12 (2002).

[3] P. Knupp, "Hexaedral and Tetrahedral Mesh Untangling," *Engineering with Computers* **17** 261–268 (2001).

[4] P. Vachal, M. Shashkov and R. Garimella, "Untangling of 2D Meshes in ALE Simulations," *Journal of Computational Physics*.

[5] J. Campbell and M. Shashkov, "A Compatible Lagrangian Hydrodynamics Algorithm for Unstructured Grids," LA-UR-00-3231.

[6] J. Campbell and M. Shashkov, "A Tensor Artificial Viscosity using a Mimetic Finite Difference Algorithm," *Journal of Computational Physics* **172**, 739–765 (2001).

[7] E. J. Caramana and M. Shashkov, "Elimination of Artificial Grid Distortion and Hourglass-Type Motions by Means of Lagrangian Subzonal Masses and Pressures," *Journal of Computational Physics* **142**, 521–561 (1998).

[8] E. J. Caramana, D. E. Burton, M. J. Shashkov, and P. P. Whalen, "The Construction of Compatible Hydrodynamics Algorithms Utilizing Conservation of Total Energy," *Journal of Computational Physics* **146**, 227–262 (1998).

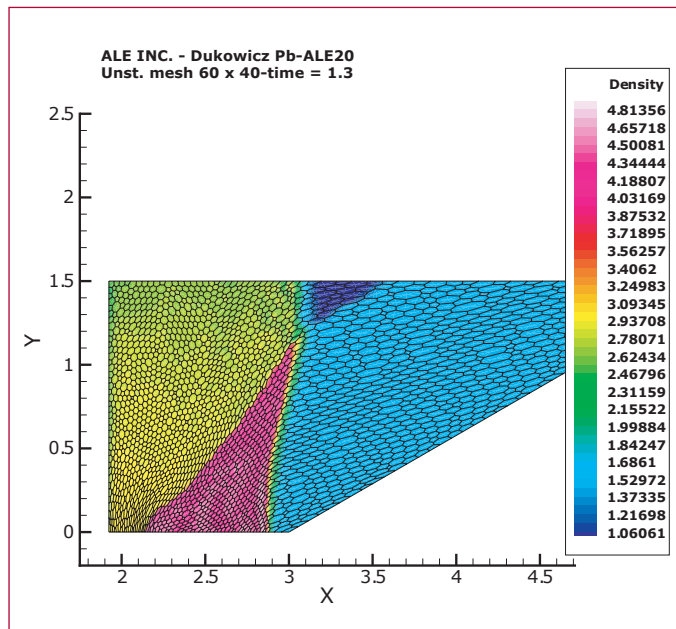


Figure 2—
Dukowicz problem,
unstructured
polygonal
mesh, density
and mesh at
 $t = 1.3$.

[9] P. Vachal, R. Garimella, M. J. Shashkov, and R. Loubere, "Untangling of meshes in ALE simulations," *7th U. S. Nat. Congress on Computational Mechanics*, Albuquerque (July 2003).

[10] M. Kucharik, M. J. Shashkov, and B. Wendroff, "Efficient Local Bound-preserving Conservative Interpolation," *7th U. S. Nat. Congress on Computational Mechanics*, Albuquerque (July 2003).

[11] M. Kucharik, M. J. Shashkov, and B. Wendroff, "An Efficient Linearity and Bound-preserving Remapping Method," *Journal of Computational Physics*.

2

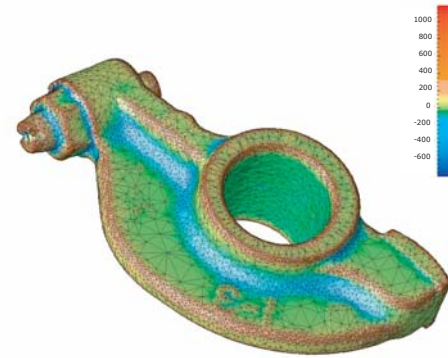
Curvature Estimation for Unstructured Triangulations of Surfaces

Rao V. Garimella and Blair K. Swartz,
T-7; rao@lanl.gov

Knowledge of the curvature of surfaces is important in a number of applications such as flow simulations, computer graphics and animations, and pattern matching. It is of particular importance to applications dealing with evolving surface geometry. Such applications usually do not have smooth analytical forms for the surfaces forming the model geometry. Instead, they have to deal with discrete data consisting of points on the surface connected to form an unstructured triangulation. Hence, it is important to be able to reliably estimate local curvatures at points on discrete surfaces.

In this study, a comparative analysis and convergence study were done of several curvature estimation methods suggested in the literature and a new, improved method was proposed as an extension of one of those methods [1]. The new method robustly estimates normals, principal curvatures, mean curvatures, and Gaussian curvatures at vertices of general unstructured triangulations. The method has been tested on complex meshes and has provided very good results shown in the examples.

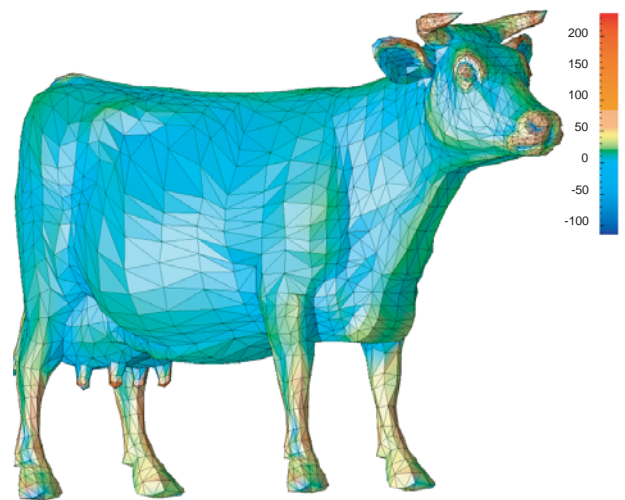
It was found that the most reliable methods are those that fit a smooth surface to a set of nodes in the local neighborhood of each node and use its curvature as the estimate of the curvature for the discrete surface [2]. Since surface curvatures are based on second order derivatives, it is common to use quadratic polynomials as a local approximation to the surface. In each of these methods, a quadric of the form



$Z' = f(X', Y')$ is fitted to the nodes in a local coordinate system (X', Y', Z') whose origin is at the node under consideration and the Z' axis is along an estimated surface normal at the node.

The simplest of the surface fitting methods performs a least squares fit of the quadric $Z' = aX'^2 + bX'Y' + cY'^2$ to the 1-level or edge-connected neighbors of the node mapped to a local coordinate system. The Z' -coordinate of the local coordinate system is along a normal that is estimated by averaging the normals of the triangles connected to the node.

A more robust version of the quadric fitting method includes linear terms in the quadric, i.e., $Z' = aX'^2 + bX'Y' + cY'^2 + dX' + eY'$. This results in an improved estimate for the tangent plane and normal at the node. The improved



normal is then used to calculate a new local coordinate frame in which to fit a new quadric. This iterative process is carried out until the local coordinate frame does not change much. The extended quadric fitting works well but requires more points than the simple quadric without which the system of equations becomes under-determined and does not have a unique solution. It is also possible to use a full quadric in which the addition of the constant term allows the surface to not pass through the node under consideration.

The method devised by Garimella and Swartz fits an extended quadric to the one-level neighborhood of the node whenever possible and includes the two-level neighbors of the node (neighbors of the node neighbors) when the system is under-determined. The method also includes a technique for estimating curvature at vertices on surface boundaries where a full cycle of faces may not exist around the vertex. At such boundary nodes, existing neighbors are reflected to form ghost nodes that can then be used for fitting the surface.

In the study, convergence tests were performed by estimating the curvature at the central node of a shrinking hexagonal patch of triangles superimposed on a cylinder. The hexagonal patch was shrunk in a nearly self-similar way so that the quality of and relative sizes of the triangles did not change significantly. It was found that the simple quadric fitting had higher errors and converged to the wrong answer while the extended quadric technique showed very good accuracy and convergence to the right solution. In other tests involving the triangulation of a sphere, similar results were obtained with the addition that the extended quadric, extended patch



method of Garimella and Swartz, was needed to get an estimate at points in the mesh that did not have enough one-level neighbors. Surprisingly, the full quadric method gave very high errors for this test case.

The modified curvature estimation method was tried on complex meshes and has shown to give very good results. The accompanying illustrations show mean curvature estimates for unstructured meshes of complex geometric models.

[1] S. Petitjean, "A Survey of Methods for Recovering Quadrics in Triangle Meshes," *ACM Computing Surveys* **34**, 211–262 (June 2002).

[2] A. M. McIvor and R. J. Valkenburg, "A Comparison of Local Surface Geometry Estimation Methods", *Machine Vision and Application* **10**, 17–26 (1997).

2

Mimetic Finite Difference Methods for Diffusion Equations on Non-Orthogonal AMR Meshes

Konstantin Lipnikov and Mikhail J. Shashkov, T-7; Jim E. Morel, CCS-2; lipnikov@lanl.gov

The predictions and the insights gained from simulations are no better than the physics models or the numerical methods used to solve them. The discrete approximations used to predict diffusion of heat or matter on a mesh covering the domain is often the determining factor for the reliability, accuracy, and efficiency of the simulations. One of the most effective approaches to derive these discrete approximations is to preserve and to mimic the underlying mathematical properties of the physical system. This task is made more difficult when the mesh is distorted and/or locally refined so that it can conform and adapt to the physical domain and problem solution.

In our research [1] we have extended a class of mimetic finite difference approximations for modeling the diffusion equations on distorted locally refined meshes of a particular type of importance to the ASCI projects. Our new method is both accurate (second-order accurate on nonsmooth nonconformal meshes with or without material discontinuities) and it produces a linear system with symmetric positive-definite matrix, which is relatively easy to solve. The new method is a major advance over the capabilities of the existing discrete approximations and will lead to more accurate and robust predictions.

It is slated for immediate use in the ASCI projects.

We use the local support-operators, SO, method to generate mimetic discretizations on nonorthogonal quadrilateral meshes having hanging nodes. Hanging-node meshes are generally used in adaptive mesh refinement algorithms. Note that a hanging node occurs when two cells share a face with one cell, see the figure below. We do not allow any cell to share a face with more than two cells, or equivalently, there is never more than one hanging node associated with an interface. This is a restriction motivated by considerations of both simplicity and accuracy that is usually seen in quadtree-based adaptive-mesh algorithms. While the vast majority of existing adaptive mesh refinement (AMR) schemes use orthogonal meshes, it is clear that nonorthogonal mesh schemes are more versatile. Nonorthogonal hanging-node meshes have been used in adaptive Arbitrary Lagrangian-Eulerian, ALE, hydrodynamics algorithms [2]. Our scheme would be suitable for coupled radiation diffusion/hydrodynamics calculations on such meshes.

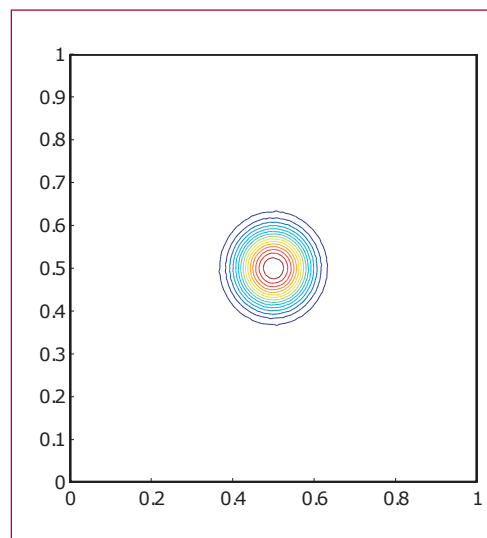
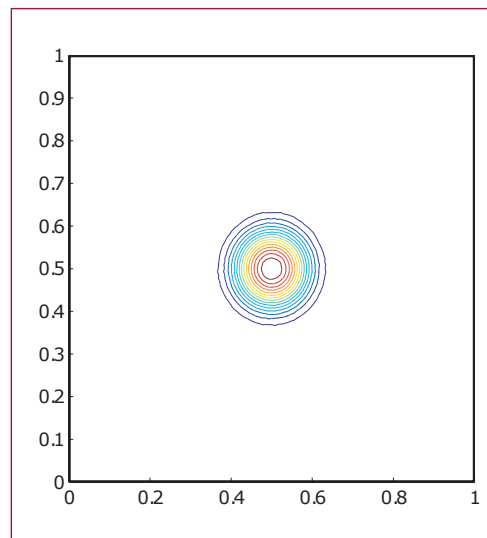
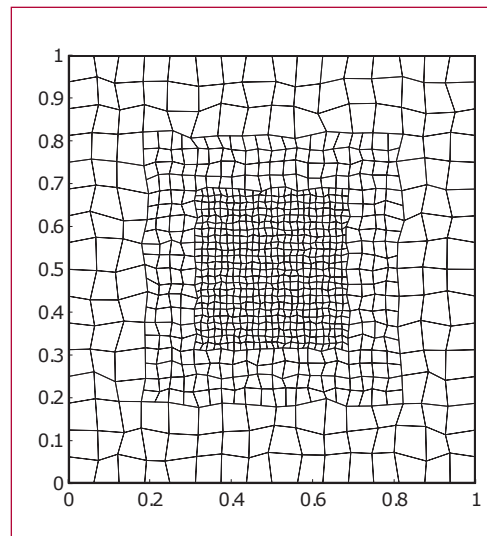
The local SO method is particularly amenable to hanging-node meshes, because the discretization process occurs in two steps. The first step is to consider each cell in the mesh as an independent domain and generate an independent discretization for each cell. The second step is to obtain a global discretization by imposing continuity of the intensity and continuity of the normal component of the flux across cell interfaces. Since each cell in a hanging-node mesh is a quadrilateral, the first step in applying the SO method is identical to that for standard quadrilateral meshes. However, imposing continuity of the intensity and continuity of the normal component of the flux is not straightforward on hanging-node meshes because the intensity and flux unknowns do not coincide as they do on standard meshes. Thus, one of our new results determines

how to impose continuity of the intensity and the normal component of the flux at three-cell hanging-node interfaces. The most accurate results were obtained when we imposed strong continuity of fluxes (the flux on the coarse-grid interface coincides with the fluxes on the fine-grid interface) and weak continuity of intensities.

The new discretization has been tested on a number of cases. It has been shown that the discretization preserves the uniform flow. A textbook example is shown in the top figure. The solution of the diffusion equation has a sharp peak in the middle of the domain and close to zero near the domain boundary. The calculations were performed on locally refined and quasi-uniform grids. As shown in the figure, the adaptive grid has three levels of refinements. The solution obtained with this grid is very close to the solution computed on a quasi-uniform grid with approximately four times more mesh cells.

[1] Konstantin Lipnikov, Jim Morel, and Mikhail Shashkov. "Mimetic Finite Difference Methods for Diffusion Equations on Non-Orthogonal, AMR Non-conformal Meshes," LAUR-03-1765, submitted to *J. Comput. Phys.* <http://cnls.lanl.gov/~shashkov>.

[2] R. Anderson, R. Pember, and N. Elliott. "An Arbitrary Lagrangian-Eulerian Method with Local Structured Adaptive Mesh Refinement for Modeling Shock Hydrodynamics," presented at the 40th AIAA Aerospace Sciences Meeting and Exhibit, January 14–17, 2002, Reno Nevada, AIAA paper 2002-0738, published by the *American Institute of Aeronautics and Astronautics*, 1801 Dr. Alexander Bell, Suite 500, Reston, VA 20191-4344.

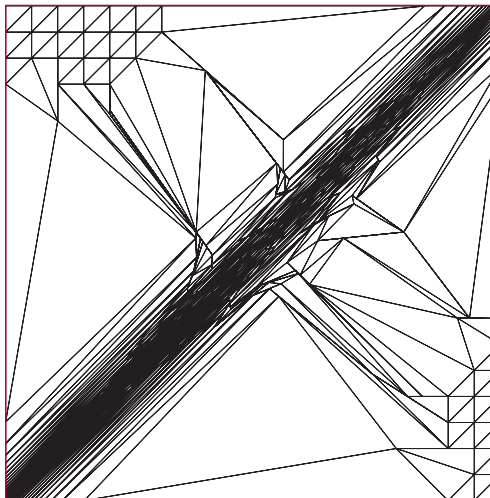


Figures—
The textbook example showing the locally refined mesh (top picture) and isolines of discrete solutions computed on locally refined mesh (middle picture) and quasi-uniform mesh with approximately four times more elements (bottom picture).

Multilevel Accelerated Optimization for Problems in Grid Generation

Markus Berndt and Mikhail J. Shashkov,
T-7; berndt@lanl.gov

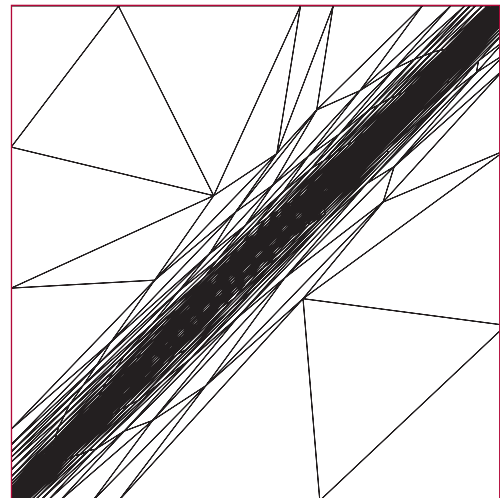
The quality of numerical simulations of processes that are modeled by partial differential equations strongly depends on the quality of the mesh that is used for their discretization. This quality is affected, for example, by mesh smoothness or discretization error. To improve the mesh, a functional that is in general nonlinear must be minimized. This minimization is constrained by the validity of the mesh, since no mesh folding is allowed. Classical optimization techniques, such as nonlinear CG or Gauss-Seidel steepest descent, perform very poorly on this class of minimization problems. We introduce a new minimization technique that utilizes the underlying geometry of the problem. By coarsening the mesh successively in a multilevel-like fashion, minimizing appropriate coarse grid quality measures, and interpolating finer meshes from coarser ones, a more rapid movement of fine mesh points results, and the overall convergence of the minimization procedure is accelerated [1].



We first describe the coarsening strategy. In an initial step in Delaunay coarsening [2], the list of vertices is reordered in such a way that all boundary vertices come first. In a loop over this list of vertices, the current vertex is added to the list of coarse vertices and its neighbors are deleted from the list of vertices. Hence, initially the boundary is coarsened, and then the interior is coarsened. As a slight modification of this algorithm, we first consider such boundary vertices that are necessary to properly resolve the shape of the domain. An example for such vertices are the four corner vertices of a square. The resulting list of coarse vertices is then triangulated using a Delaunay algorithm, e.g. [3].

Interpolating a grid from a coarser one is achieved by injection in the case of coarse vertices that are also fine vertices. All other fine vertices are interpolated using their barycentric coordinates with respect to their underlying coarse triangle as interpolation weights. In this procedure, the resulting grid might be tangled in some places. We handle this situation by using the untangling procedure described in [4].

For an approximate minimization procedure, we will call it relaxation, we use a few iterations standard gradient-



based optimizer, such as Gauss-Seidel steepest descent.

The three components restriction, interpolation, and relaxation are combined to yield a multigrid-style V-cycle iteration [5] In the figure, we show the final grid after 500 iterations of Gauss-Seidel steepest descent (left), and the final grid after three iterations of our new V-cycle optimization procedure (right). The objective was to minimize the approximation error of a given function with a steep gradient by moving the underlying grid. In both cases the initial grid was a regular triangular grid. The V-cycle procedure was completed in 25.9 seconds, while 500 iterations of the fine level Gauss-Seidel steepest descent procedure took more than 1000 seconds.

For this approach it is essential that a coarse grid representation of the objective function that is to be minimized can be derived. In other words, the change in the initial grid that is required to obtain the optimal grid must be expressible as small changes of vertex positions relative to the positions of neighbor vertices, plus larger changes of positions of groups of vertices. This is possible for applications where the objective is to find a grid that is optimal for the approximation of a function. We plan to extend this work to include the case where an error estimate, and not the actual error, is to be minimized.

[1] Markus Berndt and Mikhail Shashkov, "Multilevel Accelerated Optimization for Problems in Grid Generation," Proceedings of the 12th International Meshing Roundtable, 2003, Santa Fe, NM, USA.

[2] H. Guillard, "Coarsening Unstructured Meshes by Edge Contraction," INRIA Report No. 1898, 1993.

[3] S. J. Fortune, "A Sweepline Algorithm for Voronoi Diagrams," *Algorithmica*, 153–174 (1987).

[4] P. Vachal, R. V. Garimella, and M. J. Shashkov, "Untangling of 2-D Meshes in ALE Simulations," under review in *J. Comput. Phys.*

[5] U. Trottenberg, C. W. Oosterlee, and A. Schueller, "Multigrid," (Academic Press, 2001).



Numerical Methods for Simulation of the Heating through Electromagnetic Induction

Mikhail J. Shashkov, T-7
and Neil Carlson, Independent
consultant; shashkov@lanl.gov

The Telluride Code Project is tasked to develop and apply a new simulation tool designed to model and optimize the gravity-pour casting processes that are currently ongoing at LANL foundries in support of the U. S. Department of Energy (DOE) alloy manufacturing needs. The Telluride simulation tool must accurately model the entire alloy casting process in one integrated simulation. This process begins with molten alloy-free surface flow characteristic of the pouring and filling of a mold cavity. Cooling and solidification of the alloy follows shortly thereafter, followed by a more gradual cooling of the solid alloy to room temperature, which completes the casting process. Further homogenization heat treatment and machining prepare the alloy part for integration into the engineering system for which it is designed.

This work comes out of the development of an electromagnetic modeling capability for the Telluride project's materials processing/metal casting simulation tool Truchas. Of particular importance is the simulation of the heating of heavy metals and graphite mold and filling structures through electromagnetic induction. We have constructed reliable discretizations for the solutions

to Maxwell's equations on general 3-D unstructured meshes for media with strongly discontinuous properties. These discretizations are based on discrete analogs of differential operators that satisfy the identities and theorems of vector and tensor calculus in discrete form. Our new methods mimic many fundamental properties of the underlying physical problem, including the conservation laws, the symmetries in the solution, and the nondivergence of particular vector fields. These methods do not allow spurious modes.

Here we present numerical results for the modeling of the following problem: a finite-length graphite cylinder exposed to an external, alternating magnetic field directed along its axis. The sinusoidally varying field induces an azimuthal current near the surface of the cylinder, which, because of the finite conductivity, dissipates energy in the form of a Joule heat in the graphite. Symmetry is exploited by modeling only a 60-degree wedge of the top half of the cylinder.

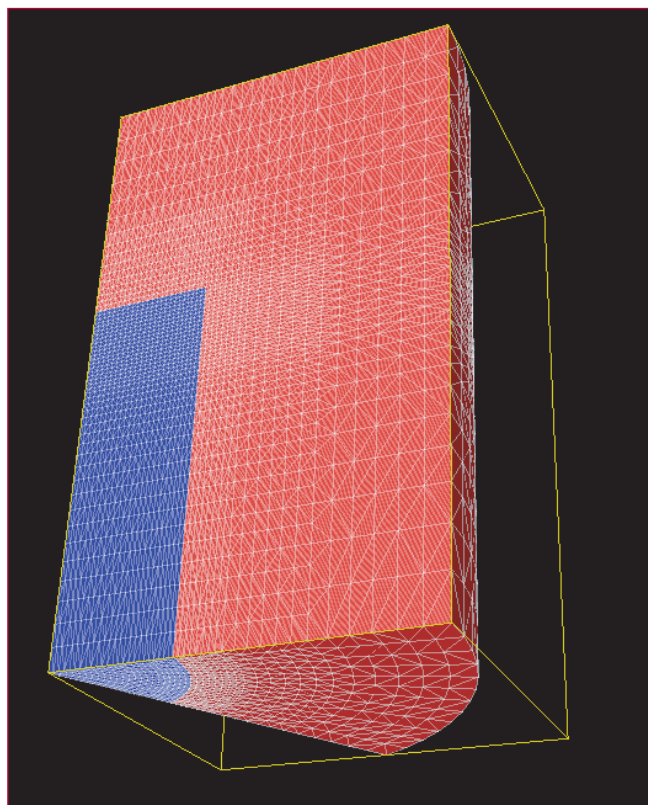


Figure 1—
Shows the computational domain and grid (200-K tets). The blue region is the graphite cylinder, and the red region is free space.

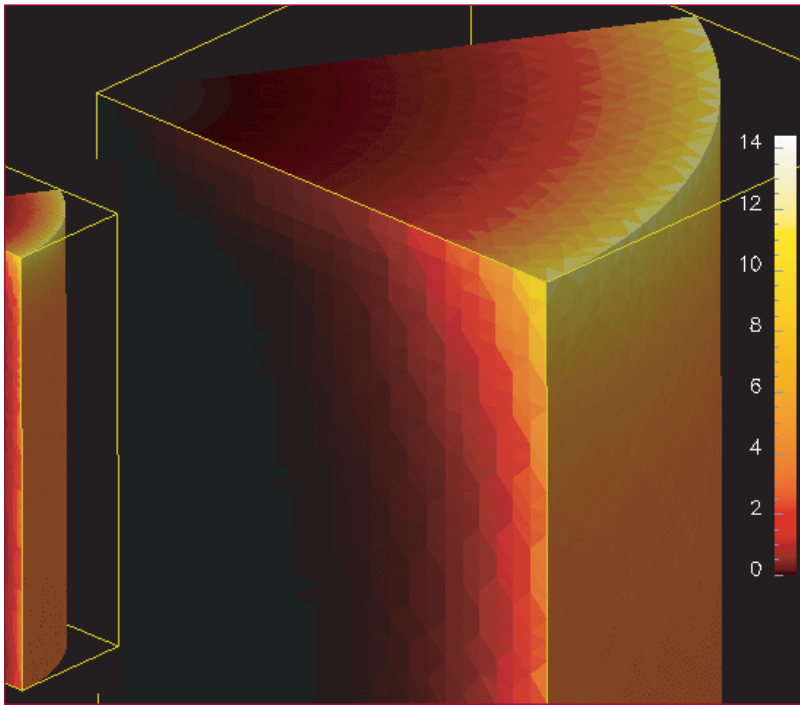


Figure 2— Shows the average of the Joule heat in the graphite cylinder over a cycle of the external field. This is the effective heat source that is used to model the heat conduction.

[1] James M. Hyman and Mikhail J. Shashkov, “Mimetic Discretizations for Maxwell’s Equations,” *Journal of Computational Physics* **151**, 881–909 (1999).

[2] James M. Hyman and Mikhail J. Shashkov, “The Orthogonal Decomposition Theorems for Mimetic Finite Difference Methods,” *SIAM Journal on Numerical Analysis* **36**, No. 3, 788–811 (1999).

[3] James M. Hyman and Mikhail J. Shashkov, “Mimetic Discretizations for Maxwell’s Equations and the Equations of Magnetic Diffusion,” *Progress in Electromagnetic Research, PIER* **32**, 89–121 (2001).



Parallel, Scalable, and Robust Multigrid for Diffusion Problems on Structured Grids

John D. Moulton, Travis M. Austin, Markus Berndt, Benjamin K. Bergen, Joel E. Dendy, T-7; moulton@lanl.gov

Introduction:

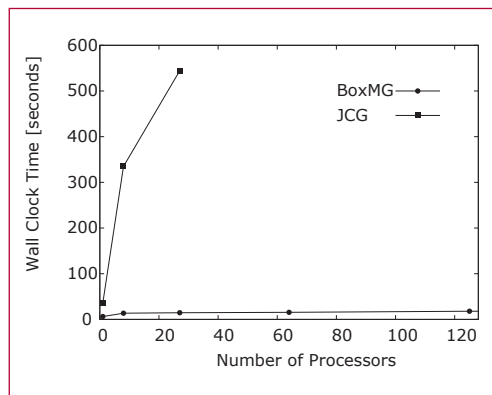
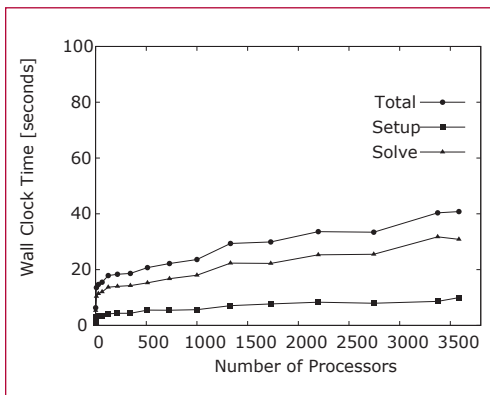
Robust and efficient multilevel iterative solvers are vital for the predictive simulation of complex multiscale and multicomponent nonlinear applications. Specifically, diffusive phenomena play a significant role in applications of interest to ASC, including radiation transport, flow in porous media, and composite materials. In fact, the solution of the diffusive component (elliptic component) of these systems frequently dominates the simulation cost because it is characterized by a discontinuous diffusion coefficient with fine-scale spatial structure. Thus, efficient multilevel iterative methods are crucial because their solution cost scales linearly with the number of unknowns (i.e., optimal algorithmic scaling). In particular, this optimal scaling facilitates the efficient three-dimensional multiscale simulations of linear problems. It also expands the applicability and enhances the effectiveness of large three-dimensional multicomponent nonlinear simulations that advance

implicitly in time (e.g., matrix-free Newton-Krylov methods) through efficient and robust preconditioning of the Krylov iteration.

Robust Multigrid Algorithms:

Multigrid methods gained recognition in the late 1970s as an efficient algorithm for the solution of the discrete linear systems that arise from models of diffusive phenomena (e.g., heat conduction, neutron diffusion, single-phase saturated flow). These methods achieve their efficiency through the recursive use of successively coarser discrete problems (i.e., a sequence of coarse-grid discrete operators) in conjunction with smoothing on each level (e.g., a single Gauss-Seidel iteration on each level) to damp the highly oscillatory errors associated with each grid. Unfortunately, early multigrid algorithms were fragile, with their efficiency strongly dependent on the variability of the model's coefficients. Considerable research in the early 1980s, much of it in T-7, led to the first multigrid algorithms that could be used reliably for a large class of practical problems. The key to the success of these robust *Black Box* methods, was the use of the fine-scale discrete model to construct, through a variational principle, the successively coarser coarse-grid operators. More recently, this class of practical problems has been expanded further by using multigrid methods as preconditioners for various Krylov methods.

Figure— A scalability study of the three-dimensional BoxMG code on QB for a standard discretization of a Poisson problem on the unit cube is shown in the left plot. The local problem size of $100 \times 100 \times 100$ is kept fixed while the global problem size grows with the increasing number of processors. In the right plot the scalability of BoxMG is contrasted with the poor scaling of Jacobi preconditioned conjugate gradient iterations.



A Parallel Scalable Implementation of BoxMG:

We implemented an MPI-based parallel version of Dendy's Black Box Multigrid Code for structured grids [1] in both two and three dimensions that scales well over one sector of Q. In particular, we developed a customized version of the Message Passing for Structured Grid Toolkit (MSG) from netlib, created the necessary data structures, and established the necessary communication patterns to facilitate the reuse of the core computational kernels from the serial BoxMG code. At present, these codes have been tested on QSC, Q, and Theta, as well as T-7's Linux-based Beowulf clusters. As part of the SC&S Q milestone we demonstrated the scalability of these codes for a standard finite difference discretization of the Poisson equation. Specifically, for the three-dimensional case, shown in the figure, we considered a fixed local problem size of $100 \times 100 \times 100$, growing the global problem size by increasing the number of processors. A common measure of parallel efficiency for this type of scalability study is the ratio of the time to solution on one processor to the time on N processors. For perfect scaling the ratio is one; very poor scaling is near zero. When solving a problem with over three billion unknowns to a relative residual in the 2-norm of 10^{-12} in 40 seconds, the three-dimensional BoxMG code achieved a parallel efficiency of 15.5%. A similar study in two dimensions achieved a parallel efficiency of 25.8%.

We anticipate that the BoxMG solvers will have a positive impact on ASC-related code projects. Thus far, we have integrated the two-dimensional parallel BoxMG code into the ZATHRAS

gray thermal radiation transport equation solver. Although ZATHRAS is designed primarily for simulation on unstructured grids, it is also used for computations on structured grids. For this case we created the necessary interface routines to map the unstructured storage to the structured data structures of BoxMG. The initial timing results on small problems are very promising, and likely to improve with larger problems on more processors. Based on this success we plan to continue this collaboration and integrate the three-dimensional parallel BoxMG code into ZATHRAS in an analogous fashion.

[1] J. E. Dendy, Jr., "Black Box Multigrid," *Journal of Computational Physics* **48**, 366–386 (1982).



A Software Component for a Sign-Preserving and Linearity-Preserving ALE Remapping Method

Martin F. Staley and Mikhail J. Shashkov,
T-7; mstaley@lanl.gov

Background

We have developed a software component implementation of the remapping algorithm described in [1].

Consider that we have a two-dimensional grid consisting of nonoverlapping cells that cover some region. Call this the old grid. Next, consider that we have another grid, with the same number of cells and the same connectivity, and that covers the same region. Call this the new grid. We assume that the new grid is a small perturbation of the old grid.

This situation arises in the context of arbitrary Lagrangian-Eulerian (ALE) methods, in which the old grid is the result of the Lagrangian step, and the new grid is the result of a rezoning step in which the quality of the Lagrangian grid is improved in some way. This remapping algorithm is effective as long as the new grid is a small perturbation of the old grid. It is not required that the grids arise in an ALE context.

Algorithm

The remapping problem we will address here can be stated as follows: given mean densities of cells on the old grid, compute mean densities of cells on the new grid. The algorithm achieves this by performing three stages: density reconstruction, mass exchange, and mass repair. We will henceforth consider *density* to mean *mean density*.

For the *density reconstruction* stage, consider that the cell densities obey some

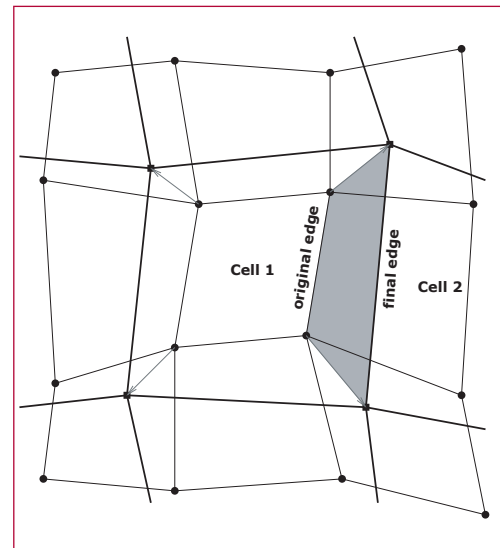


Figure 1—
Swept region of
an edge. When the
original edge moves
to its final position,
the shaded region
is swept.

underlying, theoretical density function ρ . We don't know what ρ is, but if we assume it is piecewise linear—one piece per cell—then we can use our discrete densities to reconstruct a reasonable candidate for ρ . For each cell, we consider a linear density function that achieves the cell's density at the cell's center of volume. Then, we use values of density in nearby cells to compute a reasonable gradient for the function. With a point and a gradient, we have our linear density function.

For the *mass exchange* stage, consider that each edge of the grid has two adjacent cells. For each edge, we identify which cell the edge “moves into” more when we go from the old grid to the new grid. We then compute the integral of that cell's reconstructed density over the region swept by the edge as it moves. The resulting mass is removed from that cell, and added to the other cell.

For the *mass repair* stage, we first recognize that the mass exchange stage involved inexact integration of the overall density function ρ , in the sense that the mass exchange term was obtained by computing the integral over the swept region of the reconstructed density function on one particular cell, even though the swept region may have intersected

other cells. This made the algorithm efficient, because we did not need to compute exact intersections of new cells with old cells. However, as a result of inexact integration, new densities in individual cells can conceivably violate local bounds. The repair stage fixes out-of-bounds masses and densities while still conserving total mass.

Figure 1 shows the swept region of an edge. If we imagine moving the illustrated edge from the old grid (thin lines) to its position on the new grid (thick lines), then the shaded region is swept by the edge as it changes position. In the case illustrated, the edge moves into Cell 2 more so than into Cell 1, and therefore, the algorithm integrates the reconstructed density function for Cell 2 over the entire swept region. In the mass exchange stage, the resulting mass is subtracted from Cell 2 and added to Cell 1. In the mass repair stage, we recognize that the integration was inexact because the swept region intersected with the cells above and below Cell 2, not just with Cell 2 itself, and that there may therefore be out-of-bounds physical quantities in need of repair.

Software Component

The remap library is written entirely in ANSI standard C++, and is designed to be a true software component. It provides a structure into which you place a minimal set of geometry information, consisting of node coordinates on the old and new grids, and vertices (in counterclockwise order) of each cell. From this information, the library computes all other geometry information it needs. To make the remap library work with your grid, then, you must only provide an interface to put your grid into the remap library's simple form.

All relevant constructs in the library are written generically, with C++ templates, so that you can tell the remapper to use any suitably equipped array or array-element type.

The entire library consists of C++ header files, not C++ source files, and therefore requires no compilation—that is, no complicated configuration scripts or makefiles. To use the library with your C++ source file, you include a single C++ header file called `remap` at the top of your code, and then compile your code in whatever way you usually do.

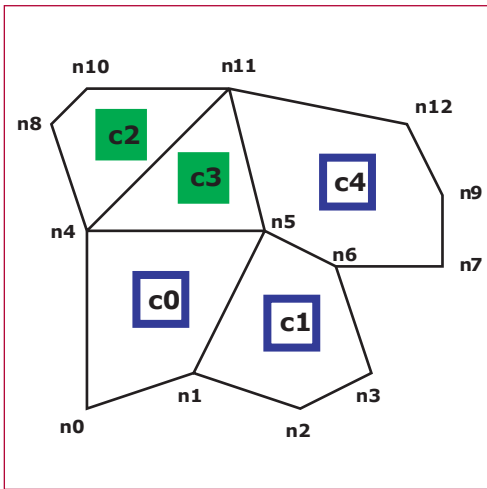
Users may provide plug-ins to redefine stages within the remap process, including computation of cell volumes, cell centers-of-volume, minimum and maximum density bounds, density gradients for the piecewise-linear reconstruction, cell masses, mass exchange terms, minimum and maximum mass bounds, and finally mass repair and recomputation of densities given repaired masses.

Remaps may be performed on general unstructured two-dimensional Cartesian (x,y) and cylindrical (r,z) grids. The library does not require, say, that your cells are triangles or quadrilaterals. Cells may have any number of vertices greater than or equal to three. The library does assume, as the underlying remap algorithm does, that the cells are convex and that the grid's boundary is stationary.

Parallel Remapping

You may use the remap library on a serial machine or a SIMD (single instruction, multiple data) parallel machine. No special actions are required on a serial machine. On a parallel machine, you must provide either one (for a simple global mass repair) or two (for an iterative local mass repair)

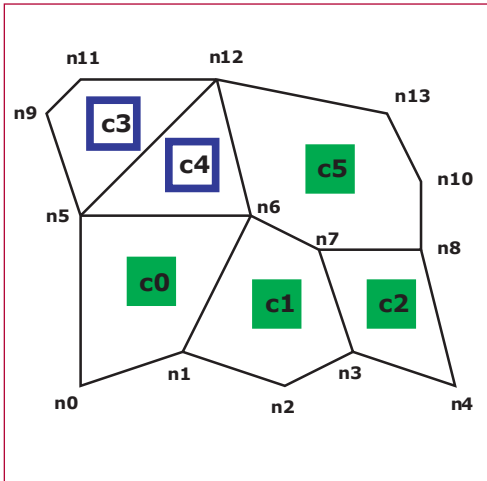
Figure 2—
Geometry for the first processor. Cells shown in green are on-processor cells. Cells shown in blue are off-processor cells that touch on-processor cells.



plug-ins to perform parallel communication steps. The remap library itself makes no assumptions about your parallel communication library.

Consider a six-cell grid on a two-processor machine, with two cells on the first processor and four cells on the second processor. Figure 2 shows the portion of the grid on the first processor. There are 13 nodes, labeled n0 through n12, and five cells, labeled c0 through c4. Cells c2 and c3 are on this processor. Cells c0, c1, and c4 are not, but they

Figure 3—
Geometry for the second processor. Cells shown in green are on-processor cells. Cells shown in blue are off-processor cells that touch on-processor cells.



must be known to this processor because they touch one or more of its cells.

Figure 3 shows the portion of the grid on the second processor. There are 14 nodes, labeled n0 through n13, and six cells, labeled c0 through c5. Cells c0,

c1, c2, and c5 are on this processor. Cells c3 and c4 are not, but they must be known to this processor because they touch one of more of its cells.

In general, each processor must know about its own cells (numbering, say, $O(n^2)$), plus the small number (typically $O(n)$) of touching off-processor cells.

For each processor, you supply the old and new node coordinates, a list of each cell's vertices in counterclockwise order, and a flag telling whether the cell is on- or off-processor. Then, for each cell, you provide an input physical quantity, for example density, and tell the library to perform the remap.

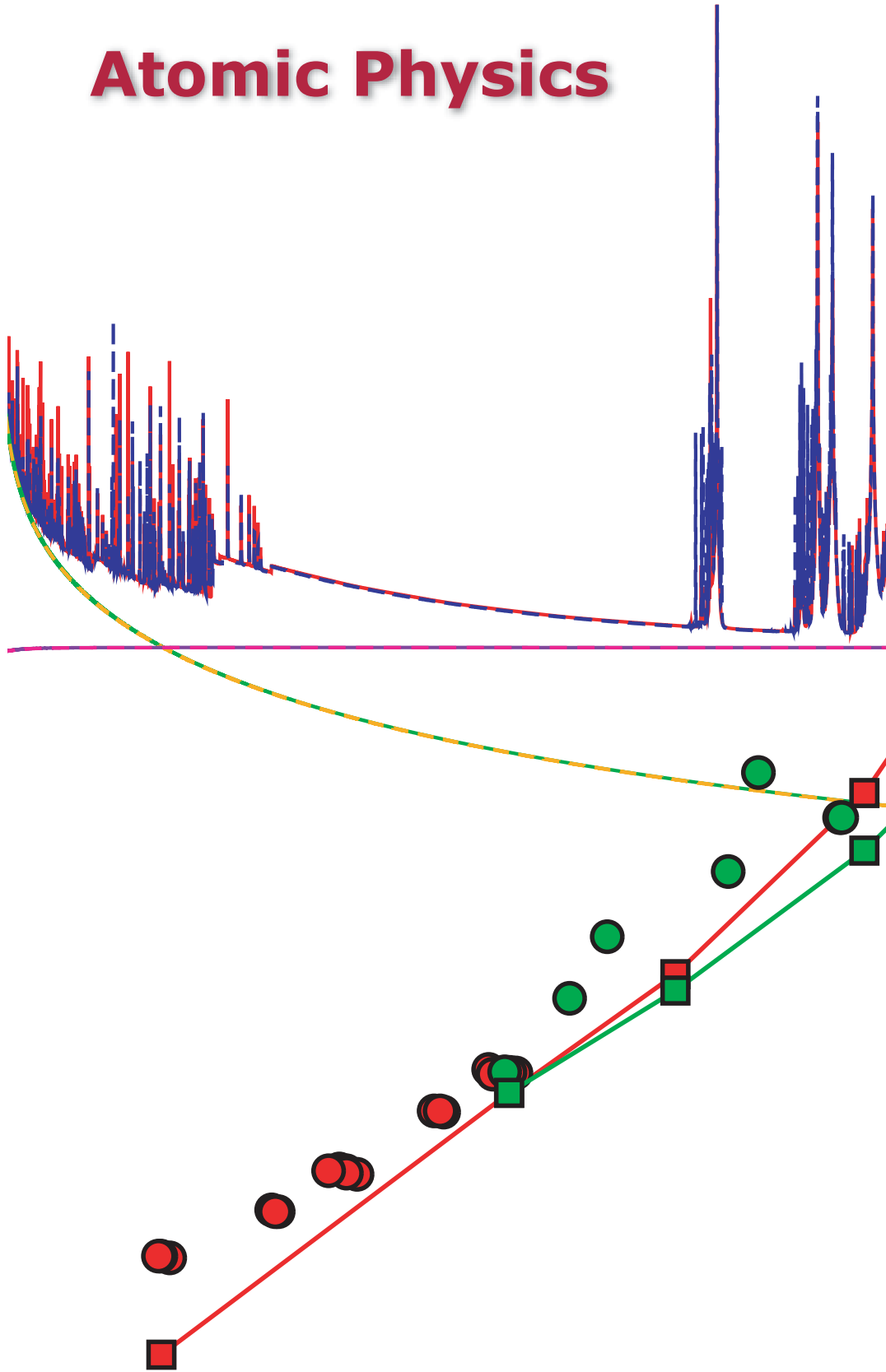
Acknowledgements:

This work was funded under the Component Definition and Architecture R&D sub-subcomponent of ASCI. Project Leaders: R. Lowrie and T. Urbatsch.

[1] M. Kucharik, M. Shashkov, and B. Wendroff, "An efficient linearity-and-bound-preserving remapping method," *J. Comput. Phys.* **188**, 462–471 (2003).



Atomic Physics

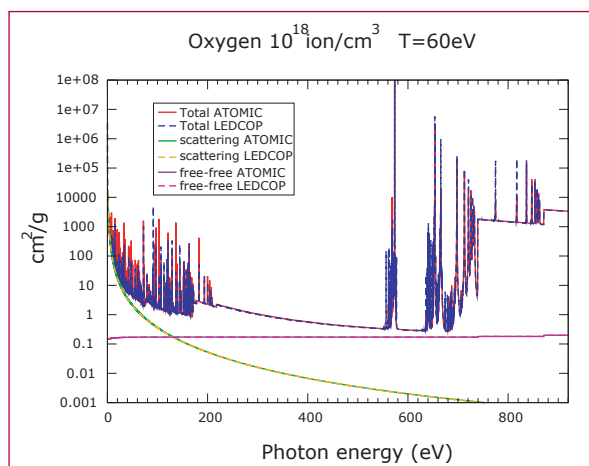


ATOMIC Benchmark Opacity Calculation

Joseph Abdallah, Jr., Peter Hakel, David P. Kilcrease, Norman H. Magee, Stephane F. Mazevet, and Manolo E. Sherrill, T-4; Christopher J. Fontes and Honglin Zhang, X-5; abd@lanl.gov

We report on meeting the first milestone for the development of ATOMIC, a code designed to compute opacities under both LTE (local thermodynamic equilibrium) and non-LTE conditions for a large range of elements. ATOMIC will become the successor of the T-4 opacity code LEDCOP, and our first milestone calculation centers on a direct benchmark comparison of opacities computed by each code. This benchmark calculation aims at demonstrating that all the major physics capabilities of LEDCOP have been successfully transferred to ATOMIC.

The basis of ATOMIC is the FORTRAN 90 reconstruction of the FINE nonequilibrium spectral modeling code, to which physics packages extracted from the T-4 opacity code LEDCOP have been added. ATOMIC provides improved atomic physics data, a user-friendly interface, modularity to facilitate code improvements, platform independence, and less manipulation of the atomic physics databases than is currently necessary for LEDCOP. The development of ATOMIC in FORTRAN 90 also provides a platform for parallelization of both LTE and non-LTE calculations in the future. The bound-bound and bound-free treatments from FINE remain mostly intact in ATOMIC. The LEDCOP physics packages necessary to compute opacities, the free-free, Thomson and Compton scattering,



Stark and collisional broadening as well as conductive opacity were converted to FORTRAN 90 and implemented in ATOMIC.

ATOMIC makes use of a new scheme to include plasma and density effects. A preliminary package has been developed, implemented in ATOMIC and tested against the LEDCOP results. It is hoped that this package will also overcome some of the limitations of the equation of state (EOS) used in LEDCOP. A method involving histograms for binning the line strength as a function of photon energy was also developed and implemented in ATOMIC to process the enormous amount of spectral line information that is required. This method greatly reduces the amount of computer time necessary over traditional methods where a shape is computed separately for each spectral line. Parallel implementation of the calculation of the bound-bound contribution has also been explored. The initial scaling obtained, which corresponds to number of processors divided by two for up to eight processors, is encouraging and the will method be further developed and implemented in ATOMIC in the coming year. In the FORTRAN 90 conversion of FINE every effort was made to preserve

Figure 1— Comparison of the frequency dependent opacities calculated by ATOMIC and LEDCOP.

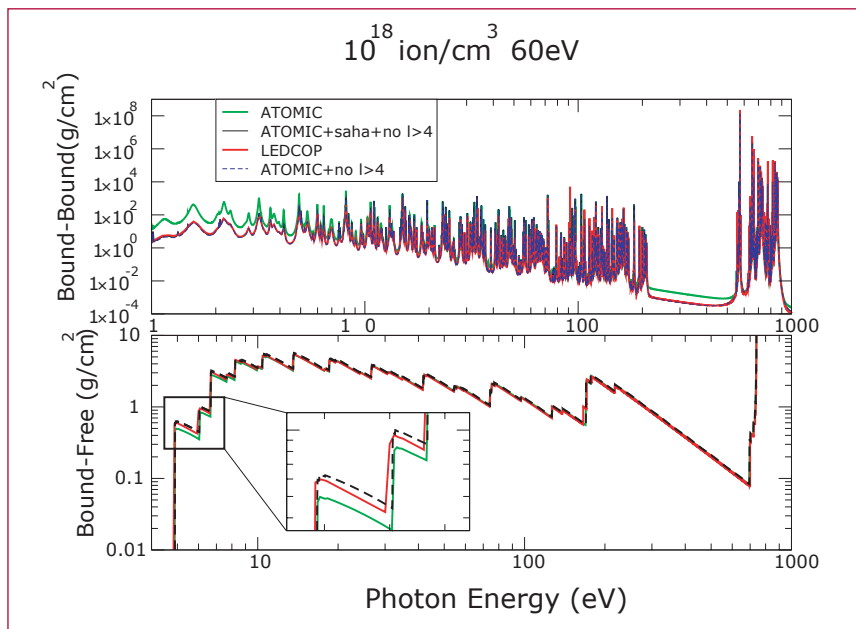


Figure 2—
Comparison of the bound-bound and bound-free contributions between ATOMIC and LEDCOP.

(cm ² /g)	κ_R^{AT}	κ_R^{LED}	κ_P^{AT}	κ_P^{LED}
$\rho = 1.10^{18}$ ion / cm ² T=30eV	1.06×10^1	1.02×10^1	1.03×10^2	1.16×10^2
$\rho = 1.10^{18}$ ion / cm ² T=60eV	9.48×10^{-1}	9.32×10^{-1}	7.97×10^3	4.64×10^3
$\rho = 2.5 \times 10^{19}$ ion / cm ² T=30eV	3.39×10^2	3.46×10^2	1.94×10^3	1.72×10^3

Table—
Comparison between the ATOMIC and LEDCOP opacity calculations for oxygen. AT: ATOMIC, LED: LEDCOP, R: Rosseland, P: Planck.

the non-LTE capabilities. Most of the important non-LTE options in ATOMIC have been debugged, tested, and give identical results to the F77 FINE code. ATOMIC has been used to calculate test cases for the upcoming NLTE3 workshop being held in December 2003 at NIST in Gaithersburg. A suite of regression tests for ATOMIC was developed for quality control. This project also makes use of the RAZOR database management software for version control.

Figures I and II and the table show a sample of the initial comparison between ATOMIC and LEDCOP. This initial comparison shows that ATOMIC has been successfully

converted into an opacity code and contains the main components required for an opacity calculation. This effort will continue in the coming year by extending the temperature-density range of the new EOS model, by improving the physics models used in the transferred LEDCOP packages, and by developing an edge broadening model to account more accurately than in LEDCOP for the density effects on the bound and continuum states. The parallel calculation of different density-temperature points and the bound-bound contribution will also be implemented in ATOMIC.



Benchmarking Aluminum Opacity Libraries Using Quantum Molecular Dynamics

Stephane F. Mazevet, Lee A. Collins, and Norman H. Magee, T-4; Joel D. Kress, T-12; Eric D. Chisolm and Scott Crockett, T-1, and M. Desjournais, Sandia National Laboratory; smazevet@lanl.gov

Many opacity libraries commonly in use for standard macroscopic modeling programs such as in hydrodynamic codes use absorption cross sections derived for isolated atoms or ions while many-body and plasma effects are modeled as perturbations to the population distribution over these atomic states, reintroduced as adjustments to the final results, or both. In the mean time, developments in a wide variety of fields, including dense plasma, inertial confinement fusion, and astrophysics, require an extension of the opacity libraries into new and complex regimes where such a simple approach to the many-body effects quickly becomes questionable.

The relatively low-temperature, high-density regime (a few eV and few g/cm^3), often labeled as “warm dense matter,” is an example of such a situation where the intricate nature of the medium, partially dissociated and ionized, intermediate coupling, $\Gamma \sim 1$, and partially degenerate $\eta \sim 1$, requires a careful validation of the physical models that produce the opacity data either from experiments or more sophisticated theoretical methods. In this regime, usually reached experimentally by shock compression in the Mbar range, the accurate knowledge of opacities drives the modeling of diverse systems from white dwarf atmospheres, which play a key role in latest attempts to date various astrophysical objects, to strongly coupled plasmas produced by exploding aluminum wires.

Quantum Molecular Dynamics (QMD) simulations provide an effective venue to calculate and benchmark Rosseland mean opacities in this regime [1,2]. This *ab-initio* approach produces a consistent set of material, electrical, and optical properties from the same simulation and can be applied without restriction to various mixtures of atomic, ionic, or molecular species [3,4]. This contrasts

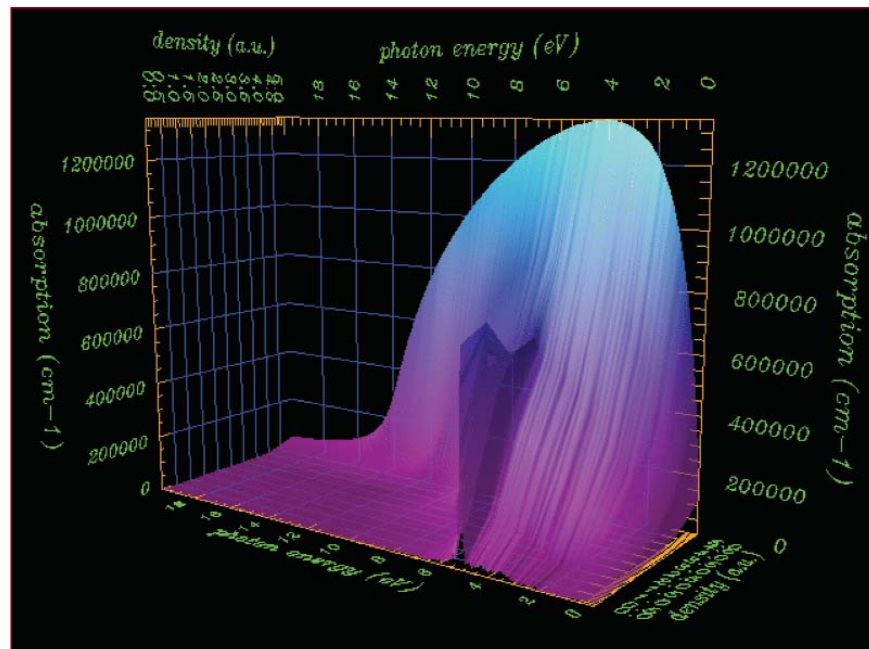


Figure 1—Variation of the QMD aluminum absorption coefficient as a function of density and for a temperature of 10000 K.

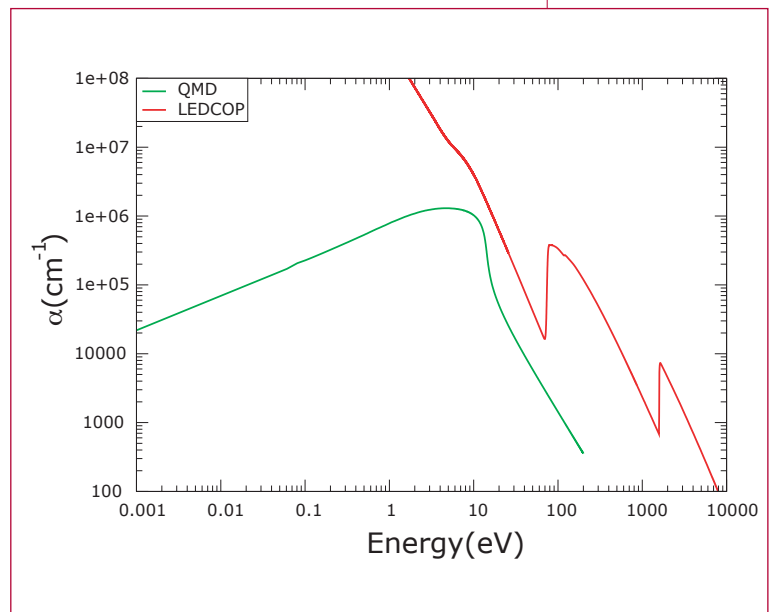
with the opacity libraries, which consist of an integrated collection of approximate models leading sometimes to inconsistencies on the overall nature of the medium. This situation is illustrated here, for the case of aluminum, where we use QMD to benchmark the opacities calculated using the Los Alamos Light Element Opacity code, LEDCOP, for densities and temperatures ranging from gas ($\sim 0.01 \text{ g/cm}^3$ and $T = 10,000 \text{ K}$) to liquid density ($\sim 2 \text{ g/cm}^3$ and $T = 10,000 \text{ K}$). We choose aluminum in this particular density-temperature range as it exacerbates the limitation of the model used in the LEDCOP opacity code and illustrates the difficulty in extending current opacity libraries into the warm dense matter regime.

For a density varying from 0.01 g/cm^3 to 2 g/cm^3 and temperatures ranging from $10,000 \text{ K}$ to $30,000 \text{ K}$, aluminum, which starts as an atomic gas, gradually becomes a liquid metal at the highest density. This situation is illustrated in Figure 1, where we show the absorption coefficient calculated using the QMD method at a fixed temperature of $10,000 \text{ K}$ and for the density range given above. At the lowest density, $\rho = 0.01 \text{ g/cm}^3$, the QMD absorption coefficient exhibits a maximum centered around 5.1 eV . This maximum corresponds to the atomic $3s-3p$ transition, which value is in good agreement with the averaged configuration energy value of 5.18 eV . As the density slowly increases, the maximum at 5.1 eV gradually decreases with a rise of the absorption coefficient at zero photon energy corresponding to an increase in conductivity. This clearly indicates that as the density increases, aluminum gradually ionizes and forms a metal. At the highest density shown, $\rho = 2 \text{ g/cm}^3$, and a temperature of $10,000 \text{ K}$, aluminum is known to be a

metal and the absorption coefficient shows a broad maximum around 15 eV , characteristic of the optical response for a plasma [1]. For this photon energy region, the corresponding index of refraction shows a broad minimum with a value less than unity centered at a photon frequency corresponding to the plasma frequency of the system. In this regime, the low-frequency part of the QMD absorption coefficient, AC conductivity, and index of refraction, all related by the Kramer relations, can be easily fitted by a Drude form.

In Figure 2, we show a direct comparison of the QMD and LEDCOP absorption coefficients at this same density-temperature point. The two maxima around 100 and 1000 eV for the LEDCOP absorption coefficient correspond to the ionization of the $2s$, $2p$, and $1s$ inner shells of atomic aluminum. While formally an all-electron potential can be used in the QMD, these electronic shells are not included in the current calculations. For the density-temperature case considered here, this has little effect on the calculation of the Rosseland opacity

Figure 2— Comparison between the QMD and LEDCOP absorption coefficient for a density of 2 g/cm^3 and a temperature of $T = 10,000 \text{ K}$.



as the derivative of the Planck function, and hence the Rosseland mean, samples the absorption coefficient at photon energy around 4 eV. For photon energies less than 10 eV, we see in Figure 2 a significant deviation between the two calculations. This can be traced back to the inadequacy of the free-free approximation used in the LEDCOP calculation. This limitation was already pointed out for the case of hydrogen [1,2], and a free-free approximation accounting for the metallic behavior of the sample at these conditions needs to be developed to enable the extension of the opacity library into this regime.

We now turn to the second major limitation for extending the current LEDCOP opacity library to the warm dense matter regime. We show in Figure 3 the calculation of the 10,000 K and 30,000 K isotherms for densities corresponding to the range shown in Figure 1. First, for the whole density range and for both isotherms, we find a remarkable agreement between the QMD and the predictions of the best current SESAME EOS

for aluminum [6], and another aluminum EOS developed for high densities using lattice dynamics, Wallace's liquid dynamics, and density functional theory [7]. This confirms that QMD captures the physical processes in action as the media evolves from an atomic system to a metallic fluid. For densities below 0.1 g/cm^3 , we also find a good agreement between the QMD and the LEDCOP isotherms. As the density increases and density effects become more important, the LEDCOP isotherms drastically deviate from the other calculations for densities between 0.2 g/cm^3 and 2 g/cm^3 . For this density range, the LEDCOP inaccurate isotherms are due to limitations in the EOS model. In this regime, the effect of the environment on the atomic system can no longer be treated as a perturbation and the competing ionization and recombination processes need to be accounted for accurately. The current LEDCOP EOS model, while appropriate for low-density calculations, is pushed here outside of its range of validity.

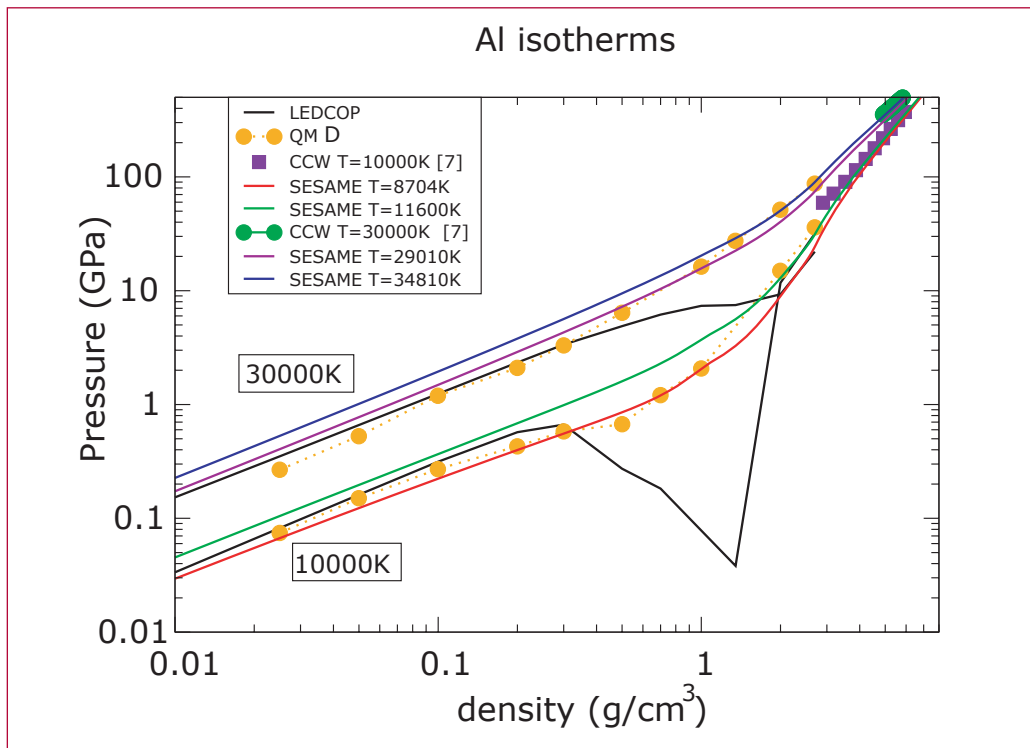


Figure 3—
Comparison of the
QMD aluminum
isotherms with
SESAME and LED-
COP isotherms.

In conclusion, we benchmarked the aluminum opacity calculations performed by the LEDCOP opacity code using QMD. We find that to extend the library into the warm dense matter regime, a new model of the free-free contribution, accounting for the metallic behavior of the media, is required. A new EOS model is also needed to successfully describe the smooth transition from an atomic system to a metallic fluid. This requires us to account more accurately for density effects and how the atomic bound states are gradually depopulated due to the increasing density. This issue is at the heart of the new EOS model developed for the new T-4 opacity code named ATOMIC.

- [1] S. Mazevet et al., LANL report, LA-UR-02-1342 (2002).
- [2] S. Mazevet et al., *Astronomy & Astrophysics* **405**, L5 (2003)
- [3] S. Mazevet et al., *Phys. Rev. B* **67**, 054201 (2003).
- [4] L. A. Collins et al., *PRB* **63**, 184110 (2001).
- [5] C. Neuforge-Verheecke et al., *APJ* **561**, 450 (2001).
- [6] SESAME EOS 3717, found in S. P. Lyon and J. D. Johnson, "T-1 Handbook of the SESAME Equation of State Library," LANL report, LA-CP-98-100.
- [7] E. Chisolm, S. Crockett, and D. Wallace, *Phys. Rev. B* **68**, 104103 (2003).



Generating a Portable Version of CATS

Manolo E. Sherrill, T-4. manolo@lanl.gov

To calculate opacities, the energy level structure and oscillator strengths of the element of interest are required. For low-Z elements, these two quantities are typically obtained from the CATS [1] program. Due to the state of the Fortran 77 (F77) version of CATS, with its computer architecture specific features needed for memory management [2] and the expectation of future CATS execution on different computer platforms, a more portable version of CATS was needed. Since much of the basic syntax would remain the same, reducing the probability of introducing errors into the code during the conversion, along with the ability to include all the memory management requirements under one portable standard. CATS was ported by T-4 opacity group to Fortran 90.

Accomplishments

The porting of CATS to Fortran 90 (F90) began in the second week of April, 2003; by July 9th of the same year, after passing a small number of preliminary tests, the first Beta version of the new code was announced. Extensive testing and fine tuning through the month of July lead to the August 6th reproduction and replacement of the 56-gigabyte Oxygen database used in the development of the new opacity model by T-4. Comparisons against the binary output files generated by the old Fortran 77 version with the new Fortran 90 version of CATS showed that all 56-gigabytes were bit wise equivalent. As a further consistency check, ATOMIC was ran using the new CATS generated data through its seven standard test cases, and the final

results were identical to the results obtained earlier. In addition, even with the inclusion of extensive error checking code, the F90 version of CATS produces nominally identical execution times as its F77 predecessor.

Motivated by discussions with members of X-5 about the growing desire by the Laboratory to increase the number of codes maintained under formal version control with regression tests (version control is currently not required for CATS), a series of tests with the original F77 version of CATS was preemptively created to examine all CATS's options used in generating atomic databases. With this regression test, the new version of CATS has been shown option-by-option to produce the same results as its predecessor.

[1] Los Alamos Report LA-11436-M Theoretical Atomic Physics Code Development I CATS: Cowan Atomic Structure Code.

[2] Dynamic memory allocation is not a Fortran 77 feature. It was introduced into CATS through the use of in-house C programs and the use of the platform dependent CRAY pointers.



Quantum Molecular Dynamics Simulations of Shocked Nitrogen Oxide

Stephane F. Mazevet and Lee A. Collins, T-4; Joel D. Kress, T-12; and P. Blottiau, DPTA; smazevet@lanl.gov

The study of materials under extreme conditions of temperature and pressure has made significant progress in the past few years due to noticeable advances in both the experimental and theoretical techniques. On the experimental side, Z-pinch and laser-driven experimental setups have pushed Hugoniot measurements up to the Mbar range. On the theoretical side, simulation methods, such as Quantum Molecular Dynamics and Path Integral Monte Carlo, now allow the study of materials under such conditions from a mostly “ab-initio” standpoint. Up to now, however, applications of these methods primarily focused on pure systems such [1] as hydrogen, nitrogen [2], and oxygen, and lately on complementing the study of the equation of state (EOS) with the determination of the associated optical and electrical properties [2–5].

We report here on the study of the EOS and dissociation of NO along the principal and second shock Hugoniots using Quantum Molecular Dynamics (QMD). While NO presents a natural extension to study the EOS of multicomponents systems, it also serves as a prototype for the study of explosive compounds and their associated reactive chemistry. Furthermore, the determination of reactive potentials, necessary for the study of technologically relevant and more complex systems such as H-C-N-O, also requires first a calibration to the NO system. Up to now, this calibration has been solely supported by the experimental measurements of the first- and second-

shock Hugoniots. To complement the latter, we calculate the first- and second-shock Hugoniots as well as the corresponding temperature up to pressures of, respectively, 80 GPa and 65 GPa. We further pay particular attention to the constituency of the fluid along each Hugoniot since the chemistry induced by such an increase of pressure and temperature remains among the most challenging aspects in the modeling of such systems. Quantum molecular dynamics methods, where the electrons receive a fully quantum mechanical treatment, are particularly suited for the study of such chemical processes as ionization, recombination, dissociation, and association of the various atomic species present in the media are treated on an equal footing within the framework of the Density Functional Theory (DFT).

In Figure 1 we compare the results of initial QMD calculations, using 54 atoms in the simulation cell, with the available experimental measurements for the principal (first) and highest second-shock Hugoniots. Principal Hugoniot points are the density-pressure (and internal energy) points reached when the shock wave crosses the media while the second-shock Hugoniots occur experimentally when the shock wave bounces back across the sample a second time. For the first shock, we plot the individual measurements instead of the averaged ones as the highest density points represent the initial conditions for the second shock points that will be discussed below. For the highest density reached experimentally along the first shock, $\rho = 2.38 \text{ g/cm}^3$, we find good agreement between the calculations and the measurements. The QMD pressure at this density is $P = 26.87 \text{ GPa}$ and compares well with the experimental one $P = 28.47 \text{ GPa}$. This agreement carries over to the particle and shock velocities where we obtain $u_p = 3.16 \text{ kms}^{-1}$ and $u_s = 6.73 \text{ kms}^{-1}$ compared to the

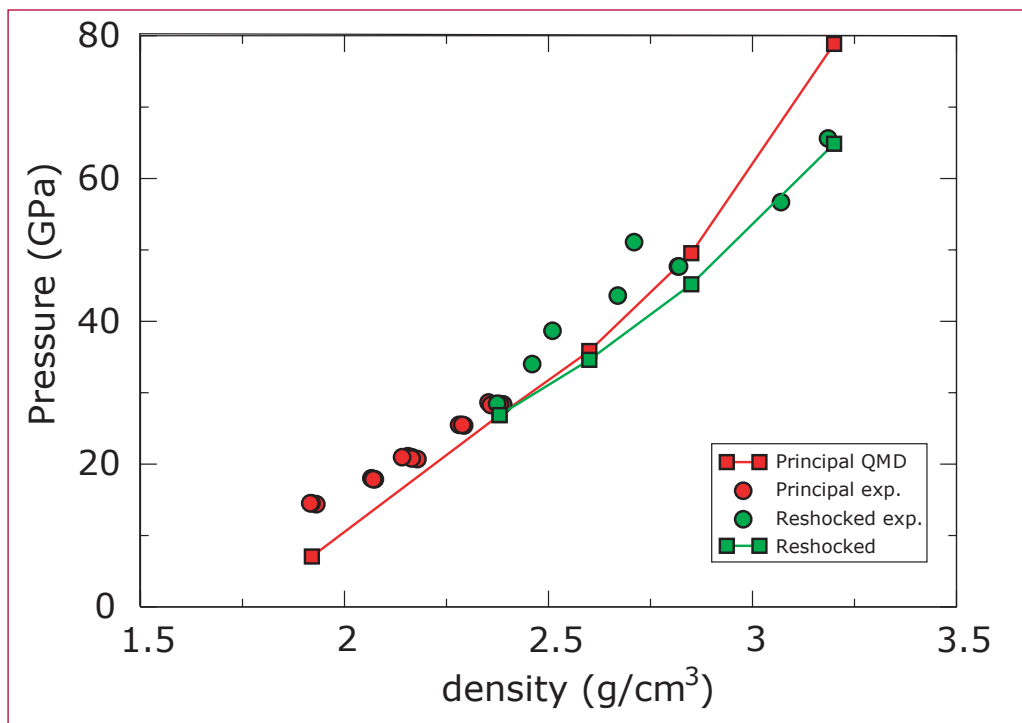


Figure 1—
Principal and
reshocked NO
Hugoniots.

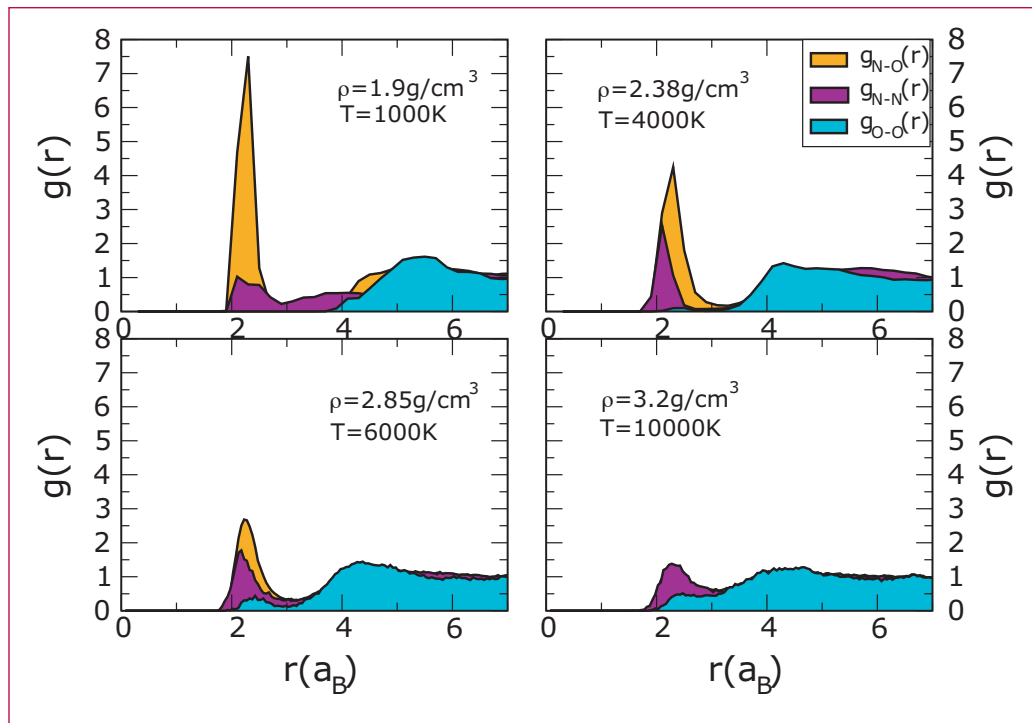
experimental results of, respectively, 3.245 and 6.94 kms^{-1} . The agreement along the first-shock Hugoniot deteriorates as the density is lowered, with a factor of two lower for the QMD pressure at the lowest density measured. This disagreement could be due to the limited number of particles used in the simulation and is currently under investigation using a larger sample in the simulation cell.

For the second-shock Hugoniot, we plotted as experimental results the pressure points obtained for the highest first-shock densities, between 2.28 and 2.38 g/cm^3 . The theoretical second-shock Hugoniot is calculated using the calculations performed at $\rho = 2.38 \text{ g/cm}^3$ only. Such a small variation in the initial conditions does not substantially affect the final second-shock pressures. This variation does not, for example, explain the consistently higher experimental pressures measured for the second shock at densities

between 2.5 and 2.75 g/cm^3 . However, a closer inspection of Figure 1 reveals that, first, this disagreement mostly disappears as the density increases and, second that a significant scatter exists in the experimental data for densities above 2.75 g/cm^3 . These two points combined with the good description of the first-shock Hugoniot in the region around 2.38 g/cm^3 suggests that QMD provides a satisfactory description of the state of the fluid as the simultaneous increase in pressure and temperature breaks the molecular bonds.

To quantify the state of the fluid as the density increases, we calculate the pair correlation functions representative of each possible diatomic species, NO, O_2 , and N_2 . Figure 2 shows such a result along the first Hugoniot and extend beyond the density range explored experimentally. At the lowest density, $\rho = 1.92 \text{ g/cm}^3$, the NO correlation function $g_{N-o}(r)$ peaks at around $2a_B$, the internuclear distance of the NO

Figure 2—
Pair correlation
functions along the
Principal NO
Hugoniot



molecule. The lack of structure in the pair correlation functions of the other two species indicates that the fluid mostly consists of NO molecules at this condition. As the density increases to $\rho = 2.38 \text{ g/cm}^3$, the sizable reduction and broadening of the maximum of $g_{N-O}(r)$ around $2a_B$ indicates that the fluid has partially dissociated. At this density, a similar structure is now also present for the nitrogen pair correlation function $g_{N-N}(r)$. As the equilibrium internuclear radius of N_2 and NO are similar, $r_{\text{N-O}} = 2.17a_B$ and $r_{\text{N}_2} = 2.06a_B$, the pair correlation functions at 2.38 g/cm^3 indicate that the NO fluid has partially dissociated and is constituted of a mixture of NO and N_2 molecules, as well as atomic oxygen. We also notice that at this density, the lack of structure in the oxygen correlation function $g_{O-O}(r)$ indicates that, in contrast to nitrogen, oxygen does not recombine upon dissociation of NO at this density. Figure 2 shows that the constituency of the fluid preserves the same characteristics up to a density of 3.2 g/cm^3 . While NO and N_2 continue to dissociate as the

density increases, molecular nitrogen represents a significant fraction of the molecules in the sample while oxygen stays mostly in an atomic state.

Despite the limited number of atoms used in the simulations, the variation of the molecular fraction of each species along the Hugoniot can be understood by an inspection of their respective dissociation energies. Nitrogen has the highest dissociation energy of the molecular species considered here and, as such, is expected to be the last molecular species present in the sample as both the density and temperature increase. Furthermore, that oxygen has a lower dissociation energy than nitrogen oxide also suggests that oxygen is less likely to associate for density-temperature conditions where NO is dissociated. While this argument, based on the dissociation energy of the isolated molecular species, explains the simulation results, the sensitivity of the QMD results to the number of particles used requires further exploration and validation by performing larger scale simulations.

In summary, we studied the dissociation of nitrogen-oxide along the first-and second-shock Hugoniot. We find that QMD provides a good description of the experimental data for both Hugoniot. Initial simulations with a restricted number of particles (54 atoms) show that molecular nitrogen is forming in the media along both Hugoniot when NO dissociates. As the constituency of the fluid is highly sensitive to the number of particle used in the simulation, this result is currently being verified by performing larger scale simulations.

This work was performed under the auspices of an agreement between CEA/DAM and NNSA/DP on cooperation in fundamental science.

- [1] T. J. Lenosky et al., *Phys. Rev. B* **61**, 1 (2000).
- [2] S. Mazevet et al., *Phys. Rev. B* **65**, 014204 (2001).
- [3] S. Mazevet et al., *Phys. Rev. B* **67**, 054201 (2003).
- [4] S. Mazevet et al., *Astronomy & Astrophysics* **405**, L5 (2003).
- [5] L. A. Collins, *Phys. Rev. B* **63**, 184110 (2001).



Time Dependent Boltzmann-Kinetic Model of the X-rays Produced by the Ultrashort Pulse Laser Irradiation of Argon Clusters

Joseph Abdallah, Jr. and George Csanak, T-4; Y. Fukuda, Y. Akahane, M. Aoyama, N. Inoue, H. Ueda, and K. Yamakawa, Advanced Photon Research Center; A. Ya. Faenov, A. I. Magunov, T. A. Pikuz, and I. Yu. Skobelev, Multicharged Ions Spectra Data Center; abd@lanl.gov

The Boltzmann equation and a detailed collisional radiative model are solved simultaneously as a function of time to model the time integrated X-ray spectra of the transient plasma produced by a high, intensity ultra-fast laser source. Level populations are calculated by solving the rate equations as a function of time using rate coefficients corresponding to a time varying electron energy distribution function (EEDF) determined by the solution to the Boltzmann equation including inelastic and elastic collision processes. The elastic electron-electron interactions are included through the solution of the Fokker-Planck equation. To our knowledge, this is the most detailed calculation of the spectroscopic properties of a plasma using nonequilibrium electron energy distribution functions. The calculations solve for the distribution of 100 electron energy bins simultaneously with the populations of over 3000 levels for Ne-like to H-like argon. The calculations took 215 hours of CPU time on a single processor of an SGI Origin 200 computer.

It is assumed that all the ions are initially in the Ne-like ground state as a result of irradiation by the laser prepulse with an electron density of 6×10^{20} . Initially all

the free electrons are assumed to have a mono-energetic distribution of 5 KeV as a result of the fast laser deposition from the main pulse. The results are compared to highly resolved F-like to He-like K-shell emission spectra recorded recently during ultra-short laser experiments with argon cluster targets in Japan. The laser had a 30fs duration and an intensity of 1.3×10^{19} W/cm³.

Figure 1 shows the calculated EEDF for various times between 0 and 3 picoseconds. Note that the 0 ps EEDF is spiked at 5 KeV and corresponds to the initial conditions discussed above. At first, the EEDF broadens very quickly around 5 KeV and starts building up a small low-energy component. As time increases the low-energy component gets larger and the beam-like component around 5 KeV gets smaller. By 3 ps the tail is gone and the EEDF is completely Maxwellian with a temperature near 1500 eV. The calculated timescale for emission is consistent with estimates of cluster decay times for these conditions.

Figure 2 shows a comparison of the calculated time integrated spectra to 3 ps compared to the experimental measurement. The agreement with experiment for the He-like to Be-like emission is quite good. Note that the experimental spectral line occurring near 4 angstroms is spurious and corresponds to He radiation from a different order of crystal reflection. Also note that for Li-like to B-like that the fine details of the calculated spectra within an ion stage, including relative line positions and intensities are in remarkable agreement with experiment. However, the calculated relative intensities of the lower charged ions, C-like to F-like are somewhat low. The calculations also show the typical Li-like and Be-like satellite structure, sometimes attributed to a hot electron component in the EEDF, can also be due to transient effects in a high-temperature ionizing plasma.

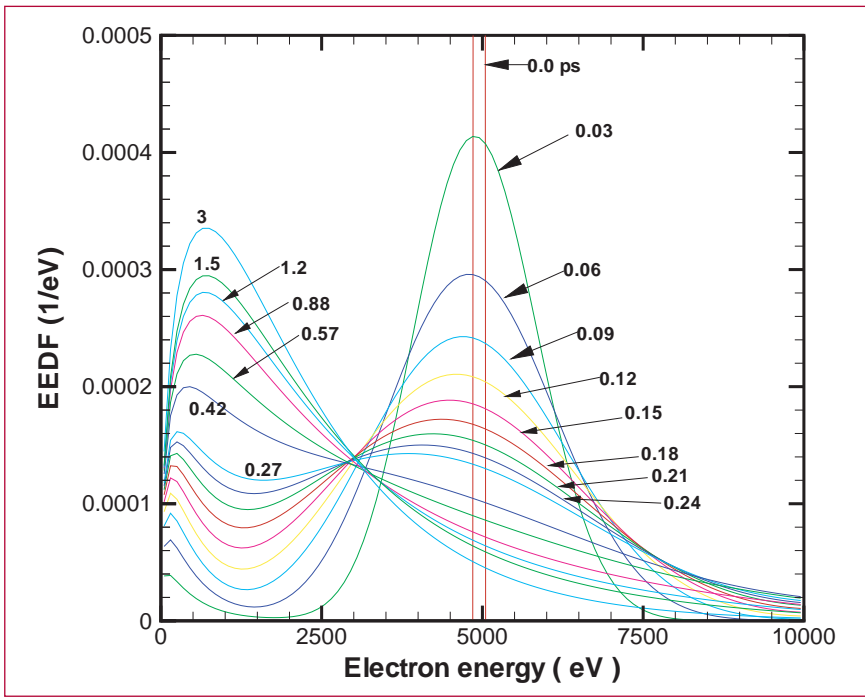


Figure 1—
The calculated
EEDF at various
times between
0 and 3 ps.

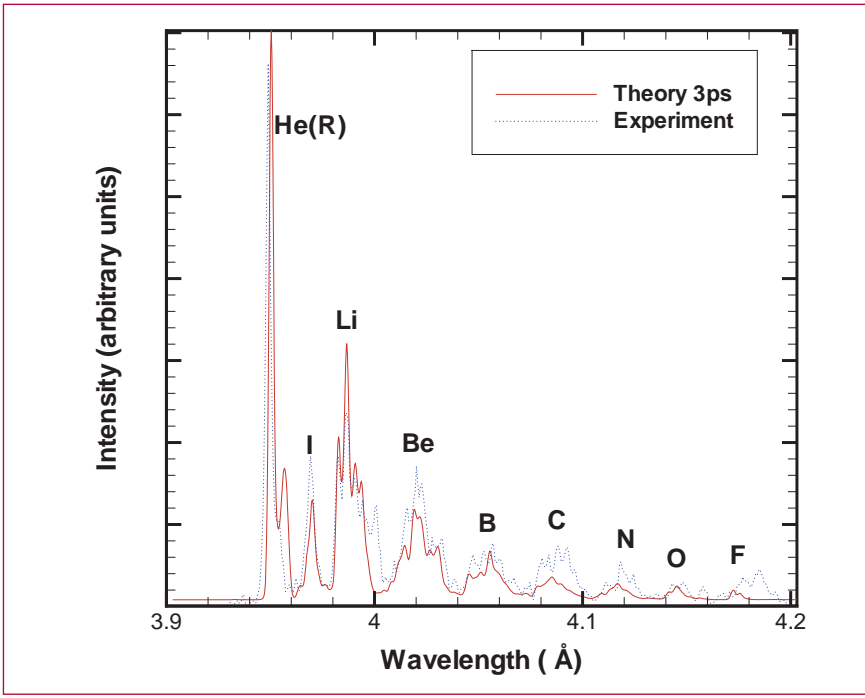
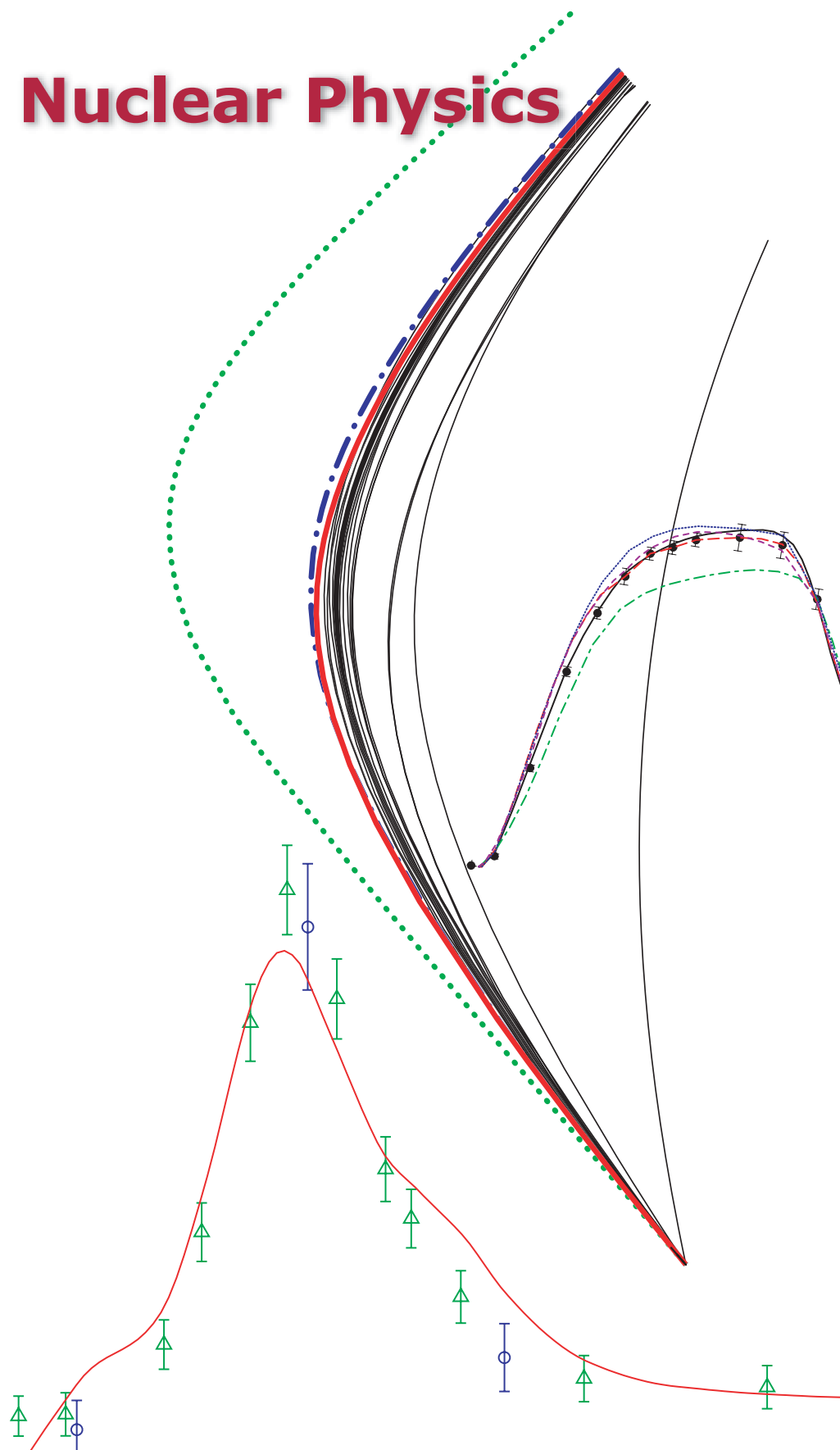


Figure 2—
Comparison of
spectra calculated
at 3 ps and
experiment.

Nuclear Physics



Data for Charged-Particle Capture Reactions

Gerald M. Hale, T-16; ghale@lanl.gov

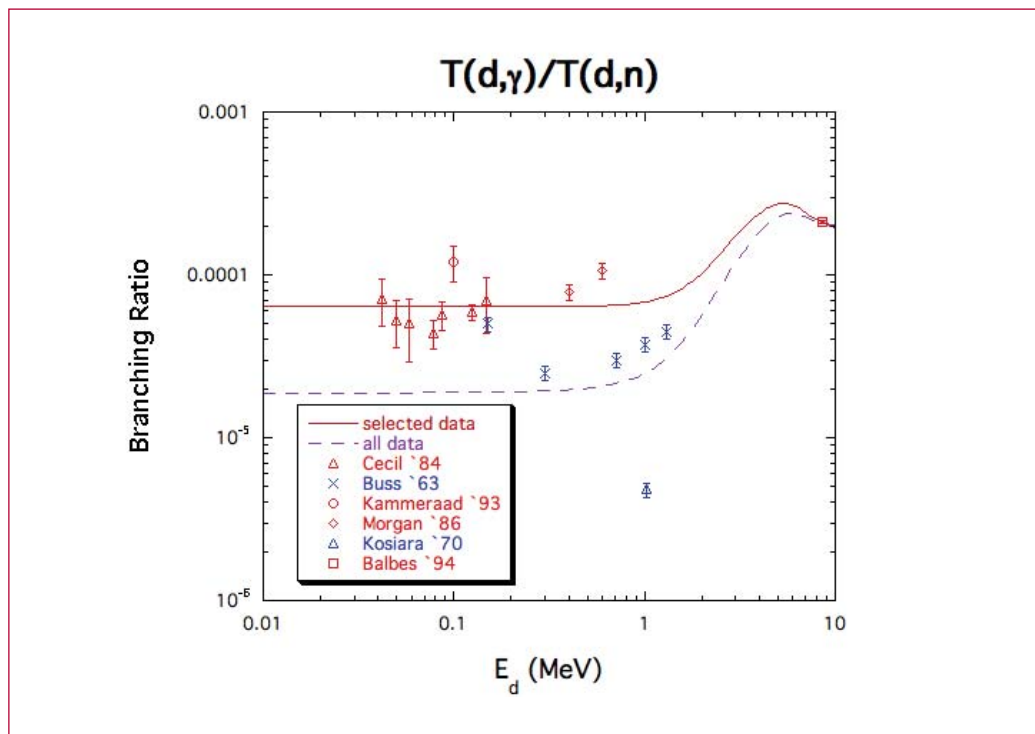
During the last fiscal year we have studied the capture processes associated with the thermonuclear burn (TNB) reactions for light systems in the mass range $A=4-9$. In some cases, these reactions are of interest as diagnostics of TNB in hot plasmas, and in all cases they are desired to give a more complete set of charged-particle reactions for the light nuclei. The study resulted in a new approach [1] to including photon channels in R-matrix theory, which is the primary theory we have used to describe nuclear reactions in the light systems. It also involved a generalization of the thermally-averaged quantities normally given for TNB to the limiting case of zero-mass particles (photons).

An example of the types of data analyzed is given in the figure, showing the calculated branching ratio for the $d+t$ reactions compared to some of the data. Note that disagreements among the measurements are larger than a factor of three in some cases. The red curve shows the result finally used for this reaction. New measurements are planned later this year at the Omega facility at the University of Rochester to test this choice in a laser-imploded (ICF) $d-t$ capsule.

[1] G. M. Hale and A. S. Johnson, "Results for $n+p$ capture from an R-matrix analysis of N-N scattering," 17th Intl. IUPAP Conf. on Few Body Problems in Physics, Durham NC (June 2003).

2

Figure—
Branching ratio for the $d+t$ reactions. The red curve, resulting from considering only the most recent measurements (red points), was used to produce the evaluated capture cross section.



Iridium Nuclear Cross Sections for Radchem

Patrick Talou, Mark B. Chadwick, and Robert E. MacFarlane, T-16; Ronald O. Nelson and Nikolaos Fotiadis, LANSCE-3; Holly R. Trelue, D-5; Morgan C. White and Stephanie C. Frankle, X-5; talou@lanl.gov

Iridium plays a unique role in radiochemical diagnostics of nuclear weapons performance. Many detectors were developed to study high-energy (~14 MeV) fusion reactions using threshold (n,2n) reactions, and to study low-energy processes via the (n, γ) capture process. However, iridium is uniquely used to study fast neutrons in the few-MeV region, particularly prompt fission neutrons.

The $^{193}\text{Ir}(n,n')$ reaction to the isomer is used for these diagnostics. Measuring the production of the isomer is also a uniquely difficult problem, and was solved by some of the great figures from LANL's radchem past, such as Jim Gilmore, Don Barr, and Moses Attrep. The experimental problem was so difficult that other labs, such as Livermore and AWE, relied upon Los Alamos radiochemistry for this task!

However, to interpret the Nevada Test Site (NTS) post-detonation data, one needs an accurate cross section for the isomer production. Some earlier measurements were made above 7.5 MeV at Los Alamos, by Bayhurst *et al.*, but no data existed below this energy, and the historic cross section data set was based purely on nuclear theory predictions from T-Division.

Our new results represent a LANSCE – T-Division collaboration, where the

GEANIE gamma-ray detector was used to measure important contributions to the cross section, and the GNASH code was used to predict important (but unmeasured) additional contributions. The GEANIE/GNASH results cover the whole energy range of interest, from threshold at 80 keV to above 20 MeV. Figure 1 validates our GNASH theory code through comparisons with the gamma-ray measurements. Figure 2 shows our new evaluated cross section for the isomer production, that is needed in the X-Division applications.

In the few-MeV region we have additional measurements from a critical assembly experiment at LANL's LACEF facility at TA-18, and these comparisons provide an important validation of the energy-dependence of our cross section. Our new results are being provided to X-Division in different nuclear data table formats by X-5.



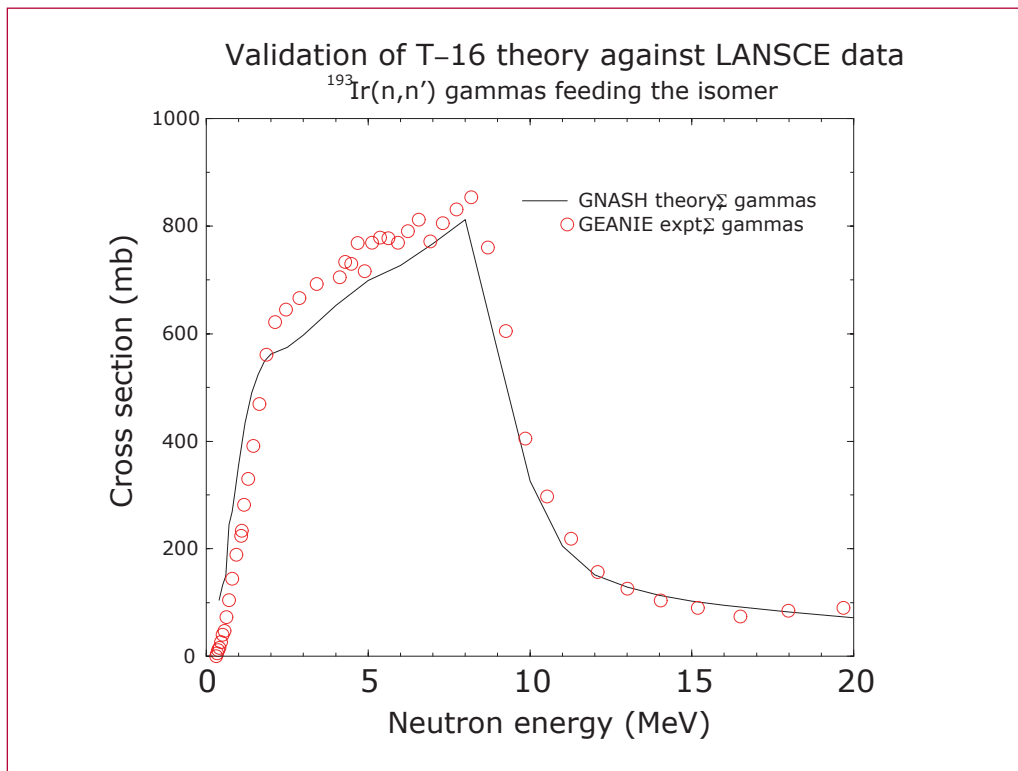


Figure 1— Validation of our theoretical (GNASH) calculations against LANSCE data for the sum of the four strongest gamma-lines feeding the isomer.

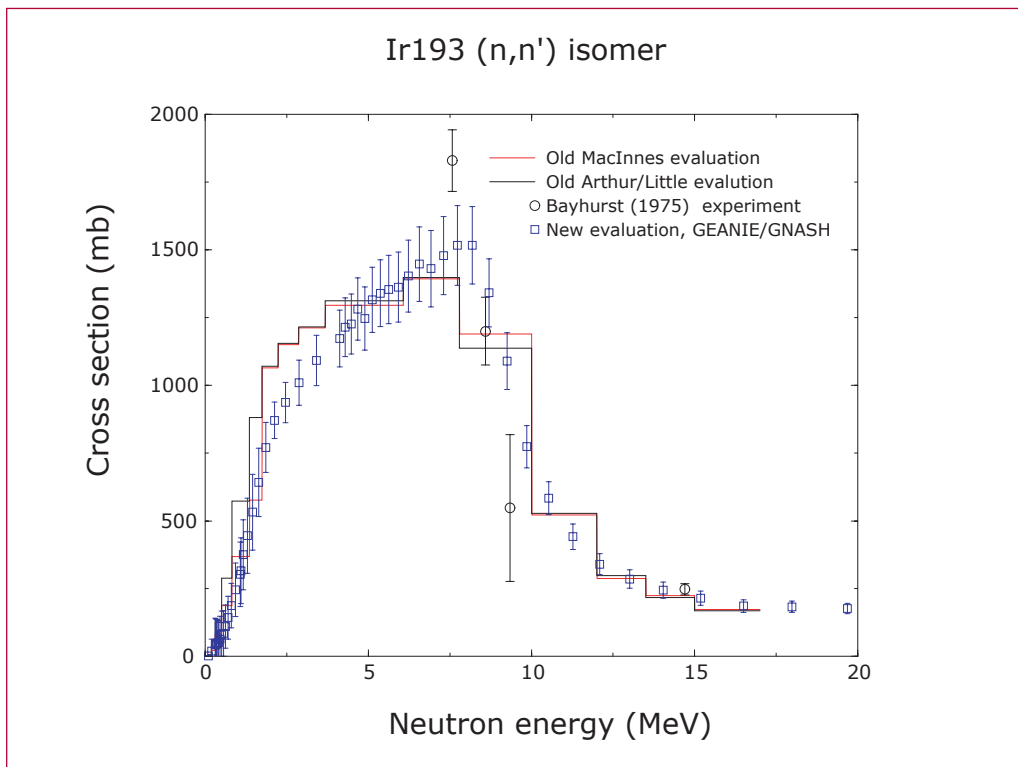


Figure 2— New evaluated cross section for the Ir-193 (n,n') Ir-193m isomer production vs. older existing evaluations and activation measurement data.

New Suite of Evaluated Nuclear Reaction Cross Sections on Uranium Isotopes

Phillip G. Young Jr., Patrick Talou, Robert E. MacFarlane, Mark B. Chadwick, Toshihiko Kawano, David G. Madland, Peter Möller, and William B. Wilson, T-16; pgy@lanl.gov

Group T-16 has completed a new suite of evaluated neutron reaction cross section files for uranium isotopes ranging from $A = 232$ to 241. The new cross section evaluations are important for weapons simulations of yield and inventory diagnostics. The nuclear data have been processed by X-5 into a number of different formats (including NDI), for use in a variety of ASCII and legacy X-Division burn codes. We have received useful and positive feedback on their performance, and further feedback from X-Division users will lead to future improvements to these cross section sets.

These files were released in the standard ENDF format and provide a complete representation of all important reaction cross sections, such as capture, fission, inelastic, $(n,2n)$, $(n,3n)$, etc., as well as energy spectra of the emitted neutrons (prompt and delayed). These studies encompass the neutron incident energy range from sub-keV to 30 MeV, and the files were combined with existing ENDF/B-VI data files at lower energies to form a complete evaluation from 10^{-5} eV up to 30 MeV. These evaluations represent a major improvement over the previous available US database for these elements.

Because some of these isotopes are unstable, very few measurements exist, in particular for capture and fission

reactions, to guide the evaluations, and the role of nuclear modeling therefore plays a very important role. The theoretical analyses involved complex coupled-channels optical model calculations with the ECIS code and statistical Hauser-Feshbach plus preequilibrium computations with the GNASH code. Both codes have been developed and tested over the years and constitute the backbone of most modern T-16 evaluation studies.

A very important ingredient entering in such calculations is a reliable optical model potential, which is used not only to get accurate neutron total, elastic and inelastic cross sections (and angular distributions), but also to provide reliable particle transmission coefficients for the GNASH calculations. Therefore, a large part of the analysis consisted in obtaining such a reliable optical model potential, and involved assessing various existing potentials.

The relative strength of the fission channel is notoriously very difficult to obtain accurately with theoretical input only. In our reaction calculations, the fission channel importance depends on so-called fission barrier parameters that are quite difficult to estimate accurately, and even small variations of their values can often lead to quite different fission cross sections. In this study, an effort was made to obtain/refine these parameters from a combined analysis of all uranium target isotopes studied in the present work. Some parameters were finally optimized to better fit experimental data available for some isotopes.

As an integral part of this evaluation process, the new released files have been tested in Monte-Carlo MCNP simulations of critical assemblies at the LACEF experimental facility. The new files performed very well in these new

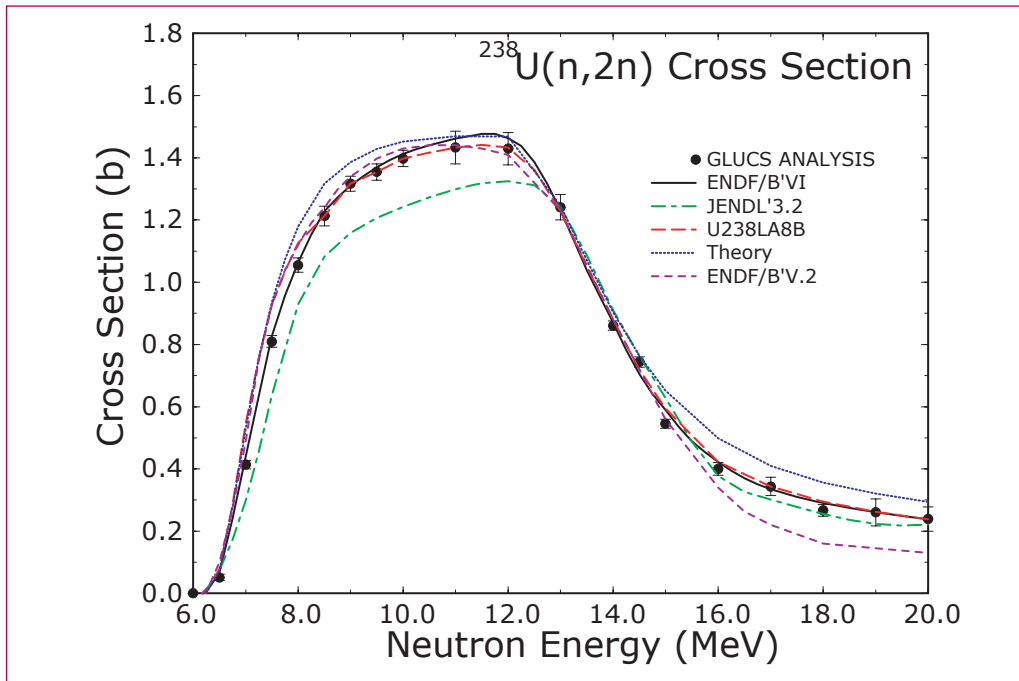


Figure 1—
The $^{238}\text{U}(n,2n)$ cross section from threshold to 20 MeV. The solid circles (GLUCS ANALYSIS) are a composite of the available experimental data obtained in a covariance analysis. The smooth curves compare our current analysis (U238LA8B) with existing ENDF/B-VI, JENDL-3.2, and ENDF/B-V.2 data evaluations and with a theoretical calculation using the GNASH nuclear theory code.

Critical Assembly Data Testing of LANL ENDF6++

	Old ENDF/B-VI	New ENDF6++
Godiva (^{235}U)	0.9961	0.9993
Flattop- ^{235}U	1.0018 (bias)	1.0024
Jezebel (^{239}Pu)	0.9978	1.0004
Flattop- Pu	1.0033 (bias)	1.0019
Jezebel-23 (^{233}U)	0.9925 (v. bad!)	0.9987
Flattop- ^{233}U	1.0024 (bias)	0.9999
BigTen (lots of 238)	1.0127 (v. bad!)	0.9985

k-eff C/E shown

Notes:

ENDF6++ more reactive with better k-eff

^{233}U greatly improved

^{238}U reflection problem largely improved (flattop versus unreflected k-eff)

BigTen now much better (due to 238 inelas)

BUT: Godiva spectral index $^{238}\text{f}/^{235}\text{f}$ C/E=0.961 (calc = too soft)

calculations, with some major improvements, compared to previous evaluations. Note that in order to be used in such MCNP simulations, the files were first successfully processed through the NJOY nuclear data processing code.

Studies of Fission-Product Yields with Improved Data Bases for β -Decay Half-Lives and β -Delayed Neutron-Emission Probabilities (II)

Peter Möller and William B. Wilson, T-16;
moller@lanl.gov

Delayed neutrons (DN) are important for the nuclear weapons ASCI program. Specifically we perform actinide integral data testing against unclassified critical assembly measurements and one must account for DN in the simulations of these experiments. DN also play a role in nonproliferation projects at the Laboratory, including detecting clandestine HEV using active interrogation.

We have previously discussed how we have extended our original, microscopic QRPA-FY model to account also for first-forbidden decays in a statistical model. This and other models of ours are able to provide not only calculated values for β -decay half-lives $T_{1/2}$ and β -delayed neutron-emission probabilities P_n for decays from the nuclear ground state, but also provide these for decays from spin-isomeric states. In addition, they provide single-particle levels and complete β -strength functions for nuclei throughout the nuclear chart.

We have now applied the model to the calculation of $T_{1/2}$ and P_n for nuclei throughout the periodic system. This calculated data set [1] has been incorporated into the CINDER data libraries and it also serves as a data base in various astrophysical nucleosynthesis calculations. In our CINDER data libraries we use experimental data for $T_{1/2}$ and P_n where available. In last year's report [2] we used, for experimental data, an evalu-

ated experimental data (MED) set provided by the Mainz group and based the calculations of temporal delayed-neutron production in ^{235}U , ^{238}U , and ^{239}Pu fission systems on the CINDER'90 library corresponding to this set supplemented by calculated values. The calculations with this data set appeared in the previous report to NW.

The MED set was not maintained by Mainz in a simple computer-readable form. Furthermore, we have now become aware that it lacks version control, is not referenced in a way that is subject to analysis, and review by the full collaboration. Since the work presented in the previous report [2] was completed we also discovered two misprints in the computer-readable file as implemented at LANL (due to inadequate procedures in maintaining, updating, and transmitting this data file). We therefore now use the (1997) NuBase data file [3] as our reference source of experimental data to supplement calculated data in the CINDER data libraries. However, the MED data is still useful for informative parameters studies. Specifically we have

1. previously calculated temporal DN production with the originally implemented MED set (which is now known to contain two misprints) supplemented by our model calculations. (MED-1);
2. corrected the two known misprints to obtain set MED-2, created new CINDER'90 libraries based on these experimental values and when such are not available used calculated values, and calculated the corresponding temporal DN production; and
3. created new CINDER'90 libraries based on NuBase experimental values and when such are not available used calculated values, and have calculated the corresponding temporal DN production.

Six-group parameters for this case are presented in Table 1.

A brief summary of our results are as follows. We calculated temporal DN production rates for ^{235}U thermal fission with our three libraries as shown in Figures 1–3. The temporal DN production rates with set MED-1 in general agree much better with the recommended experimental data than do calculations based on the England evaluation as we learned last year. However, calculations with set MED-2 actually agree less well with the recommended data set than calculations based on the England 94 evaluation. This is the situation for most of the eight reactions studied. Calculations with NuBase agrees better with data in 6 cases, about equally well with data in one case and less well in one case than calculations based on the MED-2 set. The NuBase calculation agrees better with data than do calculations based on the England evaluation in seven out of eight studied reactions and about equally well in the remaining reaction.

While we are extremely pleased with the current convergence of the calculated and recommended experimental DN temporal production data, we make the following further observations. It is somewhat disconcerting that different data values for just two (high-yield) fission isotopes affect the calculations enormously. This indeed shows that the evaluated experimental data set needs to be maintained in a form that is easily subject to analysis and review. Moreover, it is clear that accurate (preferably experimental) data for high-yield isotopes are necessary. We are currently establishing collaborations to set up such a data base for $T_{1/2}$ and P_n . It is also highly desirable to understand details of the fission

yield with high accuracy.

More details about our work can be found in the publications listed below, and other publications available at <http://t16web.lanl.gov/Moller/abstracts.html>.

[1] URL:

<http://t16web.lanl.gov/Moller/publications/tpnff.dat>

[2] β -Delayed Neutron Emission, Peter Möller, William B. Wilson, Bernd Pfeiffer, and Karl-Ludwig Kratz, Los Alamos Report LA-UR-03-2682 (2003)

[3] D. Beck, F. Ames, G. Audi, G. Bollen, H. J. Kluge, A. Kohl, M. König, D. Lunney, I. Martel, R. B. Moore, H. RaimbaultHartmann, E. Schark, S. Schwarz, M. deSaintSimon, and J. Szerypo, *Nucl. Phys. A* **624** (1997).

Publications:

New calculations of gross beta-decay properties for astrophysical applications “Speeding-up the classical r-process,” Peter Möller, Bernd Pfeiffer, and Karl-Ludwig Kratz, *Phys. Rev. C* **67**, 055802 (2003). (Los Alamos Preprint LA-UR-02-2919.)

“Beta-Decay Properties of the Neutron-Rich $^{94-99}\text{Kr}$ and $^{142-147}\text{Xe}$ Isotopes,” U. C. Bergmann, C. A. Diget, K. Riisager, L. Weissman, G. Aubock, J. Cederkall, L. M. Fraile, H. O. U. Fynbo, H. Gausemel, H. Jeppesen, U. Koster, K.-L. Kratz, P. Möller, T. Nilsson, B. Pfeiffer, H. Simon, K. Van de Vel, and J. Aysto, *Nucl. Phys. A* **714**, 21–43 (2003). (Los Alamos Preprint LA-UR-02-6963.)



Table 1. Six-Group Parameters from calculations based on ENDF/B-VI decay data, QRPA+ff/Nubase $T_{1/2}$ and P_n Values, and England 1994 Yields

ID	Deviation, %		Time Group Parameters					
	RMS	Max	Group 1	Group 2	Group 3	Group 4	Group 5	Group 6
227 _{Th(t)}	0.007	0.495	λ_i : 0.1292312	0.2029314	0.2780183	0.1948296	0.1750600	0.0199294
229 _{Th(t)}	0.097	0.409	λ_i : 0.0124721	0.0305061	0.0592290	0.1695127	3956902	1.9291590
			α_i : 0.0849543	0.1674253	0.3015874	0.2151063	0.1935090	0.0374176
232 _{Th(f)}	0.299	0.941	λ_i : 0.0124736	0.0311536	0.0584445	0.1816179	0.4497747	1.7126360
			α_i : 0.0280144	0.0916151	0.1227336	0.4223792	0.2449293	0.0903285
232 _{Th(h)}	0.412	1.457	λ_i : 0.0124886	0.0362370	0.0863971	0.2736182	0.7041045	2.5702160
			α_i : 0.0204106	0.0791193	0.0959675	0.5132086	0.2072341	0.0840598
231 _{Pa(f)}	0.134	0.517	λ_i : 0.0124960	0.0329775	0.0919227	0.3059121	0.9226738	3.8409090
			α_i : 0.0722509	0.2052627	0.1587965	0.2793855	0.2389419	0.0453624
232 _{U(t)}	0.105	0.379	λ_i : 0.0124770	0.0308992	0.0607216	0.1869274	0.4225065	2.1350360
			λ_i : 0.0956297	0.2347905	0.1902077	0.2794189	0.1658479	0.0341052
233 _{U(t)}	0.222	0.790	λ_i : 0.0124758	0.0308768	0.0598942	0.1807552	0.4284089	2.1305240
			λ_i : 0.0607851	0.2071999	0.2335315	0.3251233	0.1402901	0.0330700
233 _{U(f)}	0.122	0.422	λ_i : 0.0124813	0.0310932	0.0666856	0.2377543	0.6411835	3.0853340
			α_i : 0.0740917	0.2026600	0.2115201	0.2789128	0.1929212	0.0398941
233 _{U(h)}	0.228	0.894	λ_i : 0.0124769	0.0309449	0.0614588	0.1883680	0.4415044	2.1105080
			α_i : 0.0601363	0.1639592	0.1291882	0.3831378	0.1955701	0.0680085
234 _{U(f)}	0.160	0.589	λ_i : 0.0124823	0.0329665	0.0722578	0.2287396	0.5594706	2.5679020
			λ_i : 0.0478088	0.1908902	0.2011645	0.2956977	0.2100283	0.0544105
234 _{U(h)}	0.225	0.893	λ_i : 0.0124773	0.0302827	0.0624229	0.1957002	0.4713513	2.2390180
			λ_i : 0.0663001	0.1648863	0.1298366	0.3907585	0.1851014	0.0631171
235 _{U(t)}	0.358	1.1729	λ_i : 0.0124815	0.0327937	0.0727469	0.2367216	0.5810631	2.6868270
			λ_i : 0.0294499	0.1669662	0.1731284	0.3628756	0.1907954	0.0767844
235 _{U(h)}	0.312	1.126	λ_i : 0.0124875	0.0307048	0.0712765	0.2590071	0.8042168	.9640060
			α_i : 0.0294200	0.1506091	0.1546921	0.3845914	0.2040556	0.0766318
235 _{U(h)}	0.297	1.282	λ_i : 0.0124869	0.0311016	0.0699959	0.2387034	0.6289090	2.8402280
			α_i : 0.0314888	0.1311334	0.1204841	0.3879087	0.2426965	0.0862885
236 _{U(f)}	0.292	1.088	λ_i : 0.0124845	0.0318524	0.0670421	0.2256260	0.5490793	2.6090610
			λ_i : 0.0229121	0.1725287	0.1565871	0.3501743	0.2070217	0.0907762
236 _{U(h)}	0.313	1.198	λ_i : 0.0124857	0.0301928	0.0694438	0.2360582	0.6397050	2.6521260
			α_i : 0.0328840	0.1402174	0.1268260	0.4135744	0.1944162	0.0920820
237 _{U(f)}	0.329	1.160	λ_i : 0.0124867	0.0311822	0.0769355	0.2514053	0.6949807	2.8849290
			α_i : 0.0138816	0.1619886	0.1345297	0.3556484	0.2333220	0.1006297
238 _{U(s)}	0.360	1.166	λ_i : 0.0124893	0.0299597	0.0700269	0.2412707	0.6623021	2.7874130
			α_i : 0.0082613	0.1019767	0.0966469	0.3815679	0.2630525	0.1484947
238 _{U(f)}	0.411	1.69	λ_i : 0.0124899	0.0297261	0.0748041	0.2775981	0.8216328	2.8775250
			λ_i : 0.0096578	0.1106294	0.1075423	0.3772216	0.2680777	0.1268712
238 _{U(h)}	0.421	1.752	λ_i : 0.0124940	0.0300641	0.0779419	0.2695441	0.7745456	2.9936880
			λ_i : 0.0143813	0.1084504	0.1237007	0.3924145	0.2321731	0.1288800
237 _{Np(t)}	0.225	0.702	λ_i : 0.0124945	0.0306168	0.0804072	0.2690133	0.8168173	3.1747860
			λ_i : 0.0229204	0.1971350	0.1581610	0.3314493	0.2111655	0.0791688
237 _{Np(f)}	0.234	0.716	λ_i : 0.0124819	0.0297684	0.0671848	0.2222502	0.5579912	2.3919430
			α_i : 0.0286363	0.1744048	0.1587643	0.3520085	0.2090626	0.0771235
237 _{Np(h)}	0.278	0.941	λ_i : 0.0124827	0.0302117	0.0688021	0.2284235	0.5609904	2.4250590
			λ_i : 0.0227229	0.1599667	0.1365217	0.3919793	0.1882372	0.1005722
238 _{Np(f)}	0.241	0.754	λ_i : 0.0124846	0.0301003	0.0711867	0.2358184	0.6177693	2.6067060
			λ_i : 0.0165678	0.2110959	0.1509632	0.3392045	0.2055013	0.0766673
238 _{Pu(f)}	0.208	0.629	λ_i : 0.0124842	0.0295572	0.0702193	0.2326980	0.6043050	2.5479330
			α_i : 0.0305363	0.1977924	0.1844649	0.3374062	0.1841872	0.0656131
			λ_i : 0.0124813	0.0299842	0.0663596	0.2248711	0.5638572	2.5300620

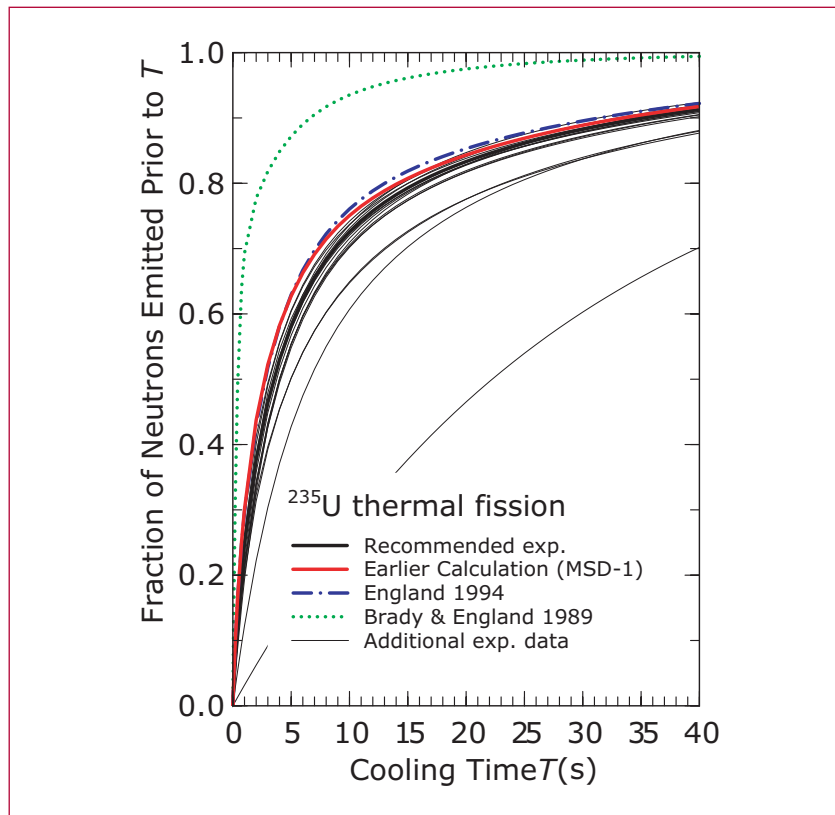
Table 1. Six-Group Parameters (continued)

ID	Deviation, %		Time Group Parameters					
	RMS	Max	Group 1	Group 2	Group 3	Group 4	Group 5	Group 6
239Pu(t)	0.213	0.936	β_i : 0.0217329	0.2415547	0.1899606	0.2966484	0.1869457	0.0631577
239Pu(f)	0.192	0.618	λ_i : 0.0124795	0.0293796	0.0681307	0.2183230	0.5420050	2.3638680
			α_i : 0.0285311	0.2330284	0.1973689	0.2930540	0.1874713	0.0605464
239Pu(h)	0.261	0.995	λ_i : 0.0124792	0.0295816	0.0669461	0.2134332	0.5408889	2.4237590
			α_i : 0.0402107	0.1473574	0.1205726	0.3986323	0.2138447	0.0793821
240Pu(t)	0.220	0.705	β_i : 0.0124840	0.0318021	0.0681643	0.2426150	0.5901634	2.6784400
			λ_i : 0.0124823	0.0294350	0.0661293	0.2346443	0.6125605	2.5262910
240Pu(f)	0.220	0.699	β_i : 0.0182924	0.2252949	0.1794028	0.3183644	0.1885810	0.0700646
			λ_i : 0.0124815	0.0294410	0.0673958	0.2325402	0.6073893	2.5377160
240Pu(h)	0.283	1.006	α_i : 0.0325824	0.1618339	0.1330570	0.4007291	0.1874554	0.0843423
			β_i : 0.0124856	0.0307335	0.0731230	0.2516266	0.6769348	2.8217540
241Pu(t)	0.244	0.773	β_i : 0.0110756	0.2220934	0.1706997	0.3180191	0.2045600	0.0735522
			λ_i : 0.0124846	0.0293128	0.0696969	0.2422690	0.6504749	2.6362410
241Pu(f)	0.256	0.811	β_i : 0.0122611	0.2158654	0.1617615	0.3262505	0.2019090	0.0819525
			λ_i : 0.0124848	0.0293968	0.0687101	0.2442562	0.6608573	2.6961980
242Pu(t)	0.308	1.139	β_i : 0.0080173	0.1960520	0.1417363	0.3318240	0.2239679	0.0984024
			λ_i : 0.0124896	0.0293737	0.0708827	0.2604699	0.7315337	2.9057640
242Pu(f)	0.329	1.205	β_i : 0.0082794	0.1656678	0.1456696	0.3414628	0.2324072	0.1065132
			λ_i : 0.0124899	0.0295048	0.0705367	0.2524065	0.7116908	2.8840550
242Pu(h)	0.372	1.703	β_i : 0.0142506	0.1487859	0.1205797	0.3913176	0.2191992	0.1058669
			λ_i : 0.0124904	0.0299230	0.0758626	0.2726615	0.8062181	3.1671080
241Am(t)	0.173	0.521	β_i : 0.0209879	0.2717965	0.1779746	0.2927965	0.1819254	0.0545191
			λ_i : 0.0124788	0.0292804	0.0672634	0.2194356	0.5332601	2.3315540
241Am(f)	0.153	0.434	α_i : 0.0308293	0.2709634	0.1820085	0.2859520	0.1858457	0.0444010
			λ_i : 0.0124783	0.0295082	0.0637197	0.2119157	0.4999201	2.2709850
241Am(h)	0.308	1.585	β_i : 0.0459486	0.1652282	0.1361906	0.3927880	0.1936059	0.0662387
			λ_i : 0.0124828	0.0311350	0.0719498	0.2471015	0.6658579	2.9423570
42mAm(t)	0.206	0.641	β_i : 0.0154385	0.2477729	0.1848211	0.3000742	0.1878696	0.0640237
			λ_i : 0.0124807	0.0292828	0.0663412	0.2258590	0.5795395	2.5236020
243Am(f)	0.227	0.735	α_i : 0.0148753	0.2451818	0.1584116	0.3228041	0.1849101	0.0738171
			λ_i : 0.0124823	0.0293133	0.0685707	0.2396783	0.6288450	2.6485310
242Cm(f)	0.141	0.661	β_i : 0.0480311	0.2620311	0.1695534	0.2160604	0.2561794	0.0481447
			λ_i : 0.0124706	0.0292359	0.0571184	0.1708430	0.4060983	2.0786340
243Cm(t)	0.211	0.675	β_i : 0.0249717	0.2314828	0.1738279	0.3280910	0.1665876	0.0750390
			λ_i : 0.0124797	0.0294581	0.0674095	0.2387100	0.6219259	2.6306790
243Cm(f)	0.154	0.453	β_i : 0.0349498	0.2660568	0.1968198	0.2910075	0.1660918	0.0450744
			λ_i : 0.0124781	0.0295382	0.0648071	0.2162229	0.5209544	2.3284720
244Cm(s)	0.292	0.995	β_i : 0.0099146	0.2917907	0.1787230	0.2391658	0.2398549	0.0405510
			λ_i : 0.0124400	0.0278106	0.0370428	0.0892880	0.3624131	1.7969980
244Cm(f)	0.188	0.589	β_i : 0.0209952	0.2571260	0.1908906	0.3034057	0.1713831	0.0561993
			λ_i : 0.0124794	0.0293398	0.0657399	0.2249760	0.5697132	2.4797750
245Cm(t)	0.287	0.888	β_i : 0.0133488	0.1400542	0.2013914	0.3215352	0.2278752	0.0957951
			λ_i : 0.0124852	0.0298007	0.0668038	0.2308106	0.6107698	2.6413870
246Cm(s)	0.190	0.603	β_i : 0.0073855	0.2910391	0.2261334	0.2462419	0.1755180	0.0536822
			λ_i : 0.0124811	0.0290371	0.0652393	0.2290437	0.6086516	2.5329970
246Cm(f)	0.259	0.849	α_i : 0.0084615	0.2230593	0.1735838	0.3128246	0.1982777	0.0837931
			β_i : 0.0124847	0.0292036	0.0690923	0.2427007	0.6794564	2.7626040
248Cm(s)	0.270	0.852	α_i : 0.0027444	0.2132760	0.1829415	0.2752089	0.2490385	0.0767906
			λ_i : 0.0124881	0.0290066	0.0695410	0.2449837	0.6728598	2.6503340
248Cm(f)	0.348	1.367	β_i : 0.0031304	0.1742198	0.1463449	0.3107029	0.2512126	0.1143894
			λ_i : 0.0124924	0.0291272	0.0724360	0.2651818	0.7971841	3.0517260

Table 1. Six-Group Parameters (continued)

ID	Deviation, %		Time Group Parameters					
	RMS	Max	Group 1	Group 2	Group 3	Group 4	Group 5	Group 6
249 _{Cf(t)}	0.194	0.760	α_i : 0.0195442	0.2675632	0.2247435	0.2556427	0.1531110	0.0793954
			λ_i : 0.0124778	0.0292032	0.0638095	0.2518917	0.7134392	3.0095010
250 _{Cf(s)}	0.179	10.728	α_i : 0.0096491	0.2850415	0.2477649	0.2043638	0.1984101	0.0547704
			λ_i : 0.0124761	0.0289779	0.0634851	0.1967180	0.5347291	2.3037350
251 _{Cf(t)}	0.243	0.755	β_i : 0.0017475	0.2795886	0.2091647	0.2394708	0.2068880	0.0631405
			λ_i : 0.0124887	0.0289220	0.0672436	0.2383558	0.6595719	2.7150740
252 _{Cf(s)}	0.309	1.295	α_i : 0.0056775	0.1718836	0.2289944	0.2829420	0.2236189	0.0868836
			λ_i : 0.0124880	0.0292668	0.0650696	0.2535023	0.7560873	2.9814750
253 _{Es(s)}	0.204	0.656	β_i : 0.0089857	0.2603740	0.2392249	0.2642611	0.1702706	0.0568837
			λ_i : 0.0124807	0.0290798	0.0648475	0.2426269	0.6519779	2.7383450
254 _{Es(t)}	0.309	1.166	β_i : 0.0003626	0.2737461	0.1891974	0.2507694	0.2194293	0.0664952
			λ_i : 0.0125038	0.0288691	0.0672482	0.2460063	0.6827338	2.9527120
254 _{Fm(s)}	0.136	0.413	α_i : 0.0039906	0.3666340	0.3033126	0.1683042	0.1309564	0.0268022
			β_i : 0.0124775	0.0288544	0.0632960	0.2116710	0.5787126	2.5167200
255 _{Fm(t)}	0.125	0.358	α_i : 0.0010248	0.4272064	0.1731960	0.1737465	0.1998139	0.0250124
			β_i : 0.0124817	0.0288162	0.0631937	0.1530683	0.4550737	1.7977630
256 _{Fm(s)}	0.172	0.529	β_i : 0.0028143	0.3382557	0.2516742	0.1958809	0.1718497	0.0395250
			β_i : 0.0124813	0.0288761	0.0651532	0.2188997	0.5957580	2.4102350

Figure 1— Comparisons of measured temporal DN production following ²³⁵U thermal fission and calculations based on CINDER'90 with $T_{1/2}$ and P_n from set MED-1 when available, otherwise from our theoretical model.



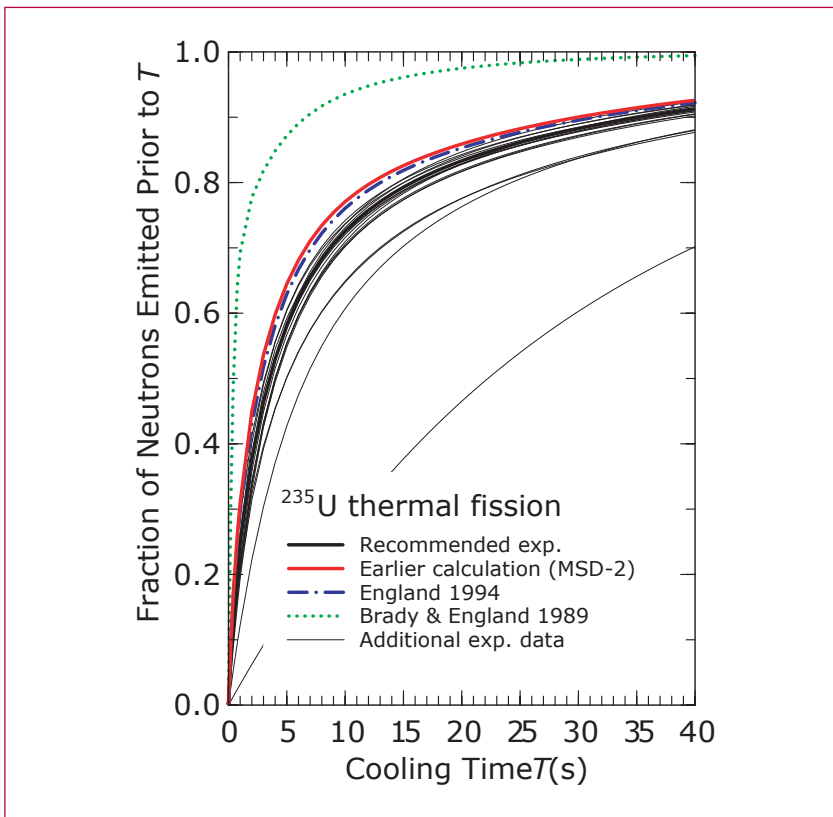


Figure 2— Comparisons of measured temporal DN production following ^{235}U thermal fission and calculations based on CINDER'90 with $T_{1/2}$ and P_n from set MED-2 when available, otherwise from our theoretical model.

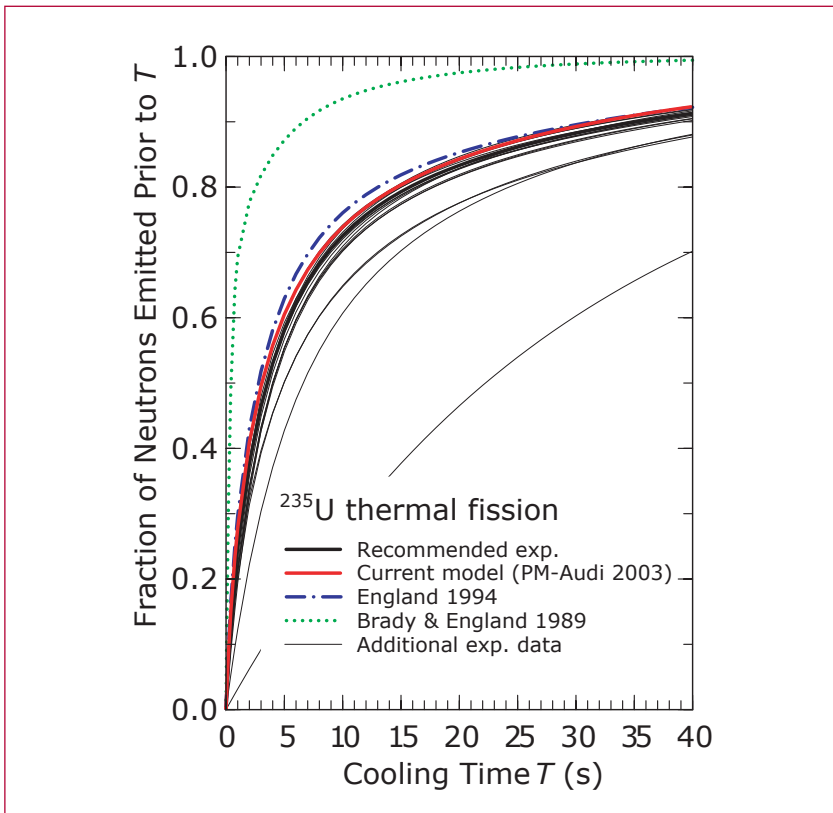


Figure 3— Comparisons of measured temporal DN production following ^{235}U thermal fission and calculations based on CINDER'90 with $T_{1/2}$ and P_n from set NuBase when available, otherwise from our theoretical model. The current model exhibits a striking improvement relative to the calculations based on the (at the time) existing $T_{1/2}$ and P_n values and the England 94 yields.

The ^8Be Nuclear Data Evaluation

Philip R. Page and Gerald M. Hale, T-16,
prp@lanl.gov

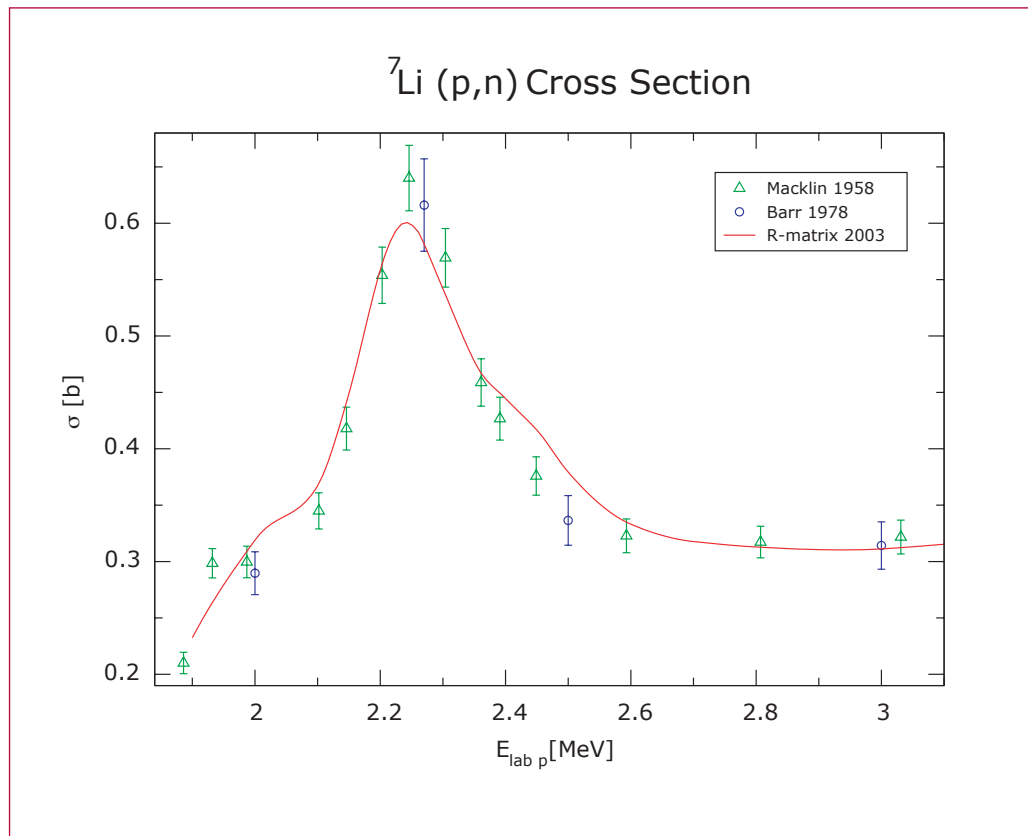
AR-matrix analysis of experimental nuclear data on the reactions $^4\text{He}(\alpha,\alpha)$, $^4\text{He}(\alpha,p)$, $^7\text{Li}(p,\alpha)$, $^7\text{Li}(p,p)$, $^7\text{Li}(p,n)$, $^7\text{Be}(n,p)$, $^6\text{Li}(d,\alpha)$, $^6\text{Li}(d,p)$ and $^6\text{Li}(d,n)$ leading to the ^8Be intermediate state is being performed. The excitation energy above the ^8Be ground state has been brought up to 22–24 MeV for all reactions except $^4\text{He}(\alpha,\alpha)$ and $^7\text{Be}(n,p)$. The data for the reactions $^4\text{He}(\alpha,\alpha)$ and $^4\text{He}(\alpha,p)$ do not fit well, but the other six reactions fit with a reasonable $\chi^2/(\text{point})$. The possibility of two units of orbital angular momentum between ^7Li and p , and between ^7Be and n , was added. Most of the resonances found in

the R-matrix analysis correspond to resonances formerly known from experiment. There are 17 resonances in the 2003 analysis, while there were only 10 resonances in the 2002 analysis. The figure indicates the 2003 R-matrix analysis cross section in barns for the $^7\text{Li}(p,n)$ reaction up to a proton laboratory energy $E_{\text{lab } p}$ of 3 MeV. Two sets of experimental data are also showed.

Details of the 2003 analysis are available in [1].

[1] P. R. Page, “Status of ^8Be Nuclear Data Evaluation,” LANL Memo T-16: NW-125/9-03 (2003).

2



Figure—
indicates the 2003
R-matrix analysis
cross section.

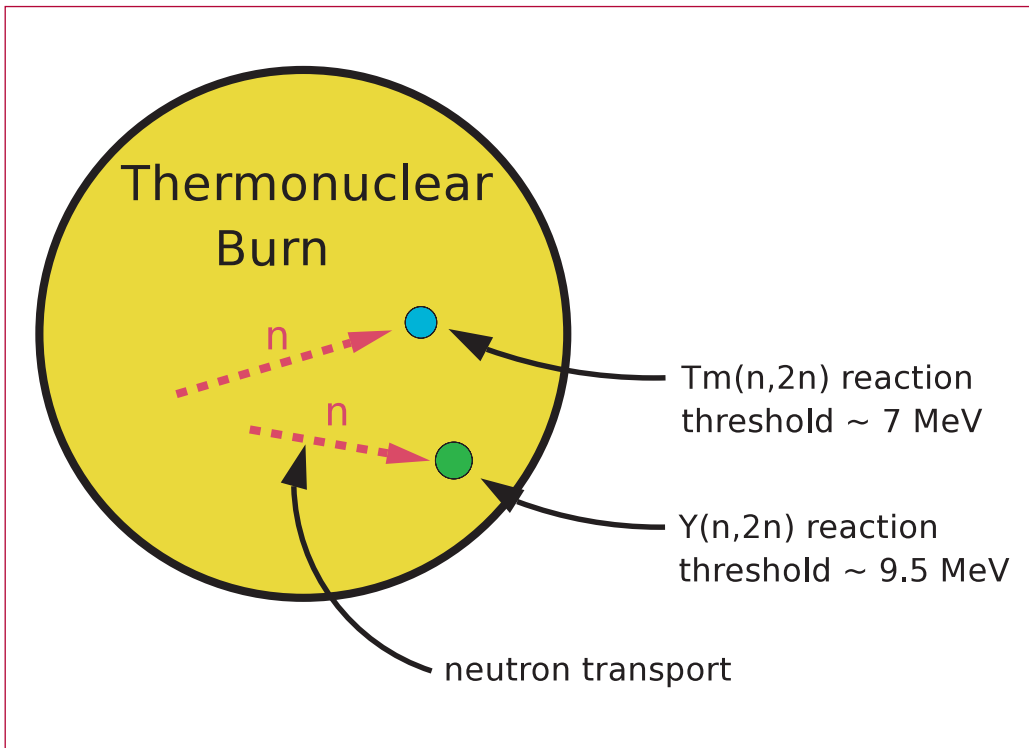
The Physics of Yttrium Equivalence for Radiochemical Detectors

Anna C. Hayes and Gerard Jungman, T-6;
anna_hayes@lanl.gov

Radiochemical detector systems provide the fundamental method for measurement of neutron properties in the thermonuclear environment. These measurements are important in the determination of fission and fusion yields, and therefore provide a basis for interpretation of Nevada Test Site (NTS) data.

The key diagnostic for fusion yields is the ratio $^{87}\text{Y}/^{88}\text{Y}$ in the Yttrium system, which is determined by neutron fluence in the high-energy region, above about 8 MeV. Other radiochemical isotope systems provide additional information. The information from these other systems is typically converted into “Yttrium equivalences.” For a short introduction to Yttrium equivalences, see [1].

The basic point about equivalences is that, since systems utilizing different isotope networks are sensitive to different parts of the neutron spectrum, equivalence measurements yield differential information about the neutron spectrum. By comparing NTS data on equivalences to theoretical calculations, we test our understanding of the physical processes which affect the neutron spectrum. Our collaborators in C-INC provide data on equivalences. With collaborators in X-2, we are able to perform sophisticated calculations using weapons codes. We also perform simplified analytic and semi-analytic calculations which expose the fundamental physics of the processes determining Yttrium equivalences. Some results from this study were presented at an X-2 seminar by Jungman in July 2003. For a general overview of our recent work on radiochemical system, see reference [2].



[1] Anna C. Hayes and Gerard Jungman,
“Yttrium Equivalences in Weapons
Radiochemistry and Fusion Yields,”
in *T-Division Activities in Support of the
Nuclear Weapons Program: 2002/2003*,
LA-UR-03-0001 (2003).

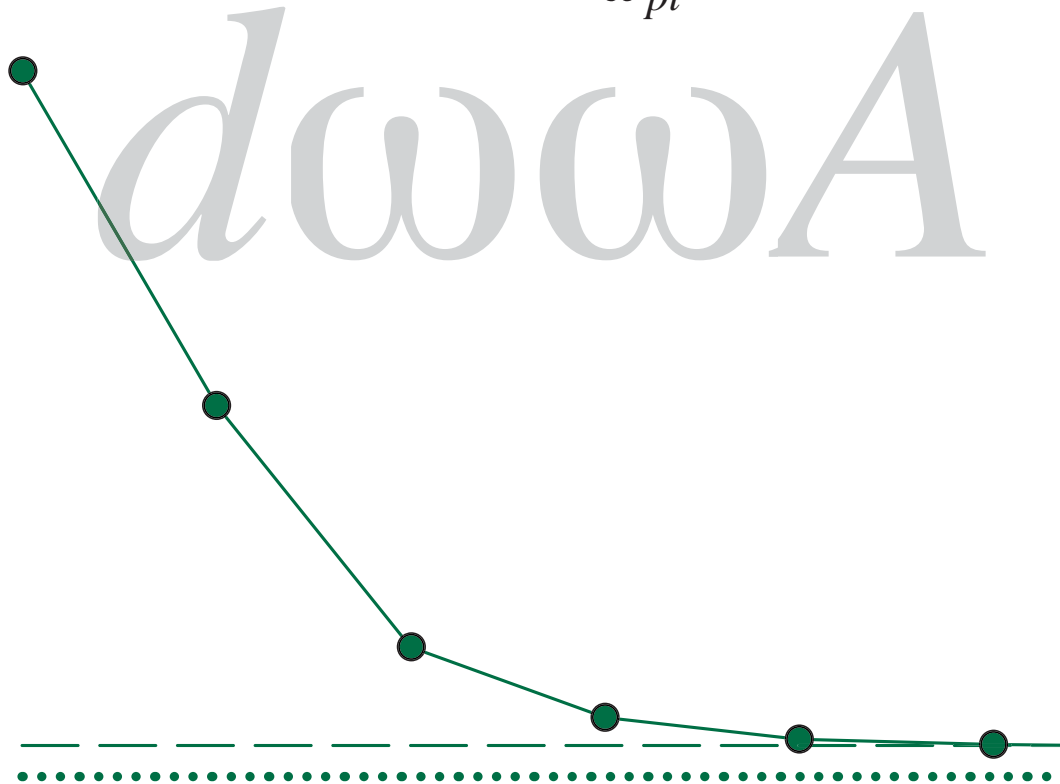
[2] Anna C. Hayes and Gerard Jungman,
“Weapons Sensitivity Studies for Nuclear
Physics (U),” LA-CP requested (2003).



Plasma Physics

$\epsilon_i(q, \omega, T$

$$\epsilon_i(q, \omega, T_i) = \int_{\omega_{pl} + \delta}^{\infty} d\omega \omega A^i(q, \omega)$$



Plasmon Pole Approximation for Warm Dense Matter Calculations: Application to Temperature Relaxation in Nonequilibrium Systems

Michael S. Murillo, T-15 and George Csanak, T-4, murillo@lanl.gov

Warm dense matter is defined as matter that is partially degenerate, moderately to strongly coupled, and has important atomic physics. It is believed that collective modes can play an important role in determining a wide variety of microscopic properties, such as stopping power, opacities, and temperature relaxation. Our goal is to develop reduced models for these processes that capture most of the important physics while being useful within hydrodynamic modeling codes. Our strategy is to evaluate highly accurate expressions for validation of the reduced models. The highly accurate forms, however, include the collective behavior through a linear response function that has very narrow peaks at the resonance frequency.

We have developed several approximate numerical techniques that allow us to perform integrations over the narrow peaks, which yield very accurate results that can validate the simpler models. As an example, consider how a fast particle (e.g., a fission fragment) slows down due to energy transfer to a dense electron gas. Part of the energy loss is due to plasmon excitation that appears as a very narrow peak within an integral. Since the plasmon is well defined at long

wavelengths, the peak is too narrow to directly integrate numerically. This problem is usually solved by resorting to a sum rule that becomes exact in some limit; however, the limit may not apply to all cases. For stopping power calculations a useful limit is that of a very fast particle, which is obviously violated as the particle slows and thermalizes.

We have generalized the sum rule approach for use in calculations for which a sum rule does not exist, or is difficult to calculate. The basic idea is to factorize the integrand $I(x)$ into a product of two functions $I(x)=J(x)D(x)$ where one of the functions $D(x)$ is a so-called delta function distribution. We then break the integral into two regions: one that is easy to integrate numerically and one for which the limit to the delta function $D(x) \rightarrow \delta(x)$ is approximately valid. The use of a delta function $\delta(x)$ for $D(x)$ is the “plasmon pole approximation” and can be integrated analytically. A priori it is not clear that such an approach will work, since there may be a region for which the brute force integration fails *and* the delta function limit is too inaccurate.

We have tested our simple model for the problem of temperature relaxation [1]. Physically we consider two-temperature warm dense matter and calculate the relaxation time to equilibrium; such a quantity is important since warm dense matter is often created through a nonequilibrium process, such as laser radiation or charged particle deposition into the electron subsystem. We employ fully quantal linear response functions for the electrons and a semi-classical version for the ions. Strong coupling is accounted for via local field corrections. Physically the process of interest is energy exchange between the species

through collective modes, as opposed to simple binary collisions. We have computed the relaxation rate using both the plasmon pole approximation just described, brute force integration, and using a sum rule approach [2] as a check. The results are shown in the figure for ion temperature of $T_i=3.75, 10.01, 100.14$ eV and three electron temperatures $T_e=0.35, 10.0, 100.0$ eV, respectively. In the figure we vary the point at which we break the integration between brute force integration and the plasmon pole approximation. Larger values correspond to breaks at longer wavelengths where the collective behavior is strongest (the width is smallest). We see that the method works very well for higher temperatures, but the warm dense matter region is particularly difficult to compute.

to more sophisticated relaxation models for which the sum rule approach cannot be used as a test. Such calculations, which describe the coupling between various modes of the multi-species system, are underway.

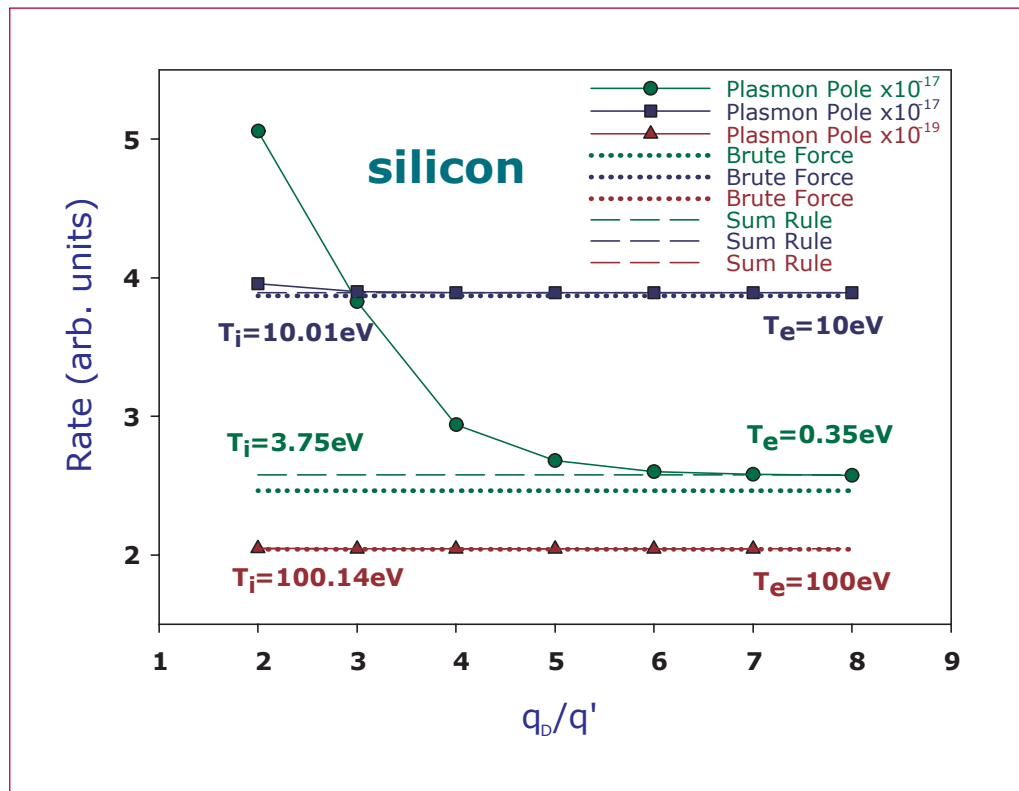
[1] See the related article in this volume for a detailed description of the relaxation model.

[2] H. H. Brouwer, W. D. Kraeft, M. Luft, T. Meyer, P. P. I. M. Schram, B. Strege, *Contrib. Plasma Phys.* **30**, 263 (1990).

Acknowledgement: We thank Dirk Gericke, T-15, for drawing our attention to reference [2].



In the future we will apply these results



Figure—
The energy relaxation rate versus inverse wavevector of the break between the plasmon pole approximation and a brute force integration that employs an adaptive procedure. Results for three temperatures are shown; the results have been scaled by the numbers given in the legend. Calculations have been performed using the plasmon pole approximation (solid), brute force integration (dotted), and with a sum rule approach (dashed). The larger the number q_D/q' , the longer wavelength of the transition. It is clear that all methods yield essentially the same result at high temperatures with much larger discrepancies in the warm dense matter regime.

Exact Treatment of Ion Collective Modes in the Fermi Golden Rule FGR Description of Temperature Relaxation

George Csanak, T-4; Michael S. Murillo, T-15; William S. Daughton, X-1; georgec@lanl.gov

Introduction

The purpose of the present work is to present results from a calculation using the Kogan formula that explicitly incorporates the plasmon poles into the calculation. This calculation uses the method of Brouwer *et al.* [1] for this purpose. The essence of the method of Brouwer *et al.* is that a small region from the integral around the plasmon pole is excluded from the numerical integration, and the contribution from the small region to the integral is obtained by the explicit use of the f-sum rule. The results obtained by this method agree well with the MKF (modified Kogan formula) results.

The Kogan formula and the Modified Kogan Formula

We begin with the formula for the energy relaxation rate in the FGR approximation (the Kogan formula), which describes the relaxation rate in terms of the imaginary parts of the dynamic electron and ion response functions

$$\frac{dE_i}{dt} = \int_0^\infty \frac{d\omega}{2\pi} \omega \int \frac{d^3q}{(2\pi)^3} |U_{ei}(q)|^2 \times A^e(q, \omega, T_e) A^i(q, \omega, T_i) N_{ei}(\omega, T_e, T_i), \quad (1)$$

where $N_{ei}(\omega)$ is the difference of the Bose factors. The electron-ion coupling constant g is then defined by

$$\frac{dE_i}{dt} = (T_e - T_i) g.$$

There are two essential approximations that lead from the FGR or Kogan formula (1) to the MKF. The approximations are: linearization of the Bose function and the low-frequency approximation (linearization) for the electron response function. We can use the exact f-sum rule and obtain the MKF in the form,

$$g = 4 \int \frac{d^3q}{(2\pi)^3} |U_{ei}(q)|^2 \frac{\chi''_{ee}(q, \omega)}{\omega} \Big|_{\omega=0}. \quad (2)$$

The Explicit Incorporation of the Plasmon Pole Contribution into the Numerical Evaluation of the Kogan Formula

In the calculation of the energy relaxation rate according to the Kogan formula, as given by (1), first the ω integral can be calculated:

$$I(q) = \int_0^\infty \frac{d\omega}{2\pi} \omega A^e(q, \omega, T_e) \times A^i(q, \omega, T_i) N_{ei}(\omega, T_e, T_i). \quad (3)$$

As discussed earlier, for small q values the $A^i(q, \omega, T_i)$ function displays sharp peaks (plasmon poles) that are not easily incorporated into numerical integration schemes. A special technique is needed to ensure that the contribution from those peaks are taken into account in the calculation of the above integral.

This technique, introduced by Brouwer *et al.* [1], is based on the f-sum rule for the ion spectral function, $A^i(q, \omega, T_i)$. The essence of the technique is that if we denote the location of the plasmon pole by ω_{pb} then the

integration range in calculating $I(q)$, as given by (3), is divided into three segments: $(0, \omega_{pl} - \delta)$, $(\omega_{pl} - \delta, \omega_{pl} + \delta)$, and $(\omega_{pl} + \delta, \infty)$ where δ is a small frequency range compared to ω_{pl} . The crucial step now is to calculate the contribution from the middle range accurately. With the help of the f-sum rule this integral can be written in the following way:

$$\int_{\omega_{pl} - \delta}^{\omega_{pl} + \delta} d\omega \omega A^i(q, \omega, T_e) = \pi \frac{n_i}{m_i} q^2 - \int_0^{\omega_{pl} - \delta} d\omega \omega A^i(q, \omega, T_i) - \int_{\omega_{pl} + \delta}^{\infty} d\omega \omega A^i(q, \omega, T_i). \quad (4)$$

The last thing we need to discuss is the choice of ω_{pl} . A simple formula for the location of such plasmon-like peaks was provided by Kraeft *et al.* [2] in the form,

$$\omega_{pl} = \omega_{ip} + \Delta \quad (5)$$

where ω_{ip} is the ion plasma frequency, and Δ is a correction term.

Numerical Results

We have used the above scheme in the numerical implementation of the Kogan formula. We have explicitly included the plasmon pole contribution to $I(q)$ for $q < q_D$ where q_D is the Debye wave-vector. The numerical results are summarized in the table, where they are compared with FGR (Kogan formula) results and with MKF results. Clearly, the original Kogan calculation results disagree with the MKF results at low temperatures, which can be attributed to the inability of the numerical integration technique to integrate through the very narrow plasmon poles. Since this direct integration technique often misses the very narrow plasmon poles, it underestimates the value of the electron-ion coupling constant. Furthermore our numerical results demonstrate that the approximations that led to the MKF introduce only extremely small errors (or none at all) for the cases considered. Therefore, based on just this one study, it appears promising that the numerically much easier MKF can be applied for the calculation of the electron-ion coupling constant. Other cases need to be investigated.

$g \text{ (W / Km}^3\text{)}$				
$T_e \text{ (eV)}$	$T_i \text{ (eV)}$	Kogan (numerical)	Kogan (plasmon)	MKF
0.10	3.75	2.47×10^{17}	2.57×10^{17}	2.58×10^{17}
0.25	3.75	2.46×10^{17}	2.57×10^{17}	2.58×10^{17}
0.35	3.75	2.45×10^{17}	2.56×10^{17}	2.57×10^{17}
0.50	3.75	2.44×10^{17}	2.55×10^{17}	2.55×10^{17}
0.75	3.75	2.44×10^{17}	2.55×10^{17}	2.55×10^{17}
0.95	3.75	2.43×10^{17}	2.54×10^{17}	2.54×10^{17}
1.65	3.75	2.42×10^{17}	2.53×10^{17}	2.54×10^{17}
3.74	3.75	2.30×10^{17}	2.41×10^{17}	2.42×10^{17}
10.0	10.01	3.87×10^{17}	3.89×10^{17}	3.89×10^{17}
30.0	30.01	3.13×10^{18}	3.13×10^{18}	3.13×10^{18}
100.0	100.14	2.04×10^{19}	2.04×10^{19}	2.04×10^{19}
300.0	300.14	4.39×10^{18}	4.39×10^{18}	4.39×10^{18}
1000.0	1001.4	2.09×10^{18}	2.09×10^{18}	2.09×10^{18}

Table 1—
Kogan and MKF results for the coupling constant of solid density shocked silicon. Here “Kogan (numerical)” refers to our results obtained via double numerical integration. “Kogan (plasmon)” refers to our results that includes the plasmon pole contributions explicitly. MKF refers to our MKF results.

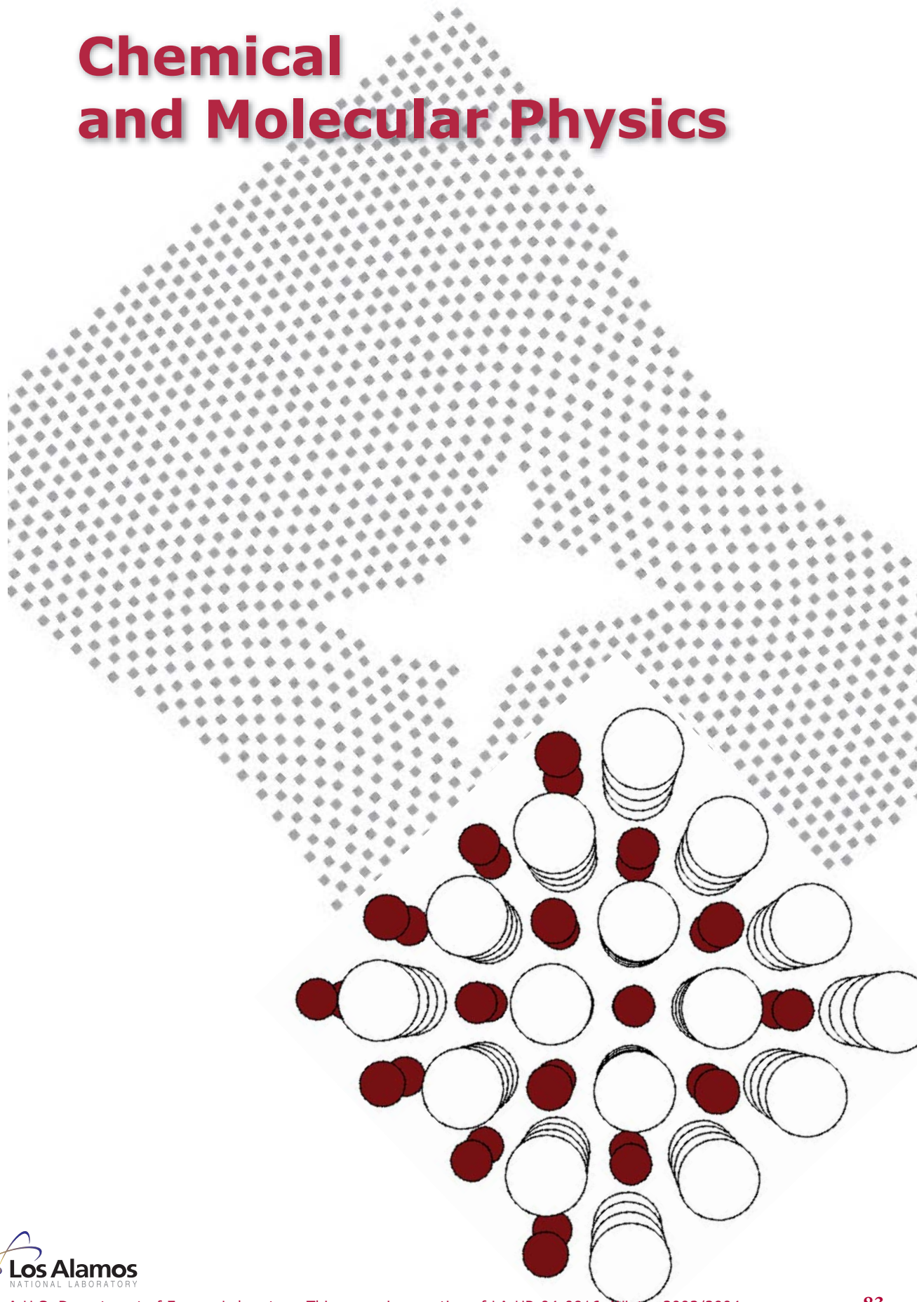
[1] H. H. Brouwer, W. D. Kraeft, M. Luft, T. Meyer, P. P. I. M. Schram, and B. Strege, “Stopping Power of Charged Particles I,” *Contrib. Plasma Phys.* **30**, 263 (1990).

[2] W. Kraeft, D. Kremp, W. Ebeling, and G. Ropke, *Quantum Statistics of Charged Particle Systems* (Plenum Press, New York, 1986) pp. 98–99.

See article in this document by Michael Murillo and George Csanak, “Plasmon Pole Approximation for Warm Dense Matter Calculations: Application to Temperature Relaxation in Nonequilibrium Systems.”



Chemical and Molecular Physics



Theoretical Studies of Surface Chemistry and Bulk Electronic Structure of Actinide Materials

P. Jeffrey Hay, Joel D. Kress, and Hank Ashbaugh; T-12, pjhay@lanl.gov

The surface chemistry of actinide materials plays an important role in corrosion and other processes involving adsorption of molecular species. When exposed to air, the actinide metals form oxide layers PuO_2 and Pu_2O_3 in the case of Pu and UO_2 in the case of U. The reactions of hydrogen with actinide metals represent another important area which involves a complex series of chemical reactions involving oxide and metal surfaces and their interfaces.

We have been exploring two aspects of this chemistry using density functional theory. One part of the current study has focused on H_2O adsorption on PuO_2 surfaces and comparison with previous calculations on UO_2 surfaces. The other part has examined the electronic structure and thermochemistry of bulk PuH_2 . These studies represent a first step towards obtaining a detailed understanding of how species such as O_2 , H_2O and H_2 react with actinide surfaces such as Pu and PuO_2 . Comparisons can be made with surface probes such as thermal desorption studies and bulk measurement of structural, electronic and magnetic properties.

In the case of a surface, periodic models are used to represent a slab of material interacting

with adsorbates. The calculations used the Vienna *ab initio* Simulation Package (VASP) with the following common characteristics: a plane-wave basis for the electronic wavefunction, the generalized gradient approximation (GGA) density functional, relativistic PAW (projector augmented wave) pseudopotentials without spin-orbit coupling.

H₂O adsorption on PuO₂. Bulk PuO_2 has the fluorite structure in which each actinide ion is surrounded by eight oxygen ions, and each oxygen has four nearest neighbor Pu ions. Two of the most widely observed surfaces on oxides with this structure are the (111) and (110) crystal faces that typically have the lowest surface energies. On the (111) surface the bulk oxide has been cleaved leaving the Pu ions with seven O neighbors and missing only an axial O ion lying perpendicular to the face. In the (110) surface the Pu has only six O neighbors. In the calculations we have examined the adsorption of H_2O on each surface both as molecularly adsorbed form, $\text{H}_2\text{O}(\text{ad})$, and in dissociated form in which one proton has been transferred to a neighboring O atom to form two hydroxy groups, $\text{OH}(\text{ad})$. With a five-layer slab model, the positions of the atoms in the top two layers and the adsorbed H_2O molecule are relaxed while the remaining atoms are fixed at their bulk positions.

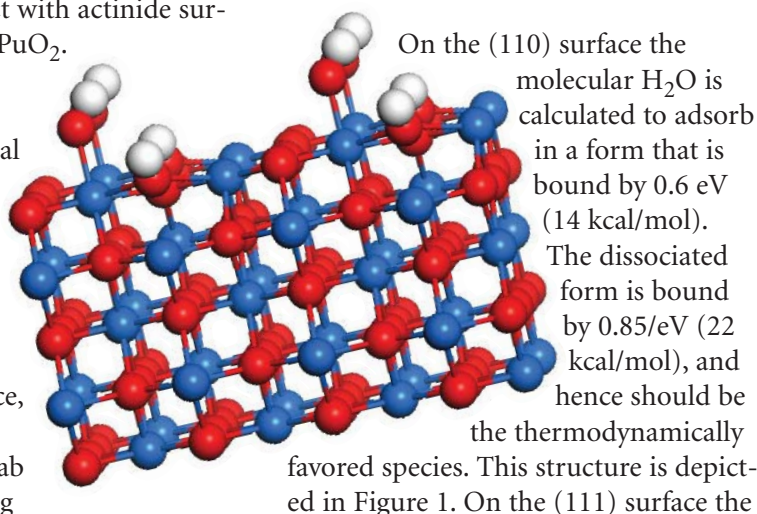


Figure 1—
Calculated structure of dissociated H_2O molecules on PuO_2 (110) surface showing several unit cells of periodic five-layer slab.

molecularly adsorbed H₂O is found to be the more stable species that is bound by ~ 0.75 eV (17 kcal/mol). These results are qualitatively similar to earlier calculations on the UO₂ surface where the (110) surface was also found to be the more reactive one.

Electronic structure of Pu and PuH₂. In bulk Pu metal, the ground state phase (α -Pu) is a monoclinic crystal structure that consists of a 16-atom unit cell with eight distinct atomic sites. At a temperature of about 600 K, bulk Pu metal exists in a fcc phase (δ -Pu) that consists of a one-atom unit cell. In calculations of the electronic structure of Pu, the magnetic behavior (electron spin) must also be considered. Three different spin-orderings were studied with VASP:

(1) nonmagnetic (NM), with spin nonpolarized density functional theory; (2) ferromagnetic (FM), with all spins aligned in one direction, and; (3) antiferromagnetic (AF), with spin directions alternating up and down. The present results for the equilibrium volume, magnetic moment, and relative energy of δ -Pu are presented in the table along with the LCGTO (Linear Combinations of Gaussian Type Orbitals) results [1] of J. Boettger, X-7. Both VASP and LCGTO predict the AF state as the ground state. The predicted volume of the AF state is within 8% and 4% of the experimental volume for VASP and LCGTO, respectively. Although the AF state has a net zero magnetic moment for the bulk, the magnitude of the local magnetic

moment on each atom can be calculated. VASP predicts a larger magnetic moment than LCGTO by about 1 μ_B (bohr magneton).

In bulk PuH₂, the ground state is the CaF₂ crystal structure (as in PuO₂ discussed above), where the Pu atoms form a fcc lattice and the H atoms are located in the tetrahedral interstices (see Figure 2). VASP calculations were performed on the NM, FM, and AF spin-orderings. The FM and AF were found to be nearly energetically degenerate, while experimentally the ground state is AF. The lattice constants for FM and AF were 5.32 and 5.33 Å, respectively, which compare favorably with the experimental value of 5.359 Å. The magnetic moment of the FM state = 5.4 μ_B per PuH₂ unit. Finally, the energy of formation of PuH₂ (solid) from Pu(solid) + H₂ (gas) was calculated to be $\Delta E = -30$ kcal/mol that compares favorably with the experimental enthalpy of formation, $\Delta H = -37$ kcal/mol.

[1] J. C. Boettger, *Int. J. Quantum Chem.* **95**, 380 (2003).

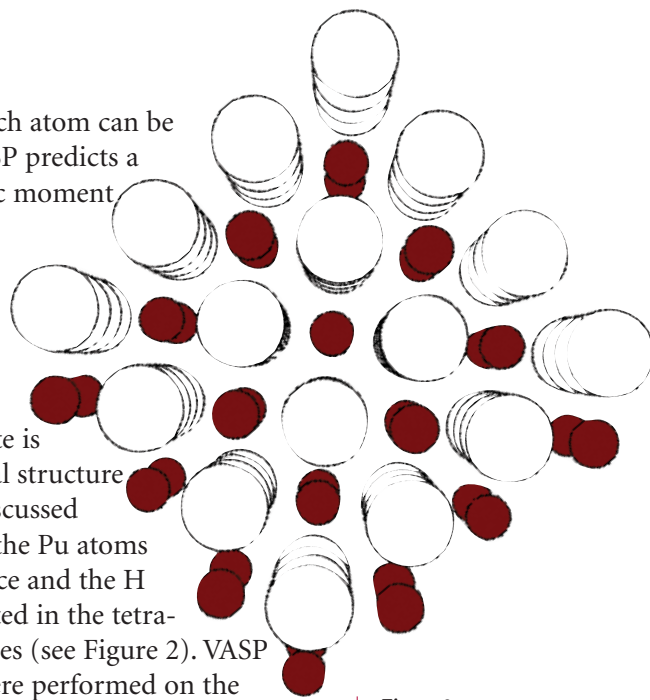


Figure 2—
Crystal structure of PuH₂. White = Pu and Brown = H.

⌘

	Eq. Volume (Å ³)		Magnetic Moment (μ_B)		ΔE (eV/atom)	
	VASP	LCGTO	VASP	LCGTO	VASP	LCGTO
Nonmagnetic	18.0	18.1	0.0	0.0	0.0	0.0
Ferromagnetic	27.0	27.1	5.6	5.7	-0.54	-
Antiferromagnetic	23.2	24.2	4.4	3.2	-0.75	-0.54
Experiment	25.2					

Table—
Electronic structure of fcc δ -Pu calculated with VASP and LCGTO.

Mesoscale Modeling of Nanocrystalline Metals

Cynthia J. Reichhardt, Brad Lee Holian, Joel D. Kress, and Antonio Redondo, T-12; cjrx@lanl.gov

The goal of mesoscale model development is to provide a bridge between the atomistic level, where interactions are known ab initio, and the macroscopic level, where the physics is determined by a complex interplay of interactions at smaller length scales. Simulating the macroscopic scale at an atomistic resolution remains beyond the reach of even the largest computing resources. On the other hand, continuum simulations such as finite element mesh models suited for much larger scales are very limited in the degree to which discontinuities such as fractures can be included in the model. These discontinuities appear in a very natural way in atomistic simulations, due to the discreteness of the system arising from the fact that the individual elements being simulated are atoms. The time and length scales that are accessible through atomistic modeling are much shorter and smaller than those that appear in engineering applications, so a pressing problem is how to bring pertinent atomistic information up to the

mesoscale level, while discarding unneeded details, and then to repeat this process from the mesoscale level to the macroscopic level. Such information propagation is the primary goal of this project.

It is natural to consider extending the discrete simulation technique to systems in which the individual elements are grains rather than atoms. Each grain is composed of a large number of atoms, but the individual atoms are not treated separately. Instead, the small-scale dynamics are averaged away, and we treat only the dynamics on a time scale relevant to the size scale of individual grains. We focus here on nanocrystalline metals, which are of significant practical interest due to their extremely high hardness and strength. Nanocrystallites can also form upon work hardening, such as when two metals wear against each other. This can change both the strength and the stress transmission properties of the materials.

Our model for mesoscopic grains is based on the Rydberg interaction potential between individual atoms, which has been shown to provide a good approximation to the actual atomic interactions in a wide range of materials. We replace groups of individual atoms with a single

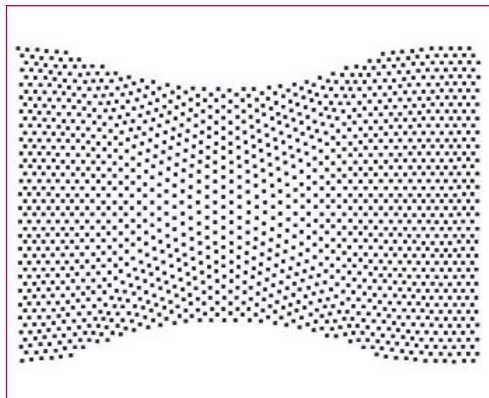


Figure 1—
(a) Mesograin sample deforming under tension at a low-strain rate.

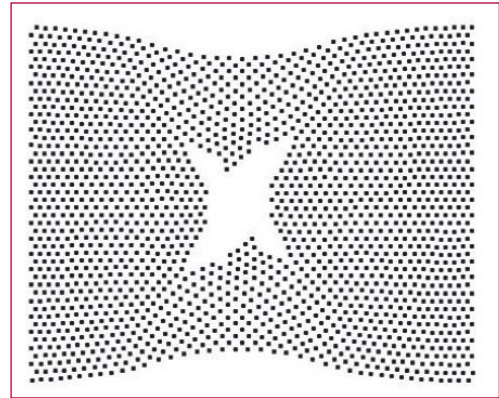


Figure 1—
(b) Mesograin sample failing under tension at a high-strain rate.

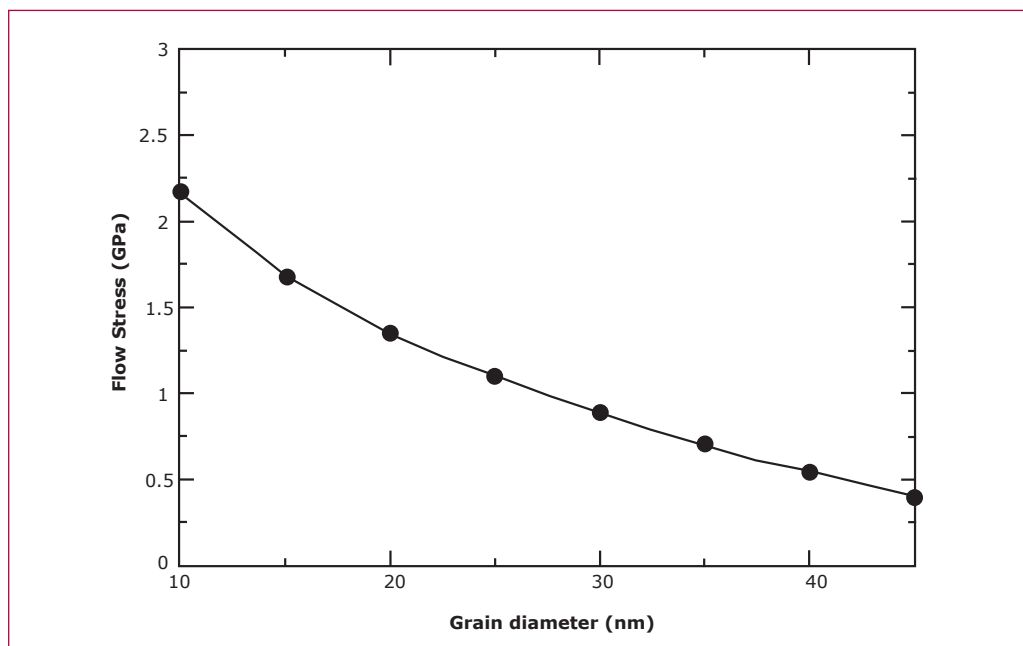


Figure 2—
Yield strength
from mesograin
simulations of
nanocrystalline
copper.

grain, and implement a grain-grain interaction given by the form of a Rydberg interaction at larger length scales. The relevant energy scale is the binding energy along the interface between two grains, rather than the atom-atom binding energy. We match the speed of sound between our mesoscale model and the atomistic model. The resulting interaction produces a tensile strength that diminishes as the grain size becomes larger, due to the decreasing ratio of surface area to grain volume with increasing grain size.

Figure 1 illustrates the mesoscopic grain model subjected to tension, where each dot represents a single grain that is 25 nm in size. Plastic deformation is illustrated in Figure 1(a), while failure of the sample under tension is illustrated in Figure 1(b). The failure occurs along the interfaces between different grains, and not internally to the grains. This feature of our model is reasonable since the bond energy between adjacent grains is weaker than the bond energy within a given grain. A major advantage of the

mesoscale modeling method is the ability to simulate samples of large spatial extent. In the sample shown in Figure 1, the 1600-grain sample is 1 micron across. Atomistic simulation of a sample of this size in 2-D would require 100 times as many particles.

The mesoscale model accurately reproduces the material strength of nanocrystalline materials. Shown in Figure 2 is a plot of the flow stress as a function of grain size. The strength decreases with increasing grain size according to the square root of the grain size, in good agreement with the Hall-Petch relationship that has been observed experimentally for a wide range of nanocrystalline materials. The magnitude of the material strength is in reasonable agreement with that observed in atomistic simulations.



All-Electron Density-Functional Studies of Hydrostatic Compression of Pentaerythritol Tetranitrate (PETN)

Chee Kwan Gan, T-12, Thomas D. Sewell, T-14, and Matt Challacombe, T-12; ckgan@lanl.gov

Table I—
Equilibrium lattice parameters and unit cell volumes for PETN.

Pentaerythritol tetranitrate [PETN, $C(CH_2ONO_2)_4$] is an important secondary high explosive. PETN has received a lot of attention due to interesting anisotropic, nonmonotonic shock initiation sensitivity. The room temperature linear and volumetric hydrostatic compression of PETN has been measured by Olinger and co-workers [1] using x-ray diffraction for pressures up to 10.45 GPa.

In this work, we report condensed phase electronic-structure calculations of the hydrostatic compression of PETN at absolute zero and pressures up to 25 GPa. We employ an all-electron density-functional method using the PBE functional in conjunction with the 6-31G** Gaussian basis set.

Calculations were performed using a parallelized version of MondoSCF [2], a suite of programs for linear scaling electronic-structure theory and *ab initio* molecular dynamics. Periodic boundary conditions were used to study the PETN crystal. The MondoSCF code employs a number of advanced $O(N)$ techniques. We used a cluster of 256 4-CPU HP/Compaq Alphaservert ES45 to perform the calculations in this work.

Calculated and measured lattice parameters are compared in Table I, where we also include the experimental results of Olinger *et al.* [1] and Conant *et al.* [3].

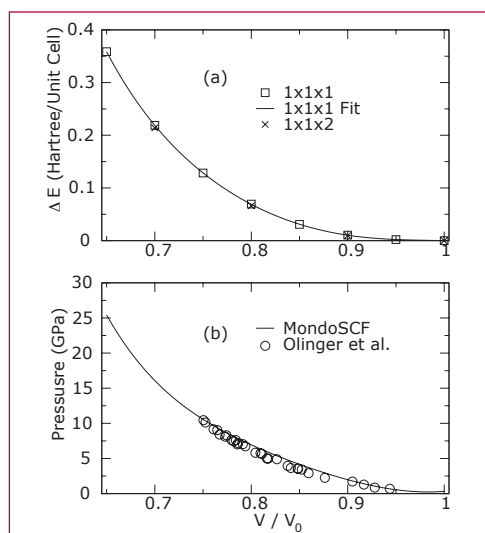
Percent errors in our calculations relative to the experimental results of Conant *et al.* [3] are 0.51%, 0.75%, and 1.8% for a_0 , c_0 , and V_0 respectively.

The volumetric hydrostatic compression is summarized in Figure 1. The variation of the energy with compression ratio V/V_0 is shown in Figure 1(a). The pressure is shown in Figure 1(b). The open circles in Figure 1(b) are the experimental data of Olinger *et al.* [1]. The calculated volumetric compression is in remarkably good agreement with experiment.

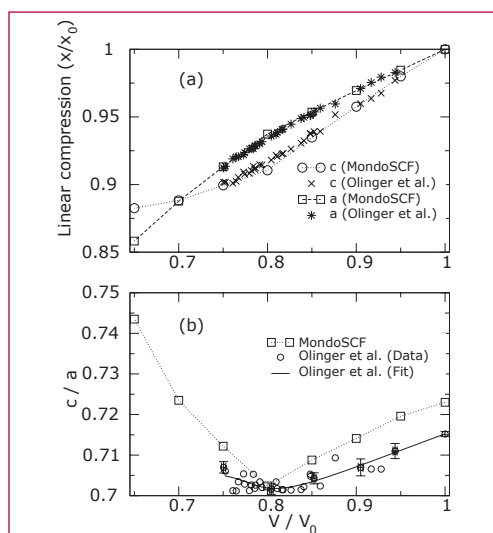
a (Å)	c (Å)	V (Å ³)	Source
9.425	6.758	600.3	This work
9.383	6.711	590.8	Olinger <i>et al.</i> [1]
9.3776	6.7075	589.9	Conant <i>et al.</i> [3]

The linear compression along the a and c crystallographic directions is shown in Figure 2. Figure 2(a) reveals good

Figure 1—
Volumetric hydrostatic compression for PETN. (a) Energy difference ΔE . Crosses are calculations for a $1 \times 1 \times 2$ supercell. (b) Pressure-volume relationship.



agreement between our predictions and the experimental data for the relative compressions of a/a_0 and c/c_0 . In Figure 2(b) we show the variation of the c/a ratio as a function of compression. The solid line is based on polynomial representations of $a = a(V)$ and $c = c(V)$ due to Olinger *et al.* [1]. We observe in both cases an initial decrease in the c/a ratio



with increasing compression, followed by an increase toward a more “cubic-like” lattice structure. The positions of the minima in the curves are in fairly good agreement, and correspond to a volume ratio of 0.8 and a pressure of about 7 GPa. Our calculations indicate essentially rigid-molecule compression for $p < 7$ GPa, with the onset of significant intramolecular distortions for higher pressures.

We can obtain the bulk modulus $B_0 = -VdP/dV$ and its initial pressure derivative $B'_0 = dB_0/dP$ using different equation of state fitting forms. The first form is the conventional Murnaghan equation. The second form is the third-order Birch-Murnaghan equation. The third form is derived from the shock Hugoniot conservation equations.

Calculated and measured values for the initial bulk modulus and its pressure derivative for PETN are summarized in Table II. The results among the fits of our isotherm to the three equations of state are fairly consistent, with $B_0 = 14.5\text{--}16.0$ GPa and $B'_0 = 5.2\text{--}6.7$.

Applying the same fitting forms to the experimental data of Olinger et al. [1], we obtain $B_0 = 9.4\text{--}12.2$ GPa and $B'_0 = 6.4\text{--}11.3$.

The average theoretical bulk modulus, which corresponds to zero Kelvin, is 32% larger than the corresponding average experimental value based on the room-temperature isotherm.

The success of these all-electron calculations for PETN demonstrates the precision of our $O(N)$ algorithms, and suggests that it may be practical to undertake similar calculations on significantly larger, more complicated systems that are well outside the capabilities of conventional algorithms.

B_0 (GPa)	B'_0	Source	Fitting form
15.8	5.3	This week	Murnaghan
14.5	6.7	This work	Birch-Murnaghan
16.0	5.2	This work	Hugoniot
11.7	6.8	Olinger et al. [1]	Murnaghan
9.4	11.3	Olinger et al. [1]	Birch-Murnaghan
12.2	6.4	Olinger et al. [1]	Hugoniot

A full-length version of this report appears in *Physical Review B* **69**, 35116 (2004).

- [1] B. Olinger, P. M. Halleck, and H. H. Cady, *J. Chem. Phys.* **62**, 4480 (1975).
- [2] M. Challacombe, E. Schwegler, C. Tymczak, C. K. Gan, K. Nemeth, A. M. N. Niklasson, H. Nymeyer, and G. Henkleman, *MONDOSCF v1.0α7, A program suite for massively parallel, linear scaling SCF theory and ab initio molecular dynamics.* (2001).
- [3] J. W. Conant, H. H. Cady, R. R. Ryan, J. L. Yarnell, and J. M. Newsam, Tech. Rep. LA-7756-MS, Los Alamos National Laboratory (1979).

Figure 2—
Linear compression of PETN. (a) Relative linear compression of the lattice parameters. (b) Ratio of c to a . Circles are experimental data [1].

Table II—
Calculated and measured bulk moduli B_0 and pressure derivative B'_0 for PETN.

Quantum Chemical and Classical Studies of the High Pressure Phase of Teflon

Holmann V. Brand, Jessica M. Ryan, and Kerri J. Kress; X-7, Dana M. Dattelbaum, MST-7; and Neil J. Henson, T-12; neil.henson@lanl.gov

Polytetrafluoroethylene (or Teflon) is a convenient, extensively studied system for many halogenocarbon polymers used as binders in high-explosive formulations. The Polymer DOE/DoD MOU project focuses on experimental and theoretical studies of Teflon under extreme conditions in order to understand the relationship of bulk properties with polymer structure. Experimental measurements are made on teflon samples that contain both crystalline and amorphous domains. This computational study investigates the structure and properties of pure Teflon phase III crystals.

Teflon exists in several crystalline phases as shown in Figure 1. Phases II and IV are based on helical chain structure, whereas phase III features a linear fluorocarbon chain and is the best characterized structurally (Figure 2).

The crystal structure for phase III has been proposed by Flack [1]. Models for phase III were constructed from this structure. Calculations were performed with two programs :

MOPAC – a general-purpose semiempirical quantum mechanics package for the study of chemical properties and reactions in gas, solution, or solidstate.

DISCOVER – a molecular simulation program for applications in computer-assisted molecular design. Initially, lattice energy minimisation calculations were performed on supercells of the phase III unit cell to determine the minimum model size required to converge the

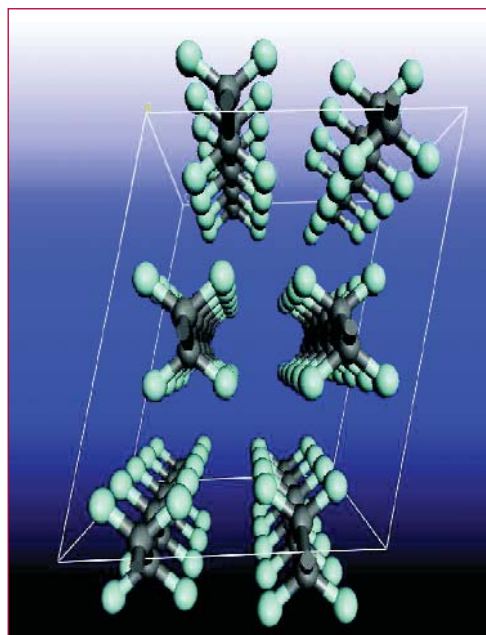


Figure 1—
The crystal structure of phase III of Teflon.

lattice energy per CF_2 group. The $1 \times 4 \times 2$ supercell with 32 CF_2 units was found to be optimal.

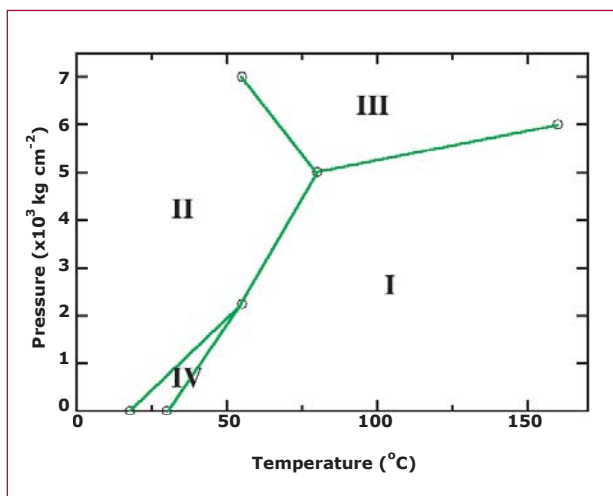


Figure 2—
Phase diagram of Teflon.

An isotropic compression and expansion scan was performed to obtain the minimised lattice energies at different volumes. The normalized volumes ranged from 0.97 to 1.03 times the initial volume. This allows the optimal cell vectors to be determined for each volume. The importance of conducting this scan can be seen in Figure 3. The scan results in lower energy structures for points far from the equilibrium geometry.

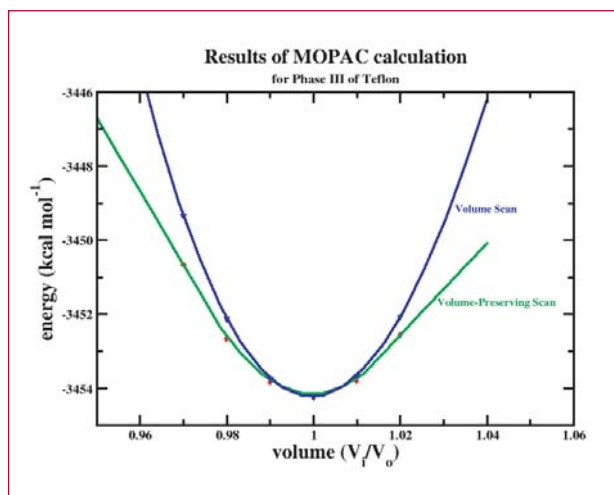


Figure 3—
The effect of the
volume preserving
scan.

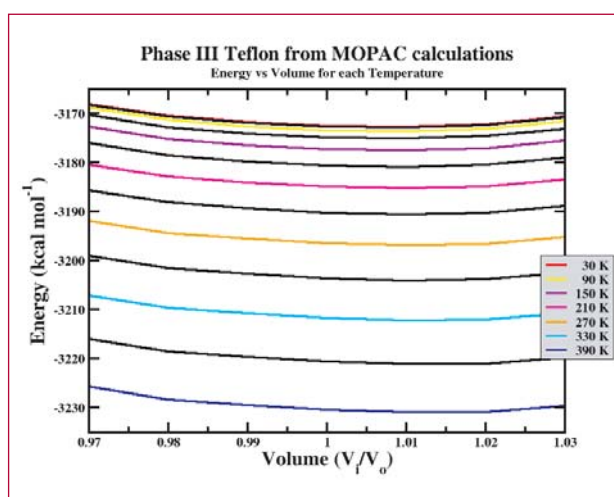


Figure 4—
Variation in free
energy as function
of temperature.

Using the minimum energy geometries, vibrational spectra were calculated using MOPAC and DISCOVER. The vibrational frequencies can be used to calculate the free energy of the system using

$$F(V, T) = E(V) + F_{\text{vib}}(V, T) = E(V) + k_B T \sum_j \ln \left\{ 2 \sinh \left(\frac{h\nu_j}{2k_B T} \right) \right\}$$

the quasiharmonic approximation: where $F(V, T)$ is the free energy, $E(V)$ is the minimised lattice energy, and ν_j are the vibrational frequencies. The calculated free energy as a function of temperature is shown in Figure 4.

Using this data, the free energy was fitted to a cubic equation from which the bulk modulus was determined by analytical differentiation. We are currently repeating this method for lower pressure phases II and IV which have a helical structure.

[1] H. D. Flack, *J. Poly. Sci. A2* **10**, 1799–1809 (1972)

2

Models for the Aging of Fogbank

Edward M. Kober, T-14; emk@lanl.gov

We continue our assessment of the physical and chemical aspects of the aging of this material and how it could interact with other materials in the Canned Sub-Assembly (CSA). An impurity, which we had previously predicted the existence of, has now been observed, and we are involved in analyzing its role in the aging properties.



Theory and Simulation of Polymer Aging: Degradation via Free-Radical Oxidation

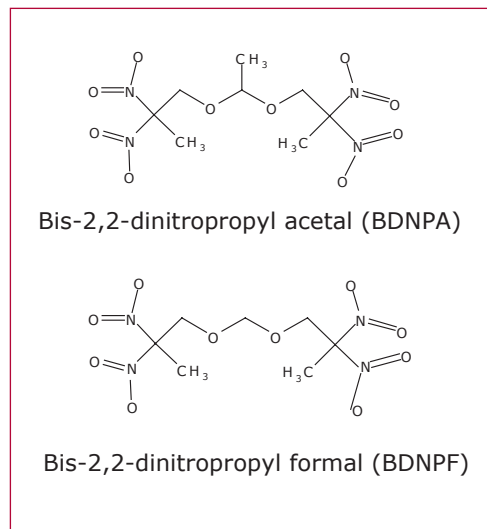
Joel D. Kress, T-12; Mike Salazar, Union Univ.; and Russell T Pack, T-12; jdk@lanl.gov

The plastic-bonded explosive PBX 9501, used in weapons, is 94.9% by weight HMX explosive, 2.5% nitroplasticizer (NP), 2.5% Estane[®] 5703, and 0.1% Irganox 1010 stabilizer (anti-oxidant). Estane[®] 5703, made by B. F. Goodrich, is a poly(ester urethane) random copolymer which serves as a glue. The urethane units segregate into “hard” domains that act as physical crosslinks between the “soft” polyester domains. The NP softens the Estane, and together they markedly decrease the mechanical sensitivity of the PBX. However, the Estane slowly degrades in time, and the effect of that on the mechanical properties of the PBX raises safety and reliability concerns. Hence, the study of polymer aging is task LA-24, an integral part of the Enhanced Surveillance Campaign.

We are studying the chemical mechanisms and kinetics of degradation processes in PBX 9501. We are working very closely with a large number of experimentalists at LANL and Pantex (PX) to determine and connect the chemical and mechanical properties of the PBX. A great deal of work on many reactions and processes is being done. Up until now, task LA-24 has focused on the hydrolysis of the ester links in the soft domains. During this last year we have embarked on a new study of another degradation mechanism, the free-radical oxidation of the urethane segments. Which mechanism dominates in weapons storage? Free-radical oxidation may be as important as hydrolysis, especially as the PBX dries out, since the

storage environment has both low moisture and oxygen content. In contrast, at “normal” relative humidity in the atmosphere, hydrolysis dominates over oxidation.

Figure 1—
Chemical structures of the two nitroplasticizer molecules.



The nitroplasticizer (NP) is composed of a mixture of two molecules (Figure 1). The mixture usually used is 45% BDNPA and 55% BDNPF by weight because this is a eutectic that is a liquid at room temperature that can plasticize (soften) polymers. Various research efforts are showing that upon heating NP loses nitro (NO₂) groups and produces oxidizing free radicals that can degrade Estane. The evidence includes (from experiments all carried out in MST Division): (1) identification of nitroxide radicals by Electron Spin Resonance (ESR) after exposing 50/50 mixtures of NP/Estane to X-rays and oxygen (W. Cooke et al.); (2) the observation of small changes in the NO₂ region of the ¹⁵N NMR spectrum after reacting isotopically labeled NP with labeled Estane or an Estane analog (D. Wroblewski et al.); and, (3) loss of infrared (IR) transmission intensity in the NO₂ region after heating neat NP in a diamond anvil cell (D. Dattelbaum et al.).

Also, exciting results on the oxidative degradation of Estane are coming out of the Constituent Aging Study (CAS, conducted by M. Lightfoot, B. Russell, and

coworkers at Pantex). The goals of the CAS are to age PBX 9501 constituents (HMX, Estane, NP, stabilizer) in various combinations at accelerated rates, detect chemical reactions that take place, identify reaction products and possible degradation mechanisms, and provide data for lifetime prediction modeling. The samples are aged at different temperatures (ranging from 40° to 64° C) in a dry, oxygen-free environment for a period of three years with most samples extracted and analyzed at 1/2-year intervals. One of the most striking findings is that combinations containing NP (NP + Estane and NP + Estane + stabilizer) show a strong correlation between the total amount of gas products generated and significant changes in the molecular weight (MW) of the Estane. The NP is reacting with the Estane polymer and causing chain scission (decreased MW) and crosslinking (increased MW and gel formation), while small molecule remnants of the reactions are presumably being detected in the gas analysis. Such large changes in MW can have drastic (and undesirable) effects on the mechanical properties of the elastomer. Finally, the preliminary findings of the CAS suggests that the stabilizers currently in use may not be optimum as the anti-oxidant is intended to prevent (and not enhance!) crosslinking (one of the free-radical degradation reactions).

The overall goal in the modeling and simulation effort is to construct a detailed chemical kinetics mechanism that describes the oxidation of Estane in the presence of NP, which is consistent with the data provided by the CAS and other experiments. A first question to ask is: Where along the Estane hard segments is the chemistry taking place and what is the chemical identity of the

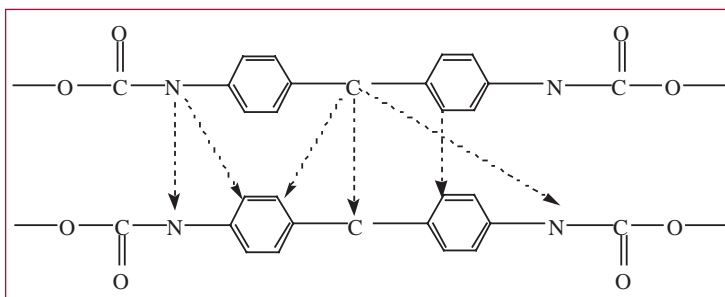
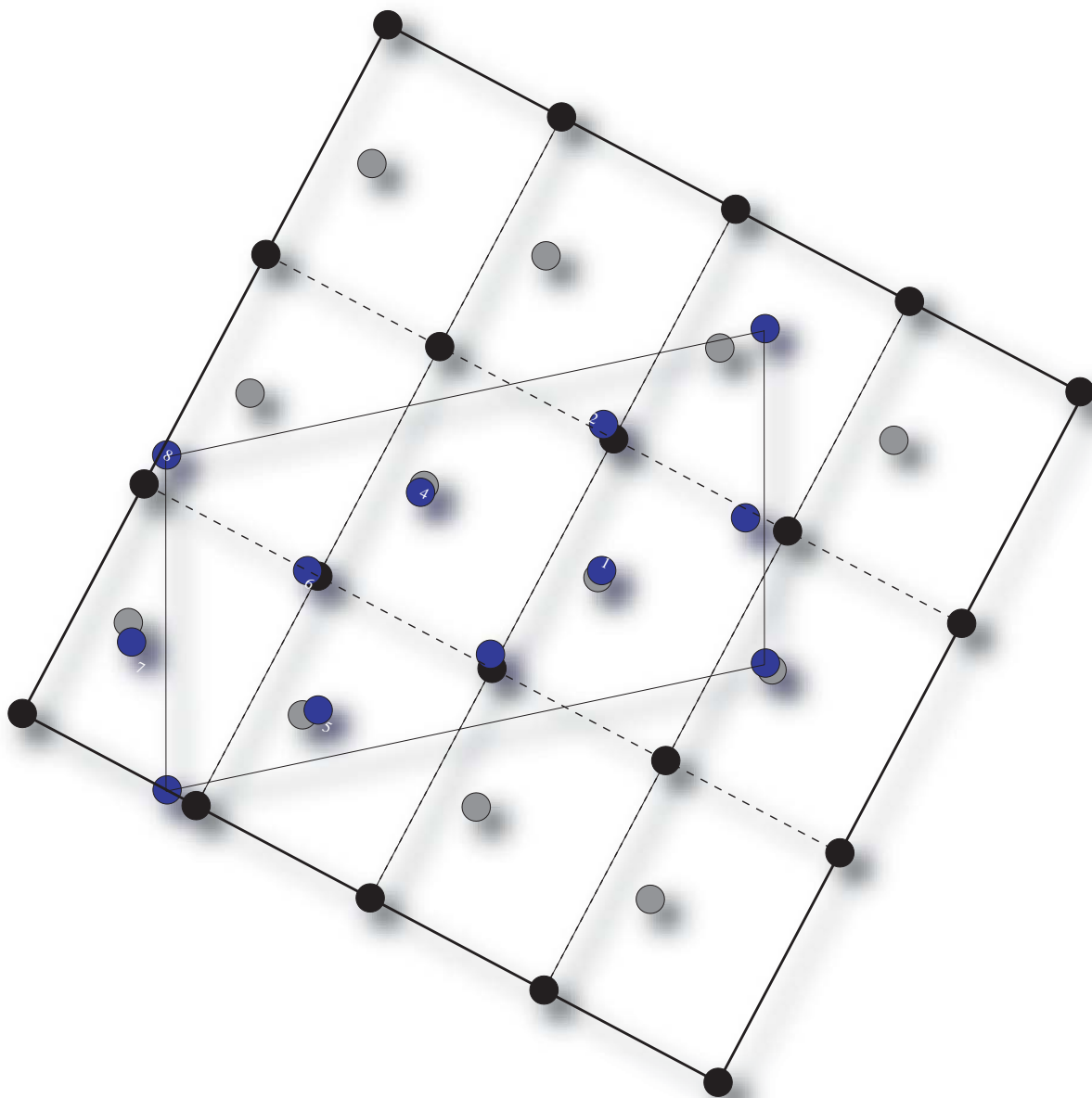


Figure 2—*Schematic of the chemical structure of two Estane hard segments side-by-side. (H atoms suppressed for clarity.) Possible crosslinks indicated by the dashed arrows.*

reactants? Both the location of the chain scissioning and the location and chemical identity of structures of the crosslinks needs to be determined. Figure 2 displays a schematic of the chemical structure of two Estane hard segments. Does scissioning take place as depolymerization (forming isocyanate and alcohol) by breaking the bond between the O and C atoms on the backbone? Does crosslinking happen at the C atom on the methylene bridge between the two aromatic rings (as suggested by ¹³C NMR studies and identification of the aldehyde oxidation product conducted in MST-Division)? At the N atom on the amide group (as suggested by IR spectroscopy studies of the products of oxidation of urethane by atmospheric molecular oxygen)? At a C atom on the aromatic ring? Do the crosslinks consist of fragments from the NP molecules (Figure 1)? Fragments from the stabilizer molecules? Perhaps NMR analysis of the gel (crosslinking) formed from isotopically labeled NP and/or stabilizer could provide some clues to the identity of the crosslinker.

In future reports, we will describe our progress in identifying key reactions in the chemical mechanism and in determining rate constants necessary to perform numerical simulations of the kinetics of the free-radical oxidation of Estane. We would like to thank our experimental collaborators at Los Alamos and Pantex for providing preliminary analyses of their data.

Condensed Matter and Material Science



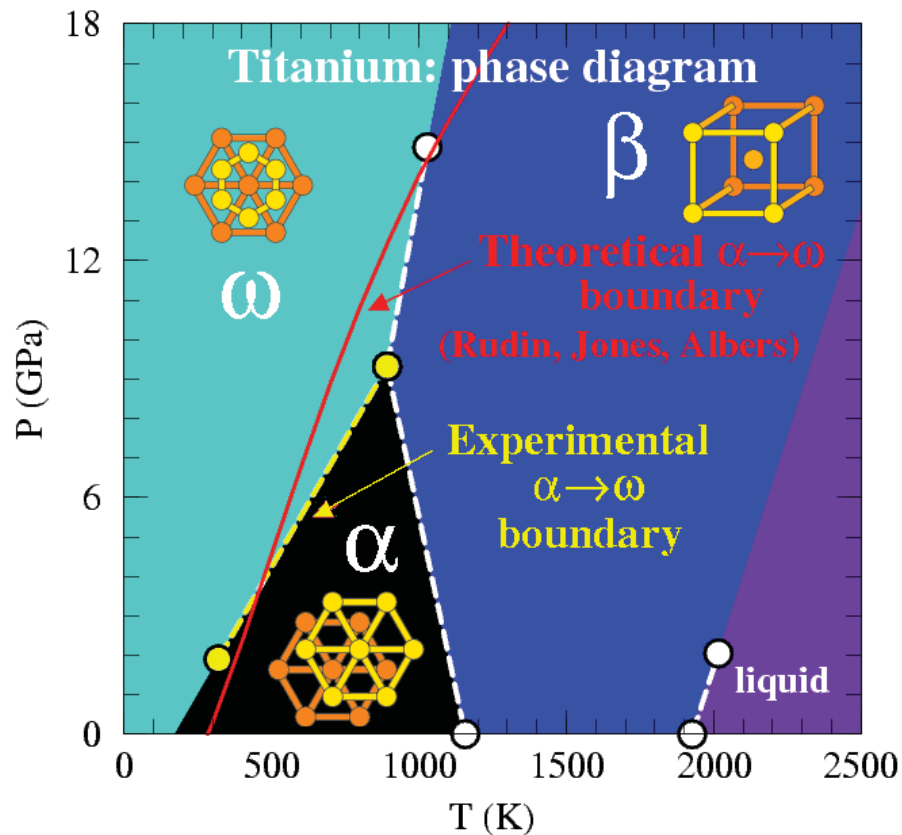
Atomistic Understanding of Ti Phase Transformations

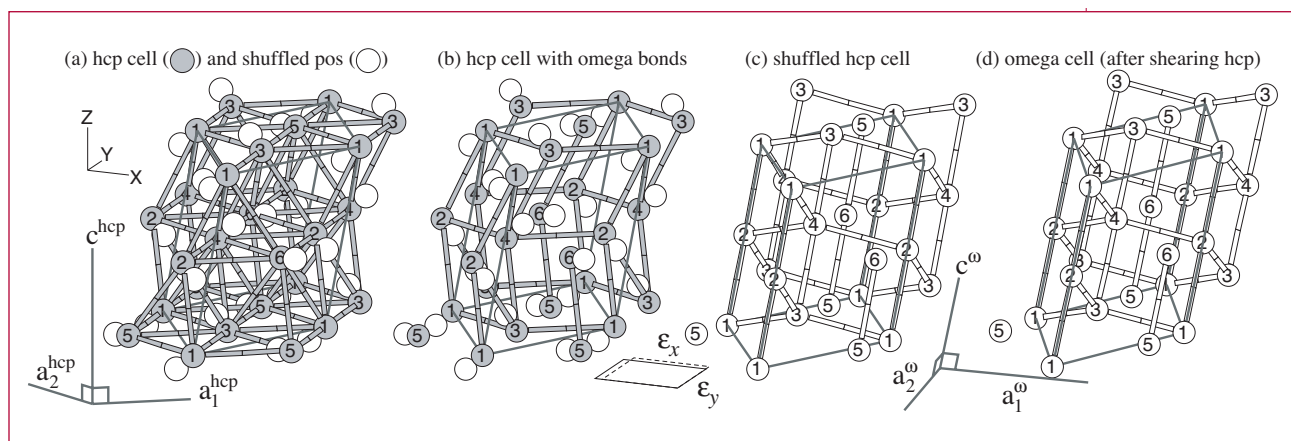
Robert C. Albers, T-11; Sven P. Rudin, T-1; S. G. Srivilliputhur, MST-8; in collaboration with M. D. Jones, SUNY-Buffalo; R. G. Hennig, D. R. Trinkle, and J.W. Wilkins, Ohio State; D. M. Hatch and H. T. Stokes, BY Univ.; rca@lanl.gov

Titanium is an important surrogate material for understanding the effects of structural phase transformations in shocked materials. We have recently developed a detailed atomistic explanation of many of the details of the most important solid-solid transformation for this material (equilibrium α hcp and high-pressure ω). We have first studied the equilibrium phase diagram of Ti, using a tight-binding model that is fit to first-principles

electronic-structure calculations for Ti to calculate quasi-harmonic phonons and the Gibbs free energy of the hexagonal close-packed (hcp) and omega (ω) crystal structures. The hcp phonon dispersion agrees with experiment; the ω phonon dispersion has yet to be measured. The model predicts that the true zero-temperature ground state is the ω structure and that it is the entropy from the thermal population of phonon states, which stabilizes the hcp structure at room temperature. We present the first completely theoretical prediction of the temperature-and pressure-dependence of the hcp- ω phase transformation and show that it is in good agreement with experiment. The quasi-harmonic approximation fails to adequately treat the bcc phase because the zero-temperature phonons of this structure are not all stable. Our predicted phase diagram [1] is shown in Figure 1.

Figure 1— The phase diagram of titanium. The dashed lines connect the experimental data points; the solid line shows our calculated α (hcp) to ω transformation. Thermal stabilization explains why at room temperature the experimentally observed hcp structure is favored over the ω structure (the calculated zero-temperature ground state).





We have also studied the details of how the atoms continuously move between the two crystal structures. We have found a new mechanism [2] for this movement (shown in Figure 2), which has a lower energy barrier than the previously suggested mechanism. This new homogeneous transformation was found by systematically generating and sorting possible α to ω pathways by their energy barriers.

[1] Sven P. Rudin, Matthew D. Jones, and Robert C. Albers, "Thermal Stabilization of the HCP Phase in Titanium," *Phys. Rev. B*.

[2] D. R. Trinkle, R. G. Hennig, S. G. Srinivasan, D. M. Hatch, M. D. Jones, H. T. Stokes, R. C. Albers, and J. W. Wilkins, "A New Mechanism for the Alpha to Omega Martensitic Transformation in Pure Titanium," *Phys. Rev. Lett.* **91**, 025701 (2003).



Figure 2—
Our proposed α to ω transformation pathway. The direct 6-atom transformation is visualized (i) as a two-step process, (ii) with 21 additional atoms outside the heavy gray parallelepiped supercell. In α , atoms 1,3,5 and 2,4,6 are in the A and B stacking planes, respectively; whereas in ω , atoms 1–4 are in the Wyckoff d position of space group P6/mmm, and atoms 5–6 are in the Wyckoff a position. (a) The gray atoms in the α cell shuffle to new positions (white atoms), with atoms 1–4 shuffling 0.63 Å, and atoms 5–6 shuffling 0.42 Å. (b) The α cell is redrawn with the "bonds" of the ω structure. Step 1: Shuffling the gray atoms to the white positions, the α cell (b) produces a strained ω cell (c), contained in the same supercell. Step 2: Straining the supercell (c) $e_{xx}=-0.09$, $e_{yy}=0.12$, and $e_{zz}=-0.02$ produces the final ω supercell (d).

Modeling Phase Transformations in Solids

Francis L. Addessio, T-3 and Dennis B. Hayes, DX-2; in collaboration with Frank J. Cherne, DX-2; Eric D. Chisolm, T-1; Brad E. Clements, T-1; Carl W. Greeff, X-7; Eric N. Harstad, T-3; James N. Johnson, Eric M. Mas, Sven P. Rudin, and Duane C. Wallace, T-1; Todd O. Williams, T-3; John M. Wills, T-1; and Q. Ken Zuo, T-3; addessio@lanl.gov

A material model that includes phase transformations in solids is being developed. Consideration has been provided to deriving a model that is compatible with weapons engineering design computer analyses. The model is derived from thermodynamic considerations for a multi-component, multi-phase mixture. The model includes both pressure driven phase transformations [1,2] as well as shear-dominated transformations [3] that are characteristic of displacive or martensitic transitions. Consider the Helmholtz free energy

$$\Psi = \sum_k \xi_k \psi_k + \Psi^{\text{mix}} \quad (1)$$

where the sum is over the material phases and Ψ^{mix} accounts for the mixing of the different components and inhomogeneities in the material eigenstrains that result from phase transformations. In (1), ξ_k is the mass fraction of the k^{th} phase. The free energy for each phase is written

$$\psi_k(\bar{\epsilon}_k^e, T, \epsilon_k^p, \bar{\alpha}_k^p) = \psi_k^{\text{EOS}}(\epsilon_k^e, T) + 2\nu_k \mu_k \bar{\epsilon}_k^e \bar{\epsilon}_k^e + \psi_k^p(\epsilon_k^p, \bar{\alpha}_k^p). \quad (2)$$

In (2), $\bar{\epsilon}_k^e$, T , ϵ_k^p , $\bar{\alpha}_k^p$ are the elastic strain, temperature, effective plastic strain, and back stress, respectively. Also, μ_k and ν_k are the shear modulus and specific volume ($\nu_k=1/\rho_k$). Barred

quantities are second order tensors. The first term in (2) is the component of the free energy that is used to provide the pressure versus specific volume (equation of state) response of the material.

Functional forms for this term may be obtained from lattice dynamics calculations [4,5]. The second and third terms account for the deviatoric component of the deformation (shear) and inelasticity (plasticity), respectively. Included in the plastic model are strain hardening (ϵ^p) and a back stress ($\bar{\alpha}^p$). A back stress has been included to allow the modeling of materials that exhibit different strengths in compression and tension.

Knowing the free energy, either from a functional or tabular form, the material response may be obtained

$$\bar{\sigma} = \bar{s} - P\bar{\delta} = \rho \frac{\partial \Psi}{\partial \bar{\epsilon}^e} \quad (3)$$

where $\bar{\sigma}$ is the stress deviator, P is the pressure, and $\bar{\delta}$ is the Kronecker delta. The kinetics of the phase transformation is required for closure. An empirical form that will drive the system to thermodynamic equilibrium has been selected:

$$\frac{d\xi_i}{dt} = - \sum_{k \neq i} \frac{g_i - g_k}{\tau_{ik}}. \quad (4)$$

In (4), g is the Gibbs free energy, which may be obtained from the Helmholtz free energy ($g = \Psi + \nu \bar{\sigma} \bar{\epsilon}$) and τ_{ik} is a material parameter that provides the transformation rate from phase i to phase k . A simulation, which models the response of a single computational cell in compression, is provided for bismuth in Figure 1 for different values of τ_{ik} .

In principle, this approach requires few modifications to the models that are currently being used in engineering design codes. If a free energy is not available, a formulation based on an equation of state and a strength model may be used in place of (3). A phase diagram may be used to obtain reference energies and entropies

$$de = \sum_k \xi_k \left[\frac{\partial e_k}{\partial v_k} dv_k + \frac{\partial e_k}{\partial T} dT + \frac{\partial e_k}{\partial \bar{e}_k} d\bar{e}_k + \frac{\partial e_k}{\partial \epsilon_k^p} d\epsilon_k^p + \frac{\partial e_k}{\partial \bar{\alpha}_k^p} d\bar{\alpha}_k^p \right] + \sum_k e_k d\xi_k + de^{mix}. \quad (5)$$

for the pure phase. However, additional terms now appear in expressions of the internal energy (e), for example: The relative magnitude of the terms that appear in (5) are under investigation, Figure 2. Currently, it appears that although the additional dissipation terms are small with respect to the terms containing the specific volume (v_k) and the temperature, they are not negligible. Consideration is being given to implementing the model into a three-dimensional, Lagrangian, finite-element analysis.

[1] D. J. Andrews, "Equation of state of the alpha and epsilon phases of iron", *J. Phys. Chem. Solids* **34**, 825 (1973).

[2] D. B. Hayes, "Wave propagation in a condensed medium with N transforming phases: Application to solid I –solid II-liquid bismuth", *J. App. Phys.* **46**, 8, 3438 (1975).

[3] F. L. Addessio, Q. H. Zuo, T. A. Mason, and L. C. Brinson, "Model for high-strain-rate deformation of uranium-niobium alloys", *J. Appl. Phys.* **93**, 12, 9644, (2003).

[4] C. W. Greeff, D. R. Trinkle, and R. C. Albers, "Shock-Induced α - ω transition in titanium", *J. Appl. Phys.* **90**, 5, 2221 (2001).

[5] J. C. Boettger and D.C. Wallace, "Metastability and dynamics of the shock-induced phase transition in iron", *Phys. Rev. B* **55**, 5, 2840, (1997).

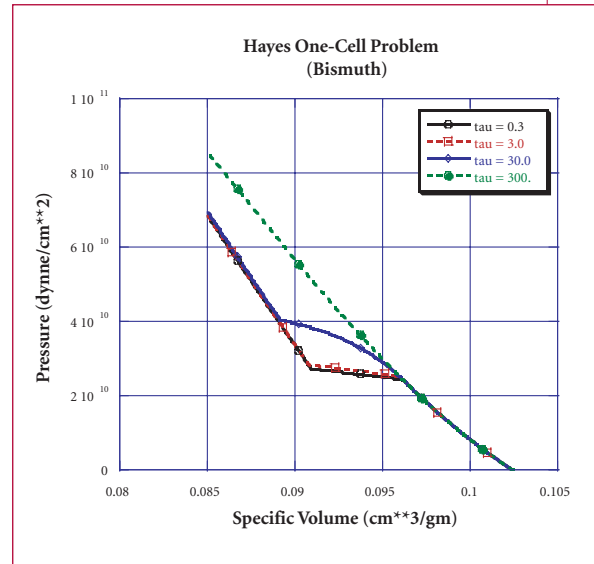


Figure 1— Simulation of a single computational cell in compression for the phase transformation of bismuth for different values of τ .

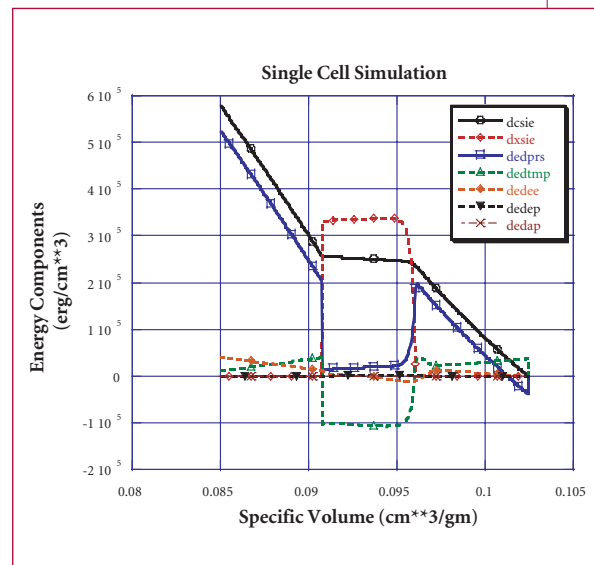


Figure 2— Investigation of the relative magnitude of terms appearing in the internal energy.

Structural Phase Transitions in Ga: Massive Parallel Implementation and Application of the Modified Embedded-Atom Method

Kai Kadau, T-11; Timothy C. Germann, X-7; Peter S. Lomdahl, T-11; and Brad Lee Holian, T-12; kkadau@lanl.gov

The Modified Embedded Atom Method (MEAM) [1] applies to metals with greater covalent bonding than the conventional Embedded Atom Method (EAM) [2], which is restricted to nearly-free-electron (simple fcc) metals. MEAM can also describe different crystallographic structures of one element or compound correctly. As a result of the angular bonding terms, semiconductors like Ga [3] and Si [4] can be described reliably. An important aspect is the possible screening of the pair potential between two atoms, as well as the atomic electron

densities. Screening takes place within an ellipse that is defined by the pair of atoms of interest, and limits the range of interactions in a natural and more physical manner than the usual radial cut-off of the involved functions. For instance, screening leads to different effective cut-off distances for different atomic arrangements, which might be important for the description of the dynamics of phase transformations. Since screening is continuous in space, it also has a contribution to the forces. Because of the more global description of the solid phase diagram, it is of great interest to study the dynamics of a solid-solid phase transformation using the MEAM framework. However, such a study requires the implementation of the MEAM formalism into a parallel molecular-dynamics (MD) code [5] like SPaSM [6], in order to describe the dynamics of millions of atoms. The principal challenge for the parallel implementation of MEAM is the treatment of the screening in the interatomic forces.

The pressure-induced solid-solid transformation of Ga will be investigated.

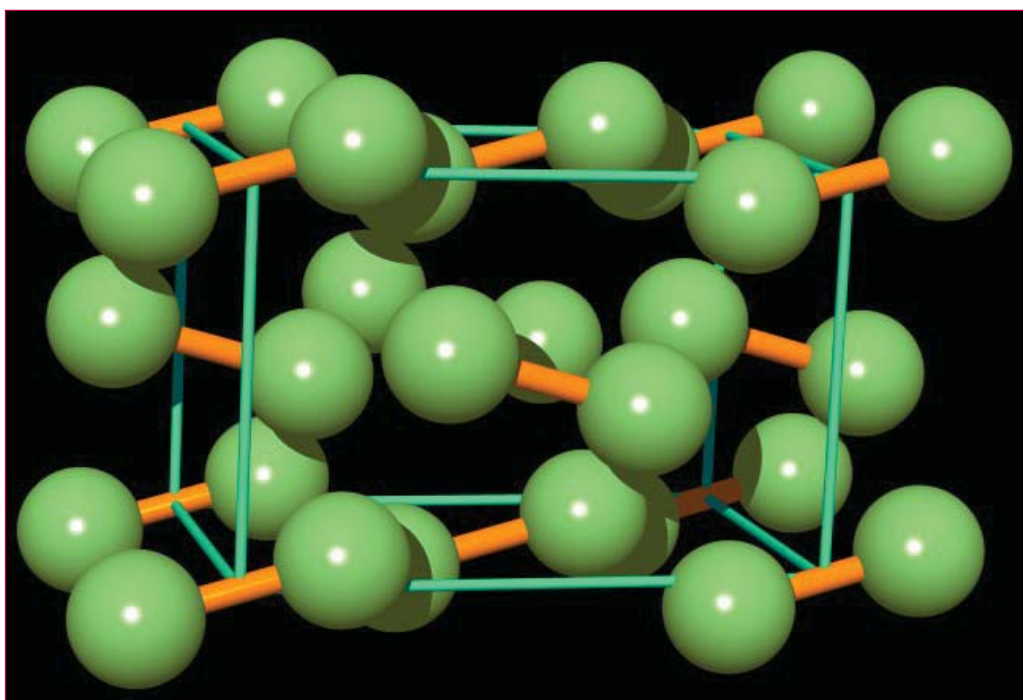


Figure 1—
Unit cell of the Ga
All ground-state
structure.
The structure is
achieved by Ga
dimers occupying
an orthorhombic
cell.

Using the MEAM potential for Ga recently proposed by Baskes *et al.* [3], loading and unloading cycles of simulation cells of Ga will be performed. The pressure-induced A11, see Figure 1, to bcc transition will be discussed and compared to experimental diamond anvil cell data. A next step will be to describe the dynamics of the shock-induced structural phase transformations [7] for Ga and Pu-Ga alloys.

Acknowledgements:

This work has been supported by the U. S. Department of Energy LDRD-DR 20020053. It is also a pleasure to thank M. I. Baskes, S. G. Srinivasan, and R. Ravelo.

[1] M. I. Baskes, *Phys. Rev. B* **46**, 2727 (1992).

[2] M. S. Daw and M.I. Baskes, *Phys. Rev. Lett.* **50**, 1285 (1983); M. S. Daw and M. I. Baskes, *Phys. Rev. B* **29**, 6443 (1984); M. S. Daw, S. M. Foiles, and M. I. Baskes, *Mater. Sci. Rep.* **9**, 251 (1993).

[3] M. I. Baskes, S. P. Chen, and F. J. Cherne, *Phys. Rev. B* **66**, 1041007 (2002).

[4] J. G. Swadner, M. I. Baskes, and M. Nastasi, *Phys. Rev. Lett.* **89**, 085503 (2002).

[5] M. P. Allen and D. J. Tildesley, *Computer Simulation of Liquids* (Clarendon Press, Oxford, 1987); D. C. Rapaport, *The Art of Molecular Dynamics Simulation* (Cambridge University Press, Cambridge, 1995); W. G. Hoover, *Time Reversibility, Computer Simulation, and Chaos* (World Scientific, Singapore, 1999).

[6] The SPaSM (“Scalable Parallel Short-range Molecular dynamics”) code is described in: P. S. Lomdahl, P. Tamayo, N. Grønbech-Jensen, and D. M. Beazley, in *Proceedings of Supercomputing 93*, G. S. Ansell, Ed. (IEEE Computer Society Press, Los Alamitos, CA, 1993), 520; D. M. Beazley and P. S. Lomdahl, *Computers in Physics* **11**, 230 (1997); see also <http://bifrost.lanl.gov/MD/MD.html>.

[7] Kai Kadau, Timothy C. Germann, Peter S. Lomdahl, and Brad Lee Holian, *Science* **296**, 1681 (2002).



Molecular Dynamics Study of Mechanical Deformation in Nano-Crystalline Metals

Kai Kadau, T-11; Timothy C. Germann, X-7; Peter S. Lomdahl, T-11; and Brad Lee Holian, T-12; kkadau@lanl.gov

Nano-crystalline metals exhibit physical properties different from ordinary polycrystalline materials, which make these materials of technological interest [1]. One important example is the increasing hardness with decreasing grain size mostly blamed on dislocation immobilization at the grain boundaries, and this is known as the “Hall-Petch effect” [2,3]. However, when decreasing the grain size below a critical value, sliding processes between the grains decrease the hardness, and is called the inverse Hall-Petch effect [4,5].

Here we report on large-scale molecular-dynamics simulations [6] investigating the tensile testing of nano-phase Al and Cu, Figure 1. The atomic interactions

were described by an embedded-atom method (EAM) potential especially designed to model Al [7] and Cu [8]. For grain-sizes below 12 nm we found the inverse Hall-Petch relation as shown in Figure 2. The deformation processes here are dominated by grain-rotation, grain-sliding, and grain-growth-mechanisms that result from the large fraction of grain-boundary atoms. In the case of nano-phase Al, we found that inter-grain fractures can occur, identified by a sudden drop in the stress-strain plot shown in Figure 3.

In the case of Cu we found a cross-over from the inverse Hall-Petch relation to the ordinary Hall-Petch relation for grain-sizes larger than 12 nm. In this regime dislocation activity becomes more and more active, whereas the inter-grain activities become less important. We have observed for the first time, using atomistic simulations, a cross-over between two regimes: one dominated by inter-grain activity and the other by an intra-grain mechanism.

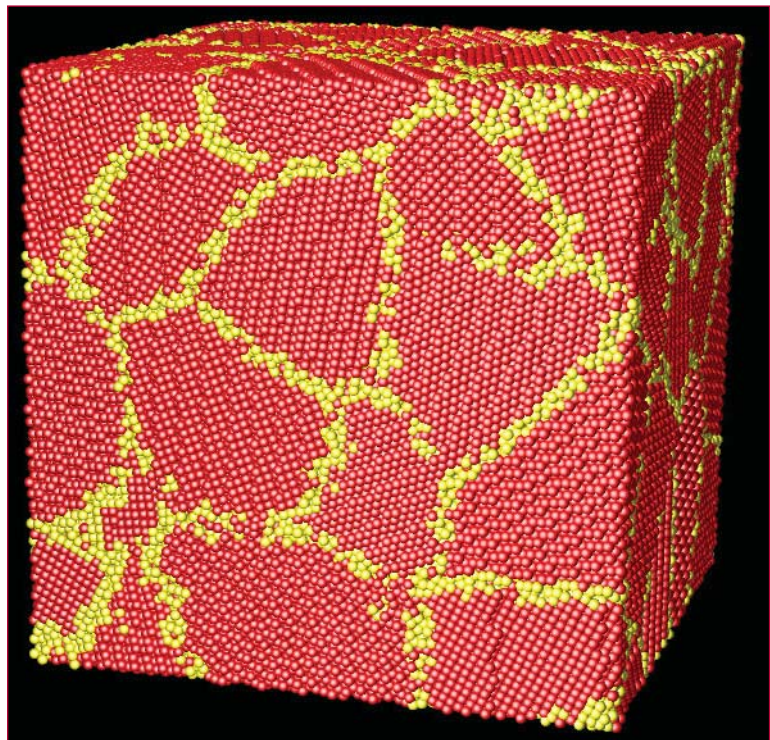


*Figure 1—
A nano-crystalline sample containing some 200,000 atoms, with an average grain-size of 4.73 nm. Grain-boundary atoms are yellow, and bulk atoms are marked red.*

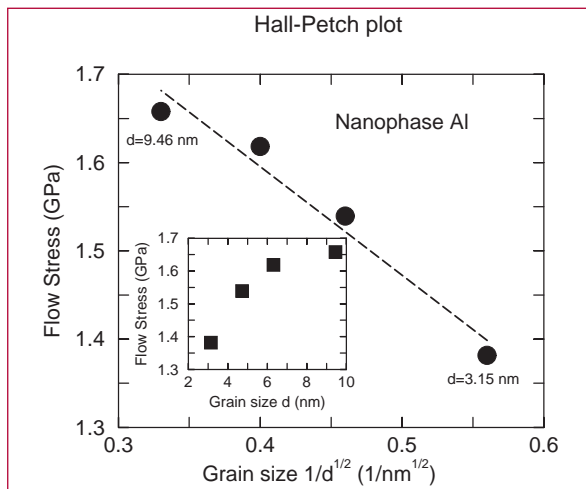


Figure 2— Hall-Petch plot for nano-phase Al showing the inverse Hall-Petch relation, i.e., softening with decreasing grain-size due to inter-grain processes. The inset shows the “raw-data” (squares) suggesting the cross-over between the inverse Hall-Petch and the Hall-Petch regime at larger grain-sizes.

Acknowledgements:

This work has been supported by the U. S. Department of Energy.

[1] R. W. Siegel, in *Physics of New Materials*, F. E. Fujita, ed., 1994, Springer-Verlag, Heidelberg, p.64; C. L. Liu, J. B. Adams, and R. W. Siegel, *NanoStructured Materials* **4**, 265 (1994).

[2] E.O. Hall, *Proc. Phys. Soc. London* **64**, 747 (1951).

[3] N. J. Petch, *J Iron Steel Inst.* **174**, 25 (1953).

[4] T. G. Nieh and J. Wadsworth, *Scripta Metallurgica et Materialia* **25**, 955 (1991).

[5] J. Schiotz, F. D. Di Tolla, and K. W. Jacobsen, *Nature (London)* **391**, 561 (1998).

[6] The SPaSM (“Scalable Parallel Short-range Molecular dynamics”) code is described in: P. S. Lomdahl, P. Tamayo, N. Grønbech-Jensen, and D. M. Beazley, in *Proceedings of Supercomputing* **93**, G. S. Ansell, Ed. (IEEE Computer Society Press, Los Alamitos, CA, 1993), 520; D. M. Beazley and P. S. Lomdahl, *Computers in Physics* **11**, 230 (1997); see also <http://bifrost.lanl.gov/MD/MD.html>.

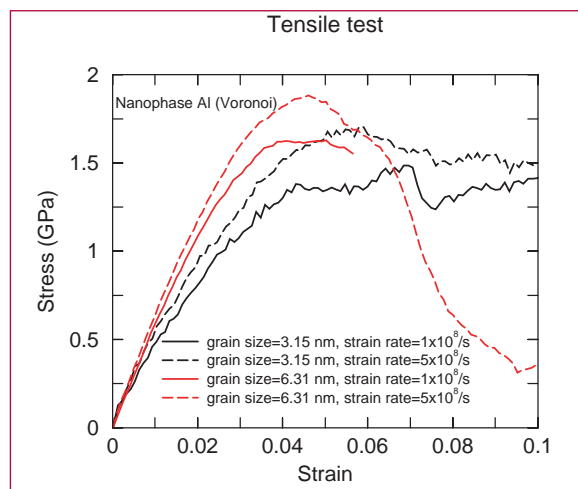


Figure 3— Stress-strain relation for tensile testing of nano-phase Al. Inter-grain fracture can occur, identified by the sudden drop in the stress-strain curves.

[7] S. Grabowski, K. Kadau, and P. Entel, *Phase Transitions* (2002).

[8] A. F. Voter, *Phys. Rev. B* **57**, 13985 (1998).

[9] T. Campbell, R. K. Kalia, A. Nakano, F. Shimojo, K. Tsuruta, and P. Vashishta, “Structural Correlations and Mechanical Behavior in Nanophase Silica Glasses,” *Phys. Rev. Lett.* **82**, 4018 (1999).



Elastic Moduli of Multiblock Copolymers

Russell B. Thompson,
Kim Ø. Rasmussen, and Turab Lookman,
T-11; and Edward M. Kober, T-14;
rthompson@lanl.gov

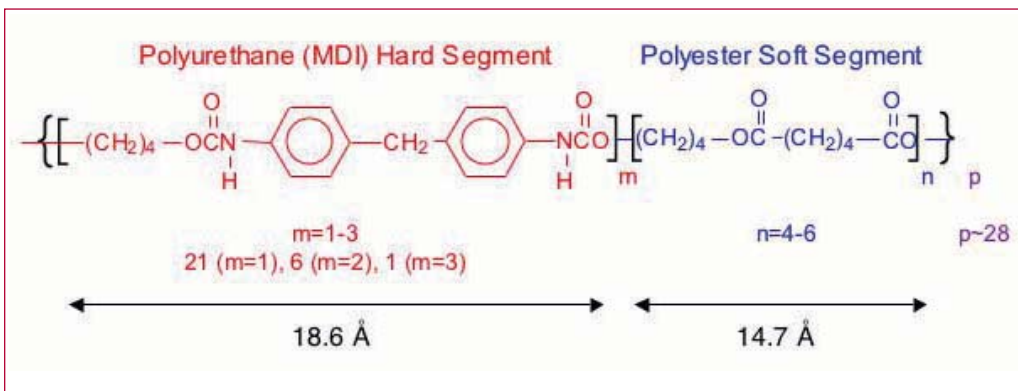
We have developed a methodology based on self-consistent field theory by which we can calculate the linear elastic response of multiblock copolymer melts in terms of elastic moduli.

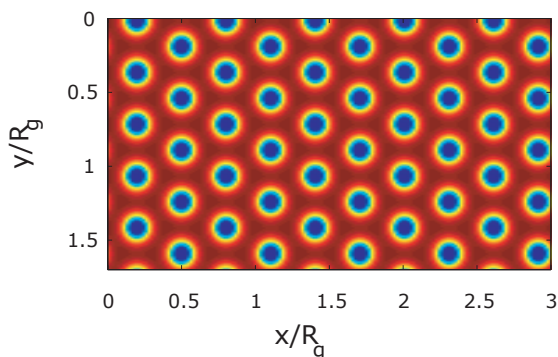
Multiblock or segmented block copolymers belong to a class of materials, which is used in a wide variety of industrial and strategic applications, consisting of covalently tethered blocks of homopolymer sequences (e.g., A_m and B_n). These sequences are thermodynamically incompatible under ambient conditions and undergo spontaneous phase separation. However, due to the covalent tether, they can only achieve microphase separation. The resulting micro (or nano) structures are of a length scale smaller than the total length of the polymer macromolecule. The details of how they are knitted together by the polymer chains, are what create the elastomeric properties of these materials.

Self-consistent field theory (SCF) is widely recognized as a powerful tool for determining the morphological behavior of block copolymer materials. We have developed a number of algorithmic

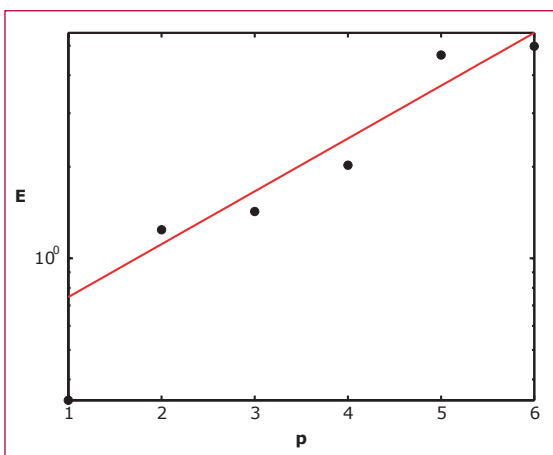
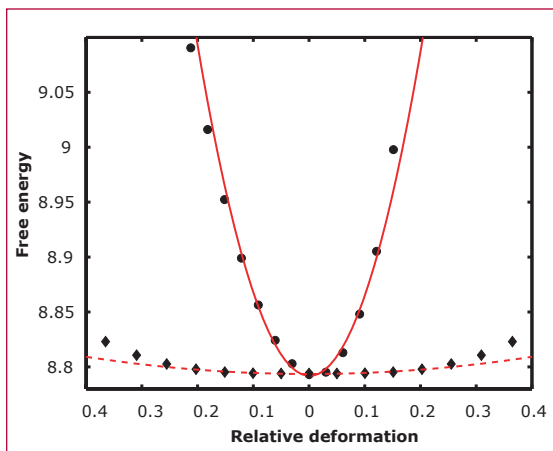
improvements [1,2] allowing us to handle the increased complexity of multiblock copolymers efficiently. SCF is based on a free-energy functional, whose minimum is realized by balancing entropic stretching effects with molecular interaction and excluded volume effects. The foundation of the SCF free energy functional is first principles and thus retains information about the polymeric nature of the molecule and aspects of connectivity. We are particularly interested in modeling and understanding Estane[®] 5703, which is the polymeric binder component used in the high explosive PBX9501, because it has been strongly suggested that aging effects in this composite arise from chemical and physical changes in the binder. Estane[®] 5703 is a segmented block copolymer whose strength arises from the self-organization it undergoes. The chemical structure is shown in Figure 1. The “hard” segments are comprised of methylenediphenylisocyanate (MDI) unites (with 1–3 repeats), and the “soft” segments are butyleneadipate (BA) oligomers of five segments. These components are repeated about 28 times as shown in Figure 1. Because of our algorithmic improvements we can apply SCF to determine the morphology of this highly segmented system where the overall volume fraction of hard segments is experimentally known to be 24%, see Figure 2.

Figure 1—
Estane chemical structure. The resulting morphology is shown in Figure 2.





Having obtained the equilibrium structure of a given system from SCF we can further calculate the increase in the free energy as a function of small deformations and thereby extract the elastic moduli of the equilibrium structure. Depending on the symmetry of the equilibrium morphology, there is a



finite number of deformations needed to extract all elastic moduli of the system. A simple example is the lamellar morphology (uniaxial) where only two elastic moduli (extensional and shear) are needed to describe the complete elastic response of the system. To extract these two moduli we need to calculate the change in free energy due to extensional (compressional) deformation and due to shear deformations. The results of such calculations are shown in Figure 3. The respective moduli are found from the curvature of these free energy curves. In this way we can determine the moduli's dependence on, for instance, the number of segments, which is thought to be a critical parameter in the aging process of Estane®. A result of such a calculation is shown in Figure 4.

In summary we have advanced SCF theory to enable calculations of structure for self-assembled materials. We have also developed the SCF methodology to extract elastic moduli of polymer materials with self-organized structure. These techniques will be applied towards formulating a “response” model.

[1] G. Tzeremens, K. Ø. Rasmussen, T. Lookman, and A. Saxena, *Phys. Rev. E* **65**, 041806 (2002).

[2] R. B. Thompson, K. Ø. Rasmussen, T. Lookman, “Improved convergence in block copolymer self-consistent field theory by Anderson mixing,” in press *J. Chem. Phys.* **120**, 31 (2004).

[3] R. B. Thompson, K. Ø. Rasmussen, T. Lookman, “Elastic Moduli of Multiblock Copolymers in the Lamellar Phase,” submitted to *J. Chem. Phys.* **120**, 3990 (2004).

Figure 2—
Equilibrium
structure of 28
segment Estane®
polymer system.

Figure 3—
Plot of free energy
versus relative
distortion for a
tetrablock copoly-
mer in a lamellar
morphology. The
points are the
values calculated
from SCF with the
black dots denoting
an extension and
the black diamonds
indicating shear.
The red lines are
parabolic fits to the
data with the solid
line fitting the
extension data and
the dashed line the
shear. All units are
dimensionless.
After [3].

Figure 4—
Plot of the
dimensionless
tensile (Young's)
modulus versus
diblock number p .
The black dots are
the data points
while the solid red
line is an exponen-
tial regression. The
data is plotted on a
semi-log scale.
After [3].

Improved Continuum Models for Polymers and Associated Experiments

Brad E. Clements and Eric M. Mas, T-1; Dana M. Dattelbaum, Edward B. Orlor, and Eric Brown, MST-7; Philip Rae and George T. Gray III, MST-8; Stephen Sheffield and David L. Robbins, DX-2; Neil J. Henson, T-12; Eric N. Harstad, T-3; Luca A. Maciucescu and Matthew W. Lewis, ESA-WR; Holmann V. Brand, Kerri Jean Kress, and Jessica M. Ryan, X-7; bclements@lanl.gov

A new project titled “Polymer Behavior under Dynamic Loading,” with Project Leader Brad Clements, under the Joint DoD/DOE Munitions Technology Development Program has the goal of producing improved physics-based polymer models. This project will have an impact on any DOE and DoD system where the use of polymeric materials is crucial to the functioning of the system.

- The project will strive to
- improve our understanding of system survivability,
 - reduce uncertainties in performance assessments,
 - improve our understanding of conditions for chemical reaction (reactive material and high-explosive safety),
 - achieve a predictive capability of polymer impact and penetration, and
 - advance material models for improved composite and energetic material design.

The technical goal of this project is to generate high-quality experimental data for polymers of interest to the DOE and DoD, develop physics-based continuum models for these polymers, and validate the models by implementing them into

finite element codes and comparing their predictions to further experiments.

Experiments include

- compressive stress-strain measurements over many temperatures and rates.
- tensile stress-strain measurements.
- Split Hopkinson Pressure Bar (SHPB).
- Taylor impact tests, see Figure 1.
- plate impact data (for Hugoniot, sound speed, and damage), see Figure 2.
- differential scanning calorimetry (DSC) measurements, see Figure 3.
- Torsional and Youngs dynamic mechanical analysis (DMA) (for viscoelasticity).
- high-pressure diamond anvil cell (DAC) and Raman analysis (for EOS), see Figure 4.
- Neutron scattering data.

Figure 1— Taylor impact studies on PTFE.



Figure 2— Hugoniot measurements on PTFE.

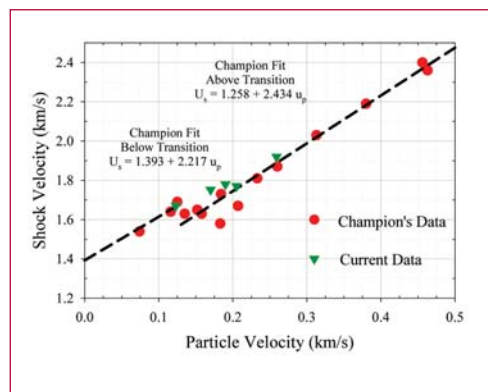
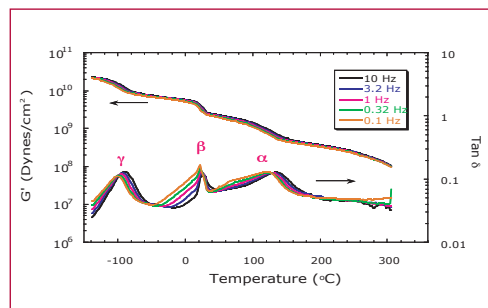


Figure 3— DMA measurements on PTFE.



In FY03 the polymers Kel-F and PTFE (Teflon) were investigated. Our theoretical model being developed is based on finite deformation analysis enabling us to simulate large deformation processes important to the DoD and DOE. Teflon and Kel-F are semicrystalline, which implies that they are heterogeneous at the crystalline domain-size scale. Our model uses the generalized method of cells (GMC) to handle this heterogeneity.

Small crystalline domains of Teflon (Kel-F) are embedded in the amorphous Teflon (Kel-F) matrix. The GMC analysis is sufficiently general to allow the treatment of loaded Teflon in future studies. The amorphous background is treated as nonlinear hyperelastic-viscoelastic, with viscoelastic properties determined by (DMA) over a large range of frequencies and temperatures. The elastic properties of the various crystal structures relevant to the crystalline domains are calculated using ab initio first principal electronic structure theory (Figure 5).

Presently, slip planes and yield processes important to the crystalline phases are treated using classical Bodner-Partom plasticity theory. The parameters in the model are fit to a host of experiments: MTS, SHPB, and plate impact, all of which are discussed. Equation of state input from the model comes from (DAC) and plate impact studies. All constitutive models, and the GMC analysis are written in a finite deformation framework. The associated computer algorithm has been implemented in the finite element code EPIC. Figure 7 shows a simulation of a Taylor impact test.

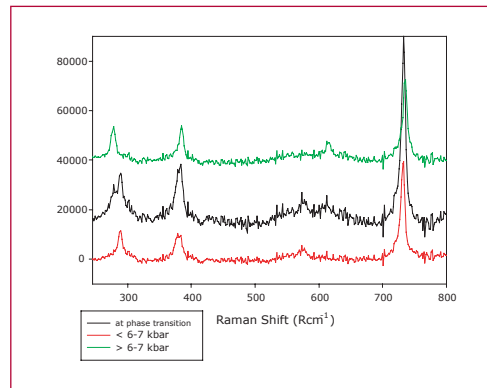


Figure 4—
Raman measurements on PTFE.

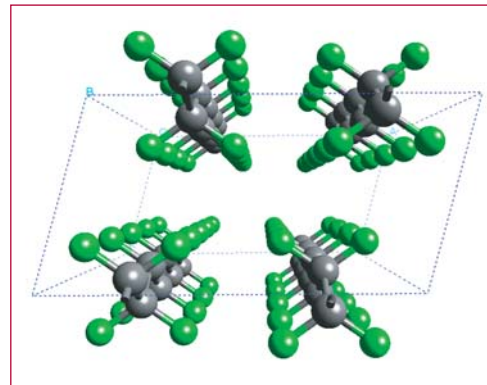


Figure 5—
Crystal structure of the high-pressure phase of PTFE.

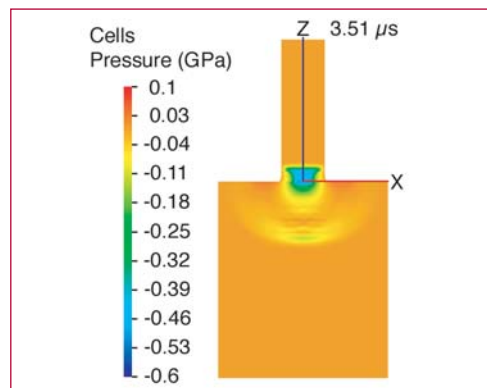


Figure 6—
Finite element simulation of PTFE impacting steel.

Direct Numerical Simulations of PBX 9501

Eric M. Mas, Brad E. Clements, and Denise C. George, T-1; mas@lanl.gov

We have conducted direct numerical simulations (DNSs) on the high-explosive composite PBX 9501 using finite element analysis (FEA). As much of the microstructure is explicitly gridded as is numerically tractable, this resolution allows us to observe some of the localization effects. PBX 9501 has a very complicated microstructure, consisting of high-melting explosive (HMX) grains (95 wt %) embedded in a plasticized estane polymer matrix (5 wt %). The HMX grains range in size from several hundred micrometers to sub-micrometer diameters.

To conduct DNSs on PBX 9501, two key factors must be addressed: first, a finite element grid must be created that captures as much of the microstructure as possible without being too complex to simulate in a reasonable amount of time, and second, the constitutive models must capture the necessary physics while also being numerically efficient.

In 1997, a study in DX-Division by Skidmore, Phillips, Son, and Asay reported a study of HMX grain sizes in PBX 9501. They removed the plasticized estane binder with a solvent and measured the particle size distribution by laser diffraction. That study provides us with an experimentally derived grain size distribution. In our DNSs we approximate their continuous distribution with seven discrete grain diameters (450, 350, 250, 200, 150, 100, and 50 μm), effectively accounting for grains down to a 25- μm diameter. Assuming one 450- μm grain, we used the distribution to calculate the approximate number of other grains, leading us to a total of approximately 1600 grains.

The finite-element grid was generated using LaGriT, the Los Alamos Grid Toolbox, on a regular tetrahedral mesh of approximately one million elements. A picture of the grid after the last 200- μm -diameter grain has been positioned is shown in Figure 1. A picture of the final microstructure model is provided in Figure 2. The front surface represents a slice that is approximately 20% of the way through the sample. Individual grains can be observed, as can percolating paths of dirty binder. This appears to

Figure 1—
A picture of the finite-element grid after grains of 450, 350, 250, and 200 μm in diameter have been allocated (80 total grains).

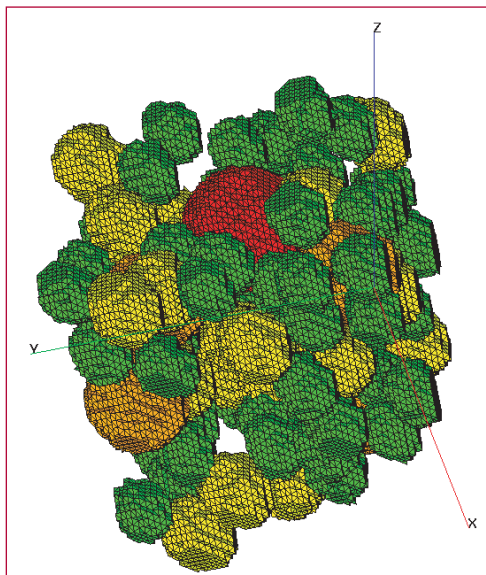
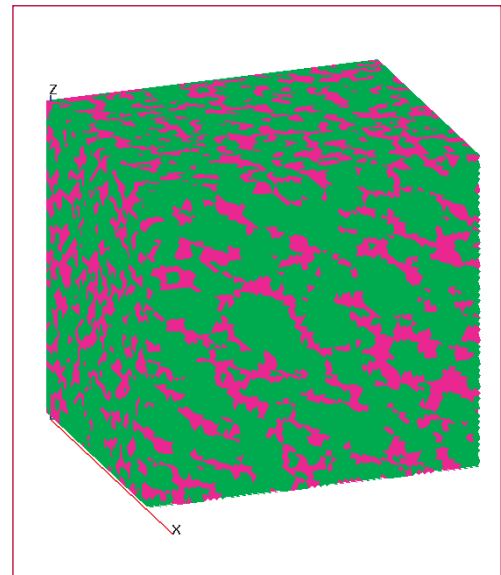


Figure 2—
A direct numerical simulation picture of the microstructure of the high-explosive PBX 9501. Green denotes HMX and pink is the “dirty binder.”



be a much better representation of PBX 9501 than has previously been seen in the modeling literature.

Parameters for our model come from three sources; values calculated directly from experiments (elastic moduli, densities, etc.), values fit to experiments on constituents (relaxation spectra of the viscoelastic binder, etc.), and those fit to experiments on the composite (parameters in our HMX micro-crack growth model and plastic yield stress). The latter were determined by our method of cells (MOC)-dirty binder hybrid model fit to experiments. The resulting stress-strain fit is shown in Figure 3.

The DNSs, using the above constitutive theories and finite element grid, were carried out using the FEA code EPIC. We modeled a load similar to a split Hopkinson pressure bar experiment, specifically uniaxial stress with an applied strain rate of 2000 s^{-1} , by applying velocity boundary conditions on the top and bottom nodes of the sample box. A simulation to a strain of 8% took about 4 days on a single-processor alpha workstation. In the future, and with the arrival of a parallel version of EPIC, we plan to simulate larger, more representative samples of PBX 9501 under more complicated loading conditions.

The purpose of the results is twofold: to show agreement with experiment to validate the above-described procedure and to analyze the DNS data for information elucidating qualitative or quantitative information about the deformation processes occurring in the composite as it is loaded. This information can then be used as a tool for general understanding of explosives and as a guide for other meso- and macro-models that might

be missing important properties of the composite.

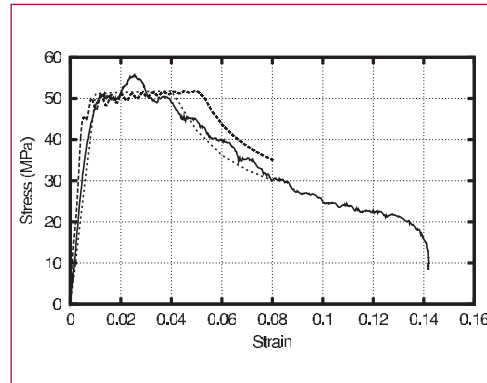


Figure 3—
A comparison of model stress-strain curves to experiment. Experimental data are represented by the solid line, the direct numerical simulation is the dashed line, and the method of cells simulation is the dots.

The DNSs agree satisfactorily with the experimental stress-strain curve, as shown in Figure 3. The agreement is also close to the MOC simulation described above that produced the parameters used in the simulation.

Other information gleaned from these simulations is more interesting. In the course of a simulation, we observed stress bridging between HMX crystals, as one might expect. We also observed that the distribution of most quantities, the

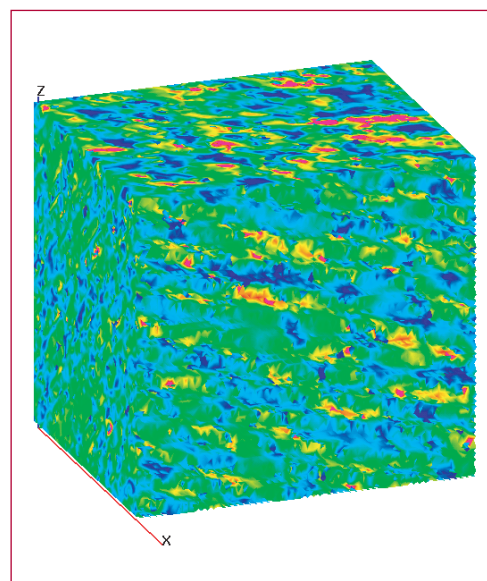


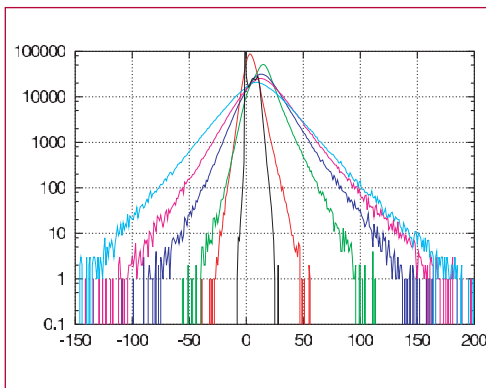
Figure 4—
Pressure distribution at the same surface as shown in the Figure 2 simulation at 17 μs , or a 4% volume-averaged strain. Blue, light blue, green, yellow, and red denote 0, 10, 25, 35, and 45 MPa, respectively.

including stress, pressure, and crack size, varied considerably from grain to grain and within grains. Figure 4 shows the distribution of pressures at the same surface shown in Figure 2, at an applied volumetric strain of 4%. As can be seen, the distribution is far from uniform. In fact, the volume average of the pressure is about 17 MPa (light blue-green in the figure) and the pressures are seen to reach easily three times that in some grains. Further, there are regions that are predicted to be in tension (very dark blue). None of these results would be observed with a homogenized model of the composite. As mentioned before, similar distributions occur for other

Many processes in the chemistry of detonation are thought to be affected by high pressure. Despite this view, there is no evidence present in time-to-ignition data, ranging from thermal explosion to detonation, that indicate a kinetic affect associated with a pressure buildup. The lack of a pressure dependence observed in these experiments, coupled with the persistence of low-pressure regions observed in these simulations, offers the possible explanation that the low-pressure regions might play an important role in the initiation of high explosives.

2

Figure 5—Histogram of pressure versus the number of elements at that pressure at different times in the direct numerical simulation. Black, red, green, blue, purple, and turquoise are at 0.1, 1, 2, 5, 10, and 25 μ s, respectively (0.1 means zero elements).



observables. Figure 5 shows a histogram of pressure versus the number of elements at that pressure for different times in the simulation. We were surprised that the negative (tensile) pressures reached such high values, but for each negative pressure there is an order of magnitude more elements at the positive value of that same pressure. The distribution shows that all values of pressure are present at any given time out to a value of approximately three times the volumetric average. This is interesting from the point of view that no matter what the volumetric average of the pressure is, there are always grains at low pressure. This might be an important observation when considering the chemistry of detonation.

HMX Crystal Diameter Distributions from Image Analysis

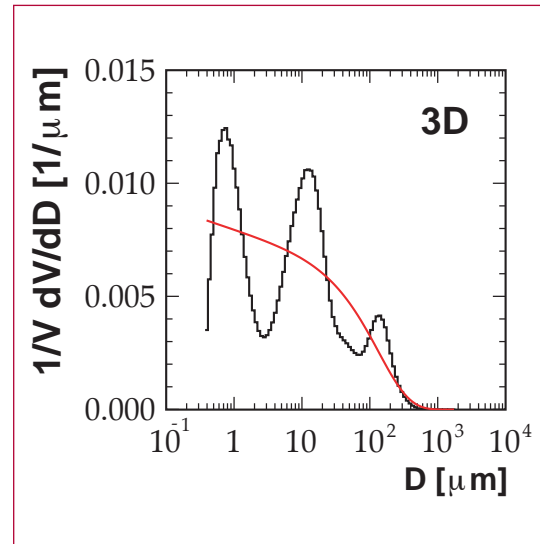
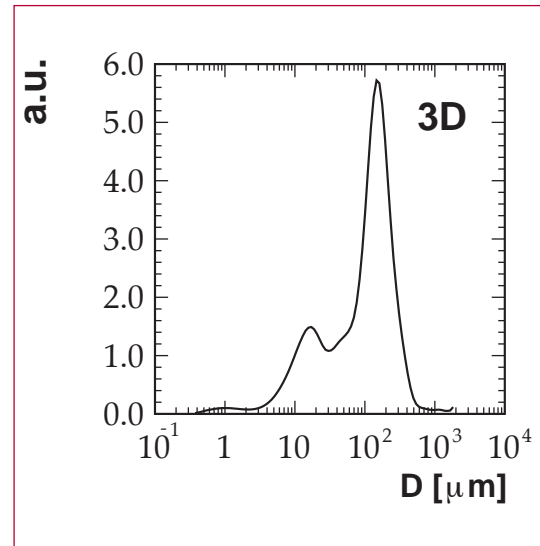
Bernd R. Schlei, T-1, schlei@lanl.gov

I perform image analysis of micrographs of high explosives such as PBX 9501 [1]. The microstructural features of these materials are of great importance to the weapon materials community.

Digital image processing as it is outlined in [1] can provide a number of different two-dimensional (2D) distribution functions for areas, aspect ratios, separations, etc., of HMX crystals (major component of the high-explosive PBX 9501). In particular, one can compute a distribution function of crystal counts, $1/N dN/dD$, as a function of the diameter D , where $D = 2r$ (cf. Figure 4, black curve). Here, r denotes the geometric mean between the length and the width of a minimum-enclosing rectangle around a single HMX crystal and it is corrected for the totally covered single crystal area.

Naturally, the question arises, how such a 2D number distribution function, $1/N dN/dD$, relates to measured three-dimensional (3D) volumetric distribution functions, $1/V dV/dD$, of HMX crystals in pressed PBX 9501. Figure 1 shows a measured volume distribution function of HMX crystals [2]. However, the authors [2] forgot to divide each bin of their histogram by the exponentially growing bin width.

The properly corrected distribution function, $1/V dV/dD$, is shown in Figure 2, and it shows three maxima (i.e., a three-modal distribution function). Assuming that $V = D^3$, one can easily-



transform the 3D volumetric distribution function, $1/V dV/dD$, into a 3D number distribution function, $1/N dN/dD$. The result is shown in Figure 3, and has been parameterized with the analytical expression

$$F(r) = 1/N dN/dD = 0.3 D^{-3.05} e^{-D/150} \quad (1)$$

The function, $F(r) = F(D)$, is shown in Figure 3 compared to the measured number distribution function. Note that the parameterization (1) does not reflect

Figure 1— Particle volume distribution of HMX after processing into PBX 9501 [2].

Figure 2— Corrected volume distribution function of Figure 1 (black) and volume distribution function (red) derived from the parameterization function in Figure 3.

the three modes of the originally measured distribution function $1/V dV/dD$ (cf. also Figure 2).

The distribution function (1) represents a power law with an exponential suppression factor as a function of the crystal diameter D . $F(r)$ is a 3D number distribution function. It can be transformed into a 2D number distribution function, $\varphi(x) = \varphi(D)$, where $x = 0.5D$, by following the work of S. D. Wicksell [3]. $\varphi(x)$ is given through the integral

$$\varphi(x) = x/r_o \int_x^R F(r) / \sqrt{r^2 - x^2} dr \quad (2)$$

In Figure 4, $\varphi(D) = 1/N dN/dD$ is compared to the 2D distribution function of crystal counts, $1/N dN/dD$, which has been obtained from digital image processing.

The agreement between the two curves in Figure 4 is quite remarkable, since it means that digital image processing can provide useful information about the microstructure of high explosives such as PBX 9501, because the results relate to the 3D experimental measurements so well. Further details, such the effects of the three modes in the experimental distribution functions, are currently being investigated.

[1] B. R. Schlei, L. Prasad, A. N. Skourikhine, "Geometric morphology of granular materials," in Vision Geometry IX, Proceedings of SPIE's 45th Annual Meeting, San Diego, CA, Vol. 4117 (2000), pp. 196–201.

[2] C. B. Skidmore, D. S. Phillips, S. F. Son, and B. W. Asay, "Characterization of HMX Particles in PBX 9501," in Shock Compression of Condensed Matter – 1997,

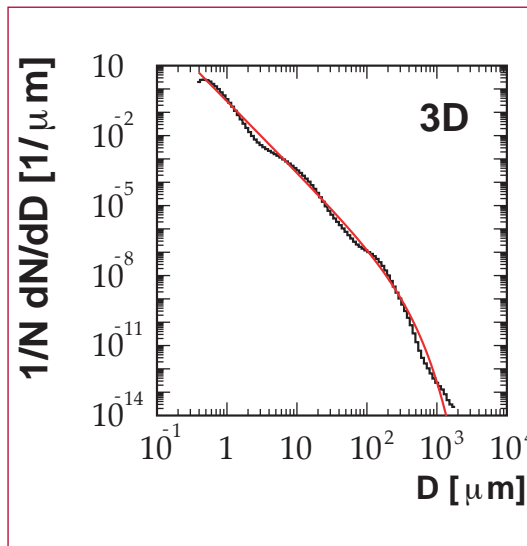


Figure 3— Three-dimensional number distribution function derived from the volume distribution function in Figure 2 (black) and its parameterization (red).

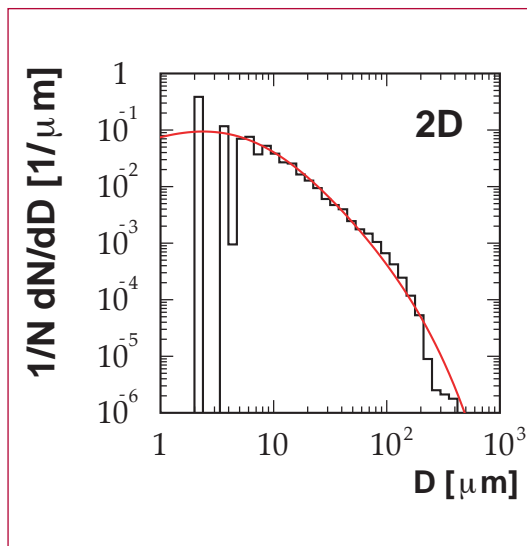


Figure 4— Two-dimensional number distribution function extracted with digital image processing techniques [1] (black) and result of the integrated three-dimensional number distribution function (red).

American Institute of Physics (AIP) Conference Proceedings Vol. 429 (1997), pp. 579–582.

[3] S. D. Wicksell, "The Corpuscle Problem," Biometrika, Vol. 17 (1925), pp. 84–99.



Developments towards a Continuum-Level Non-Spherical Void Growth Model Using a Micro-Mechanics Basis

*Brad E. Clements and Eric M. Mas, T-1;
and Paul J. Maudlin, T-3;
bclements@lanl.gov*

Metallographic fractography shows that low concentrations of manganese sulfide (MnS) impurities have a significant role in the fracture of 1080 and HY-100 steels [1]. Examination of spalled 1080 and HY-100 samples reveal that the MnS impurities act as microvoid initiation sites necessary for ductile fracture to occur. The MnS form into high-aspect ratio aligned inclusions. The alignment results in the orientation dependence observed in fracture. Consequently, to model the fracture occurring in these steels it is important to include the non-spherical shape and orientation of the MnS impurities.

While the scientific literature contains many articles on spherical void growth, substantially fewer attempts have been made to model ductile failure in materials characterized by nonspherical void growth. It is of considerable interest to inquire if a purely continuum model can be constructed that has the advantage over micro-mechanics-based models for being of greater numerical efficiency. There are several candidate theories in the scientific literature but in this work we have focused on the Continuum Damage Mechanics (CDM) that appears to have been originated by Kachanov [2] and Rabotnov [3]. Since the work of these authors, CDM has burgeoned—background literature can be found in Lemaitre and Chaboche [4],

for example. In spite of successes demonstrated by CDM very little literature is available that directly tests the conjectures of the theory. Given that the conjectures are not transparent, in the present work we have undertaken the task of applying a rigorous method, namely Green's Functions (GF), to test the reliability of CDM theory.

Kachanov [2] and Rabotnov [3] were among the first to conjecture the existence of an effective stress $\tilde{\sigma}$ defined such that the complete continuum mechanics of a damaged material can be described by invoking a corresponding set of constitutive equations, given for an undamaged material, but with the simple replacement, $\sigma \rightarrow \tilde{\sigma}$. As discussed below, this replacement includes, for example, the stresses appearing in inelastic constitutive equations. Sidoroff and Cordebois [5] conjectured that $\tilde{\sigma}$ could be uniquely determined by making an assumption of elastic energy equivalence. Chow and coworkers [6] have extended this idea and assume, in the presence of inelastic work (for example, plasticity), one should determine $\tilde{\sigma}$ and an effective strain $\tilde{\epsilon}$ by equating the total stored energies. Letting D denote a measure of the damage state, called the damage field, the conjecture states that

$$W(\sigma, D) = W(\tilde{\sigma}, D=0),$$

where the left (right) side of the equality is the energy stored in the damaged (undamaged, with $\sigma \rightarrow \tilde{\sigma}$, $\epsilon \rightarrow \tilde{\epsilon}$).

Kachanov and Rabotnov gave a physical interpretation for $\tilde{\sigma}$ by proposing that for systems with isotropic damage, $\tilde{\sigma}$, the Cauchy stress σ , and D should obey the simple relationship:

$$\tilde{\sigma} = \frac{\sigma}{1-D},$$

where D is interpreted as the fraction of damaged to the total cross-sectional

areas. These concepts have been extended to anisotropic damage, for example, a system containing aligned nonspherical voids. For that case D becomes a tensor quantity. The damage tensor $M(D)$ connects the true stress to $\tilde{\sigma}$. A large body of work has followed from these initial ideas. We refer to the book by Lemaitre and Chaboche [4] for further discussions. Interestingly, we find little theoretical work has been done to justify these conjectures.

The elastic-plastic stress and strains surrounding a void in an isotropic matrix can be calculated by Green's function techniques [7]. This requires the numerical solution of an integro-differential equation that we solve by an iterative procedure. Examples of the Green's function solutions are shown for uniaxial loading both aligned (longitudinal to the long-axis of an ellipsoidal void) and transverse to it (Figure 1). Next, we calculate, using CDM, the matrix $M(D)$ and substitute this into a standard set of equations for a homogeneous elastic perfectly plastic material with the simple substitutions $\sigma \rightarrow \tilde{\sigma}$ and $\epsilon \rightarrow \tilde{\epsilon}$ and where we take $\tilde{\epsilon} = M^{-1}(D) \epsilon$.

By comparing to the GF solution we found that the conjectures of CDM worked remarkably well for general loads (Figure 2). However, seldom could we use the exact area ratios given by the GF solution to achieve agreement. For example, the agreement in Figure 2 came about by using CDM area ratios about half the GF values, indicating that effective area ratios must be used in the CDM theory.

[1] V. Jablokov, D. Goto, D. Koss, and J. McKirgan, *Mat. Sci. Eng. A* **302**, 197–205 (2001); B. E. Clements, E. M. Mas, and G. T. Gray, III,

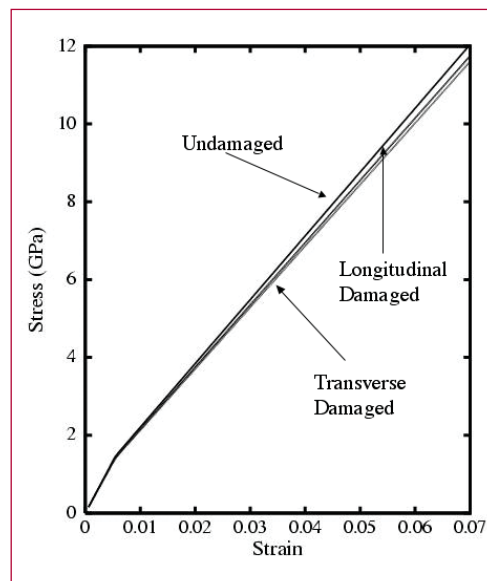


Figure 1—
Stress-strain
GF solutions.

“Shock Compression in Condensed Matter –2001,” ed. M. D. Furnish, N. N. Thadhani, and Y. Horie, AIP Conference Proceedings 620, New York, (2002), pp. 535–538.
[2] L. M. Kachanov, *Izv. Akad. Nauk USSR Otd. Tekh.* **8**, 26–31 (1958).
[3] Y. N. Rabotnov, *Creep Problems in Structural Members*, North Holland, Amsterdam (1969).

[4] J. Lemaitre and J. L. Chaboche, *Mechanics of Solid Materials*, University Press, Cambridge (1990).
[5] J. P. Cordebois and F. Sidoroff, *Euromech*, 115 ed. Villard de lans (1979).
[6] T. J. Lu and C. L. Chow, *Theoretical and Appl. Fract. Mech.* **14**, 187–218 (1990) and references therein.
[7] T. Mura, *Micromechanics of Defects in Solids*, 2nd ed., Martinus Nijhoff, Dordrecht, (1987).

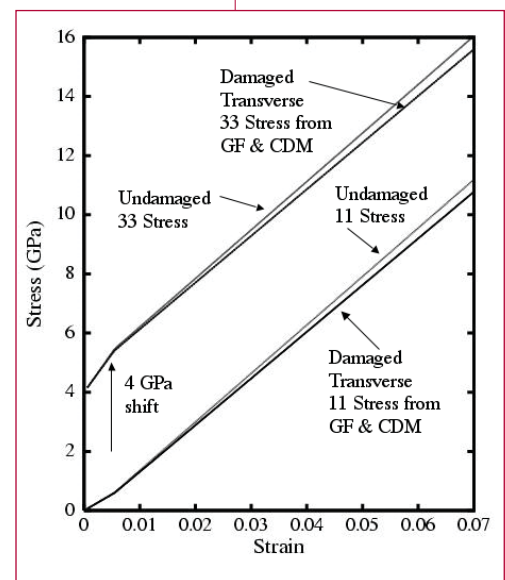


Figure 2—
Comparison
of CDM and
GF solutions.

Predicting Strain Localization in Anisotropic Materials

Q. Ken Zuo, Justin R. Smith, Paul J. Maudlin, and Francis L. Addessio, T-3; zuo@lanl.gov

We have developed a framework for predicting the onset and orientation of shear bands in metals under large plastic deformation. Shear banding refers to the formation of a highly localized deformation in the form of thin planar bands (of the order of 10 μm) caused by material softening. Material anisotropies in both the elastic and plastic responses are included in the framework. The criterion for localization is the loss-of-ellipticity condition proposed by Rudnicki and Rice, which is associated with a change of the characteristics of the governing equations. Loss-of-ellipticity occurs when the acoustic tensor becomes singular. The acoustic tensor is the inner product of the tangent stiffness tensor with a normal vector defining the localization plane. A computer program (using Mat-Lab) has been written to

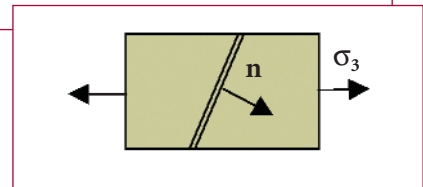
calculate the onset and orientation of the band for materials with general anisotropy (both in the elastic stiffness and the shape of the yield surface) subjected to an arbitrary, three-dimensional stress state. The program searches through all orientations to find that orientation for which the acoustic tensor becomes singular (having a zero eigenvalue) at the minimum value of the equivalent plastic strain. We have studied strain localization in several application materials (Cu, Zr, Ta) under different processing conditions (i.e., rolled, wire drawn, forged). The material anisotropy resulting from processing-induced texture can have significant effects on strain localization.

Consider the plastic deformation of a thin tantalum plate under uniaxial tension (Figure 1). During the early stage of deformation, the material is stable and the deformation is uniform with the stress state in the plate being uniaxial. As deformation proceeds, the material reaches a critical state where two thin bands (i.e., a doublet) of highly localized deformation emerges from the weakest locations in the plate (e.g., for a uniform

Figure 1—
A thin Tantalum plate under uniaxial tension showing the doublets of localized deformation.



Figure 2—
The details of the Tantalum plate showing the doublets (shear bands) and the final failure.



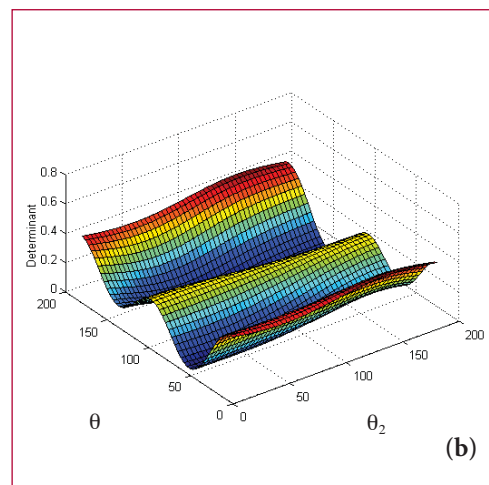
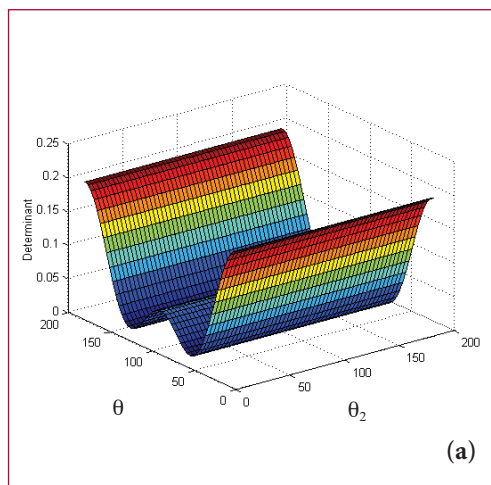


Figure 3—
The determinant of the acoustic tensor depends on the orientation of the localization plane for copper with different textures, (a) isotropic, (b) anisotropic.

plate with no defects inside, the bands initiate from the free sides and propagate towards the middle of the plate). Under further deformation, one of the bands becomes dominating while the other diminishes and the material failure occurs across the dominating band (Figure 2). Since the material often fails (either by shearing or a combination of shear and normal modes) along the localization plane, it is important to predict the orientations of the localization planes. The loss-of-ellipticity condition states that localization initiates when the acoustic tensor first becomes singular. The orientation for which the acoustic tensor first becomes singular corresponds to the orientation of localization plane. Figure 3 shows the prediction of the dependence of the determinant of the acoustic tensor (normalized to the value for the elastic deformation) on the orientation the localization planes (in terms of Euler angles for the normal) for copper with two different processing conditions. The value of the determinant measures the material's resistance to strain localization. The determinant (normalized) starts with some positive value (unit for materials with isotropic elasticity), and gradually reduces the value as the plastic deformation accumulates. Figure 3a is

for a copper plate with random initial distribution of grain orientations (hence an isotropic texture). It is seen that the determinant depends very strongly on the orientation of the band, and that localization will initiate along the planes 54° from the loading axis, a result confirmed by experiments. It also shows that the determinant of the acoustic tensor is invariant with respect to θ_2 , the angle with the thickness direction, due to the isotropic nature of the texture. Figure 3b is for a rolled copper plate with the $\langle 111 \rangle$ directions of the grains aligned along the plate thickness direction. The determinant now depends also on the angle θ_2 , due to strong texture effects. Another major effect of anisotropy (texture) is that the two localization planes are no longer symmetrically oriented with the loading axis, as in the isotropic cases.



Lattice Effects in Gallium-Doped Plutonium

Sven P. Rudin and John M. Wills, T-1, srudin@lanl.gov

The δ phase of plutonium has many advantages over the other phases when it comes to machining, but in its pure form plutonium can be found in the δ phase only at temperatures well above those practical for machining. However, by doping with a few percent of gallium, the δ phase can be made stable at room temperatures. Though this gallium-stabilized δ phase appears mostly in the face-centered cubic (fcc) crystal structure, experiments reveal in the vicinity of the Ga atom a significant departure from the fcc crystal structure.

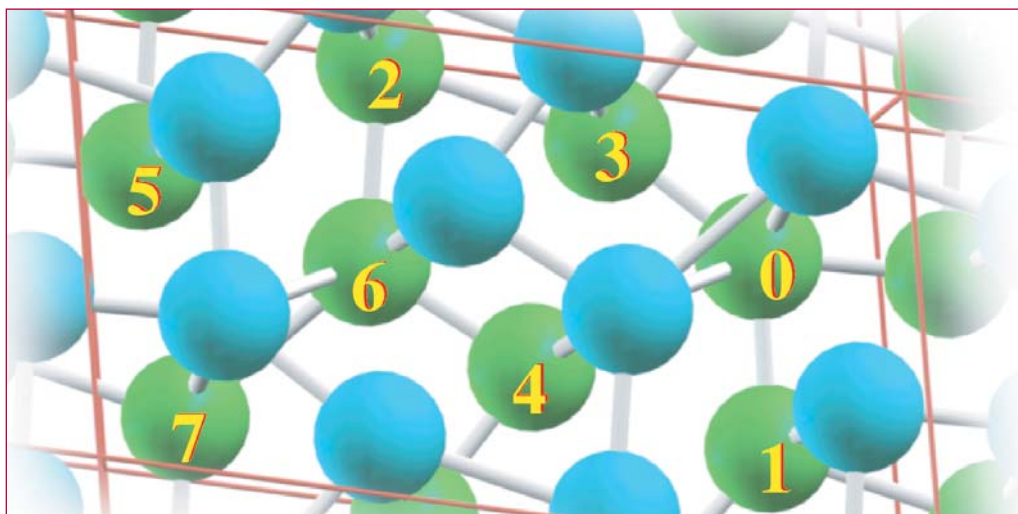
The lattice distortion in the δ phase due to the gallium doping has been studied experimentally and theoretically. But what happens in the other crystal phases when doped with gallium, and what can we learn from studying them to help us understand the gallium-stabilized δ phase? We report here work in progress on the α and ϵ phases of gallium doped plutonium. Figure 1 shows the some-

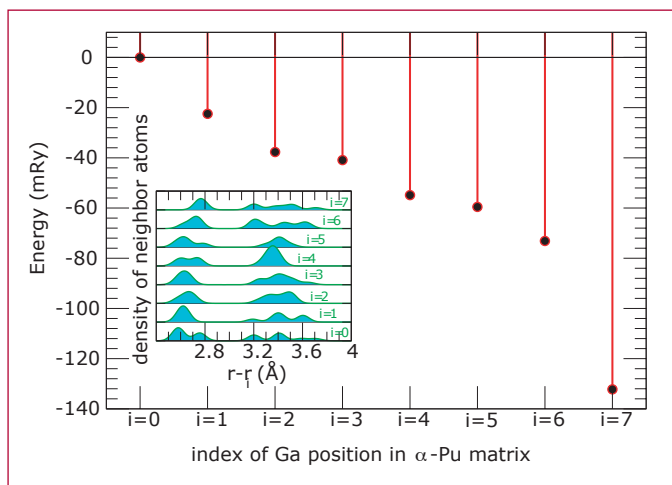
what complicated crystal structure of the α phase; the ϵ phase is simpler with a body-centered cubic (bcc) crystal structure.

The sixteen atoms in the unit cell of α -Pu see eight different environments. Some of these are more favorable for Ga substitution as shown in Figure 2, where a correlation between the energies (calculated with first principles methods) and the radial density of neighbor atom positions is evident: when the nearest neighbors are further away the site becomes more favorable.

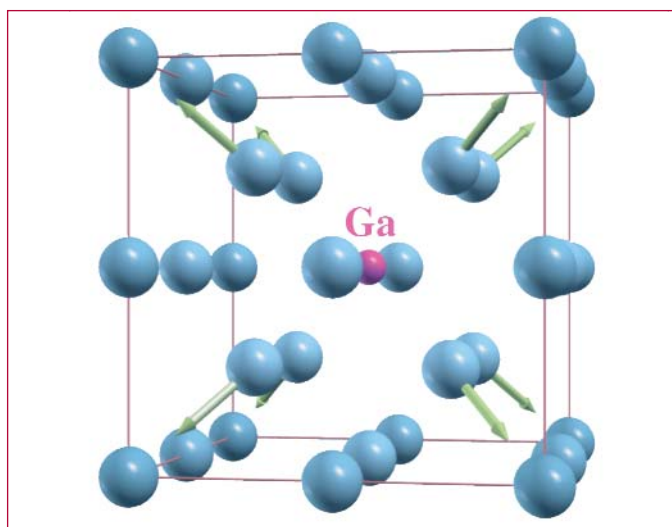
For the bcc crystal structure we are investigating the effect of a gallium atom on the surrounding lattice structure. Figure 3 illustrates our preliminary results, which indicate a roughly 2% elongation of the bonds between the gallium and its neighboring plutonium atoms. This result is somewhat surprising: the gallium atom is in some sense smaller than the plutonium atom, hence one would expect the bonds to neighboring plutonium atoms to get smaller, not larger. This is in contrast to the fcc lattice where the same computational scheme shows the plutonium atoms relaxing inward [1].

Figure 1— Sixteen atoms make up the unit cell (outlined in red) of alpha-Pu. The atoms are arranged in pairs that span two layers (shown in cyan and green). The two atoms in each pair see the same environment.





These results are preliminary: a larger simulation cell for the bcc crystal structure will reveal whether the Ga atom indeed pushes on its plutonium neighbors; a refined view of the Ga atom's preference among the eight possible substitutional sites in the α -Pu can be expected from relaxing the lattice. These results, if confirmed with additional calculations, have significant implications on the modeling of crystal phases of alloyed plutonium.



[1] J. D. Becker, J. M. Wills, L. Cox, and B. R. Cooper, *Phys. Rev. B* **58**, 5143 (1998).

Figure 2—
First principles energy for substitutional doping with gallium in the α -Pu matrix. The calculated energy is shown for the eight distinct possible sites, relative to the energy of the first case.

Inset:
radial density of neighbor atom positions as seen from each of the eight sites. For visualization purposes the density has been plotted with a 0.05 Å Gaussian broadening.

Figure 3—
Substitutional doping with gallium in the body-centered cubic (bcc) plutonium matrix. The gallium atom takes the place of a very different plutonium atom, resulting in forces on its neighbors. In the case illustrated here, the Ga atom's position in a sixteen-atom cell constrains the symmetry such that the eight nearest neighbors can move toward it—or away from it. Preliminary calculations show the Ga atom pushes its neighboring plutonium atoms away.

New Pseudostructure for α -Pu

M. Johan Bouchet and Robert C. Albers,
T-11; rca@lanl.gov

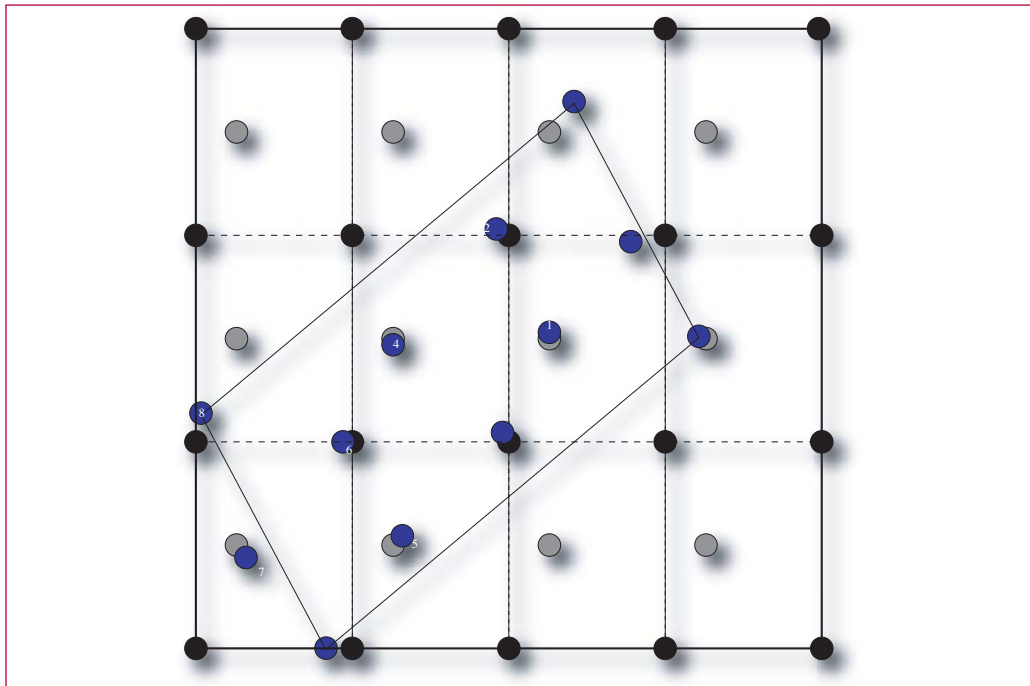
Pure plutonium (which also includes Pu with small amounts of other solute atoms) is an exotic metal that is poorly understood. The $5f$ electronic orbitals appear to be partially localizing in different ways in different crystal structures, leading to a large variation in the volumes of the different solid phases. The cause of this anomalous behavior is believed to be due to correlations between the $5f$ electrons as they try to avoid each other in each Pu atom. Theoretical approaches for understanding such effects are extremely difficult and involve very complex theories. Up until now, almost all of these approaches have been applied only to the δ -phase of Pu, which has a simple fcc crystal structure. These correlation effects are believed to be weaker in the α -phase. However, the α -structure is so complicated (16 atoms per unit cell), that it has been impractical to apply the

same approach to the α -phase.

We believe that we have now found a solution to this problem [1]. We have discovered a new pseudostructure for α -Pu that involves only two atoms per unit cell and is a relatively symmetrical orthorhombic crystal structure and can show that the real α crystal structure only involves small distortions of various atoms around this pseudostructure; the electronic-structure energy of both systems (at least at the band-structure level) is nearly identical. Sophisticated electronic-structure techniques should be just as easy for this pseudostructure as for δ Pu.

By a pseudostructure we mean a simpler crystal structure where the atoms are quite close to the positions of the more complex real structure. Pseudostructures are interesting for two reasons: (1) they provide insight into the geometrical structure of the atoms in the original structure and possible phase-transformation pathways, and (2) they provide an alternative less expensive crystal structure for complicated electronic and microstructural calculations. From

Figure 1—
Pseudostructure in the (011) direction. The blue atoms are the eight positions in the α -Pu structure.



Near-Neighbor Distances in Å (number of nn)			
	Pseudostructure	α	
1st nn shell	2.47(4)	2.46–2.55(4)	short bonds
2nd nn shell	3.31(4)		
3rd nn shell	3.49(4)	3.21–3.59(10)	long bonds
4th nn shell	3.50(2)		

Table —
Nearest-neighbour distances (in Å) for the pseudostructure and α -Pu (in parentheses are the number of atoms in each shell). These values are given for the theoretical equilibrium volume for each structure.

a physics point of view, one can view the pseudostructure as an approximation to the real structure that captures the dominant total energy of the electronic-structure (heat of formation) and local bonding effects; the real structure can then be viewed as just a minor distortion of the pseudostructure, with only a small energy difference between the two structures.

In Figure 1 we show a comparison of the atomic positions of α -Pu with our pseudostructure, and in the table a comparison of near-neighbor distances between the two structures.

[1] J. Bouchet, R. C. Albers, M. D. Jones, and G. Jomard, “New Pseudo-Phase Structure for α -Pu,” *Phys. Rev. Lett.*



Stable and Unstable Phonon Modes in and around bcc Plutonium

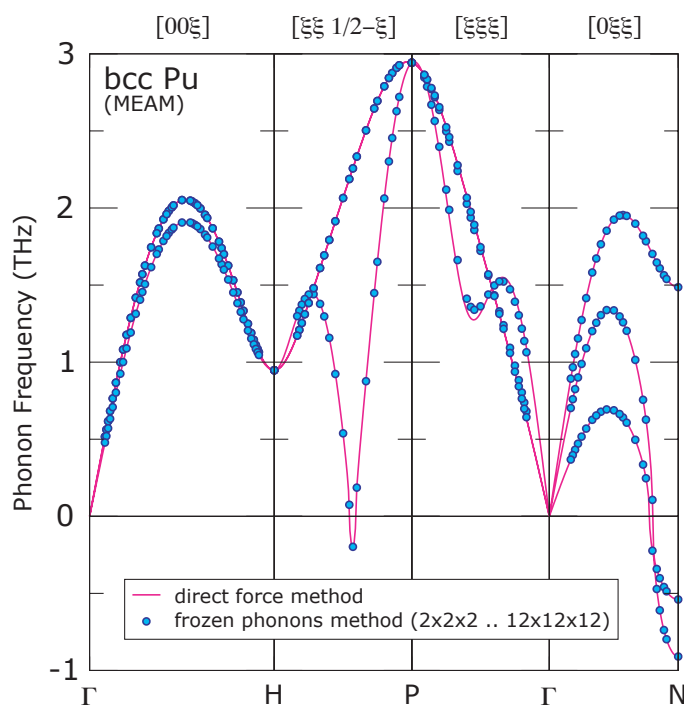
Sven P. Rudin, T-1; srudin@lanl.gov

Theoretical studies of the stability of a material's crystal structures often involve calculations of phonon frequencies, for two reasons: 1. the frequencies determine the vibrational contribution to the free energy, which can determine the energetically favored crystal structure among competing candidates; 2. any frequency calculated to be imaginary signifies an unstable phonon mode, indicating that the current crystal structure is mechanically unstable. The wave vector and polarization of the unstable phonon mode directly describe the distortion the crystal would follow to lower its energy. Reported here are distortions of the bcc phase of plutonium calculated in the modified embedded atom model (MEAM) [1], aimed at

generating a better understanding of the stability of this high-temperature phase. A popular method of calculating phonon frequencies is the frozen phonon method, most often used with first principles codes. The method is straightforward: the atoms in a simulation cell are distorted according to a phonon mode's wave vector and polarization, and the energy is calculated for several magnitudes of the amplitude, allowing direct determination of the frequency. The method requires that the simulation cell be commensurate with the wave vector and that the polarization is known, hence the method has only been used for wave vectors corresponding to high-symmetry points in the Brillouin zone.

Preliminary results from a *generalized* frozen phonon method are reported here. The method does *not* require knowledge of the polarization. Figure 1 shows the frequencies of phonon modes along high-symmetry directions of the

Figure 1— Phonon dispersion curves along high-symmetry directions of the bcc crystal for the MEAM of plutonium. The solid line is calculated using the direct force method; the circles are the values from frozen phonon calculations on regular meshes from 2^3 to 12^3 grid points. Imaginary frequencies are plotted as negative.



bcc crystal for the MEAM of plutonium. The results calculated with the generalized frozen phonon method agree with those obtained by the direct force method. The frequencies were calculated throughout the Brillouin zone on points sitting on $2 \times 2 \times 2$, $3 \times 3 \times 3$, and through $12 \times 12 \times 12$ meshes. Compared to what was previously possible, such mesh sizes are enormous.

In addition to not requiring knowledge of the polarization, the method easily allows an unstable phonon mode to be followed to the distorted crystal structure predicted to be lower in energy by the unstable mode. By proceeding stepwise from small to larger mesh sizes the possible distortions are systematically explored. Figure 2 shows that the magnitude of the imaginary frequency does *not* correlate with the resulting distorted structure's gain in energy over the original crystal.

Figure 3 shows the most favorable of the possible distorted structures, which lowers the energy of the crystal structure by 54 meV, stems from a transverse mode with wave vector $q = (2/7, 2/7, 5/7)$. Currently the phonons for the most probable distorted structures are being evaluated to investigate their stability.

[1] M. I. Baskes, *Physical Revue B* **62**, 15532 (2000).

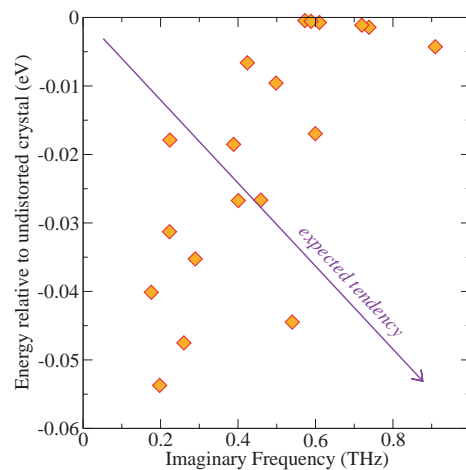


Figure 2— Energy of the distorted structures (relative to the bcc structure) plotted versus the value of the imaginary frequency. There is no systematic relationship between the two entities, i.e., the magnitude of the imaginary frequency does not determine the stability of the resulting structure.

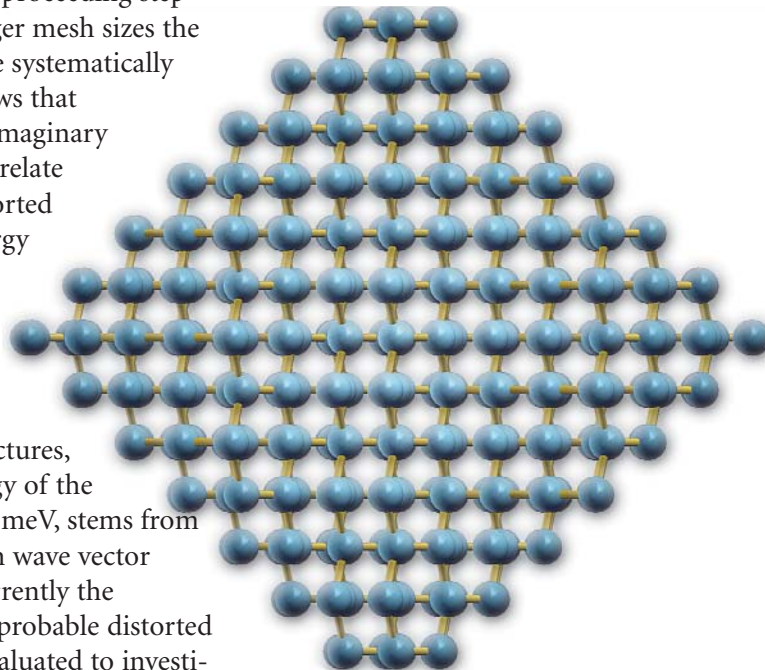


Figure 3— The most favorable of the possible distorted structures. This distortion appears on the $7 \times 7 \times 7$ mesh, i.e., in a simulation cell with 343 atoms.

Accelerated Dynamics Study of Vacancies in Pu

Blas P. Uberuaga and Arthur F. Voter, T-12; Steven M. Valone and Michael I. Baskes, MST-8; blas@lanl.gov

The importance of Pu as a material central to modern society can hardly be overstated. From its role in the nuclear weapons program to the dependence of fission reactors on Pu, it holds a prominent place in many important technologies. A complete understanding of the properties of this material is critical to being able to utilize it fully. Such an understanding begins at the atomic level, where point defects—vacancies and interstitials—dominate the behavior. Not only do these defects govern the self-diffusivity of Pu, but also the motion of impurities or dopants that might be present. The goal of this work is to study the properties of one of these defects (mono-vacancies) so that a deeper understanding of Pu can be gained.

Molecular dynamics (MD) simulation is an important tool for understanding materials at the atomic scale. Such simulations allow us to do what experiments cannot: focus on a small piece of material where we can follow the motion of individual atoms. In doing so, we can measure the properties of defects directly, providing input to higher levels of modeling. One limitation of MD, however, is that the time scales accessible—ns to μ s—are relatively short. To overcome this time scale problem, we employ accelerated dynamics techniques, developed here at Los Alamos, in particular parallel-replica dynamics [1] and temperature accelerated dynamics (TAD) [2]. Both of these methods allow us to reach longer time scales than conventional MD.

Parallel-replica dynamics involves a straight forward parallelization of time. Each processor evolves an independent replica of the entire system until a transition to a new state is detected on any of the processors. If the rare events that govern motion from state to state in the material are first order processes, then parallel-replica dynamics is exact, even correctly describing correlated events. By parallelizing on M processors, one can reach a maximum speedup compared to a single processor run of M times. Reaching this maximum efficiency depends on how infrequent the events are, as there is some overhead involved each time an event is observed.

TAD is potentially much more powerful, but involves more assumptions about the nature of the system. In particular, if the system obeys harmonic transition state theory, TAD gives nearly exact state-to-state dynamics. The algorithm involves running MD at a high temperature, T_{high} , higher than that of interest, T_{low} . The behavior at T_{high} is then extrapolated to T_{low} and an event is accepted based on this extrapolation. Using this algorithm, experimental time scales are achievable for some systems [3].

In the following work, we use the modified embedded atom method (MEAM) [4] to describe the Pu-Pu interaction. To simplify the analysis somewhat, and to simulate the stabilizing effects of Ga-doped Pu, we have used both the parameters published in [5], as well as a modified parameter set in which $t_3 = 0$. This change in t_3 corresponds to removing a sensitivity to inversion symmetry in the crystal structure and results in the stabilization of the δ -phase of Pu, relative to the other phases, much as Ga does in real Pu. In what follows, these two parameterizations will be referred to as Pu^{sym} and Pu^{no-sym}, where Pu^{no-sym} has $t_3 = 0$. Parallel-replica dynamics has been used

to study the motion of a mono-vacancy in Pu^{sym} at 900 K. Running the simulation on 38 processors, we achieved a speedup of 36 times. This simulation, taking 1 week of wall-clock time, would have taken 36 weeks on a single processor.

The δ -phase of Pu^{sym} is characterized by tetragonal distortions of the lattice in which the Pu atoms become paired to one another. The distorted structure is more stable than the perfect δ -phase structure.

At 900 K, mono-vacancy hops are relatively rare; in simulations of Pu^{sym} for a total of 3 μ s, we saw only 12 hops. Eight of these hops were simple moves, in which one Pu atom adjacent to the vacancy moves directly into the vacancy site, resulting in the mono-vacancy moving one nearest-neighbor distance. The energy profile of the minimum energy path for such an event has been calculated with the nudged elastic band (NEB) method [6], giving a barrier for the single hop of about 1.11 eV.

Surprisingly, we also saw four events in which the mono-vacancy executes a double hop. Two Pu atoms move in a concerted motion such that the mono-vacancy moves two lattice spacings during one event. Again using NEB, we find a barrier of 1.04 eV for this process.

We have performed TAD simulations for a mono-vacancy in Pu^{no-sym}. Pu^{no-sym} is more amenable to TAD than Pu^{sym} since there are fewer local minima; the global tetragonal distortions in Pu^{sym} are not present in Pu^{no-sym}. In simulations of about 0.43 μ s at T_{low} = 1000 K (using T_{high} = 2000 K), we again saw both single and double hops. (The TAD simulations resulted

in less total time than the parallel-replica simulations, but only required one processor.) The barriers for these are 1.55 and 2.18 eV, respectively.

We have estimated the rates for both of these processes for both parameterizations of Pu by finding the average rate for each at the simulation temperatures (for the parallel-replica simulations, 900 K, and for the TAD simulations, 2000 K). Assuming that the rate is Arrhenius up to these temperatures, we find

$$k_{\text{single hop, sym}} = 3.2 \times 10^{11} e^{-1.11 \text{ eV}/k_B T} / \text{s}$$

$$k_{\text{double hop, sym}} = 8.5 \times 10^{10} e^{-1.04 \text{ eV}/k_B T} / \text{s}$$

for Pu^{sym} and

$$k_{\text{single hop, no-sym}} = 3.4 \times 10^{12} e^{-1.55 \text{ eV}/k_B T} / \text{s}$$

$$k_{\text{double hop, no-sym}}$$

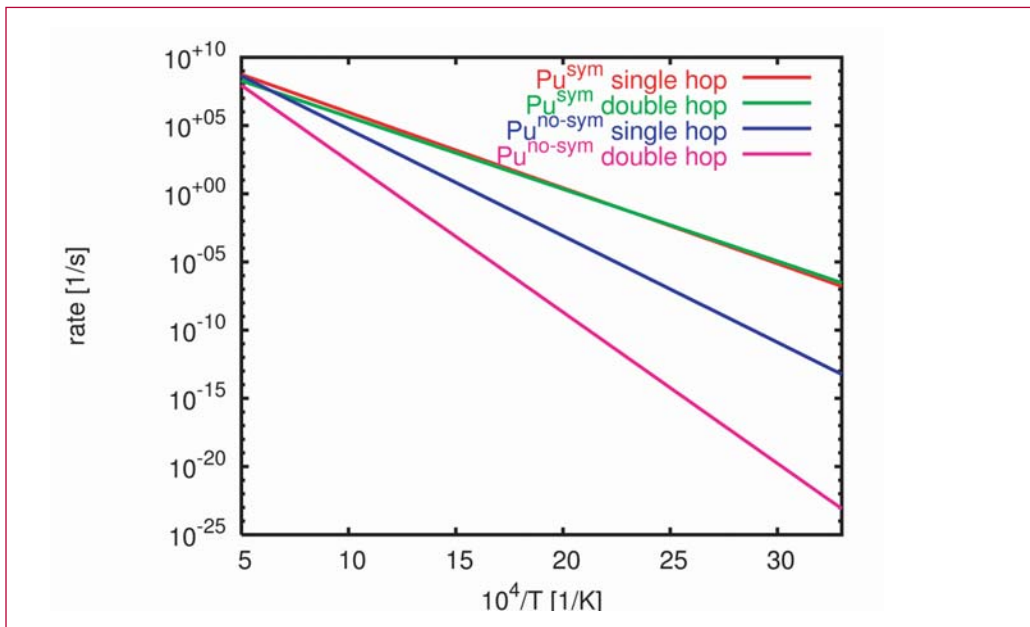
$$= 3.1 \times 10^{13} e^{-2.18 \text{ eV}/k_B T} / \text{s} \text{ for Pu}^{\text{no-sym}}.$$

These rates are summarized in the figure.

Both of the rates for Pu^{sym} are characterized by relatively low prefactors. The low prefactor is likely the consequence of the distorted ground state of the δ -Pu crystal. As mentioned above, in the distorted ground state structure, each atom is paired to one other atom and so, at any given time, the mono-vacancy only has one place to jump. Of course, the rearrangement of the distorted structure means that, over time, each of the twelve neighboring sites will become accessible to the mono-vacancy, but only one is available at any given time. This results in the lower prefactors.

The rates for both the single hop and the double hop in Pu^{sym} are very similar to one another. Because each double hop

Figure—
Arrhenius plot
of the rates
for the four
mechanisms
discussed
in the text.



results in the mono-vacancy moving twice as far as for a single hop, the contribution to the diffusion constant is four times greater. That means that any model that includes a description of mono-vacancy migration must take into account both single and double hops, as both are important.

In $\text{Pu}^{\text{no-sym}}$, there is a greater separation of rates between the single and double hops. For all temperatures, the single hop dominates. In addition, the rates of both mechanisms are significantly lower for $\text{Pu}^{\text{no-sym}}$ than for Pu^{sym} for a very large temperature range. The stabilizing effect of removing inversion symmetry (setting $t_3 = 0$) results in a reduction of the mono-vacancy hop rate.

To summarize, we are applying accelerated dynamics methods to the δ -Pu system in an effort to understand the behavior of mono-vacancies. Using parallel-replica dynamics, we have identified two different mono-vacancy diffusing events—a single hop and a double hop mechanism—in the original MEAM parameterization for Pu. We find that the rates for both processes are nearly identical for a large temperature

range with the double hop mechanism dominating the contribution to mass transport. Temperature accelerated dynamics was applied to a modified parameter set that stabilizes the δ -phase. Again, we see both types of hops, but single hops clearly dominate the behavior for this parameterization. Mono-vacancy diffusion occurs much more quickly in “pure” Pu (Pu^{sym}) than in the “Ga-stabilized” version ($\text{Pu}^{\text{no-sym}}$).

- [1] A. F. Voter, *Phys. Rev. B* **57**, R13985 (1998).
- [2] M. R. Sørensen and A. F. Voter, *J. Chem. Phys.* **112**, 9599 (2000).
- [3] J. A. Sprague, F. Montalenti, B. P. Uberuaga, J. D. Kress, and A. F. Voter, *Phys. Rev. B* **66**, 205415 (2002).
- [4] M. I. Baskes, J. S. Nelson, and A. F. Wright, *Phys. Rev. B* **40**, 6085 (1989); M. I. Baskes, *Phys. Rev. B* **46**, 2727 (1992).
- [5] M. I. Baskes, *Phys. Rev. B* **62**, 15532 (2000).
- [6] G. Henkelman, B. P. Uberuaga, and H. Jónsson, *J. Chem. Phys.* **113**, 9901 (2000); G. Henkelman and H. Jónsson, *J. Chem. Phys.* **113**, 9978 (2000).



The Promise of Liquid Dynamics Theory

Giulia De Lorenzi-Venneri and Duane C. Wallace, T-1, gvenneri@lanl.gov

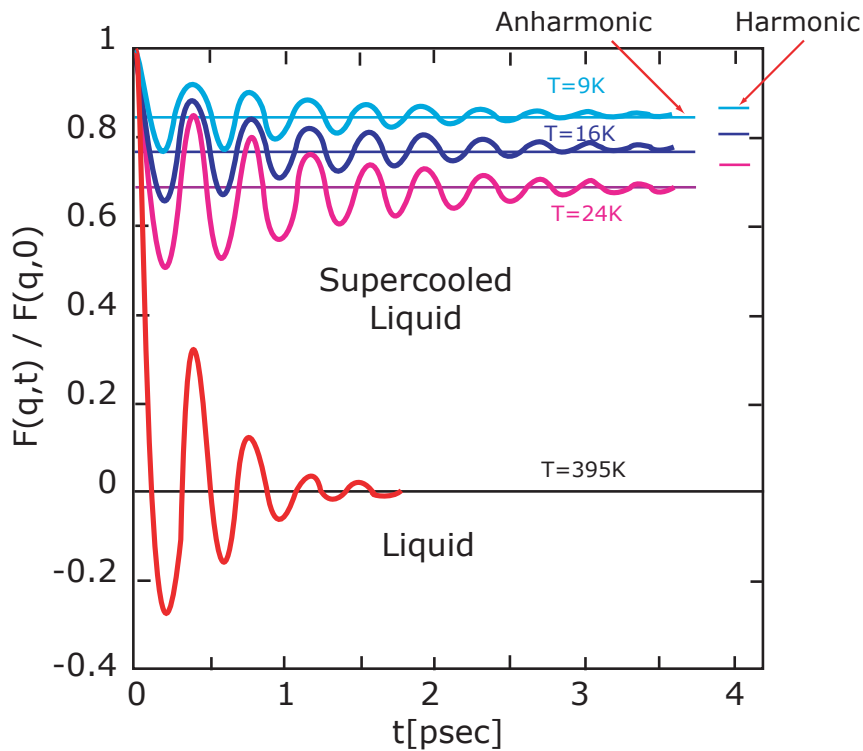
An accurate description of the atomic motional dynamics is of paramount importance in the theoretical physics of matter. This description was given to us by Boltzmann for gases, starting around 1872, and by Born and colleagues for crystals in 1912. Based on these early works, the physics community has achieved quantitative understanding of a vast range of equilibrium and nonequilibrium properties of gases and crystals, and this understanding has spawned many practical applications. As one small example, it is now possible to carry out an a priori calculation of the equation of state of a monatomic crystal at normal density, or compressed by a factor of 10, or 1000, and know that we will get the right answer.

An accurate description of the atomic dynamics of a liquid has been given only in the last few years [1], and that for the simplest case of a monatomic liquid. In this system, each atom is in continuous interaction with a dozen or so neighbors, like a crystal but not like a gas, while the atoms undergo massive diffusive motion, like a gas but not like a crystal. The corresponding atomic motion consists of two parts, nearly harmonic vibrations in one of many identical many-body potential energy valleys, and nearly instantaneous transits of small groups of atoms that carry the system from one such valley to another. The liquid dynamics Hamiltonian is tractable in leading order, and exhibits small details that

present theoretical challenges. As these challenges are solved, just as with gases and crystals, we shall achieve quantitative understanding of a wide range of liquid equilibrium and nonequilibrium properties, from equation of state to viscosity.

An example of how Liquid Dynamics Theory can explain a result otherwise unexpected, is the case of the intermediate scattering function $F(q,t)$, the Fourier transform of the inelastic neutron scattering cross section $S(q,\omega)$. Molecular dynamics calculations are shown in the figure for two cases: (a) at three temperatures below the glass transition, where the system is trapped within a single random valley, and (b) in the liquid at T just above melting. The curves are characterized by oscillations at short time, which are the source of the Brillouin peak in $S(q,\omega)$, and by long time decay to a constant value. The oscillations have approximately the same frequency in the glass and in the liquid, showing that the Brillouin peak is at the same frequency in the glass and the liquid. This confirms a prediction of liquid dynamics theory. Another prediction of liquid dynamics theory is that the long time value of $F(q,t)$ for the glass is a positive constant. This is something of a surprise, and apparently has not previously been noticed, especially since the long time constant is zero for both the liquid and crystal state. When the long time constant is calculated from liquid dynamics in the harmonic approximation, the results are close to the MD calculations, and when anharmonicity is included, the theoretical results are in excellent agreement with MD, as one can see from the figure.

Liquid Dynamics Theory
Predictions for the long-time asymptote



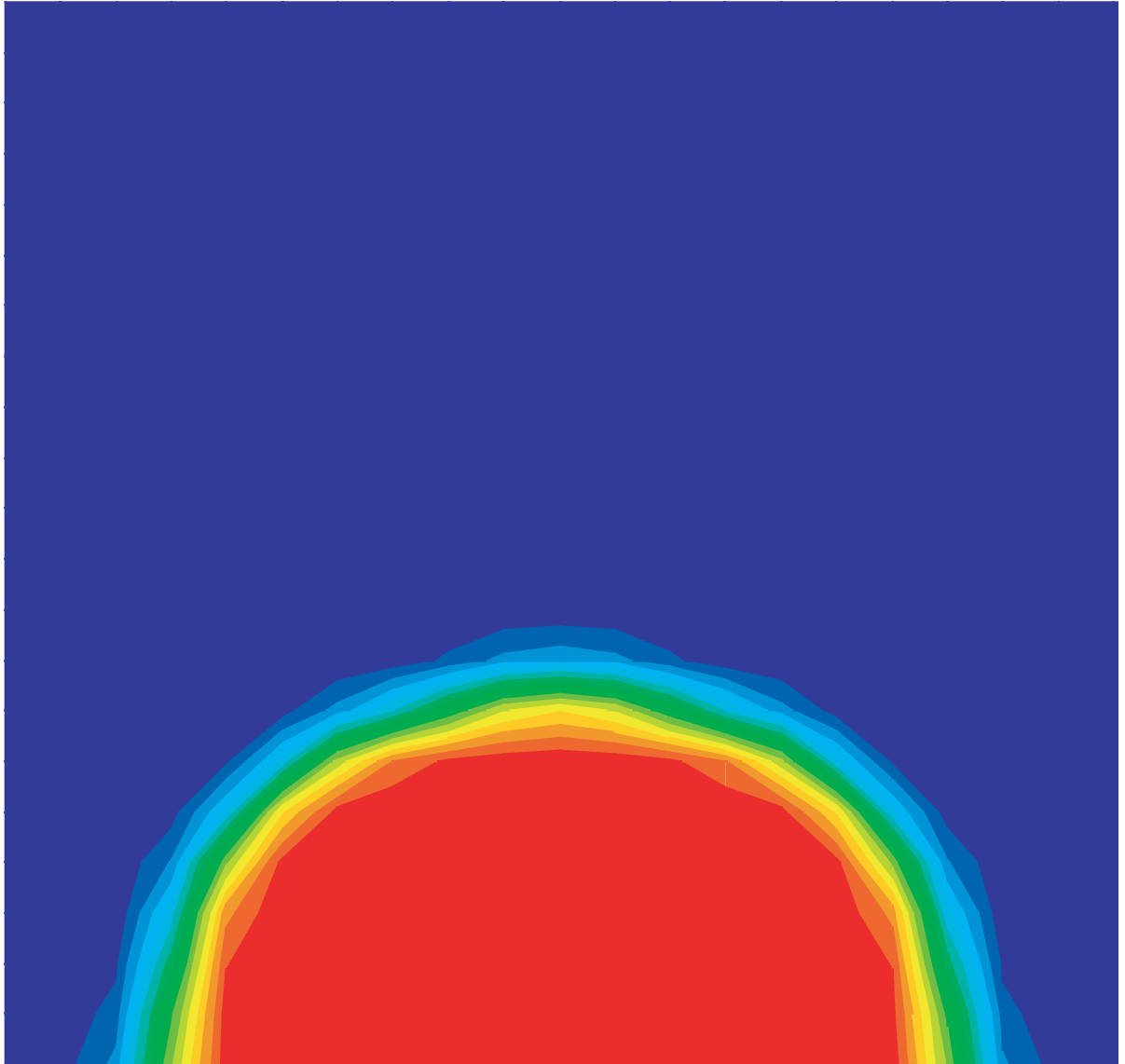
Figure—
Intermediate
Scattering Function
 $F(q,t)$ for $q=0.29711$
 a_0^{-1} , on a system of
500 particles of Na.
The functions
evaluated from
Molecular Dynamics
at four different
temperatures are
shown, together
with the predictions
for the long-time
asymptotes from
Liquid Dynamics
Theory.

This is accomplished by doing the LD calculation in the average configuration, instead of the random configuration: one effect of anharmonicity is in fact to shift the average positions away from the bottom of the valley.

[1] Duane Wallace, *Physical Review E* **56**, 4179 (1997).

29

Detonation and Shock



β -HMX Isotherms at Multiple Temperatures and Liquid HMX Equation of State

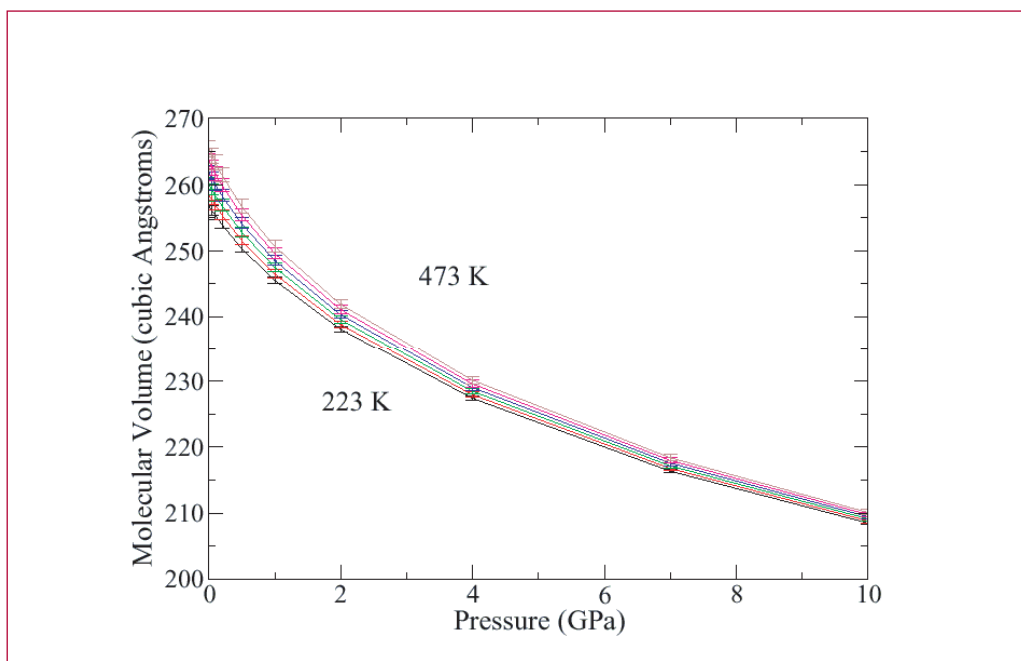
Eugenio Jaramillo and Thomas D. Sewell,
T-14; sewell@lanl.gov

In previous editions of this annual compilation we reported calculations of numerous thermophysical and elastic mechanical properties and liquid state transport coefficients of the high explosive HMX. The motivation for the work [1], which is based on classical molecular dynamics and Monte Carlo methods using an analytic force field, is to provide information needed as input to equation-of-state models for use in mesoscale simulations. (These simulations, in which the grains and binder in a plastic-bonded explosive or propellant formulation are resolved within a continuum hydrodynamic framework, are used to improve our understanding of the initiation mechanisms for such materials under various dynamic loading scenarios.) Ultimately, we hope to provide an internally consistent “model mechanics and thermodynamics” for HMX.

In last year’s report, we described calculations of the elastic tensors and isotherms for β -, α -, and δ -HMX at room temperature; that work now appears in final form in the *Journal of Chemical Physics* [2]. We also reported the development of a quantum chemistry-based force field for Estane, which is the poly(ester urethane) copolymer used in the binder formulations for the HMX-based explosives PBX-9501 and LX-14; that work has been published in the *Journal of Physical Chemistry, Part A* [3], and should enable future simulations of the HMX/binder interface. (In connection with ongoing work on force field development for the nitroplasticizer in PBX-9501 binder, we anticipate detailed studies of all essentially all major chemical interactions in PBX-9501.)

In the past year we computed six additional isotherms for β -HMX crystal, in direct response to requests from the mesoscale modeling community. In particular, we calculated isotherms at 223, 273, 323, 373, 423, and 473 K, for pressures between 0 and 10 GPa. These are shown in Figure 1. (Note that 473 K is above the nominal β - δ phase transi-

Figure 1— β -HMX crystal isotherms.



tion temperature at zero pressure, but that the β -HMX crystals are metastable at this temperature on the several nanosecond time scale of our simulations.) Our expectation is that these isotherms will be published in tandem with experimental isotherms measured by personnel from the Naval Surface Warfare Center (Indian Head) [4].

We have also undertaken simulations to predict the P-V-T equation of state of liquid HMX and calculations of the bulk modulus along multiple isotherms. Preliminary predictions of the bulk modulus at selected pressures and temperatures are shown in Figure 2.

The question arises naturally in simulations of liquid properties at elevated pressures as to the length of physical time required to adequately sample the liquid. We show one aspect of this in Figure 3, namely the autocorrelation time for molecular rotation in HMX as a function of pressure at $T = 800$ K. This temperature is close to the atmospheric pressure boiling point of HMX. For pressures of 1 GPa and below, molecular tumbling occurs on a sub-nanosecond time scale. For higher pressures, the time scale become much longer and indeed, for pressures above 4 GPa, it appears that rotational relaxation times will quickly increase to hundreds of nanoseconds or even longer.

[1] R. Menikoff and T. D. Sewell, "Constituent properties of HMX needed for mesoscale simulations," *Combustion Theory and Modelling* **6**, 103 (2002).

[2] T. D. Sewell, R. Menikoff, D. Bedrov, and G. D. Smith, "A molecular dynamics simulation study of elastic properties of HMX," *Journal of Chemical Physics* **119**, 7417 (2003).

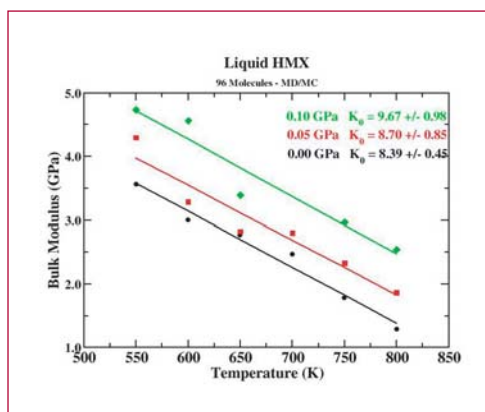


Figure 2— Preliminary predictions of temperature dependent bulk modulus of HMX liquid at three pressures.

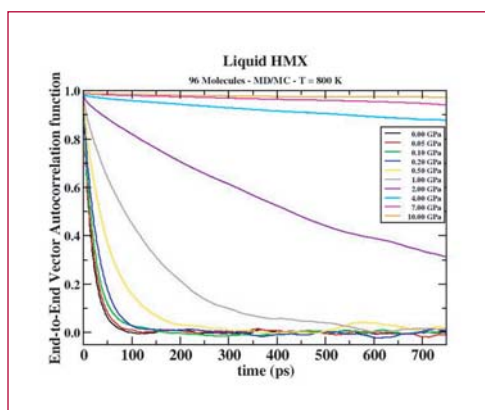


Figure 3— Time scales for molecular rotation in HMX liquid at 800 K, for ten pressures between 0 and 10 GPa. See text for details.

[3] G. D. Smith, D. Bedrov, O. Byutner, O. Borodin, C. Ayyagari, and T. D. Sewell, "A quantum-chemistry-based potential for a poly(ester urethane)," *Journal of Physical Chemistry A* **107**, 7552 (2003).

[4] S. M. Pereis and T. D. Sewell, in preparation.



Molecular Dynamics Studies of Reactive Processes in RDX II: Shock Loading

Alejandro H. Strachan, T-14;
strachan@lanl.gov

Understanding the initial chemical events in condensed-phase high-energy materials under shock loading is among the central problems in detonation theory. The coupling between the fast loading, induced mechanical response and complex chemistry makes the study of such process very challenging and there has been little progress in establishing a molecular level understanding. Recent advances in atomistic modeling techniques and the enormous increase in computer power enabled, over the last years, the atomistic simulation of thermal- and shock-induced chemistry in condensed-phase high-energy materials such as RDX and HMX. Both Quantum Mechanics-based Molecular Dynamics (MD) simulations of HMX at conditions of pressure and temperature close to the CJ point [1] as well as our nonequilibrium MD simulations of shocks on RDX using the reactive force field ReaxFF [2] show that the initial chemical events occur at very short time-scales (pico-seconds). Both these two types of simulations focused on perfect crystals while most real energetic materials are heterogeneous and

defective (polycrystalline, porous, plastic bonded, etc.). Such defects are believed to facilitate detonation initiation under shock loading. We report here on the simulation of shock propagation on defective RDX crystals and the influence of such defects on the initial chemical events using the reactive force field ReaxFF [3] with nonequilibrium molecular dynamics.

MD Shock Simulations

We simulate the impact between two two-dimensionally periodic slabs, one of which contains a gap, Figure 1 (a), of length l_{gap} . We impose free boundary conditions in the direction of the shock and periodic boundary conditions in the other two directions. The gap simulates the center of an ellipsoidal void with two long axes perpendicular to the shock direction [4]. After thermalization, we assigned the desired relative velocity (v_{imp}) to each slab on top of thermal velocities and followed the dynamics with constant energy MD. This arrangement leads to a particle velocity $v_p = 1/2 v_{imp}$. Figure 1 shows snapshots of the process at different times for $v_p = 3 \text{ km/s}$ and $l_{gap} = 20 \text{ \AA}$: we can see the initial shock propagation in perfect crystals ($t = 0.5 \text{ ps}$), the molecules ejected from the upstream surface of the gap expanding into the void ($t = 0.95 \text{ ps}$), and the ejected material colliding against the remainder of the slab and recompressing ($t \geq 1.5 \text{ ps}$). We will focus on $v_p = 3 \text{ km/s}$ since for perfect

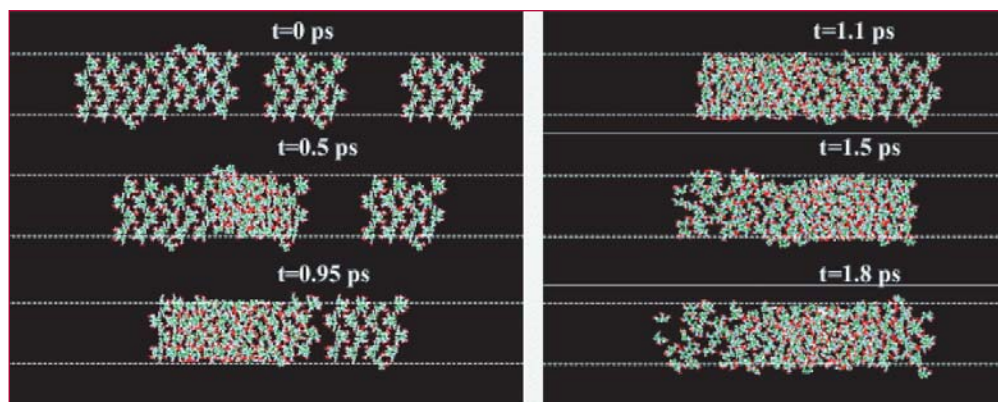


Figure 1—
Snapshots from
ReaxFF MD shock
simulation at
different times for
 $v_p = 3 \text{ km/s}$ and
gap width 20 \AA .

crystals it separates two different regimes: for shocks with $v_p > 3 \text{ km/s}$ a variety of small molecules are formed while for lower velocities only small fractions of NO_2 are observed [2].

When a strong shock reaches the upstream surface of the gap, molecules are ejected into the void; the ejecta expands and re-compresses when it collides with the remainder of the slab. This recompression can lead to significant local heating [4]. In order to quantify this effect and its dependence on gap width we plot, in Figure 2, the time evolution of the local temperature of the last two molecular monolayers on the upstream half of the defective slab for $l_{\text{gap}} = 5 \text{ \AA}$ (red), $l_{\text{gap}} = 10 \text{ \AA}$ (blue), and $l_{\text{gap}} = 20 \text{ \AA}$ (green). We also show time evolution of the local temperature of the corresponding region in the perfect (left) slab; the temperatures of the regions in the perfect slab are independent of the gap width and are displayed as black lines. We can see that the initial heating of the regions by the gap is similar to that of the ones in the perfect slab but they reach a lower temperature (independent of gap width) because some of the shock energy is used to accelerate them into the void. When the ejected (expanding) molecules collapse with the downstream part of the right slab (at a time that depends on void width) they re-compress and heat up to a temperature much higher than that attained in the perfect slab. Holian and collaborators proposed a model to explain this overheating based on the recompression of the evaporated ejecta and validated it with large-scale two dimensional MD simulations [4]. In agreement with their model we find that the over-heating increases with gap width and it can reach 1000 K even for a small gap (2 nm) for $v_p = 3 \text{ km/s}$.

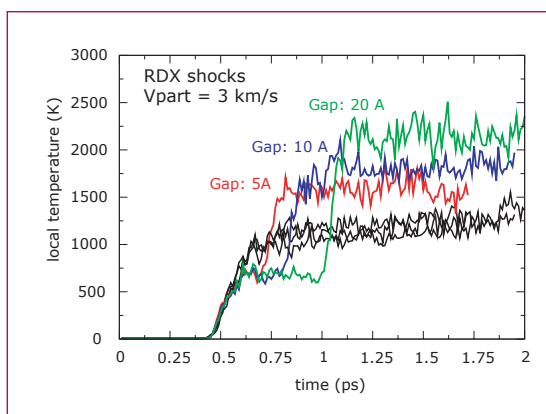


Figure 2— Time evolution of local temperature of the last two molecular monolayers of the upstream half of the defective slab for $l_{\text{gap}} = 5 \text{ \AA}$ (red), $l_{\text{gap}} = 10 \text{ \AA}$ (blue), and $l_{\text{gap}} = 20 \text{ \AA}$ (green). We also show that time evolution of the local temperature of the corresponding (mirror) region in the perfect slab (black).

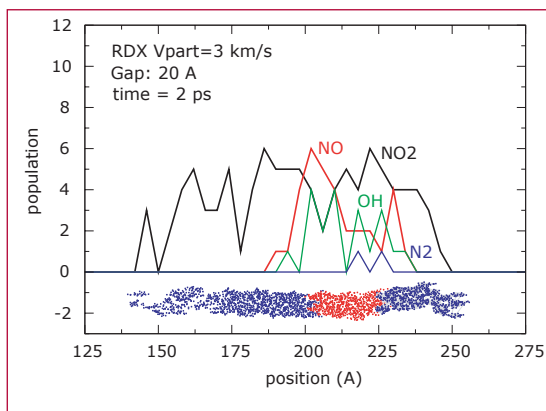


Figure 3— Profile of the population of several species for $t = 2 \text{ ps}$. RDX shock $v_p = 3 \text{ km/s}$, gap width 20 \AA .

Once we have quantified the local heating due to void-shock interaction the main question is: is the over-heating achieved with these void widths enough to significantly facilitate the chemistry? Figure 3 shows the profiles (along the shock propagation direction) of the population of four small molecules [NO_2 (black), NO (red), OH (green) and N_2 (blue)] at time $t = 2 \text{ ps}$. Blue and red circles below the profiles show the atomic positions at $t = 2 \text{ ps}$ differentiating the atoms belonging to the perfect slab and to both portions of the defective slab. It is clear from Figure 3 that the profiles are very asymmetric with a larger quantity of products formed in the defective crystal. The quantities of NO and OH produced on the defective half are comparable to those obtained in perfect crystals for stronger shocks.

Conclusions

First Principles-based atomistic modeling of shock loading of high-energy nitramines have become feasible due to the development of the reactive force field ReaxFF. ReaxFF with MD allows full-physics, full-chemistry simulations of shock waves propagating in perfect and defective HE crystals and the chemical reactions they induced. It is important to stress that no approximation is made as to what type of chemical reactions are allowed or what type of molecules can be formed.

We found that even small gaps (few nanometers) can lead to a local increase in temperature of over 1000 K on top of the shock heating. This heating enhances and facilitates the initial chemical reactions. Much larger simulations will be necessary to establish if this enhancement is enough to generate a self-sustained detonation and consequently increase the sensitivity of the material or if instead it will die out. Future work will focus on quantifying the decrease in detonation threshold as a function of void size.

[1] M. R. Manaa, L. E. Fried, C. F. Melius, M. Elstner, and T. Frauenheim, *J. Phys. Chem. A*, 9024 (2002).

[2] A. C. Stachan, T. van Duin, D. Chakraborty, S. Dasgupta, and W. A. Goddard III, *Phys. Rev. Lett.* **91**, 098301 (2003).

[3] C. T. van Duin, S. Dasgupta, F. Lorant, and W. A. Goddard III, *J. Phys. Chem. A* **105**, 9396 (2001).

[4] L. Holian, T. C. Germann, J. B. Maillet, and C. T. White, *Phys. Rev. Lett.* **89**, 285501 (2002).



Molecular Dynamics Studies of Reactive Processes in RDX I: Thermal Loading

Alejandro H. Strachan, T-14;
strachan@lanl.gov

A molecular level understanding of condensed-matter chemistry is among the central issues facing the energetic materials community. Recent breakthroughs in atomistic modeling (such as reactive interatomic potentials) enable the use of molecular dynamics (MD) to study chemistry in solid energetic materials providing unprecedented spatiotemporal resolution [1,2]. We report here the use of the reactive force field ReaxFF [2,3] to study thermal decomposition of the cyclic nitramine RDX.

Molecular Dynamics with ReaxFF

We study the decomposition of RDX at various temperatures between $T = 1200$ K and $T = 3000$ K at three densities: at normal density (volume $V = V_0$), under compression ($V = 0.8 V_0$), and at low density ($V = 8 V_0$) using the reactive potential ReaxFF with MD. We start with RDX perfect crystals using simulation cells containing eight RDX molecules (one unit cell) and 3-D periodic conditions. After relaxing the atomic positions at each density, we study the time evolution of the system at the desired temperature with isothermal isochoric (NVT ensemble) MD simulations (using a Berendsen thermostat). We then follow the decomposition of the RDX molecules using a molecule recognition method that uses not only atomic positions but also velocities to determine whether two atoms are bonded or not [2]. The lower temperatures reported here required very long times (for MD standards) of several nano-seconds (one nano-second requires 10 million steps of reactive MD).

Thermal Decomposition of RDX from MD Simulations

Figure 1 shows the time evolution of the potential energy of the RDX unit cell for temperatures $T = 1200, 1500, 2000, 2500,$ and 3000 K for normal density (V_0). Our simulations at $V = 0.8 V_0$ show faster time-scales and those at $8 V_0$ a slower rate of reactions. The time evolution of the potential energy can be described reasonably well with an exponential function:

$$U(t; T, \rho) = U_0(T, \rho) - \Delta U(T, \rho) \exp[-t/\tau(T, \rho)],$$

where U_0 is the energy of the products, ΔU is the exothermicity and τ is the characteristic time; all three parameters are temperature and density dependent.

Figure 1—
Time evolution of potential energy for various temperature and $V = V_0$ (ambient pressure volume).

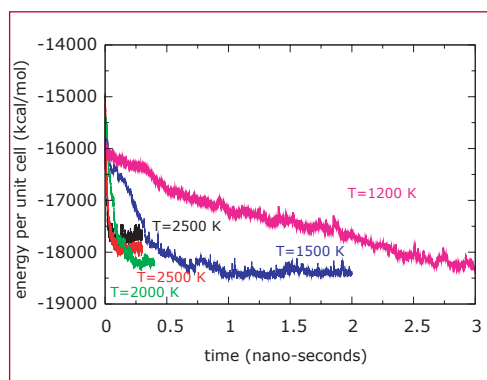
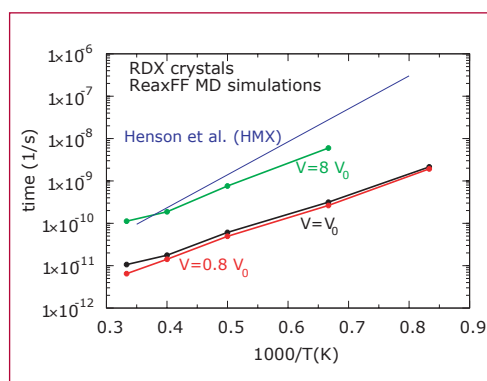


Figure 2—
Characteristic time vs. inverse temperature from ReaxFF MD simulations for different volumes: $V = 0.8 V_0$ (red line), $V = V_0$ (black line), and $V = 8 V_0$ (green line). We also include the Arrhenius behavior obtained from a wide range of experimental ignition times in HMX (blue line) [4].



In Figure 2, we plot the characteristic times (in logarithmic scale) as a function of inverse temperature (Arrhenius plot). The red line corresponds to MD results under compression ($V = 0.8 V_0$), the black line corresponds to $V = V_0$ and the

green one represents the theoretical results at $8V_0$. The blue line represents the behavior of HMX obtained from a wide variety of experimental ignition times [4]. Figure 2 shows that our first principles calculations are in reasonable quantitative agreement with experiments. The linear behavior of the MD and experimental data in the Arrhenius plot can be attributed to a single rate limiting step in the sequence of reactions that lead to decomposition. From the MD simulations we obtain an activation energy (E_a) for this limiting step that increases as the density decreases: for $V = 0.8V_0$ and $V = V_0$ we obtain $E_a \sim 23$ kcal/mol and for $V = 8V_0$ $E_a = 35.6$ kcal/mol.

Figure 3 shows the final populations of the key products (N_2 , H_2O , CO , and CO_2). We can see that at low densities, CO is preferred over CO_2 , while at high densities this relationship changes and we find almost no CO and considerable amounts of CO_2 .

In Figure 4, we show the time evolution of the population of N_2 , H_2O , CO , and CO_2 ; the time is scaled with the corresponding characteristic time obtained from the energy evolution. For each condition of temperature and density time-scales of H_2O and N_2 formations are similar to one another and to the overall characteristic time (τ); formations of H_2O and N_2 occur at the early stages of the process. The formation of CO and CO_2 shows a marked dependence on compression: while at normal or high density we find there is an induction before CO and CO_2 form (see top panel of Figure 4); at low density, CO forms promptly and with time scales similar to those of H_2O and N_2 (see bottom panel of Figure 4).

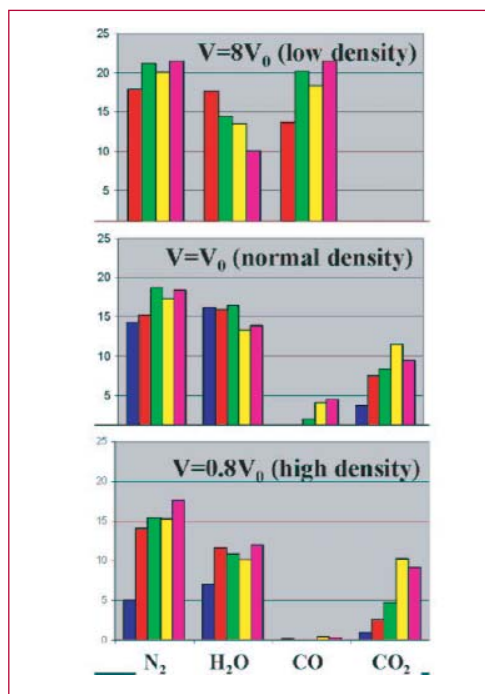


Figure 3— Final population of key molecules for various temperatures and densities. $T = 3000$ K (magenta), $T = 2500$ K (yellow), $T = 2000$ K (green), $T = 1500$ K (red), $T = 1200$ K (blue). (The simulation corresponding to $0.8V_0$ and $T = 1200$ K has not fully converged; data are preliminary.)

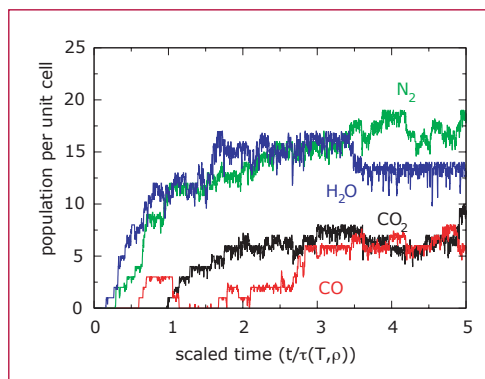
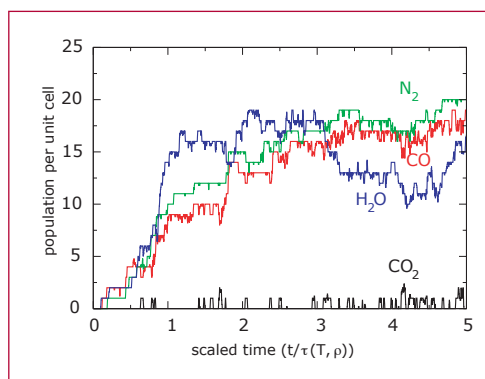


Figure 4— Time evolution of main products for $T = 2500$ K and $V = V_0$ (top panel) and $V = 8V_0$ (bottom panel). For each temperature and density, time is scaled with the corresponding characteristic time obtained from the energy evolution. The first-principles time-scales obtained from MD for the decomposition of RDX under thermal load are in reasonable quantitative agreement with experimental data.



Conclusions

Atomistic modeling with new-generation reactive potentials is becoming a very important tool to investigate condensed-phase chemistry under dynamical or static loading. Such simulations provide very detailed information regarding the decomposition and subsequent reactions in energetic materials that should allow sense to be made out of the very complex mechanical and chemical processes.

- [1] M. R. Manaa, L. E. Fried, C. F. Melius, M. Elstner, and Th. Frauenheim, *J. Phys. Chem. A* **106**, 9024, (2002).
- [2] A. Strachan, A. C. T. van Duin, D. Chakraborty, S. Dasgupta, and W. A. Goddard, III, *Phys. Rev. Lett.* **91**, 098301, (2003).
- [3] A. C. T. van Duin, S. Dasgupta, F. Lorant and W. A. Goddard III, *J. Phys. Chem. A* **105**, 9396 (2001).
- [4] B. F. Henson, L. Smilowitz, B. W. Asay, P. M. Dickson, and P. M. Howe Proceedings of the 12th Symposium (International) on Detonation (2002), <http://www.sainc.com/det-symp/technicalProgram.htm>

Fundamental Detonation Behavior from Molecular Dynamics Simulations

*Andrew J. Heim, T-14/UC-Davis;
Timothy C. Germann, X-7; Brad Lee
Holian and Edward M. Kober, T-14;
and Niels G. Jensen, UC-Davis;
aheim@lanl.gov*

While most aspects of detonation behavior of plastic-bonded explosives (PBXs) are well-understood and modeled at an empirical level, there are essentially no aspects of their behavior that can be predicted quantitatively from basic physical models. Examples include changes due to large temperature variations, curvature effects, changes in manufacturing processes, and aging phenomena. Improving our predictive capabilities in this regard is one of the primary goals of the ASC Materials and Physics Program.

To establish this predictive capability, we are using classical molecular dynamics (MD) simulations to investigate the relationship between molecular properties and the detonation response. Advances in computational resources and algorithms now make it possible to perform atomistic simulations on quite large systems. In particular, using the SPaSM parallel MD code and computer clusters available at LANL, simulations containing billions of atoms can be performed that correspond to absolute physical dimensions on the order of microns. While there are important phenomena that cannot be captured at this length scale, it has been shown that many basic detonation features can be. These include homogeneous and heterogeneous initiation, steady-state detonation propagation, failure diameter, curvature effects, and void collapse physics. Because all of the physical properties of

the system are defined by the atomistic potentials, one can then determine the fundamental relationships that control the detonation properties.

As one example of this, we are studying the detonation properties of a simple model diatomic molecule (AB) utilizing the REBO (reactive empirical bond-order) model. This system reacts exothermically by the reaction $2AB \rightarrow A_2 + B_2 + 2Q$, where Q is the amount of energy released in the reaction. A snapshot of a steady-state propagating detonation is shown in Figure 1. The complete simulation is much larger ($\sim 100,000$ atoms) to ensure that the propagation is indeed steady-state and to capture the expansion and equilibration of the gaseous products. An important point here is that the propagation properties are controlled by the equations of state (EOS) of the reactants and “products,” where the definition of “products” is the state of the reaction at the end of the very narrow compressed reaction zone associated with the shock wave. In this system, the reaction zone is ~ 2 lattice spacings long. It can be seen that the reaction does not proceed completely to products (even at the far left end of the figure), and the extent of the reaction is certainly not complete at the end of reaction zone.

To deconvolve this further, the relationship between microscopic properties that can be explicitly defined and the macroscopic response are determined. For this system, the dominant parameters are the initial A-B bond strength, the exothermicity (Q) of the reaction (determined by the differences in bond strengths), and the intermolecular interaction energy (ϵ). By decreasing either the A-B bond strength or the exothermicity of the reaction, the detonation velocity is decreased in a smooth monotonic fashion until a critical point is reached where the detonation is no

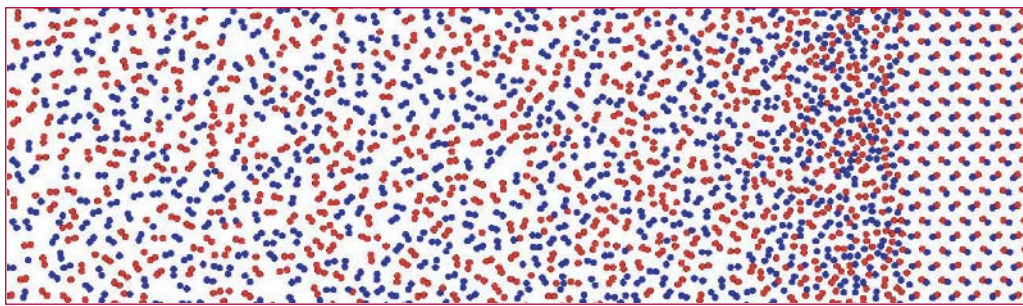


Figure 1— shows a snapshot from a propagating detonation in a model AB diatomic system. The A atoms are red, and B atoms are blue. The crystalline undisturbed reactants are at the far right, with the detonation/shock wave progressing to the right. The highly compressed region is supporting reaction zone, followed by an expanding gaseous region where the reaction continues towards an equilibrium composition. Note that some unreacted AB as well as isolated A and B atoms are present in the product mixture.

longer self-propagating. These results can be explained in terms of the amount of reaction (and related heat release) that occurs in the reaction zone. A rather interesting dependence of the detonation velocity (D) on the intermolecular interaction energy (ϵ) is shown in Figure 2. Here, two distinct linear regimes are observed. While not yet completely understood, this is attributed to contributions to the differences in the EOS of the reactants and products, and to changes in the reaction pathway/progress. Further analysis is underway.

models. This work will subsequently be extended to triatomic systems (ABC) reaction, which should make a stronger connection to real systems by extending the reaction zone. The results of this analysis will be applied to other studies on curvature effects and void collapse to attain a complete description of the physics for those phenomena.



Despite the apparent simplicity of this system, it exhibits a complexity in behavior expected and observed for real systems. Complete analysis of this system will result in a more complete formulation of our current detonation

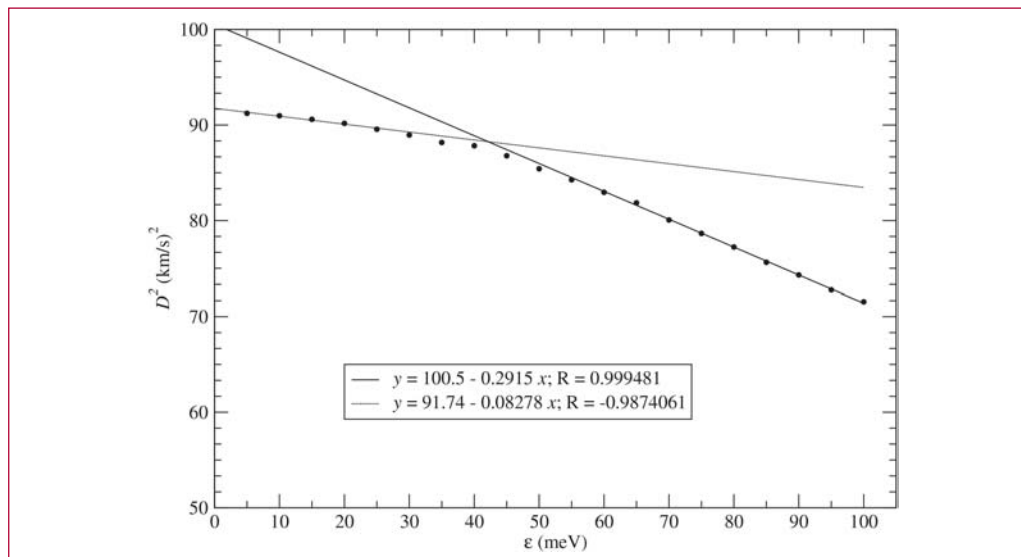


Figure 2— Dependence of the square of the detonation velocity (D) on the intermolecular interaction parameter (ϵ). Two distinct regions with a linear dependence are observed.

How Do Hotspots Happen? The View from the Atomic Scale

Brad Lee Holian, T-12 and Timothy C. Germann, X-7; blh@lanl.gov

Impacts upon perfect crystals of high explosives have to be pretty violent to get them to detonate; introduce defects into them, and the job is much, much easier. Porosity in the form of voids has been assumed to be the principal source of hot spots, or heterogeneous nuclei for chemical reaction, as a shock wave passes by. With our colleagues, Jean-Bernard Maillet of CEA (the French Atomic Energy Commission) and Carter White of the Naval Research Lab, we have investigated the interaction of shock waves with voids at the atomistic level, to see just how the hot spots are formed. B. L. Holian, T. C. Germann, J. B. Maillet, and C. T. White, "Atomistic Mechanism for Hot Spot Initiation," *Phys. Rev. Lett.* **89**, 285501 (2002).

We have used large-scale molecular-dynamics (MD) simulations to study the effect of impacts upon perfect crystals of high-explosive diatomic molecules whose interactions are modeled by a reactive empirical bond-order (REBO)

potential. Reactions are simple, in that AB molecules can form AA and BB product molecules with release of energy. Perfect crystal shock simulations lead to detonation above a threshold impact velocity, with characteristics that satisfy the simplest theory of detonations (due to Zeldovich, von Neumann, and Doering). To see if the threshold for initiation of chemical reaction can be lowered, we also introduced a variety of defects into our samples.

The first thing that we found was that defects had to be a minimum size to have any effect whatsoever. A vacancy, or even a divacancy, can be passed over by a shock wave without so much as a hiccup. However, beyond a certain size, a void (or vacancy cluster) can produce not only a warp in the shock front, but serious heating upon its collapse. Such an overheat can subsequently lead to initiation of chemical reaction originating at the void, even for a shock wave that would not have been strong enough to produce initiation in a perfect crystal (see Figure 1). For materials that don't react chemically, such hotspots can still be nucleation sites for other shock-induced phenomena, such as plastic flow or polymorphic phase transformations.

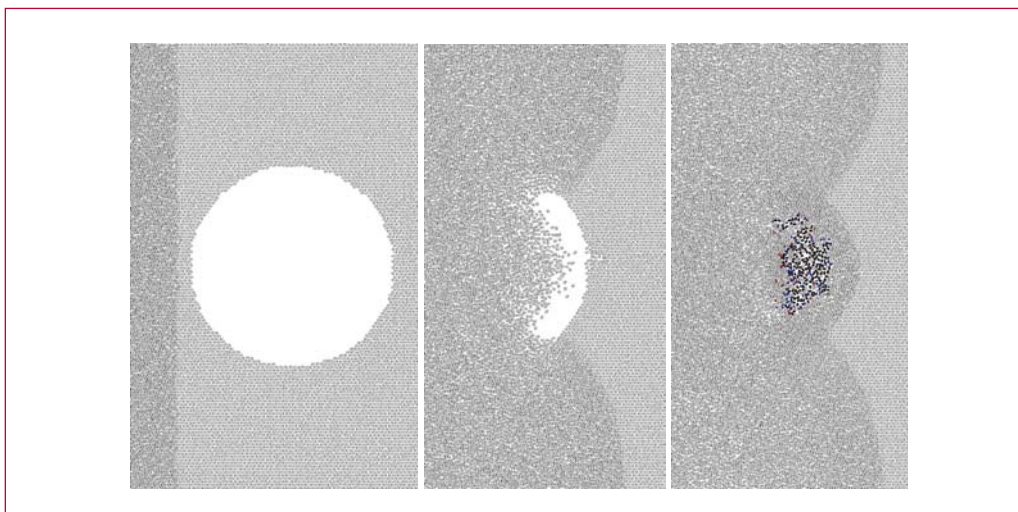


Figure 1—*Initiation of chemical reactions due to void collapse in a 2-D diatomic (AB) solid.*

Besides shock strength and void size, a third factor to be considered is the shape of the void. Consequently, that led White and co-workers at NRL to simplify the shape by considering planar gaps of varying width. They found that if the gap width was too small, no initiation occurred, unless the impact strength was above the perfect-crystal limit. No matter how wide the gap, there was a minimal velocity required to initiate chemical reactions.

We set about studying the thermal overheating that occurs in completely unreactive systems with planar gaps of varying widths, using the traditional Lennard-Jones pair potential in a monatomic solid. Again, we observed that significant overshoot in temperature occurred only when the initial impact was strong enough to eject material from the upstream side of the gap, corresponding to a shock temperature sufficient to nearly melt the material. Moreover, the gap had to be wide enough before overheating occurred at the downstream side of the gap.

In light of these observations from our MD simulations, we have proposed a simple model describing the role of shockwave interactions with microscopic voids that leads to significant heating, sufficient to thermally initiate chemical reactions in solid explosives, or phase transitions in metals. The key ingredients to this dramatic overshoot in temperature are shown in Figure 2.

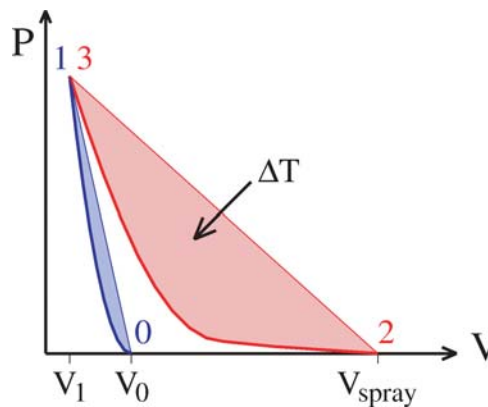


Figure 2—
Cartoon of planar gap collapse:

- (1) initial shock from specific volume $V_0 = 1/\rho_0$ to V_1 with temperature rise ΔT ;
- (2) adiabatic expansion (and cooling) of ejecta spray to a mean specific volume $V_{\text{spray}} \leq 2V_0$;
- (3) recompression at the downstream side of the gap to V_1 , with a temperature rise ΔT .

The dependencies on both shock strength and one-dimensional gap width that we observed in atomistic simulations of a two-dimensional unreactive Lennard-Jones solid for the thermal overshoot were well predicted by our straightforward model, showing how hot spots can be generated under shock wave conditions.

2

Pore Collapse and Hot Spots

Ralph Menikoff, T-14; rtm@lanl.gov

It has been known since the 1950s that initiation of a detonation wave in a plastic-bonded explosive (PBX) is due to thermal reactions but requires hot spots. Hot spots reconcile the large discrepancy between the time to detonation from Pop-plot data and the induction time based on the bulk shock temperature and the chemical reaction rate. Shock desensitization experiments and the increased sensitivity of a PBX with increasing porosity imply that hot spots generated by pore collapse dominate a shock-to-detonation transition.

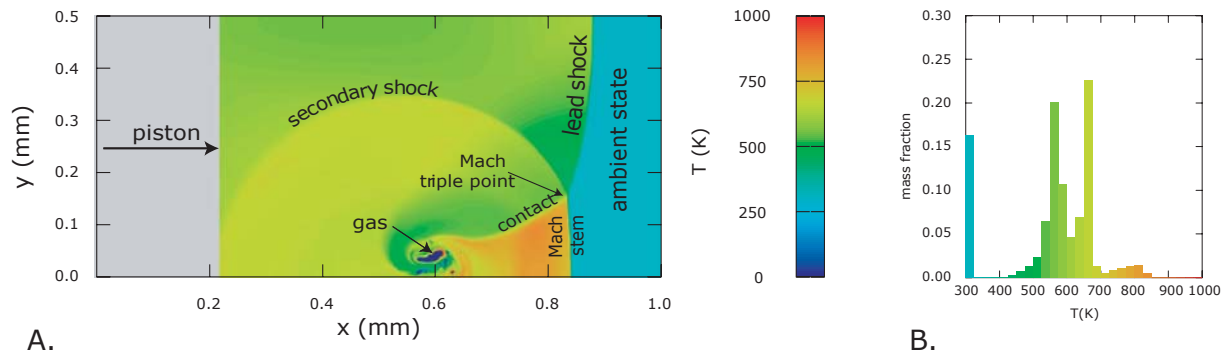
Early hydrodynamic simulations of initiation utilized artificial viscosity for shock waves as the only dissipative mechanism. They showed that, when a strong shock impinges on a pore, a micro-jet is formed and subsequently produces a hot spot on impact with the downstream side of the pore. Furthermore, simulations with arrays of pores in an explosive showed a shock-to-detonation transition. When the simulations were performed (2-D flow in the 1960s and 3-D in the 1980s), the available computer power limited the resolution. Consequently, the simulations displayed the qualitative

features of initiation but were not quantitatively accurate.

High-resolution simulations can now be run on a PC. This has led to a renewed interest in studying hot-spot ignition. As a first step, simulations of a shock wave passing over and collapsing a pore have been performed to better understand the properties of a hot spot, such as peak temperature and hot-spot mass. With shock dissipation as the dominant heating mechanism, the temperature field after a strong shock has passed over a pore is shown in Figure 1A. The collapse of the pore gives rise to an outgoing rarefaction wave in the material compressed by the lead shock, followed by an outgoing shock wave. These secondary waves give rise to the main features seen in the temperature field. For example, the secondary shock has caught up to the lead shock resulting in a Mach wave pattern. The temperature discontinuity corresponds to the contact emanating from the Mach triple point.

The temperature distribution is shown in Figure 1B. The first peak at 300 K corresponds to the ambient state ahead of the lead shock front. The second peak centered at 575 K corresponds to the material heated by the lead shock and then cooled by the rarefaction from the pore implosion. The third peak centered about 675 K corresponds to the material

Figure 1—
Temperature after pore collapse. Simulation with piston velocity of 1.3 km/s, shock dissipation only and resolution of 100 cells in the initial pore radius (0.1 mm and centered at $x=0.4$ mm, $y=0$). A. 2-D temperature field. Bottom boundary is symmetry plane. B. Temperature distribution.



heated by the lead shock and backward expanding portion of the secondary shock from the explosion of the pore. The low broad peak between 700 and 850 K corresponds to the region between the Mach stem and the material directly impacted by the micro-jet. The peak temperature is consistent with the estimates based on Riemann problems [1].

With additional dissipative mechanisms, plastic work, or viscous heating, the tail of the temperature distribution can be greatly enhanced. This is important since hot-spot reaction is due to the extreme tail of the temperature distribution. The tail of the temperature distribution is best described by the integrated temperature distribution, mass ($T1$) at $T1 > T$. It is convenient to normalize the mass relative to the equivalent mass in the pore volume at the initial explosive density.

Simulations with additional dissipative mechanisms are summarized by the integrated temperature distribution shown in Figure 2. A striking feature of the integrated distributions is that the tail of the distributions, above 600 K, is approximately linear on a log-log scale. This implies that the tail of the

distribution has a power-law behavior. Moreover, the exponent of the powerlaw is related to the viscous parameter such that the effective hot-spot mass increases as the viscous parameter increases.

The viscous parameter has not been directly measured. Instead it is usually fit to reproduce integral data for a limited class of experiments. The fact that both the viscous heating and plastic work have similar distributions implies that either dissipative mechanism can be used in a fit. To discriminate between these mechanism requires a range of experiments that are sensitive to differences in the scaling behavior of each dissipative mechanism [2].

[1]
<http://t14web.lanl.gov/Staff/rsm/preprints.html#beta-HMX>

[2]
<http://t14web.lanl.gov/Staff/rsm/preprints.html#PoreCollapse>

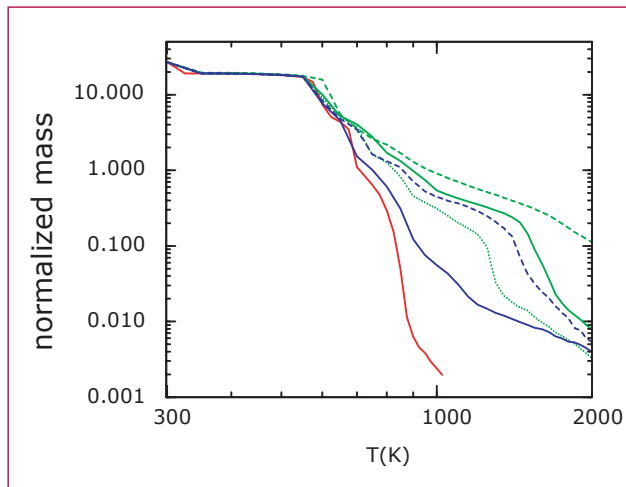


Figure 2— Variation of temperature distribution with dissipative mechanism. Dissipative mechanisms: red, shock heating; blue, shear viscosity, solid and dashed $\eta = 10$ and 100 Poise, respectively; green, rate dependent plasticity, solid, dashed and dotted $\eta = 800$, 8000 , and 80 poise, respectively.

Detonation Products Equation of State

M. Sam Shaw, T-14; mss@lanl.gov

The final major step has been completed in the development of a Monte Carlo simulation method capable of including all aspects needed to characterize detonation products EOS for real explosives of interest.

That step is the inclusion of carbon clusters with surface groups, where the amount of carbon in clusters and the composition of the surface are allowed to reach equilibrium. These features are in addition to



the other features of my new Composite Monte Carlo Method [1,2], which combines chemical equilibrium composition, fluid-fluid phase separation, and incorporation of solid forms of carbon. The extended method [3] was presented at the 2003 APS Topical conference on Shock Compression of Condensed Matter.

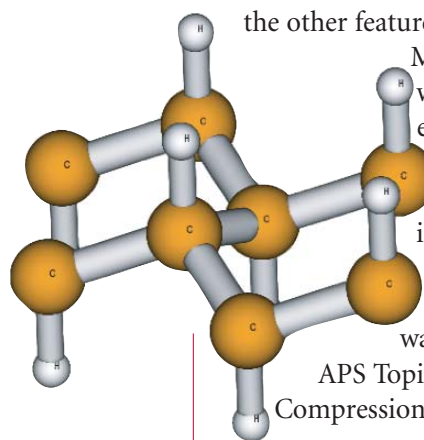


Figure 1—
A model of the cluster surface and an approaching N_2 molecule. Periodic boundary conditions are applied in the two directions perpendicular to the surface.

As with bulk carbon, the cluster is treated using a model Gibbs free-energy in the exponent of the probability distribution while the positions and interactions in the molecular fluid mixture are explicitly included in the simulation. The cluster treatment differs from the bulk in that several distinct atom groups are present; surface groups such as H and OH, surface carbon atoms, and interior carbon atoms. Instead of a single reaction adding or subtracting from the total, multiple reactions are included with changes to various combinations of atom group types. For initial simulations, the effective size of the cluster model is kept near that found in recovery experiments, around 2-nm diameter with around 1000 atoms. Instead of a very large simulation with full size clusters, the ratios of types of groups are

constrained to remain near that of the full cluster. Small variations from these ratios are allowed so that individual reaction steps can take place. The various groups are characterized by additive contributions.

One particular complication is the effective volume occupied by a cluster. A series of simulations were made with model clusters included as a single very large particle. By varying the cluster interaction with the fluid and comparing to simulations where the cluster is removed, an effective volume was established relative to the interactions. The actual interactions between the fluid and surface are not known. Electronic structure calculations have begun in collaboration with C. J. Tymczak (T-14) using the MondoSCF code[4] to evaluate the interaction of molecules from the fluid with a small scale model of the surface. In Figure 1, we see a N_2 molecule approaching a 111 surface of diamond with H-caps on the dangling bonds. Periodic boundary conditions are applied in the two directions perpendicular to the surface and a finite thickness of the surface layer is chosen. Application to larger model surfaces with various surface groups and molecules from the fluid are under development. From the first model, however, it is clear that the H-caps do not extend the effective surface by their bond distance with the carbon surface and that geometry alone doesn't determine the location of the surface.

The previous large set of simulations of HMX (high explosives) has been extended to include diamond clusters with surface chemistry. By interpolation of the tabulated points, the Hugoniot and the CJ state are calculated for HMX as a function of initial density. The calculated results for several cases of detonation velocity versus initial density are compared with experimental data in Figure 2. RDX data is included with the HMX data since the two are essentially identical for detonation velocity. The types of calculations are specified in the caption.

Work continues in collaboration with C. J. Tymczak (T-14) on the combining of Monte Carlo methods with very efficient (linear scaling) many particle ab initio electronic structure calculations using MondoSCF [4]. Having demonstrated an effective scheme to evaluate thermodynamics with a small set of configurations from a reference Monte Carlo simulation, the focus has shifted to the accurate evaluation of the many-body energy in those configurations. An extensive study of basis set dependence for individual molecules, pairs of molecules, and full many-body configurations, is in progress. In addition, the effect of relaxing the usual rigid-rotor harmonic oscillator approximation is being studied.

The equation of state (EOS) for products of polymers and foams is being studied with the chemical equilibrium thermodynamic perturbation theory code HEOS, which was originally developed for detonation products. A study of a large set of polymer and foam Hugoniot data has been used to refine the parameters for H_2 and CH_4 that are minor species for explosives, but major constituents of polymer products due to typically low oxygen content. Predictions have been made for VCE and related materials where data is limited. Because of similarities in composition of VCE to other polymers, the predictions are expected to be accurate because the materials with data are accurately represented.

In collaboration with Maria Rightley (X-4), a PBX-9501 EOS based on high- and medium-pressure data (Hugoniot, sound speed, and interface velocimetry) has been extended to match cylinder test data in the low-pressure regime. Variations in the low-pressure part are transmitted through the SESAME EOS form. Iteration through hydrodynamics calculations of the difference between the

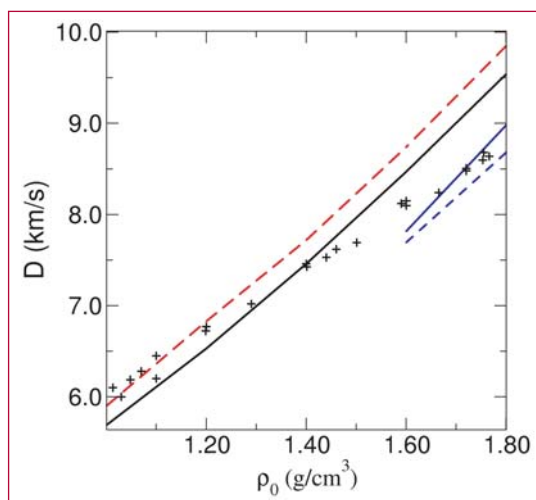


Figure 2— Detonation velocity versus initial density. HMX and RDX data (+), calculations with graphite and two different sets of cross potentials (red dash and black line), calculations with diamond clusters of two sizes (blue line, blue dash).

results for a given EOS and cylinder test data, determine the best fit of the lower pressure part of the EOS. Results indicate that the details of the low-pressure EOS depend on the higher pressure EOS assumed. That is, there is a family of curves that fit the cylinder data when other constraints are not included.

- [1] M. Sam Shaw, "Direct Simulation of Detonation Products Equation of State by a Composite Monte Carlo Method," proceedings of the 12th Detonation Symposium, to be published.
- [2] M. Sam Shaw, "A Hybrid Monte Carlo Method for Equilibrium Equation of State of Detonation Products," in Shock Compression of Condensed Matter – 2001, edited by M. D. Furnish, N. N. Thandhani, and Y. Horie, *AIP*, pp. 157–160 (2002).
- [3] M. Sam Shaw, "Direct Simulation of Detonation Products Equation of State," to be published in proceedings of the 2003 APS Topical Conference on Shock Compression of Condensed Matter.
- [4] Matt Challacombe, Eric Schwegler, C. J. Tymczak, Chee Kwan Gan, Karoly Nemeth, Anders M. N. Niklasson, Hugh Nymeyer, and Graeme Henkleman, "MondoSCF, A Program suite for massively parallel, linear scaling SCF theory and ab initio molecular dynamics." Los Alamos National Laboratory (LA-CC01-2).

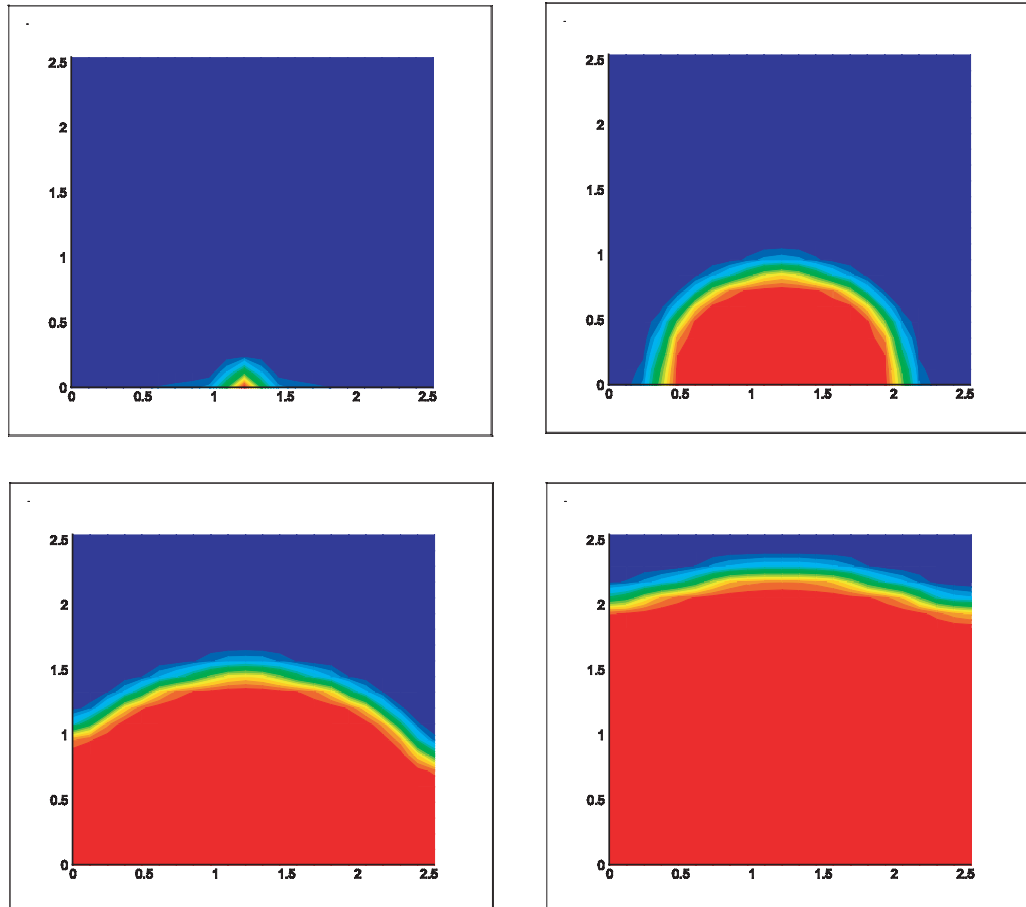
High-Explosive Safety Study, Update

Qisu Zou, Duan Z. Zhang,
W. Brian VanderHeyden, Frank H.
Harlow, and Nely Padial-Collins, T-3;
qisu@lanl.gov

We investigate nonshock initiation of high-explosive (HE) material. Currently we focus on the effects of sand grits on the surface in contact with HE. Theoretical models about frictional heating and sub-grid ignition have been developed and

implemented into a general multipurpose computation fluid dynamics (CFD) code CartaBlanca. A particle-in-cell (PIC) method is used to model the solid HE with mechanical strength. Chemical reactions, gas generation, and mechanical and thermal interactions between the solid HE and gas are considered by solving appropriated equations numerically. The figure shows the progression of an explosion in a square inch of HE, similar to the experiment performed by Dyer and Taylor. The initial hot spot temperature is 644 K.

2



Figure—
Four snapshots in
the order: top left,
top right, bottom
left, and bottom
right.

Numerical Simulation of Stress Wave Propagation in PBXs

Scott G. Bardenhagen, T-14;
bard@lanl.gov

Stewardship of the nuclear weapons stockpile places stringent demands on the understanding of materials and their behavior under extreme conditions. Homogeneous continuum models have been developed to describe the response of a material to dynamic loading, including equation of state, strength, and reactive burn models. However many strategic materials, in particular plastic bonded explosives (PBXs), are heterogeneous at the microscale (<1 mm). PBXs are composites containing energetic grains, ranging in size from less than one to a few hundred micrometers, embedded in a matrix of high-polymer binder. Low levels of applied stress can cause substantial material damage and even lead to violent reactions because of the heterogeneous nature of its distribution.

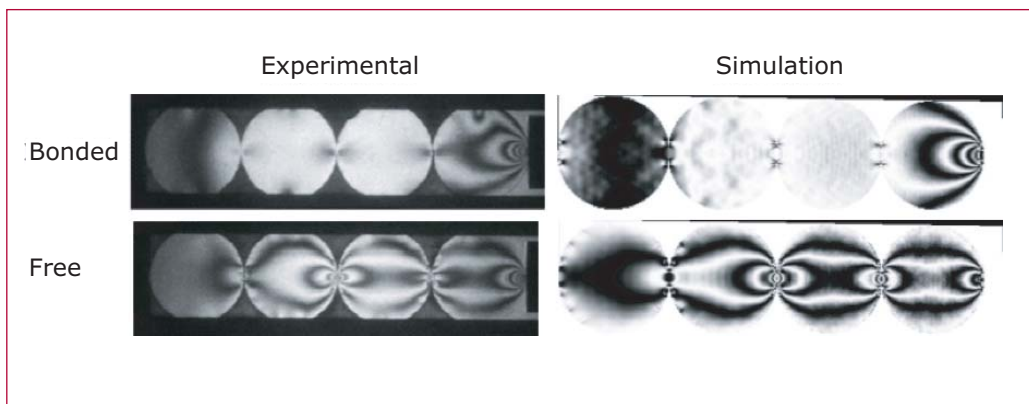
Homogeneous continuum models provide good estimates of bulk material response. However, as there is little connection to the underlying physics, these models cannot be extrapolated with confidence. The orientation dependent properties of the individual crystals and the presence of material interfaces result in strongly heterogeneous stress and

energy distribution. To develop accurate, quantitative, and predictive models it is imperative to develop a sound physical understanding of the grain-scale material response.

One approach to capturing this behavior is to perform microscale simulations where the crystals and the binder of the PBX are explicitly represented. While easy in principle, a very crucial feature is how the interfaces between materials are handled. Such contacts can be fixed with strong adhesion, free with very weak adhesion, or exhibit frictional sliding. Exactly what type of behavior is exhibited is highly dependent on the material properties and strain-rates. This behavior can not be accurately captured with conventional Lagrangean or Eulerian simulation codes for a realistic polycrystalline sample with a large number of irregular shapes and contact surfaces.

A better approach for this class of simulations is to use a particle method. One particular method, the Material Point Method (MPM), provides a convenient framework for modeling material interfaces. It has been used here to perform numerical simulations indicating the importance of accurately modeling composite material constituent interfacial conditions. The computational technique has been developed primarily by researchers at LANL and UNM, with the particular code implementation coming from the University of Utah's

Figure— Comparison of experimental data and simulation of stress wave propagation through photoelastic cylinders embedded in an opaque binder. In one case the binder is allowed to adhere (bonded) to the cylinders during casting, in the other case adhesion is prevented (free).



ASCI/ASAP program. The particular algorithm for handling interfaces was developed at LANL as part of this project.

As an example of validation, we compare our computations to a set of experiments performed by Joe Foster and coworkers at Elgin AFB. There, stress wave propagation experiments were performed on simple composite microstructures—polymeric cylindrical “grains” embedded in a polymeric binder. A comparison of results is shown in the figure. Two cases, perfect adhesion (bonded) and complete decohesion (free) of the grain binder interfaces, were examined. With perfect adhesion (bonded), a substantial amount of the stress is transferred to the binder, and there is very little localization in the crystal. With complete decohesion (free), the stress is carried almost completely in the crystals, and there is substantial stress amplification at grain contacts. Validation simulations successfully capture differences in stress distributions in near quantitative agreement. As the constitutive properties and strain-rates in these experiments and simulations are in the range of interest, the importance of properly describing the interface conditions is clearly demonstrated.

Simulations containing hundreds of crystals have also been performed in both two- and three-dimensional geometries. These have utilized particle size distributions appropriate for the PBXs. Previous work has been done without a binder, and substantial stress fluctuations were observed. It was found that these could be characterized by a power law distribution. We are in the process of redoing these simulations with binder included, to determine the factors that control the stress

distribution. The results will be used to assess and parameterize a homogenized model for the PBXs that can be used in macro-scale simulations.

2

On Validating SCRAM

*John K. Dienes, T-14; John Middleditch, CCS-3; and Q. Ken Zuo, T-3;
jkd@lanl.gov*

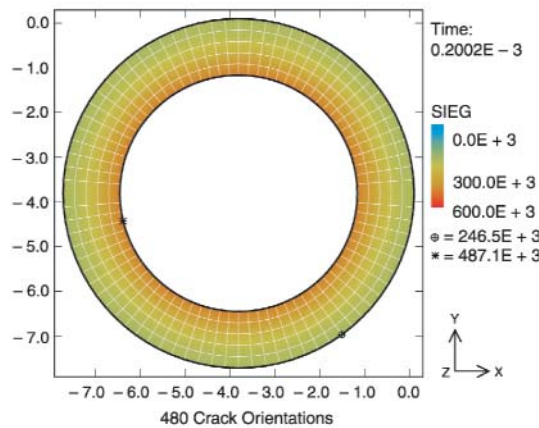
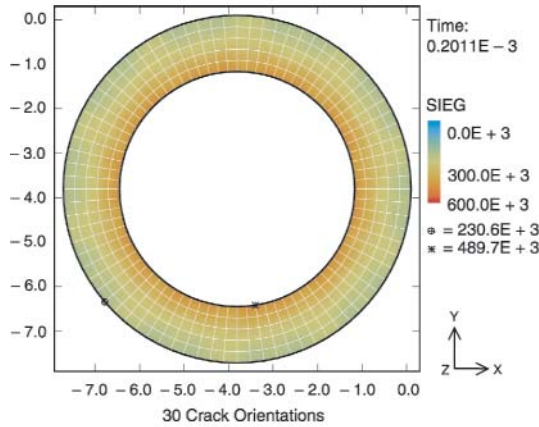
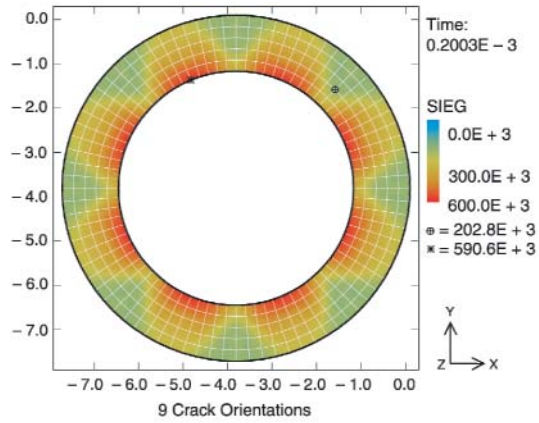
The SCRAM algorithm for modeling brittle behavior was designed to complement various algorithms that characterize ductile behavior of materials and to account for the sensitivity of explosives and propellants to very low speed impacts. In its current form it accounts for the opening, shear, growth and coalescence of an ensemble of cracks, the heating in shear (closed) cracks, and reactions in high explosives that result from crack heating; hence the acronym SCRAM, for Statistical CRACK Mechanics. The SCRAM algorithm operates over a range of scales, accounting for reactions in a zone near the crack surface that is only microns in width, while allowing for the formation of cracks that may be many centimeters in length. The algorithm has been embedded in a variety of finite-element codes so that it can compute damage in large structures. The new coalescence formulation accounts for percolation behavior representing the formation of very large cracks (visible to the naked eye).

The various concepts that contribute to SCRAM are generally wellknown, qualitatively, but they have been extended to account for complex damage processes, which require tensor constitutive laws and must be valid at large deformations. The current emphasis has been on verifying and validating the programming and physical concepts. They are considered crucial at this point because the introduction of new physics such as the set-size theory for percolation processes makes the damage behavior very complex and, consequently, it is challenging to confirm the calculations. This is especially the case where three-dimensional

behavior is involved, and three-dimensions are required to represent impacts that involve extensive damage.

One kind of test problem we have developed concerns the response of a thick uniform ring to sudden internal pressure. We have confirmed that the finite-element solution is uniform and consistent with the analytic solution. This constitutes one kind of verification because the computing is actually done in the SCRAM algorithm, though the nonlinearity is small. The primary purpose of this test, however, is to confirm that the damage is homogeneous around the ring when SCRAM is activated. This is far from trivial for a number of reasons. First, the finite-element programs are noisy. Second, there could be bugs and/or noise in the SCRAM algorithm or its implementation. Third, materials that allow only a few crack orientations are anisotropic and anisotropy would lead to inhomogeneous behavior in a symmetric geometry. By examining calculations with various numbers of orientations we can test for bugs and determine how many orientations are needed to get accurate damage response. We have found that 9 orientations is hardly enough, 30 is adequate, and 480 gives good uniformity, as shown in the figure.

⌘



Figure—
The response of a thick ring to internal pressure for three levels of resolution of crack orientation. With 9 orientations the anisotropy is quite large, while with 480 the uniformity is good. The internal pressure ramps to 25 bars in 30 μ s.

Constitutive Model Development for Filled Polymer Systems

Edward M. Kober, T-14; James S. Smith and Grant D. Smith, Univ. Utah; emk@lanl.gov

Filled polymeric systems are used for several applications within nuclear weapons systems, typically as adhesives and cushions. Many of these materials are silica-filled polydimethylsiloxane (PDMS) systems such as the foam S5370. While there is extensive literature describing various constitutive models for filled polymeric systems, these models tend to be highly empirical in nature and lack any significant predictive capability. One facet of this is that the fillers are irregularly shaped, are unevenly dispersed, tend to agglomerate in clusters, and there is limited data available characterizing those distributions in the manufactured materials. Another aspect is the large surface area of the fillers (typically 100–300 m²/g with particle dimensions of 10–100 nm), where this indicates that adhesion of the polymer to the surface will be an important parameter. This also suggests that a large fraction of the bulk polymer may be influenced by these surface interactions and may have properties modified with respect to the bulk material.

The purpose of this effort is to develop physically based constitutive models for the polymeric systems of this type, primarily the silica-filled PDMS systems. Our approach to this is to determine the fundamental properties and response characteristics of the polymer system and the polymer surface interface from a combination of atomistic molecular dynamics (MD) simulations. These results are extended to time and length scales beyond the domain of the MD simulations by the use of well-established analytic formulations and

utilizing coarse-grained simulations. The resulting properties will then be input into existing constitutive formulations or those modified to accept these properties. In particular, current formulations tend to treat the polymer bulk as an ideal elastic material whose response is entirely entropic, whereas PDMS is known to have a viscoelastic response and 10–20% of the elastic response is enthalpic in nature. Also, most formulations tend to ignore the surface boundary layer.

The first area of work was to establish an MD force-field from high-level quantum chemistry calculations. The current commonly used force-field is about 10 years old and was based on lower-level calculations. Our work found that the PDMS system was more polar than previously estimated, and that some of the bond-bending motions were not well-described. Corrections in these terms results in an improved level of agreement with the bulk polymer properties

We then characterized the silica-PDMS interaction as the second area of work. A large body of experimental work clearly demonstrates that the strength of this interaction is highly dependent on the number of surface hydroxyl groups on the silica, and that strong hydrogen-bonds occur between those hydroxyl groups and the oxygen atoms in the PDMS chains. However, a recent theoretical study concluded that this interaction did not take place, but suggested no alternative mechanism for why the hydroxyl groups affected the interaction. From a thorough quantum chemical study, we found that strong hydrogen-bonding interactions should occur and our calculated spectroscopic shifts were consistent with experiment.

This data was also then included in our MD force-field parameterization, and the effects of the surface hydroxyl groups

were studied. First, simulations were performed with a “clean” silica particle (that had no surface hydroxyl groups) immersed in a bath of PDMS oligomers. The surface would wet, but no strong interactions or ordering were found, as shown in Figure 1. This shows the concentration profiles of the silicon, oxygen, carbon, and hydrogen atoms as a function of distance from the silica surface. These profiles are all broad and diffuse and show no particular ordering, other than a preference for the methyls groups to interact with the surface rather than the oxygen atoms. The relaxation times of the PDMS chains were not significantly altered compared to what they were for a bulk solution without filler. In contrast, a hydroxyl covered silica particle showed a strong ordering effect as shown in Figure 2. The sharp oxygen peak at $\sim 3 \text{ \AA}$ is due to species involved in hydrogen-bonds with the surface. It is also interesting to note the subsequent bumps in the oxygen profile at 6 and 8 \AA (along with the associated shadows in the silicon distributions). This shows that the second and third layers of polymer chains also have a level of induced ordering arising from polar interactions. The relaxation times of the PDMS in this sample are increased by a factor of ~ 10 compared to the nonhydroxylated surface. This shows that there is an induced stiffening of the polymer near the surface, a result in agreement with NMR and neutron scattering experiments.

Therefore, it is important that a constitutive model should represent this interaction depending on the type of silica present (e.g., fumed silica with a large number of surface hydroxyl groups or quartz with a fairly “clean” surface). For fumed silica in particular, where the

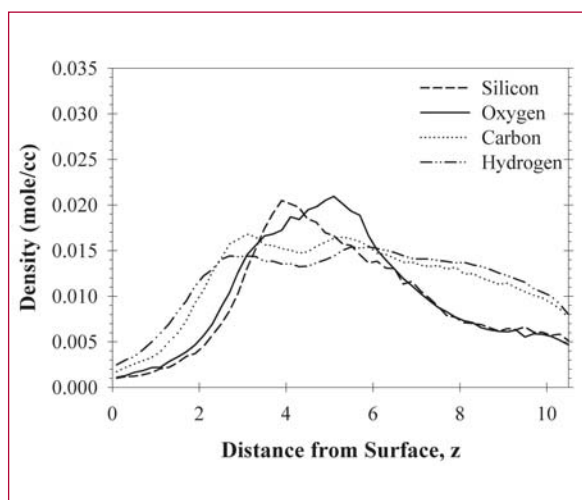


Figure 1—
The PDMS atomic profiles next to a bare (111) SiO₂ surface.

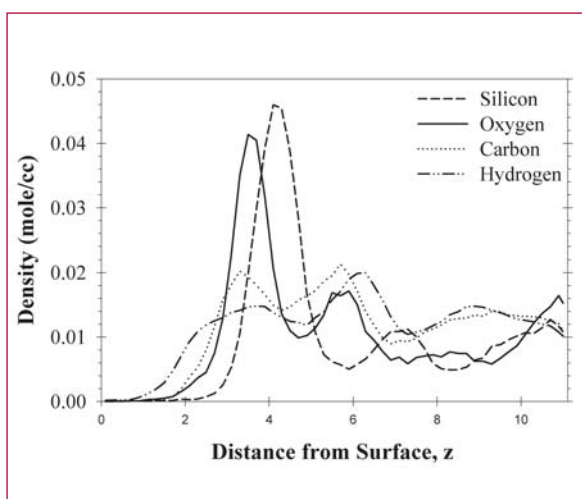


Figure 2—
The PDMS atomic density profiles next to a hydroxyl covered (111) SiO₂ surface.

basic entity particles are $\sim 10 \text{ nm}$ in size, the presence of a 1-nm stiffened surface layer could alter how one represents the system. Future work will refine the evaluation of the thermodynamic properties of these systems and their relaxation times. These will then be incorporated into existing constitutive formulations (or modified versions) and the results evaluated. Assessment of the significance of the filler distribution will then become the area of focus.



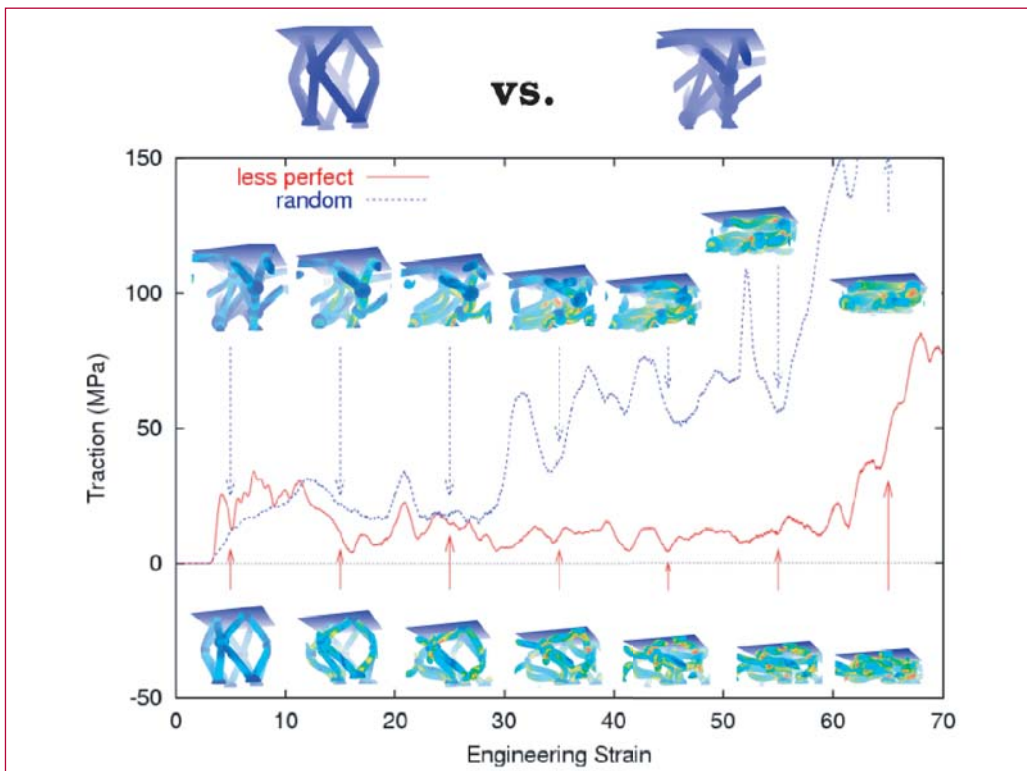
Numerical Simulation of Full Densification of Foams

Scott G. Bardenhagen, T-14;
bard@lanl.gov

Foamed materials are increasingly finding application in engineering systems because of their unique properties. They are extremely light weight and can provide gentle packaging or energy absorption during crush-up. The basic mechanics that gives rise to these properties is well established and is due to the foam microstructure, a network of struts and, possibly, membranes. Foams compress at nearly constant load (the “stress plateau”) over a large range of deformation while the load is supported primarily by strut bending. As the network begins to collapse upon itself (“densification”) the material stiffens dramatically as the primary load-carrying mechanism transitions to contact between struts. Microstructural models and simulations

have provided substantial insight regarding foam mechanics, but primarily at small deformations. Numerical simulation of foam deformation physics in the stress plateau and densification regimes, where accounting for large material deformations and contact mechanics is essential, remains a significant computational challenge.

A particle-in-cell (PIC) numerical simulation technique (a “meshless method”) has been shown to perform well-modeling precisely the physics relevant to foam mechanics, i.e., large material deformations and contact. PIC algorithms were developed at Los Alamos to model fluid flow. More recent developments have allowed the application of these methods to solid mechanics. Model foam unit cell microstructures, with relative density $\sim 90\%$, have been generated. Compression of these unit cells was simulated to full densification (90% engineering strain). These simulations are preliminary, but represent a computational “first” in this field.



Figure—
The force required,
as a function of
deformation level,
to crush up two
idealized foam
microstructures.
Insets indicate
deformed
configurations.

Simulation results were found to be in qualitative agreement with expectations and experimental work. The stress plateau and densification deformation regimes may be easily distinguished in the macroscopic stress strain response depicted in the figure. Effects due to regularity of the foam microstructures have also been identified. More regular unit cells appear to exhibit a much flatter stress plateau. Future work includes linux cluster simulations of much larger microstructures, representative of bulk foam material.



Modeling the Dynamic Response of Disordered Cellular Materials

Mark W. Schraad and Francis H. Harlow,
T-3; schraad@lanl.gov

The purpose of this project is to develop a constitutive law and a general modeling approach for describing the mechanical response of cellular materials to highly dynamic, large-strain, and high-rate loading conditions. The programmatic relevance of this project derives from the implementation and use of this modeling approach within large-scale codes for simulating the behavior of cushioning materials.

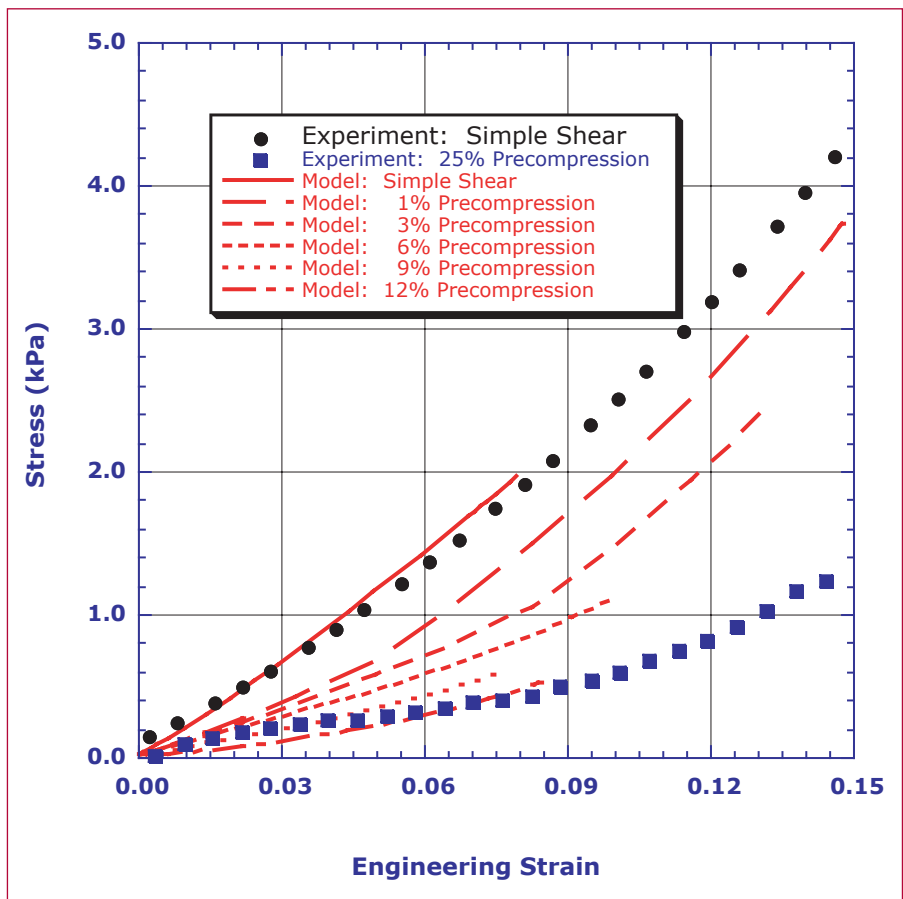
Cellular materials consist of two separate but interacting material fields—the cellular solid and the permeating fluid (e.g., usually air)—each with its own distinct velocity field. The modeling effort, therefore, begins with the derivation of a governing set of macro-scale conservation equations in two-field form. For example, the linear momentum equations for both the cellular solid and the fluid describe the response to stress gradients within the cellular solid, as well as to pressure gradients arising in the fluid and to the drag impedance arising from the relative flow between the two materials.

This form of the governing equations is chosen to allow for consideration of evolving closed-cell fluid pressure and open-cell fluid flow in the overall description of the cellular material response. Solutions to the linear momentum equations and the corresponding conservation of mass equations provide the velocities, densities, and volume fractions for each material. Models for the fluid pressure and the momentum-exchange rate,

which couples the behavior of the fluid and the cellular solid, are used to close this set of equations, along with an appropriate constitutive law for the evolving stress state in the cellular solid.

A general, three-dimensional, finite-deformation constitutive law has been developed to describe the mechanical response of a single foam cell. A probability distribution function, which describes the initial cell-size distribution and the corresponding cellular-scale structural evolution, has been formulated and is coupled with the single-cell model to form the macro-scale constitutive law. This constitutive law relates the macro-scale stress in the cellular solid to the continuum-level strain, strain rate, and stress rate. Most importantly, as the cellular structure evolves, so too does the probability distribution function, thereby bridging the cellular and macroscopic length scales by representing the cellular-scale structural evolution within the macro-scale constitutive response.

The macro-scale constitutive law has been implemented in a small-scale test code and a large-scale performance code. The material model parameters have been calibrated against both single-cell numerical simulations and macro-scale experimental data, and small-scale tests have been performed for parameter refinement. The model also has been verified and validated against experimental data for low-rate but large-deformation compressive, tensile, shear, and combined loading of a low-density, open-cell, polyurethane foam and the high-density, S-5370 silicone foam. In the near future, attention will be focused on the rate-dependent behavior of cellular materials and the effects of the permeating fluid on the cellular solid response under dynamic loading conditions.



Figure—
Shear stress versus
shear strain for
a low-density
polyurethane
foam, showing the
softening effects of
various levels of
pre-compression.

Polymer and Foam Products Equation of State

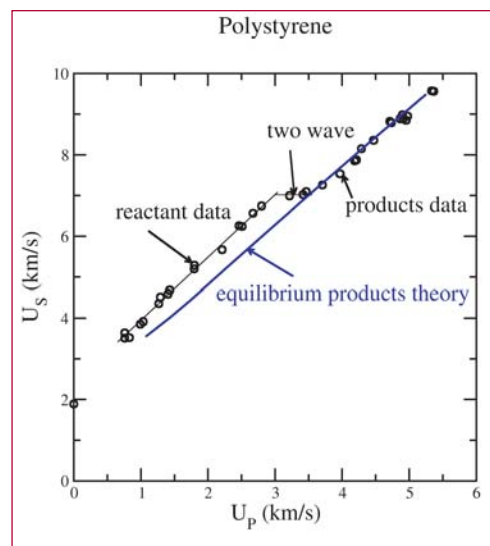
M. Sam Shaw, T-14; mss@lanl.gov

Figure 1— Shock velocity versus particle velocity for full density polystyrene. Hugoniot data (O) and equilibrium products theory (blue line).

The equation of state (EOS) of polymers are very similar to that of high explosives (HE) in that under shock conditions of sufficient strength the initial material decomposes to a mixture of molecular fluids (N_2 , H_2O , CO , CO_2 , H_2 , CH_4 , etc.) and sometimes solids (C , SiO_2 , etc.). Although the energy released in decomposition of polymers is small compared to HE, the final state can still be at high temperature due to shock heating. In the case of foams, the shock heating is quite substantial and the resulting temperature is often in the same range as for HEs. The difference between polymer products and HE products is primarily in the concentration of product species and not in the type. Consequently, the same theoretical methods can be applied to both. Having already developed a theoretical EOS for HEs, minor modifications are required to apply the same method to polymer products. Also, a limited amount of experimental calibration is needed to make the jump from HEs to polymers.

Polymer materials that have not decomposed are readily treated in the same fashion as other inert materials. Hugoniot data at full density supplies simple parameters such as a $U_s U_p$ fit for a reference curve. A set of Hugoniot data for different initial densities (e.g., foams) is sensitive to the choice of Grüneisen gamma and allows calibration of the EOS off the reference curve.

The treatment of polymers is incomplete without at least an estimate of the conditions required for decomposition. If the rate of decomposition is sufficiently sensitive to the state, then there is only a



very narrow region that requires the rate and the rest is accurately approximated as either reactant or product. This appears to be the case for some common polymers such as polystyrene. Hugoniot data in Figure 1, show two linear $U_s U_p$ segments connected by a constant region, similar to a large phase transition in an inert material. Recovery experiments by Morris et al. [1] show that the lower line results in the recovery of the initial polymer. Higher shocks, corresponding to the two-wave structure and the high-pressure phase, result in the recovery of products such as CH_4 , H_2 , and carbon. For many polymers, the transition to products seems to occur at about the same particle velocity (around 3 km/s) and consequently the same specific internal energy added by the shock.

The primary focus of the modeling has been on the EOS of decomposition products. The molecular fluid products are treated using thermodynamic perturbation theories in two steps. Nonspherical potentials are replaced by effective spherical potentials through a thermodynamic perturbation method shown to give very accurate thermodynamics [2]. Then the thermodynamic perturbation method developed by Ross [3] for spherical potentials is used to determine the EOS (including free

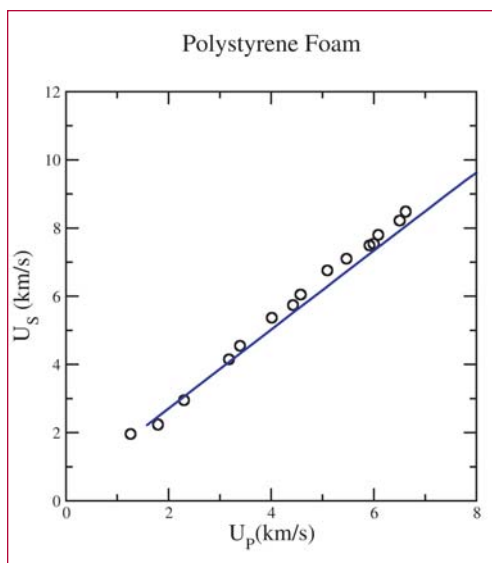


Figure 2— Shock velocity versus particle velocity for polystyrene foam at density around 0.3 g/cm^3 . Hugoniot data (O) and equilibrium products theory (blue line).

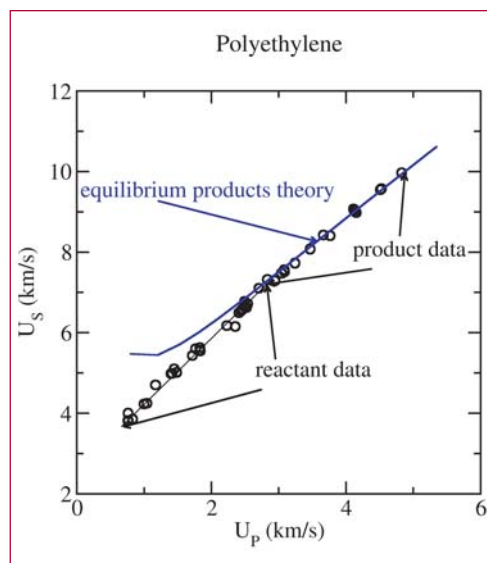


Figure 3— Shock velocity versus particle velocity for full density polyethylene. Hugoniot data (O) and equilibrium products theory (blue line).

energies) for the molecular fluid. The solid components are treated using a Murnaghan cold curve plus a Debye model. In addition, there is an option for solid carbon in the form of clusters of a size found in recovery experiments. This treatment includes variations in chemical composition of the surface groups on dangling bonds in the diamond phase. The Gibbs free energy of the mixture of all components is then minimized with respect to composition in order to generate the equilibrium EOS. This method is incorporated in a computer code, HEOS, with molecular fluid potentials and solid model parameters adjusted to match data of individual species as well as a variety of data on HE products [4].

Similar results are shown in Figure 2 for polystyrene foam. Because of the low-initial density, the polymer decomposes at a much lower pressure. The equilibrium products theory is the same as used for full density, but a different line is sampled by the Hugoniot in the two-dimensional P,T space.

The results for polyethylene are shown in Figure 3. Here the reactant and product EOSs are much closer than for

polystyrene and the two wave structure is not seen. However, recovery experiments [1] confirm that the change in slope occurs with the transition from reactants to products.

These results illustrate a small part of a much larger study to improve the EOS of CHNO polymers by comparison with a wide variety of shock data [5, 6]. An equilibrium EOS with specific choices for the H_2 and CH_4 potentials was found to be in good agreement with the data. These values do not affect the EOS for HE products because the equilibrium composition only has very small amounts of H_2 and CH_4 , mostly due to the relative abundance of oxygen compared with polymers.

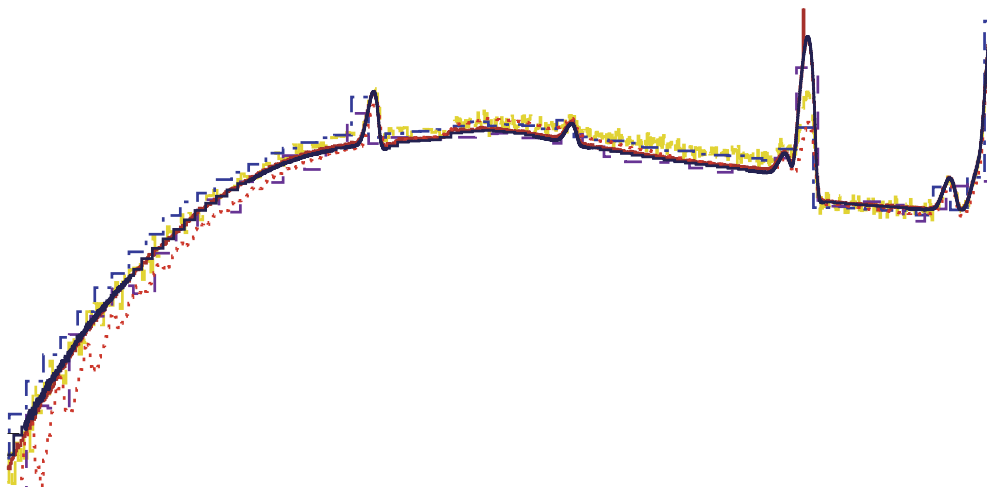
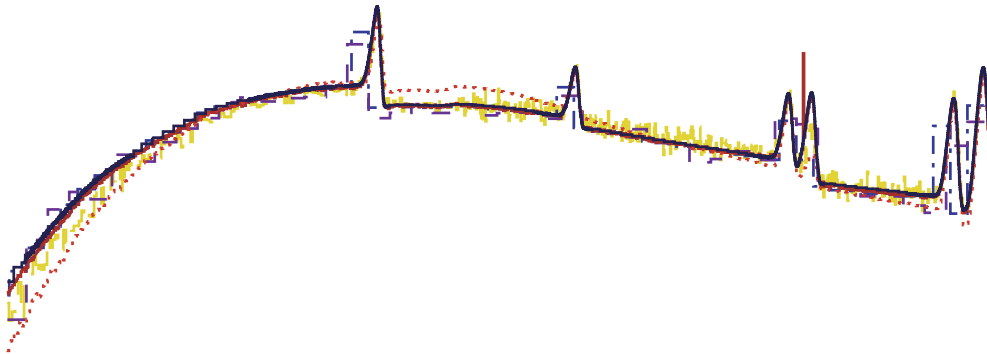
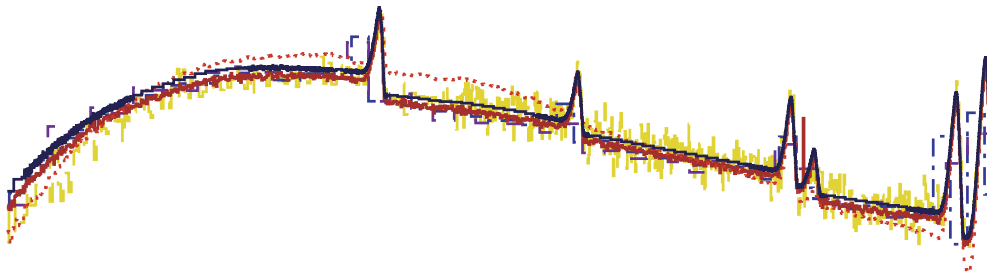
Work on Si containing polymers continues. The S5370 EOS has been converted to a SESAME tabular form for use in codes. This EOS has been passed to Maria Rightley (X-4) and Randy Bos (X-7). Specific Hugoniot state conditions were also passed along and used to verify the implementation of the EOS in SESAME form. The EOS treatment is being refined by comparison with similar materials while waiting for new S5370 data.

VCE (Ethylene-vinyl acetate-vinyl alcohol terpolymer) is a polymer where very limited data is available. The composition is approximately 84 ethylene (C_2H_4), 17 vinyl acetate ($C_4H_6O_2$), and 4 vinyl alcohol (C_2H_4O), plus an added cross-linking. In 100 g, effective formula is roughly $C_{6.11}H_{11.37}O_{0.95}$, without cross-linking. With cross-linking, this changes to $C_{6.06}H_{10.48}N_{0.09}O_{1.00}$. This composition is similar to several polymers in the large study, so the predicted EOS is expected to be accurate.

- [1] C. E. Morris, E. D. Loughran, G. F. Mortensen, G. T. Gray, and M. S. Shaw, "Shock Compression of Condensed Matter," 687 (1989).
- [2] M. S. Shaw, J. D. Johnson, and J. D. Ramshaw, *J. Chem. Phys.* **84**, 3479 (1986).
- [3] M. Ross, *J. Chem. Phys.* **71**, 1567 (1979).
- [4] M. S. Shaw, "Shock Compression of Condensed Matter— 1999," 235 (2000).
M. S. Shaw, "11th International Detonation Symposium," 933 (1998).
- [5] Stanley P. Marsh, "LASL Shock Hugoniot Data," University of California Press, Berkeley, 1980.
- [6] W. J. Carter and S. P. Marsh, LA-13006-MS (1995), edited from a 1977 report.



Astrophysics



Code Verification for Thermonuclear Supernovae

Peter A. Milne, T-6; Aimee L. Hungerford, CCS-4; and Christopher L. Fryer, T-6; pmilne@lanl.gov

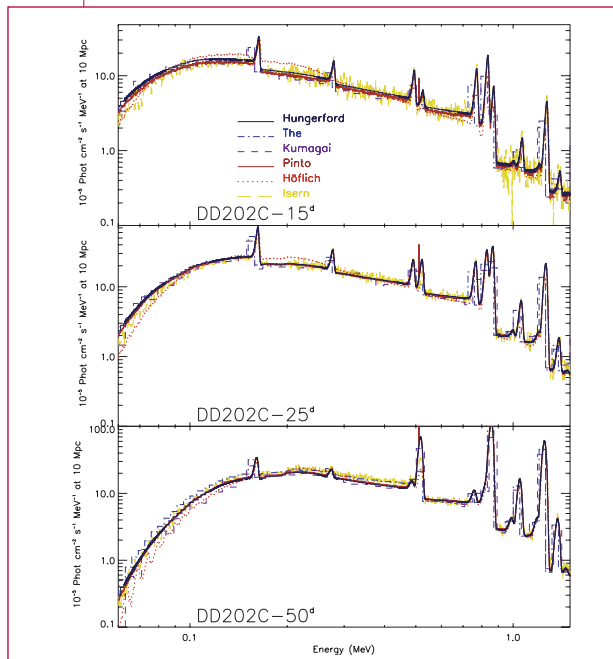
Thermonuclear supernovae are among the largest explosions in the universe, releasing 10^{51} ergs ($>10^{28}$ megatons) of energy in a fusion bomb of epic proportions. Most of this fusion energy is converted to kinetic energy and is difficult for astronomers to detect. However, these cosmic explosions produce a considerable amount of radioactive nickel (^{56}Ni) which, when it decays, releases energetic gamma-ray photons. These photons are reprocessed into optical light and are subsequently observed by astronomers. Unfortunately, using these observations to learn about the actual explosion can be problematic due to the many layers of theory that lie between models of the thermonuclear explosion and the observed optical emission.

A more direct measurement of the explosion comes from observing the

gamma-rays themselves. The opacities at these high energies are simpler (mostly continuum instead of line opacities) and don't depend strongly upon the ionization state of the material. However, until recently, the different codes calculating the gamma-ray emission for thermonuclear supernovae disagreed by nearly an order of magnitude on the gamma-ray line flux. Our project concentrated on doing detailed code comparisons of the existing gamma-ray line transport codes to apply programmatic techniques in code verification to this astronomy problem.

All in all, we compared seven different gamma-ray line codes developed across the world from simple escape techniques (Boggs: Coburn & Boggs 2003) to one-dimensional Monte-Carlo algorithms (FASTGAM: Woosley, Hartmann & Pinto 1989; The: Bussard, Burrows & The 1989, Höflich: Müller, Höflich, & Khokhlov 1991; Kumagai: Shigeyama *et al.* 1991) to three-dimensional codes (Isern: Isern, Gomez-Gomar & Bravo 1996; Maverick: Hungerford, Fryer & Warren 2003). Although these codes mostly used Monte-Carlo transport, their drivers were different and used different physics implementations. Some included additional physical effects that others did not. Using a variety of initial conditions we were able to track down many of the errors in the existing codes to get agreement in the spectra at nearly all wavelengths for these codes. Figure 1 shows the gamma-ray spectra for a specific thermonuclear supernova progenitor at a series of times in the explosion. Except at low energies for the Höflich simulation, all codes agree. Figure 2 shows the 812-keV line fluxes for our models in comparison to past work (HWK98: Höflich, Wheeler, & Khokhlov 1998; Kum 97: Kumagai & Nomoto 1997). The large discrepancies of the past, which were previously explained as differences in physics implementations,

Figure 1— A sequence of spectra for the thermonuclear model, DD202C. The spectra, at 15d, 25d, and 50d, show the level of agreement between simulations for both the line and continuum emission. Comparisons between the two algorithms that do not treat line broadening/shifting (The Kumagai) and the others that do, show the early effects of blue-shifting. The HWK98 spectra clearly transitions from being brighter than the other spectra, to being fainter.



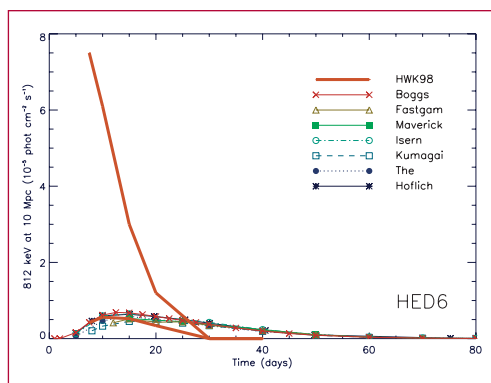
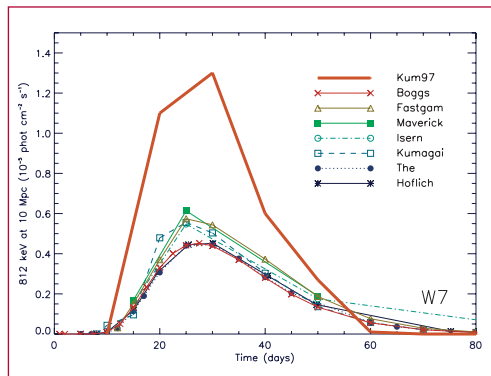
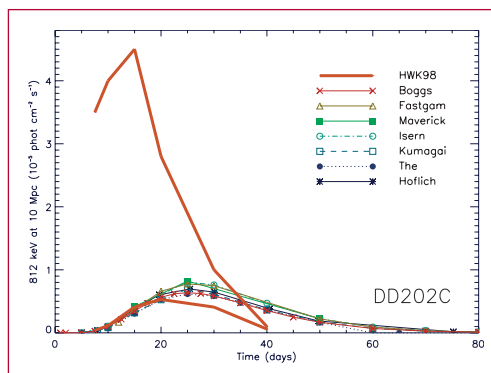


Figure 2—
Line fluxes of the 812-keV line for the supernova models, DD202C (upper panel), W7 (middle panel) and HED6 (lower panel). As with the 812-keV line emission, the spectral extraction and tagging light curves agree, and are fainter than the HWK98 and Kum97 light curves.

were merely errors in codes that we have now corrected. With the fixes, we not only can better interpret our observations, but we have gained a better understanding of the relative importance of the various physical effects included in the simulations.

With these more reliable calculations, astronomers can now more effectively interpret their gamma-ray line observations. But this project had a much more programmatic aspect. This project

allowed us to test the newly developed 3-D Direct Monte-Carlo code “Maverick” (CCS-4) on a new astrophysics problem. Using codes on as many different environments as possible can be a much more powerful test of a code than the standard test problems. The excellent performance of this new LANL-based 3-D code bolsters our confidence in its design and ultimately drives home the computational excellence at the Laboratory to the academic community.

R. W. Bussard, A. Burrows, and The L. S., *ApJ* **341**, 401 (1989).

W. Coburn and S. E. Boggs, 2003, *Nature* **423**, 415, *ApJ* **341**, 401 (1989).

P. Höflich, J. C. Wheeler, and A. Khokhlov, *ApJ* **492**, 228 (1998).

A. L. Hungerford, C. L. Fryer, and M. S. Warren, M. S. *ApJ* **594**, 390 (2003).

J. Isern, J. Gómez-Gomar, and E. Bravo, *Memorie della Societa Astronomia Italiana* **67**, 101 (1996).

S. Kumagai and K. Nomoto, “X-Ray Imaging and Spectroscopy of Cosmic Hot Plasmas”, Proceedings of an International Symposium on X-ray Astronomy ASCA Third Anniversary, 11–14 March, 1996, Waseda University, Tokyo. Edited by F. Makino and K. Mitsuda, 387 (1997).

E. Müller, P. Höflich, and A. Khokhlov, *A&A* **249**, L1 (1991).

T. Shigeyama, S. Kumagai, H. Yamaoka, K. Nomoto, and F. K. Thielemann, *A&AS* **97**, 223 (1993).

S. E. Woosley, D. Hartmann, and P. A. Pinto, *ApJ* **346**, 395 (1989).

Author Index

A

Abdallah, Jr., Joseph 42, 54
Addressio, Francis L. 100, 118
Akahane, Y. 54
Albers, Robert C. 98, 122
Alder, Berni 18
Aoyama, M. 54
Ashbaugh, Henry S. 84
Austin, Travis M. 36

B

Bardenhagen, Scott G. 154, 160
Baskes, Michael 126
Bergen, Benjamin K. 36
Berndt, Markus 32, 36
Blottiau, P. 50
Bouchet, M. Johan 122
Brand, Holmann V. 90, 108
Brown, Eric 108
Burakovsky, Leonid 8

C

Carlson, Neil N. 34
Chadwick, Mark B. 60, 62
Challacombe, William M. 88
Cherne, Frank J. 100
Chisolm, Eric D. 2, 4, 6, 10, 12, 14, 44, 100
Clements, Brad E. 108, 110, 116, 100
Collins, Lee A. 44, 50
Crockett, Scott D. 4, 6, 10, 12, 14, 44
Csanak, George 54, 76, 78

D

Daughton, William S. 78
Dattelbaum, Dana M. 90, 108
De Lorenzi-Venneri, Giulia 14, 130
Dendy, Joel E. 36
Desjournais, M. 44
Dienes, John K. 156
Dimonte, Guy 18

F

Faenov, A. Ya. 54
Fontes, Christopher J. 42
Fotiadis, Nikolaos 60
Frankle, Stephanie C. 60
Fryer, Christopher L. 168
Fukuda, Y. 54

G

Gan, Chee Kwan 88
Garimella, Rao V. 28
George, Denise C. 14, 110
Germann, Timothy C. 18, 102, 104, 144, 146
Gray III, George T. 108
Greff, Carl W. 100

H

Hadjiconstantinou, Nicolas G. 18
Hakel, Peter 42
Hale, Gerald M. 58, 70
Harlow, Francis H. 152, 162
Harstad, Eric N. 100, 108
Hatch, D. M. 98
Hay, P. Jeffrey 84
Hayes, Anna C. 72
Hayes, Dennis B. 100
Heim, Andrew J. 144
Hennig, R. G. 98
Henson, Neil J. 90, 108
Holian, Brad Lee 18, 86, 102, 104, 144, 146
Hungerford, Aimee L. 168

I

Inoue, N. 54

J

Jaramillo, Eugenio 134
Jensen, Niels G. 144
Johnson, J. D. 14
Johnson, James N. 100
Jones, M. D. 98
Jungman, Gerard 72

K

Kadau, Kai 18, 102, 104
Kawano, Toshihiko 62
Kilcrease, David P. 42
Kober, Edward M. 92, 106, 144, 158
Kress, Joel D. 44, 50, 84, 86, 94
Kress, Kerri Jean 90, 108
Kuprat, Andrew P. 22

L

Lewis, Matthew W. 108
Lipnikov, Konstantin, 30
Lomdahl, Peter S. 18, 102, 104
Lookman, Turab 106
Loubère, Raphaël 26

M

MacFarlane, Robert 60, 62
Maciucescu, Luca A. 108
Madland, David G. 62
Magee, Norman H. 42, 44
Magunov, A. I. 54
Mas, Eric M. 100, 108, 110, 116
Maudlin, Paul J. 116, 118
Mazevet, Stephane F. 42, 44, 50
Menikoff, Ralph 148
Middleditch, John 156
Milne, Peter A. 168
Möller, Peter 62, 64
Morel, Jim E. 30
Moulton, John D. 36
Murillo, Michael S. 76, 78

N

Nelson, Ronald O. 60

O

O'Rourke, Peter J. 24
Orler, Edward B. 108

P

Pack, Russell T 94
Padiál-Collins, Nely 20, 152
Page, Philip R. 70
Pikuz, T. A. 54
Preston, Dean L. 8

R

Rae, Philip 108
Rasmussen, Kim Ø. 106
Redondo, Antonio 86
Reichhardt, Cynthia 86
Robbins, David L. 108
Rudin, Sven P. 98, 100, 120, 124
Ryan, Jessica M. 90, 108

S

Salazar, Michael 94
Schlei, Bernd R. 114
Schraad, Mark W. 162
Sewell, Thomas D. 88, 134
Shashkov, Mikhail J. 26, 30, 32, 34, 38
Shaw, M. Sam 150, 164
Sheffield, Stephen 108
Sherrill, Manolo E. 42, 48
Skobelev, I. Yu. 54
Smith, Grant D. 158
Smith, James S. 158
Smith, Justin R. 118
Srivilliputhur, S. G. 98
Staley, Martin F. 38
Stokes, H. T. 98
Strachan, Alejandro H. 136, 140
Swartz, Blair K. 28

T

Talou, Patrick 60, 62
Thompson, Russell B. 106
Torres, David J. 24
Trellue, Holly R. 60
Trinkle, D. R. 98

U

Uberuaga, Blas P. 126
Ueda, H. 54

V

Valone, Steven M. 126
VanderHeyden, W. Brian 20, 152
Voter, Arthur F. 126

W

Wallace, Duane C. 2, 4, 6, 10, 12, 14, 100, 130
White, Morgan C. 60
Wilkins, J. W. 98
Williams, Todd O. 100
Wills, John M. 4, 14, 100, 120
Wilson, William B. 62, 64

Y

Yamakawa, K. 54
Young, Phillip G. 62

Z

Zhang, Duan Z. 152
Zhang, Honglin 42
Zou, Qisu 152
Zuo, Q. Ken 100, 118, 156

